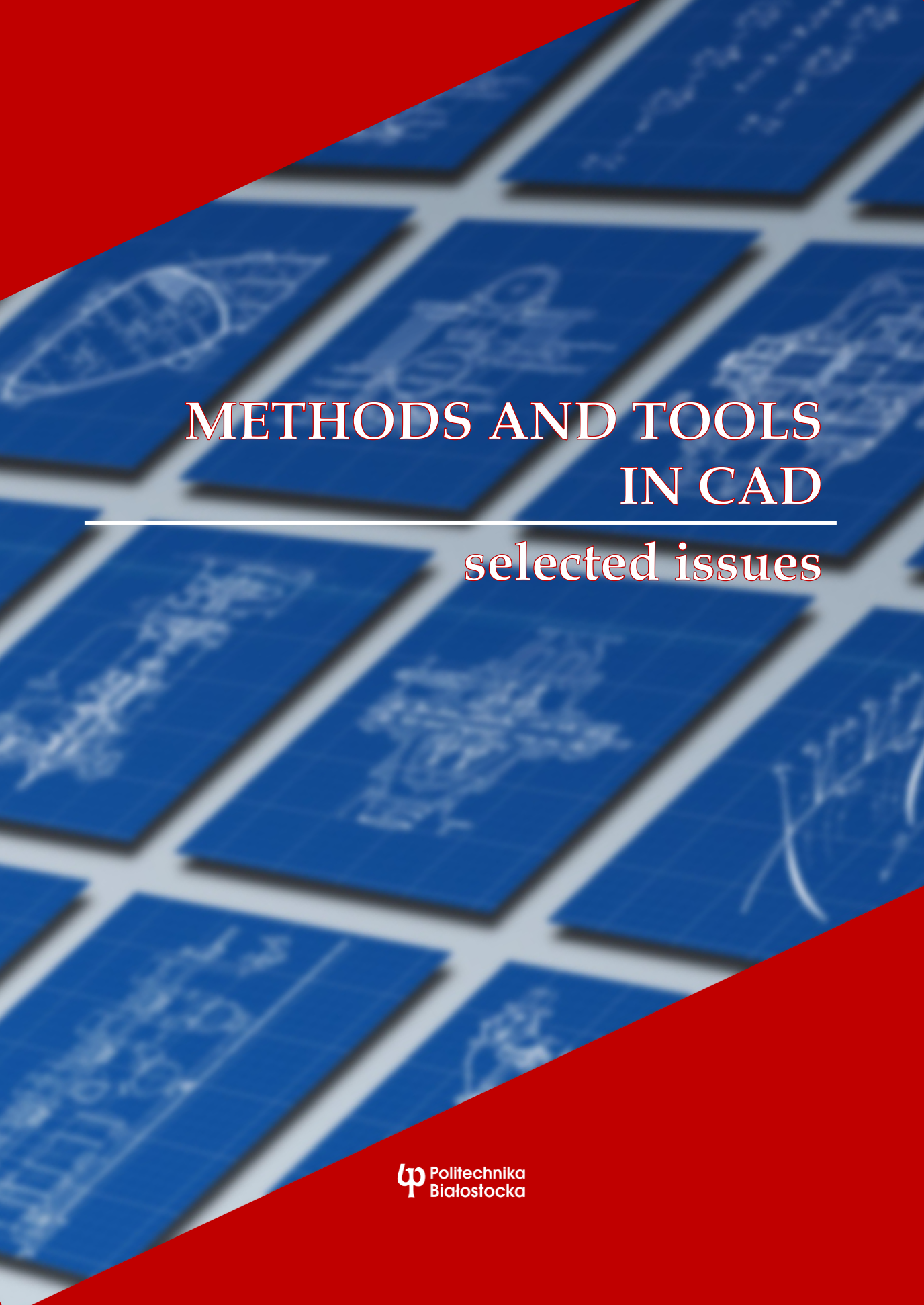

METHODS AND TOOLS IN CAD

selected issues

Politechnika Białostocka

METHODS AND TOOLS IN CAD

selected issues

Editor
Bogusław Butryło

Politechnika Białostocka

Publishing House of Bialystok University of Technology
Białystok 2021

Reviewers:
Prof. Tomasz Węgrzyn, PhD, DSc
Assoc. Prof. Bartosz Sawicki, PhD, DSc, Eng

Science editor in the discipline of automation, electronic and electrical engineering:
Prof. Jan Dorosz, PhD, DSc

Copy editor:
Andu Dukpa

Photo on the cover:
xresch, pixabay.com
https://pixabay.com/pl/photos/blueprint-techniczne-rysunek-5090067/

ISBN 978-83-66391-87-1 (eBook)
DOI: 10.24427/978-83-66391-87-1

The publication is available on the Internet
on the site of the Publishing House of Białystok University of Technology.

Publishing House of Białystok University of Technology
Wiejska 45C, 15-351 Białystok, Poland
e-mail: oficyna.wydawnicza@pb.edu.pl
www.pb.edu.pl

CONTENTS

PREFACE

Computer Aided Design (CAD), over the years, has become one of the best methodologies for fulfilling engineering and technological needs through advanced numerical methods. CAD is considered as a mature solution, however analysis of current studies and practical examples indicate it as a deceptive illusion. CAD technology remains a rapidly growing class of methods and numerical schemes with applications in industries such as electronic, automotive, civil engineering, mechanical, biomedical and multidisciplinary projects.

A number of books and papers are available on computer aided design and computer aided engineering methods. In the design, manufacturing and application processes, a thorough understanding of the properties of various technical solutions is required. Using numerical simulations, we are able to verify design assumptions, predict variations in properties and increase productivity. The current state of CAD solutions is confronted with new challenges. Specific, sophisticated engineering solutions demand the search for new algorithms as well as determine new areas of implementation. The specific methods of CAD are of interest in many industrial applications involving automation, electric and electronic instruments, electrical systems, motors, renewable energy, wireless communication, material technologies, etc. The numerical simulations can reveal valuable information on the analyzed system. Multivariate analysis and design optimization are obvious and well known extensions of CAD methods and the importance of which cannot be overestimated.

The aim of this book is to provide a broad overview of CAD algorithms and to discuss the applications of CAD methods in different areas. Presentation of issues related to diverse fields provide an opportunity to learn specific solutions and it also provides an opportunity to explore wider responses for the developed methods in other areas. The analysis of various fields serves as an illustrative presentation of the strength of CAD methods.

I would like to thank the authors for their contribution and research outputs. I am very hopeful that researchers and engineers will find this book as a useful source of information with several applications of CAD in various fields of engineering and technology.

Bogusław Butryło

Białystok, May 2021

DOI: 10.24427/978-83-66391-87-1_01

Andrzej ŁUKASZEWICZ[1], Roman TROCHIMCZUK[1],
Mykhaylo MELNYK[2], Andriy KERNYTSKYY[2]

1. DESIGN OF MECHATRONICS SYSTEMS USING CAX ENVIRONMENT

Modern mechatronic systems are a combination of mechanical engineering with electrical/electronic devices integrated by control as one real system. On the other hand, we can define mechatronic system as an intelligent connection of physical components (hardware) with information processing (software) [4, 10]. The word *Mechatronics* is described by Harashima, Tomizuka and Fukuda in 1996 [8] as: *the synergetic integration of mechanical engineering with electronic and intelligent computer control in the design and manufacturing of industrial products and processes*.

As suggested by Bishop and Ramasubramanian [1], mechatronic systems can be divided into the following modules (subsystem):

- physical systems,
- sensors and actuators,
- signals,
- computers and logic systems,
- software and data acquisition.

The complexity of mechatronic systems, resulting from the interaction of subsystems from various disciplines, requests the use of a proper, multidisciplinary design methodology and appropriate CAx (Computer-Aided technologies) tools [7, 15]. Coupling of modelling and simulation tools from the different areas of mechatronics in MCAD (Mechanical CAD) system is one of the important points to decrease the time of product development [9].

Nowadays, in addition to specialized companies, technical universities have become serious competitors in the progress of mechatronic systems. This is possible mainly because of development of new materials, manufacturing methods, computer technology and electronics. Modern computer-aided design tools are widely available and are used by both industries and universities for modern engineering education [6].

[1] Bialystok University of Technology, Poland
[2] Lviv Polytechnic National University, Ukraine

The information technology revolution, wireless communication, MEMS technology, and the development of multidisciplinary approaches (Fig. 1.1) allow the creation of new solutions [13]. Future will be dominated by mechatronics.

In this paper, functional workflow in mechatronics design process between MCAD and ECAD (Electrical/Electronical CAD) tools in one CAx environment is presented.

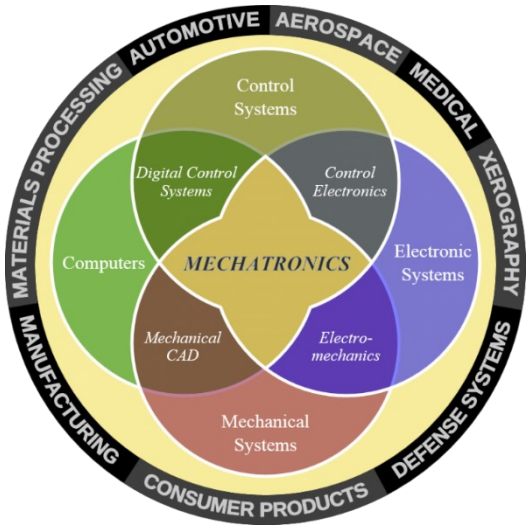

Fig. 1.1. Mechatronics system's components in a multidisciplinary space [16]

1.1. MECHATRONIC DESIGN

1.1.1. STRUCTURE OF MECHATRONIC SYSTEM

The main structure of the mechatronic system is defined by the following components: the system, the actuators and the sensors connected by the information processing unit. A flowchart of typical structure is presented in Figure 1.2.

The system unit has generally mechanical, electromechanical, hydraulic or pneumatic structure or it can be a combination of them. It means that a specified physical system can be understood as a particular system that can be characterized by a hierarchically structured system. The aim of *the sensors* is to determine a chosen state variable value of the system. The state variables can be understood as the physical variables fully determined for a sampling interval by their values at sampling time t_0. This ensures that the state variables for time $t > t_0$ are known. In this case, the sensors can be physically represented by the measured values or software sensors so called *observers*. *The sensors* supply input variables for the information processing, usually digital, i.e. discrete in terms of values and time. The information processing is done by a microprocessor although it can be also done by a fully analog or a hybrid analog/digital electronics. It determines

actions needed to affect the state variables of the system. An implementation of the actions is directly on the system by *the actuators* [2].

Relations between main units of mechatronic device: *the system*, *the sensors*, *the actuators* and *the information processing* are connected by flows. Generally, there are three types of flows [2]:

- material flow,
- energy flow,
- information flow.

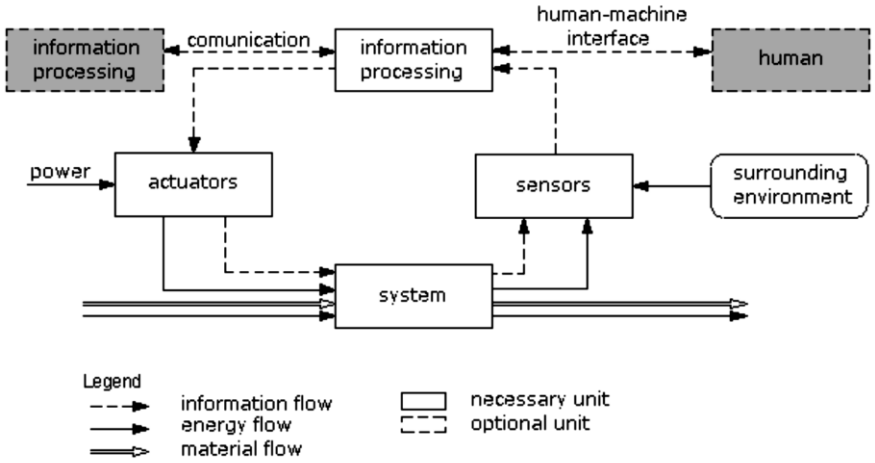

Fig. 1.2. The main structure of mechatronic system [2]

Examples of material flow between mechatronic system units are solid bodies, tested objects, processed objects, gases or liquids.

Energy flow is a different form of energy, for example mechanical, thermal or electrical but also action variables (e.g. force or current).

Information flow means the information transferred between the units of the mechatronic system, for example measured variables, pulse control or data.

1.1.2. DESIGN METHODOLOGY ACCORDING TO THE VDI 2206

The Association of German Engineers (VDI) in 2004 published the design methodology for mechatronic systems VDI 2206 [14]. The purpose of this guideline is to support the development of mechatronic products using a methodical approach. The VDI 2206 describes a flexible model, which can be used for the development of the product. The general workflow in VDI 2206 guideline is presented by the V-Model (Fig. 1.3) and can be described in the following stages:

- the main, initial model of mechatronic system is divided into modules (subsystems) with top-down direction, modules are decomposed into assemblies to obtain components like single parts (bottom level of system's structure),

- the behaviour of the system is predicted using simulation,
- bottom-up integration process with validation and verification of every level is used to obtain the main properly-defined mechatronic system (top level of structure).

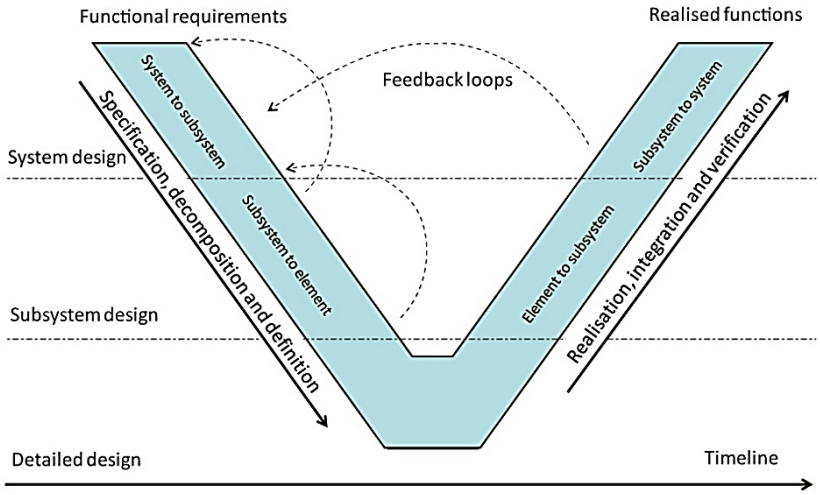

Fig. 1.3. V-model for mechatronics systems design [17]

Stages of mechatronic task solution [4]:

- problem definition of system (task to perform),
- determination of the functional structure,
- division into independent modules (subsystems),
- division of each module into the single-part structure,
- determination of the possible solution for each module,
- choose the best solution for subsystems,
- collect and/or manufacture of the components,
- integration of the components,
- functional testing of the prototype,
- documentation and presentation of the result.

1.2. MCAD POSSIBILITIES

CAx environment in mechanical engineering gives the possibility of designing a 3D virtual model (CAD) and then performing series of numerical simulations like strength analysis or flow and heat transfer (CAE), development of the technology (CAM) and creation of 2D drafting [12]. Computer-aided design however, is only a tool in the hands of engineers, therefore it is important to choose or elaborate suitable strategies for the creation of a virtual model of real objects [11]. We can distinguish various types of models such as solid, surface, hybrid (surface-solid) and multibody. Usage of these techniques depends on the complexity of the project and its purpose.

Multibody modelling technique expands the opportunities for part module and speeds up editing and possible modification of the project [3]. In single part file, we can create and adjust bodies with irregular, complicated shapes and then save them as multibody part. This kind of operation minimizes errors resulting from incorrect modelling when creating individual parts and also improves assembly stage [5].

Usage of hybrid techniques gives us possibility to create various difficult surfaces and then recreate them into solid object for proper analysis.

Complex shapes and construction of modern mechatronic solutions require the use of advanced modelling techniques based on multibody modelling combined with hybrid modelling. These techniques significantly affect the acceleration and accuracy of the design process.

1.3. MCAD AND ECAD COLLABORATION

Nowadays, CAx systems enable bi-directional collaboration between electrical (E-team) and mechanical (M-team) teams. For example, most commercial CAx systems use the ProSTEP protocol based on XML to PCB (Printed Circuit Board) design. It is an independent format that allows communication between ECAD and MCAD tools [18]. Platform for communication should allow error-free changes using only digital data. Collaboration between specialists working on the same project is carried out using PDM or PLM (Product Lifecycle Management) software dedicated for specific CAx environment. General structure of CAx tool levels and connection with IT is shown in Fig. 1.4.

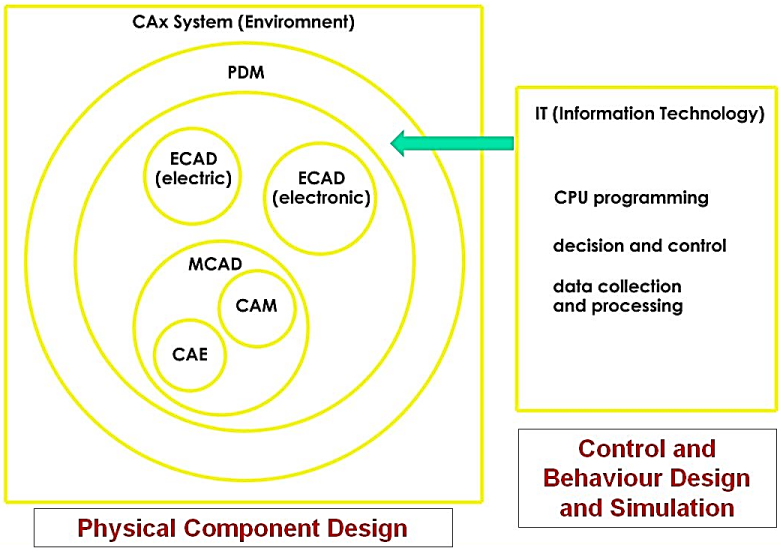

Fig. 1.4. General structure of CAx system and IT environment

Example of CAx system that use bi-directional collaboration between E-team and M-team is SolidWorks environment. Fig. 1.5 presents MCAD and ECAD tools in this CAx system. Different ECAD tools for electronic design (SolidWorks PCB) and for electric design (SolidWorks Electrical) [19] are shown here.

Electronics design solution (SolidWorks PCB) provides PCB design technology with an integrated electro-mechanical collaboration solution. It has two modules [20]:

- PCB schematics (electrical components library, schematic symbols, wiring), 2D,
- PCB layout (board shape, placement electronics components, routing of electrical traces, generate 3D electronics parts) 2D and 3D, ECAD to MCAD.

The M-team will try to mount or attach the PCB to the mechanical assembly. If the PCB does not fit perfectly with the M-design, the M-team can suggest or make some mechanical changes or modifications to the existing PCB layout. Next, push these changes back to the E-team. Example of designed PCB is shown in Fig. 1.6.

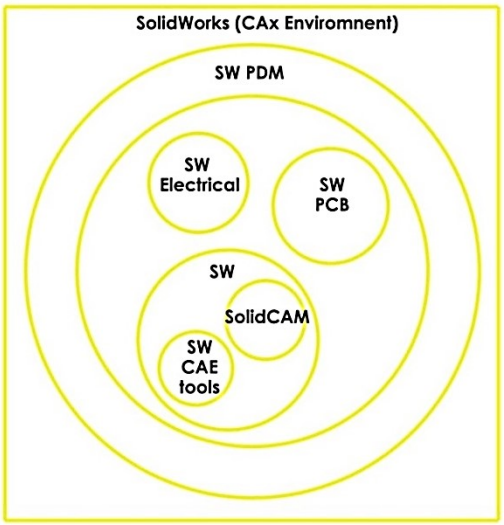

Fig. 1.5. MCAD and ECAD tools in SolidWorks environment

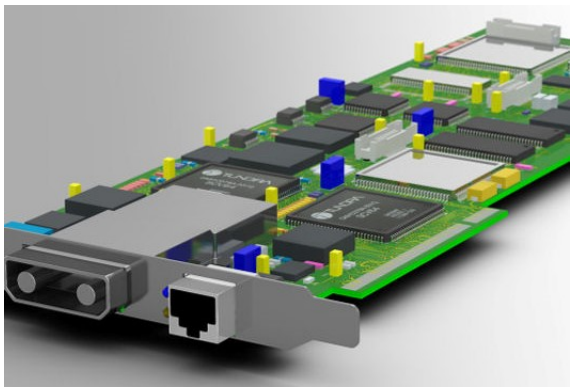

Fig. 1.6. PCB designed in ECAD (electronics design solution) [18]

Electrical 3D software (SolidWorks Electrical) enables users to convert 2D electrical system to 3D electrical system that includes: enclosure design, general arrangement, power systems, connectors, wires and cable routing and wire harness (Fig. 1.7). Capabilities include [20]:

- easy and correct placement of components,
- wire and cable length calculation,
- auto route functionality,
- create 3D general arrangement drawings based on the electrical schematic,
- harness development.

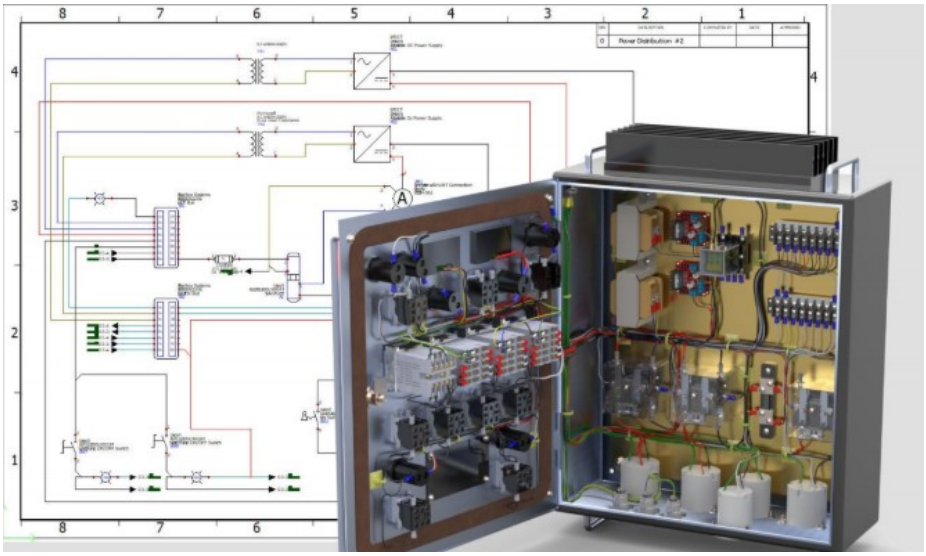

Fig. 1.7. Product designed in ECAD (electrical design solution) and MCAD [21]

1.4. CONCLUSIONS

Multidisciplinary nature of mechatronic systems enables flexible cooperation of many specialists from various industries. New methods of mechatronics systems design should include the security of product data and proper division of tasks in the team. Nowadays, it is necessary to teach both MCAD and ECAD tools in the field of mechatronics, as well as electronics and mechanical engineering.

Advanced modelling techniques minimize the possibility of errors in the early stages of design. Combining the above-described techniques provide us with an opportunity to create more advanced project in much less time than using traditional techniques. Multibody modeling used during assembly stage reduce number of parts involved in the operation tree, significantly affecting the acceleration and accuracy of the design process.

Development of data interchange protocols between MCAD and ECAD modules in CAx environment should take into account the possibility of saving data in neutral

format. Team communication and cooperation rules should be defined if team uses PDM. CAx tools must be compatible across engineering disciplines.

The information technology revolution, wireless communication, MEMS technology, development of multidisciplinary approaches allow the creation of new mechatronics solutions.

REFERENCES

[1] BISHOP R.H., RAMASUBRAMANIAN M. K., What is mechatronics, in: *Mechatronics: An Introduction*, Bishop R.H. (Ed.), CRC Press, 1.1–1.10, 2006.

[2] BREZINA T., SINGULE V., *Design of Mechatronic Systems*, Brno University of Technology, 2006 (http://www.umt.fme.vutbr.cz/images/opory/Design of Mechatronic Systems/1UM.pdf, accessed: 23.03.2020).

[3] CAMBA J. D., CONTERO M., COMPANY P., Parametric CAD modeling: An analysis of strategies for design reusability, *Computer-Aided Design*, vol. 74, p. 18–31, 2016.

[4] CARRYER J. E., OHLINE R. M., KENNY T. W., *Introduction to Mechatronic Design*, Prentice Hall, 2011.

[5] COMPANY P. et al., On the role of geometric constraints to support design intent communication and model reusability, *Computer-Aided Design & Application*, vol. 17, No.1, p. 61-76, 2020.

[6] DANKWORT C. et al., Engineers' CAx education - it's not only CAD, *Computer-Aided Design*, vol. 36, p. 1439–1450, 2004.

[7] FOTSO A. B., RETTBERG A., State of the art for mechatronic design concepts, in: *Proceedings of 8th IEEE/ASME International Conference on Mechatronic and Embedded Systems and Applications*, Suzhou, p. 232-240, 2012.

[8] HARASHIMA F., TOMIZUKA M., FUKUDA T., Mechatronics-"What Is It, Why, and How?", *IEEE/ASME Transactions on Mechatronics*, vol. 1, No. 1, p. 1–4, 1996.

[9] HEHENBERGER P. Application of mechatronical CAD in the product development process, *Computer-Aided Design and Applications*, vol. 6, No 2, p. 269-279, 2009.

[10] ISERMANN R., *Mechatronic Systems: Fundamentals*, Springer Science & Business Media, 2007.

[11] ŁUKASZEWICZ A., Modelling of solid part using multibody techniques in parametric CAD systems, *Solid State Phenomena*, vols. 147-149, p. 924-929, 2009.

[12] ŁUKASZEWICZ A., SKORULSKI G., SZCZEBIOT R., Main aspects of training in the field of computer aided techniques (CAx) in mechanical engineering, in: *Proceedings of 17th International Scientific Conference on Engineering for Rural Development*, p. 865-870, 2018.

[13] MELNYK M. et al., Custom method for automation of microbolometer design and simulation, in: *Proceedings the 22nd IEEE International Conference of Mixed Design of Integrated Circuits and Systems (MIXDES)*, p. 301–304, 2015.

[14] Verein Deutscher Ingenieure, *VDI 2206: Design methodology for mechatronic systems*, Beuth Verlag, Berlin, 2004.

[15] ZHENG C. et al., Multidisciplinary interface model for design of mechatronic systems, *Computers in Industry*, vol. 76, p. 24–37, 2011.

[16] https://www.meee-services.com/differences-between-mechatronics-and-electromechanics/ (accessed: 23.03.2020).

[17] https://rmsacoustics.nl/mechatronics.html (accessed: 23.03.2020).

[18] http://www.ecad-mcad.org/ (accessed: 23.03.2020).

[19] https://www.javelin-tech.com/blog/2018/06/ecad-connected-solution-solidworks/ (accessed: 23.03.2020).

[20] https://hawkridgesys.com/solidworks/ecad/pcb (accessed: 23.03.2020).

[21] https://www.alignex.com/solidworks-electrical-design-accelerated (accessed: 23.03.2020).

DOI: 10.24427/978-83-66391-87-1_02

Cezary MAJ[1], Jacek NAZDROWICZ[1], Adam STAWIŃSKI[1]

2. FRINGING FIELD MODELLING IN MEMS CAPACITIVE COMB-DRIVE ACCELEROMETERS

Modelling is a crucial step in designing MEMS devices. It is needed to estimate the device performance without its fabrication. Initially, simple calculations are needed to verify the possibility of device production with a given performance and to know the basic parameters necessary to achieve the desired goals. Further, optimization is commonly performed in order to improve the design. Both steps require simulation methods that are very fast and precise enough to reduce time to market. In many cases, classical, precise FEM simulations are not necessary and simple analytical models are used. MEMS devices like accelerometers, commonly uses elements of simple shapes that can be easily described with simple analytical formulas. However, analytical modelling is getting more complicated in case of capacitive transduction. Typically, these devices operate in the range of linear response but nothing can be done to avoid the influence of non-uniform electric field. Due to fringing field, a capacitance is often underestimated when using classical parallel plate formula. Therefore, there is a need for proper fringing field modelling. In this chapter, analytical modelling of fringing field on an example of MEMS accelerometer is presented. Specific structure type known as comb-drive consists of many small capacitors that enhance the impact of fringing field. Accelerometers in all axes are analyzed. Moreover, Z-axis accelerometer induces different electric field distribution due to the use of thinned fingers. Thus, analytical formulas are derived for various conditions. Finally, the model is compared with Coventor MEMS+ and fabricated strictures are measured in order to validate analytical approach.

2.1. INTRODUCTION

Accelerometers are one of the most popular devices in the world. They are used in the measurement of angular and linear acceleration of vehicles, machines and other devices

[1] Lodz University of Technology, Poland

used e.g., in inertial navigation [1]. Ever since MEMS technology appeared in the market, the production of MEMS accelerometers continues to grows every year. Due to miniaturization, they are used in almost any mobile devices in detection of spatial orientation and its function controlling with movement [2]. One estimates that there are dozens of accelerometers per person. The most attractive are the capacitive accelerometers due to their high sensitivity, low power consumption and low temperature dependence [3]. Although, the principle of operation remains the same as that of *old-type* sensors, modelling and simulation steps are still necessary to obtain the desired performance. In addition, proper design path allows the shortening of time to market and reduction in the cost of development.

One of the most common and reliable method used during the conception phase is FEM (finite element method) simulation [4]. Three-dimensional model of the sensor is built with desired precision and subsequently divided into nodes (meshing process). Each node is described with equations (the number depends on used types of domains) that are usually differential. Therefore, the complexity of the model influences the number of equations that needs to be solved. Even though the computing power of today's computer is very high, simulation may take longer time to give result. This is particularly noticeable in optimization process. Thus, a faster approach is desirable. Note that during the initial design phase, the designer needs the basic information about the possibility of creating a sensor with imposed parameters. Thereafter, the designer needs the information of the range of sensor dimensions and basic performance (needed for read-out circuit). The use of FEM simulation seems to be unreasonable as it requires the creation of a 3-D model which is time consuming.

An alternate approach is to use analytical modelling [5]. The device is considered as one element and a few analytical equations are formed to describe its behavior. In general, these equations have simplified form e.g., approximated solution of differential equation. Therefore, the solution is very fast and it may be performed without any dedicated software (e.g., with the use of spreadsheet). Moreover, this model can be simply parametrized and used for devices of almost any shape and any dimensions and also used in optimization phase [6, 7]. Note that simplified models are mostly used in devices with regular and simple shapes to obtain high precision. Nevertheless, final product should be verified with FEM simulation in order to obtain the results that takes into account all possible factors omitted in the analytical model.

The need for a simpler and faster models create demand for a software that combines the advantages of analytical modelling (simulations time) and FEM (precision, complex shapes). One of the most promising is Coventor MEMS+ that allows simulating many popular MEMS devices like accelerometers, gyroscopes, microphones, micro-switches, micro-mirrors etc. It still uses meshing but not in a conventional way. Therefore, the simulations are hundred times faster than FEM simulators with very high precision. It should be mentioned that MEMS+ does not allow simulating complex structures but this inconvenience does not reduce its functionality. It has built-in shapes that are commonly used in MEMS devices, typical feature used in analytical models. Moreover, MEMS+ is integrated with other Coventor packages and provides designing of MEMS devices with

IC circuits and packaging. The model can also be exported to Cadence environment in order to perform full IC simulation and automatic layout generation.

Accelerometers are simple devices that can be described with analytical model. They consist of elements of basic shapes where movement and deformation are described with well-known basic formulas. Combining mechanical domain with others needed for describing the type of transduction (electrical, piezoelectric, piezoresitive) is an effortless task. Sometimes, iterative calculations are required however, set of equations have polynomial form which makes it easier to solve. The only factor that affects the accuracy of calculations is the model reduction by omitting certain phenomena. In our consideration, capacitive accelerometers are analyzed. Transduction that uses electric field cannot be simply described with one formula. Fringing fields are underestimated in case of commonly used parallel plate capacitor equation. If accelerometer is a comb-drive type, the accuracy of calculation results are insufficient. In this chapter, we will show how to model fringing field accurately in capacitive comb-drive accelerometers.

2.2. MODELLING OF COMB-DRIVE ACCELEROMETER

2.2.1. PRINCIPLE OF OPERATION

Inertial MEMS accelerometers consist of a proof-mass that is suspended with springs attached to a fixed frame as shown in Fig 2.1.

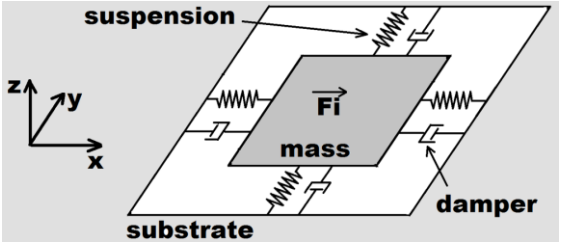

Fig. 2.1. Schematic of MEMS accelerometer

When acceleration is applied, the inertia force acts on the proof-mass causing its displacement from initial position. Springs allows to counteract the inertia force in order to get to equilibrium state. Proper design of springs allows sensing the acceleration in desired direction. The proof-mass moves in *XY* plane in case of *XY*-axis accelerometer and moves in *Z* direction in case of *Z*-axis accelerometer. Capacitive transduction uses a capacitor formed with the proof-mass and fixed part of the sensor. Therefore, two types of accelerometers are used depending on the sensing axis (Fig. 2.2). *XY*-axis accelerometers use comb-drive structure that increases the effective area of capacitor plates [10]. *Z*-axis accelerometers typically use parallel plate structure wherein, bottom plate is placed beneath the proof-mass [10]. Nevertheless, in some cases, comb-drive structures are also used due

to technological restrictions. In both cases, proof-mass movement causes capacitance change that is converted into electrical signal with read-out circuit.

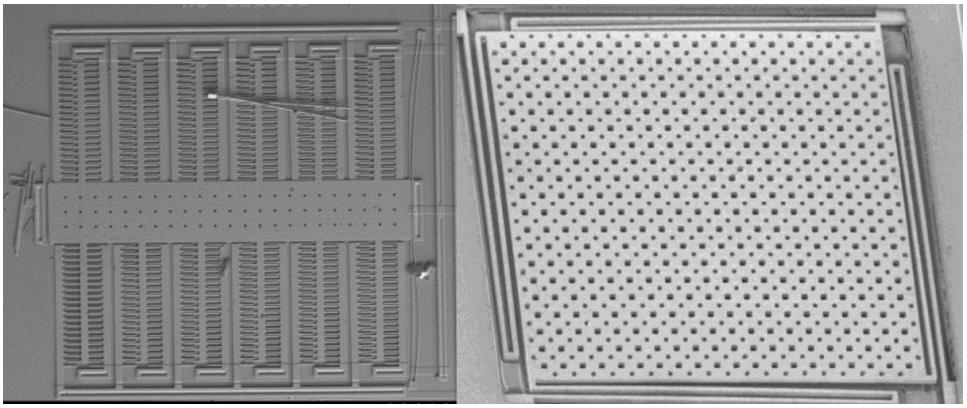

Fig. 2.2. Photos of comb-drive accelerometer (left) [8] and parallel plate accelerometer (right) [9]

2.2. FRINGING FIELD

Let us analyze a parallel plate capacitor, the most commonly used structure in electronic devices. It consists of two plates arranged in parallel. The overlapping surfaces allow to obtain uniform electrostatic field between plates when a voltage is applied on them. In MEMS devices, one of the plates is movable. Thus, the capacitor has variable capacitance. In general, this plate is moving in a direction normal to the plate plane to keep the same overlapping surface during the operation. The capacitance is then calculated with the following equation that takes into account the dimensions of the structure

$$C = \varepsilon \frac{S}{d}, \tag{2.1}$$

where ε is the permittivity of environment, S is the area of plate forming the capacitor and d is the gap distance between plates. However, this formula is valid only for infinitely large parallel plates because it takes into account uniform electric field between plates only. Therefore, devices should have plates as large as possible. In real cases, the electric field exists outside the overlapping surfaces as show in Fig 2.3.

Some works have reported that the real capacitance is almost 45% higher than the value obtained with equation (2.1) [11]. Therefore, equation 1 should be modified in order to take into account the fringing field, which is possible using the definition of capacitance (the ratio of the charge and electric potential). However, it requires solving Maxwell's equation. Thus, alternate methods that makes use of modification of equation (2.1) [12-16] are also available. Note that the influence of fringing field depends on the dimension of the plates (more precisely, the ratio of the length of the plates' edges and plates' area) and gap distance [17]. Second term plays an important role as the gap distance is usually very small and therefore, the results obtained with equation (2.1) are more accurate.

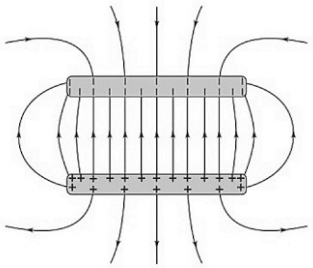

Fig. 2.3. Electric field distribution in parallel plate capacitor

2.3. COMB-DRIVE STRUCTURE

The fringing field effect in comb-drive structure is more complex. Such structure consists of several fingers that forms multiple small capacitors (Fig. 2.4). In addition, there are two capacitors for each finger, the main with small gap and parasitic between each pair of fingers. Although this second gap is much larger, it still plays a role in capacitance (up to 40%). Larger gap distance produces greater impact of fringing field as mentioned in previous paragraph. Additionally, overlapping of combs generate different electric field distribution (Fig. 2.5). In the area between fingers and fixing points, the electric field is closer to linear with rather small distance. Thus, one expects significant impact on the total capacitance.

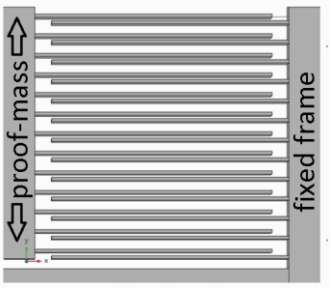

Fig. 2.4. Comb-drive structure in typical *XY*-axis accelerometer

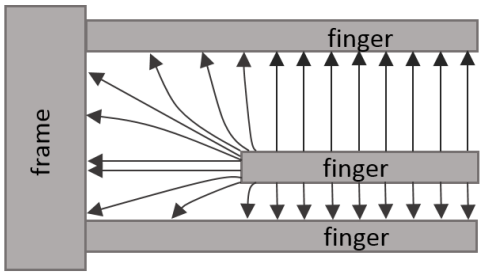

Fig. 2.5. Fringing field in comb-drive structure

The fringing field effect is more complex in the case of *Z*-axis accelerometer. Comb-drive structure is used due to the lack of cavity electrode. The design of such structure is not intuitive. If we redesign the suspension to obtain the deflection of the proof-mass in *Z*-direction, the change in capacitance is independent of the sense of the direction of acceleration. Therefore, such sensors use asymmetrical proof-mass to obtain its rotation [18]. Additional modification is the use of thinned fingers as presented on the X-FAB micromachining process description (Fig. 2.6). Thereafter, two main capacitances are distinguished: each on opposite sides of the sensor (left and right). When the proof-mass rotates in one direction, left combs move down and right combs move up (Fig. 2.7). Due to thinner fingers in the left combs, the corresponding capacitance will decrease while the second one will increase. In the case of opposite direction of proof-mass rotation, the

capacitances also change in the opposite directions respectively. Note that the suspension must be designed in such way to obtain proof-mass twisting. Moreover, suspension bending in Z direction should be negligible.

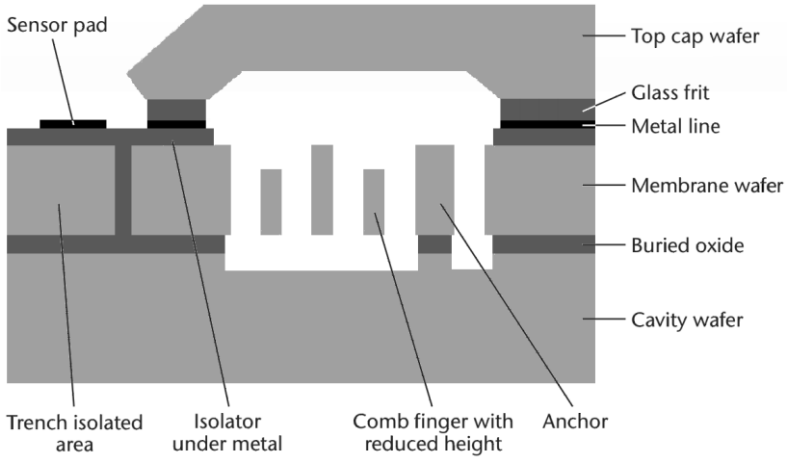

Fig. 2.6. Surface micromachining process cross section [19]

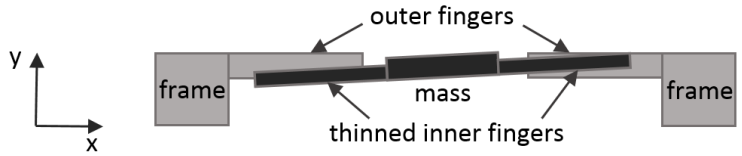

Fig. 2.7. Proof-mass rotation in *Z*-axis accelerometer

2.4. FRINGING FIELD MODELLING

The mechanical description of the sensor is described in [20]. This section will focus on the electrical domain and the computation of the initial capacitance (without acceleration). We start with the previously mentioned equation (2.1). Due to the existence of many fingers, the equation will need to be written in the following form

$$C = n\varepsilon\frac{S}{d}, \tag{2.2}$$

where n is the number of fingers in the inner or outer combs, ε is the permittivity of environment, S is the area of finger forming the capacitor (overlapping surface) and d is the gap distance between fingers. As mentioned earlier, each pair of fingers that form the main capacitance is close enough to the next pair and this capacitance has to be taken into account. Therefore, the capacitance is

$$C = n\varepsilon\frac{S}{d_1} + (n-1)\varepsilon\frac{S}{d_2}, \tag{2.3}$$

where d_1 is the distance between fingers in pair and d_2 is the distance between pairs of fingers (Fig. 2.8). Note that the number of capacitors formed by pair of fingers is one less than the number of capacitors formed by fingers in pairs.

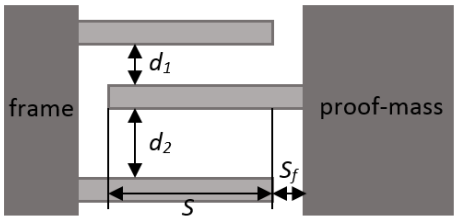

Fig. 2.8. Geometry of capacitors formed by fingers

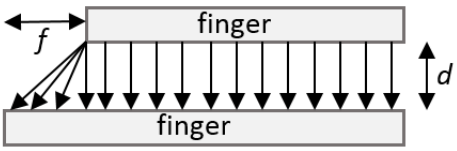

Fig. 2.9. Geometry of capacitors formed by fingers

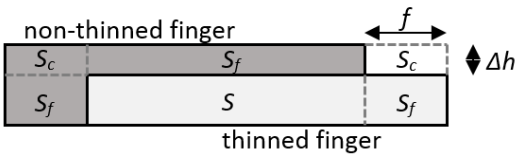

Fig. 2.10. Non-overlapping surfaces in case of thinned fingers

Equation 2.3 allows the calculation of the capacitance that results from the linear electric field between overlapping surfaces (S in Fig. 2.8). Next, the formula for calculating the capacitance resulting from fringing field will be derived. In order to simplify the calculations, suitable assumptions will need to be made. The electric field for non-overlapping area S_f is assumed to be linear as shown in Fig. 2.9. Thereafter, we can calculate the mean distance d_m between fingers and use classical formula for capacitance (equation 2.1) as follows

$$C_f = \varepsilon \frac{S_f}{d_m}, \quad d_m = 0.92 \frac{d + \sqrt{d^2 + f^2}}{2}, \tag{2.4}$$

where f is the length of non-overlapping part of the finger. The constant 0.92 in equation (2.4) is set experimentally as the calculation of the exact mean value is complicated. This value is correct for ratio f/d up to 10 (typical in most accelerometers). Equation (2.4) has to be used for all non-overlapping surfaces, those corresponding to fingers and those corresponding to proof-mass and frame. Note that in case of Z-axis accelerometer, additional non-overlapping surfaces exist due to fingers thinning. All non-overlapping surfaces are marked in Fig. 2.10. In case of corner areas S_c, the calculation is made in a similar way as previously described using the following formulas

$$C_c = \varepsilon \frac{S_c}{d_{mc}}, \quad d_{mc} = 0.92 \frac{d + \sqrt{d^2 + f^2 + \Delta h^2}}{2}, \tag{2.5}$$

where d_{mc} is the mean value and Δh is the difference in the height between fingers.

2.3. RESULTS AND COMPARISON WITH MEMS+

In our previous works, we designed *XY*-axis and *Z*-axis accelerometers [17, 20]. These accelerometers are designed in compliance with X-FAB technology [19]. Thus, the thickness of sensor layer is 30 μm and all accelerometers use comb-drive structure. *Y*-axis accelerometer uses H-shape proof-mass with four springs on each ending. This shape allows placing the combs outside and inside the proof-mass. The thickness of fingers is as small as possible in this technology (2 μm). Its length is 75 times larger (technological limit). The distance between fingers is 2 μm (as small as possible) in order to obtain high initial capacitance. The distance between each pair of fingers is set to 6 μm to minimize undesirable electrostatic force between these fingers. Separation distance between fingers and fixing points is set to 10 μm. *X*-axis accelerometer has the same structure but scaled with a factor of 1.5. The idea was to investigate the behavior of the sensor with higher sensitivity but with possible non-linear response. *Z*-axis accelerometer differs significantly due to the rotational response of the sensor. The main dimensions of fingers are taken from *X*-axis accelerometer to obtain higher sensitivity as the use of asymmetrical proof-mass reduces the total number of fingers – only outside combs may be placed. The height of thinned fingers is 20 μm. The suspensions use only two springs connected on opposite sides of the proof-mass in its axis of rotation. The total size of the sensor is similar to *Y*-axis accelerometer. All sensor dimensions are shown in Table 2.1.

Table 2.1. Accelerometers dimensions

	Y-axis	*X*-axis	*Z*-axis
Finger length	140 μm	200 μm	200 μm
Finger width	2 μm	4 μm	4 μm
Finger separation	10 μm	15 μm	10 μm
Sensor layer thickness	30 μm		
Thinned finger thickness	not used	20 μm	
Gap between fingers	2 μm		
Gap between pairs of fingers	6 μm		
Number of finger (per side)	56	80	52

These accelerometer models have been implemented in MEMS+ as shown in Fig. 2.11. Next, DC analysis has been run in order to calculate the initial capacitance of the structure. In case of analytical calculation, the results are presented for each component separately: parallel plate capacitance eq. (2.3), capacitance due to fringing field for each non-overlapping surface eq. (2.4 and 2.5) and capacitance between fingers endings and frame/proof-mass eq. (2.2). Note that the capacitance is calculated for both gap distances: 2 μm and 6 μm.

The results for *Y*-axis accelerometer are presented in Table 2.2. One has to observe that it is necessary to take into account the capacitance between each pair of fingers. Gap distance between them is only a few times larger than the one between fingers in pair.

In our case, it is about 25% of total capacitance. Capacitance due to fringing field is calculated to be about 5%. In comparison to MEMS+, analytical model is underestimated by 5%. It is understandable because no fringing field along overlapping fingers is taken into account. Estimations show that parallel plate capacitance should be increased by about 5% to cover the difference.

Table 2.2. Results for *Y*-axis accelerometer

Y-axis accelerometer		Capacitance [pF]		
		Analytical model		MEMS+
Parallel plate	*d*=2 µm	0.966	1.012	–
Separation fringing field		0.046		
Parallel plate	*d*=6 µm	0.316	0.343	
Separation fringing field		0.027		
Fingers endings		0.021		
Total capacitance		1.376		1.446

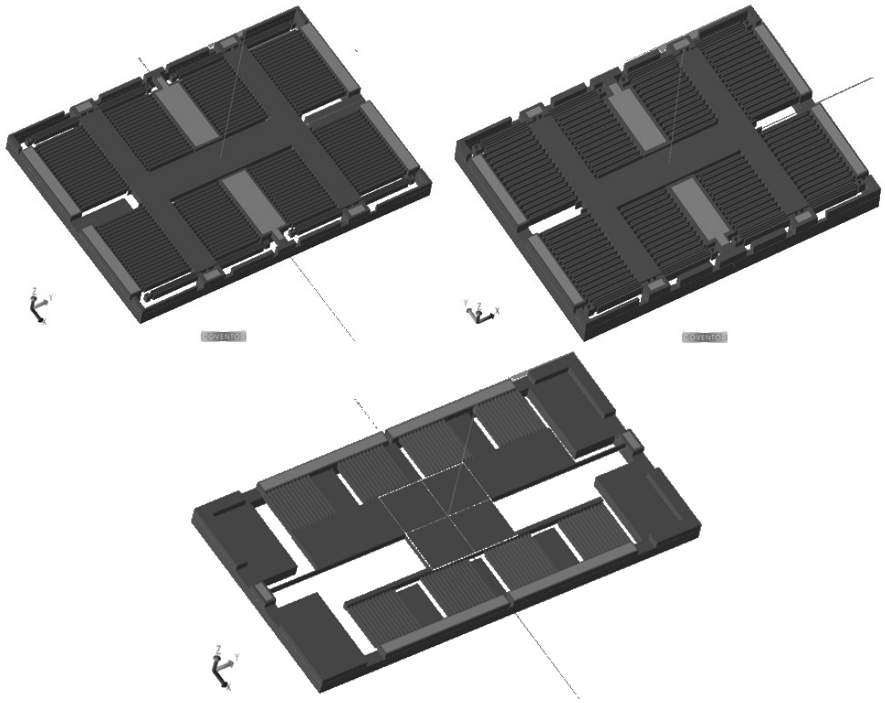

Fig. 2.11. Accelerometer models in MEMS+: *X*-axis (top-left), *Y*-axis (top-right) and *Z*-axis (bottom)

Next, *X*-axis accelerometer was analyzed. The results are presented in Table 2.3. The results are similar to the previous accelerometer. Fringing field for non-overlapping surfaces play a smaller role as separation distance is the same with 1.5 times longer fingers. This results also in larger difference compared to MEMS+ results. Now, analytical model is underestimated by about 10%. Parallel plate capacitance should be increased by about 12%. Note that in this case, finger width is two times larger. Thus, the capacitance due to fringing field for overlapping surfaces is larger than in *Y*-axis accelerometer.

Table 2.3. Results for *X*-axis accelerometer

X-axis accelerometer		Capacitance [pF]		
		Analytical model		MEMS+
Parallel plate	*d*=2 µm	1.964	2.036	–
Separation fringing field		0.072		
Parallel plate	*d*=6 µm	0.647	0.696	
Separation fringing field		0.049		
Fingers endings		0.025		
Total capacitance		2.757		3.07

Finally, *Z*-axis accelerometer was analyzed. The results are presented in Table 2.4.

Table 2.4. Results for *Z*-axis accelerometer.

Z-axis accelerometer		Capacitance [pF]		
		Analytical model		MEMS+
Parallel plate	*d*=2 µm	0.874	1.047	–
Thinned fingers fringing field		0.133		
Separation fringing field		0.028		
Corner fringing field		0.011		
Parallel plate	*d*=6 µm	0.286	0.390	
Thinned fingers fringing field		0.080		
Separation fringing field		0.017		
Corner fringing field		0.007		
Fingers endings		0.014		
Total capacitance		1.451		1.444

As seen, fringing field due to thinned fingers was taken into account in this case. The capacitance is then increased by about 18%. The total capacitance is now almost the same as the one obtained in MEMS+ although the fringing field between one of the finger edges (those in the same plane) is not taken into account. However, the capacitance due to thinned fingers fringing field is overestimated. Analytical model assumes that electric field lines are straight. Therefore, the mean distance is overestimated.

2.4. EXPERIMENTAL VERIFICATION

All of the above-mentioned accelerometers have been fabricated using X-FAB XMB10 MEMS technology. Each type of accelerometer has been placed on separate wafers. One of them is presented in Fig. 2.12. Note that this technology uses top cap wafer in bonding process. Thus, accelerometers are encapsulated and only test structures with bonding pads are visible. In the measurement of initial capacitance, FormFactor Summit 11000 probe station is used where, probes are connected to pads corresponding to capacitance terminals. Probes are connected to Keysight E4990A probe analyzer that allows the measurement of capacitance in the range of pF.

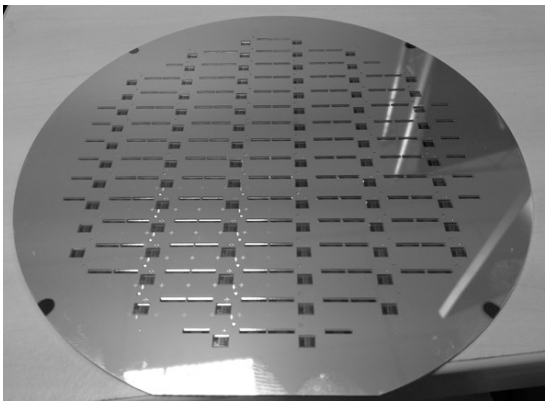

Fig. 2.12. Wafer fabricated using X-FAB technology

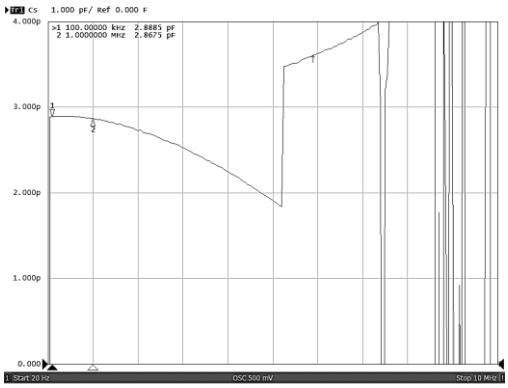

Fig. 2.13. Initial capacitance measurement for *X*-axis accelerometer

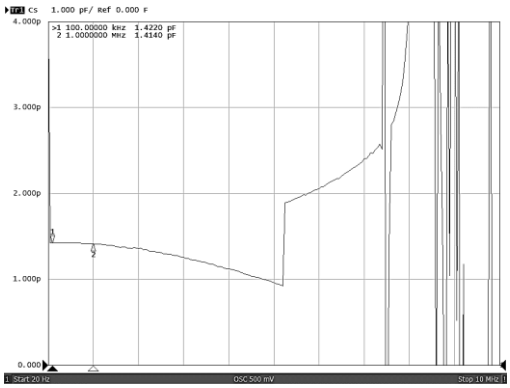

Fig. 2.14. Initial capacitance measurement for *Y*-axis accelerometer

Several structures have been measured for each type of accelerometer. Exemplary results are presented in Fig. 2.13–2.15. Initial capacitance for *X*-axis accelerometers is in the range 2.888–2.898 pF, for *Y*-axis accelerometers in the range 1.421–1.424 and for *Z*-axis accelerometers, in the range of 1.386–1.399. As seen, the measured values are very close to those obtained with MEMS+. In real device, the encapsulation and bottom wafer disturbs the electric field and influences the capacitance. Nevertheless, this impact seems to be negligible because results obtained with MEMS+ are slightly overestimated. Note that the measurement accuracy of impedance analyzer is very high (error smaller than 1%) and does not compensate the difference. In the case of *Y*-axis accelerometer, the difference is 2%, while in the case of *X*-axis and *Z*-axis accelerometers, the difference rises to 5%. It seems that MEMS+ overestimates for larger structures. However, it is possible that some mismatch results from technological process even though the measurements are very repetitive. Nevertheless, both MEMS+ results and experimental results show that analytical model gives quite accurate results.

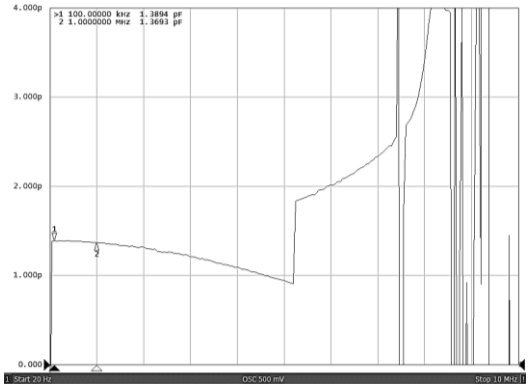

Fig. 2.15. Initial capacitance measurement for *Z*-axis accelerometer

2.5. CONCLUSIONS

In this chapter, modeling approaches of MEMS accelerometers have been described with particular reference to phenomena that may affect the precision of the results. One of the most significant considerations in capacitive structures is the fringing field. Its influence on capacitance was discussed considering the example of comb-drive structure that consists of many small parallel plate capacitors. Therefore, fringing field in such structures has to be modelled properly. In our model, the capacitance resulting from fringing field is calculated for non-overlapping surfaces using simplification that assume that the field lines are straight. The results have been compared with those obtained with MEMS+ for three types of accelerometers: *X*-axis, *Y*-axis and *Z*-axis. Analytical model is underestimated by about 5–10% and gives almost the same results for *Z*-axis accelerometer. It has been found that analytical model overestimates capacitance resulting from fringing field and therefore additional non-overlapping surface for thinned fingers in *Z*-axis accelerometer compensates the difference. In addition, it has been observed how analytical model may be simply improved to increase precision. Nevertheless, analytical model gives accurate results that can be used in the early stage of the project or in optimization phase to reduce the simulation time. One has to emphasize that the final results should be verified with a more precise simulator (MEMS+ or classical FEM simulation used in ANSYS, COMSOL). Finally, simulated structures have been fabricated and measured. Results obtained from measurements correspond to those obtained from simulations and proves that analytical model is a very efficient method in prototyping phase.

Results presented in the chapter are supported by the project STRATEGMED 2/266299/19NCBR/2016 funded by The National Centre for Research and Development in Poland.

REFERENCES

[1] ANDREJAŠIC M., *MEMS Accelerometers*, University of Ljubljana, http://mafija.fmf.uni-lj.si/seminar/files/2007_2008/MEMS_accelerometers-koncna.pdf (accessed: 11.05.2020).

[2] *Technavio Global MEMS Accelerometer Market 2015-2019*, https://www.technavio.com/report/global-mems-accelerometer-market-2015-2019 (accessed: 11.05.2020).

[3] FRADEN J., *Handbook of Modern Sensors*, Springer, New York, 2010.
[4] KORVINK J., PAUL O., *MEMS: A Practical Guide of Design, Analysis, and Applications*, Springer Berlin Heidelberg, 2006.
[5] CHOUDHARY V., INIEWSKI K., *MEMS: Fundamental Technology and Applications*, CRC Press, 2017.
[6] MAJ C. et al., A Multi-domain Electrostatic Actuator Design Tool based on Analytical Models, in: *Proc. International Conference MIXDES*, Gliwice, Poland, 2011.
[7] OLSZACKI M. et al., A multi-domain piezoresistive pressure sensor design tool based on analytical models, in: *Proceeding of 9th International Conference on Thermal, Mechanical and MultiPhysics Simulation and Experiments in Microelectronics and Microsystems (EuroSimE 2008)*, Freiburg, 2008.
[8] SZANIAWSKI K., *Projektowanie i symulacja scalonych czujników wibracji i przyspieszenia*, PhD dissertation at Lodz University of Technology, 2005.
[9] MAJ C. et al., Macro Model of Capacitive MEMS Accelerometer in Cadence Environment, in: *Proceeding of 17th International Conference on Thermal, Mechanical and MultiPhysics Simulation and Experiments in Microelectronics and Microsystems (EuroSimE)*, Montpellier, France, 2016.
[10] KANNAN A., *Design and modeling of a MEMS-based accelerometer with pull in analysis*, MASc dissertation, University of British Columbia, 2008.
[11] PARKER G. W., What is the Capacitance of Parallel Plates?, *Computers in Physics*, vol. 5(5), p. 534-540, 1991.
[12] GALLAGHER E., MOUSSA M., A Study of the Effect of the Fringe Fields on the Electrostatic Force in Vertical Comb Drives, *Journal of Sensors*, vol. 14, 2014.
[13] HOSSEINI M., ZHU G., A new formulation of fringing capacitance and its application to the control of parallel-plate electrostatic micro actuators, *Journal of Analog Integrated Circuits and Signal Processing*, vol. 53, p. 119–128, 2007.
[14] BURT S., FINNEY N., YOUNG J., *Fringe Field of Parallel Plate Capacitor*, Santa Rosa Junior College.
[15] WIAK S., SMÓŁKA K., Numerical modeling of 3-D comb drive electrostatic accelerometers structure (method of levitation force reduction), *COMPEL International Journal of Computations and Mathematics in Electrical*, 2009.
[16] CHEN X., ZHANG Z. et al., Fringing Effect Analysis of Parallel Plate Capacitors for Capacitive Power Transfer Application, in: *4th IEEE International Future Energy Electronics Conference, IFEEC 2019*, Singapore, 2019.
[17] MAJ C., SZERMER M., JANKOWSKI M., Influence of Fringing Field on Estimating of Comb-Drive Accelerometer Performance Comb-drive Accelerometer Performance, in: *Proc. of XVth International Conference on Perspective Technologies and Methods in MEMS Design (MEMSTECH)*, Polyana-Svalyava, Ukraine, 2019.
[18] MAJ C., SZERMER M., Designing of Z-axis comb-drive MEMS accelerometer, in: *Proc. of XXVI International Polish-Ukrainian Conference CAD in Machinery Design: Implementation and Educational Issues (CADMD)*, Lviv, Ukraine, 2018.
[19] https://www.xfab.com/fileadmin/X-FAB/Download_Center/Technology/MEMS/is_XMB10_MEMS_3-Axis_Inertial_Sensors_May2017.pdf (accessed: 11.05.2020).
[20] SZERMER M., ZAJĄC P. et al., Influence of Geometry Scalling on Comb-drive Accelerometer Performance, in: *Proc. of XIVth International Conference on Perspective Technologies and Methods in MEMS Design (MEMSTECH)*, Polyana-Svalyava, Ukraine, 2018.
[21] MAJ C., SZERMER M., Designing of Z-axis accelerometer with asymmetric proof-mass using surface micromachining process, in: *Proc. of 15th International Conference of Experience of Designing and Application of CAD Systems in Microelectronics CADSM 2019*, Polyana-Svalyava, Ukraine, 2019.

DOI: 10.24427/978-83-66391-87-1_03

Jacek NAZDROWICZ[1], Cezary MAJ[1], Mariusz JANKOWSKI[1],
Michał SZERMER[1], Adam STAWIŃSKI[1], Andrzej NAPIERALSKI[1]

3. MODAL ANALYSIS OF VIBRATORY MICROGYROSCOPES

The MEMS rotational velocity sensor is a well-known inertial device that consists of two main vibrating systems: resonator (drive direction) and accelerometer (sense direction). These crucial vibratory subsystems and their fit influences performance, accuracy and measurement scope of the sensor. As kinetic energy is transferred between both vibratory directions, vibratory modes must be analyzed to obtain the optimal response of the device. As MEMS gyroscope is a complex device whose operation depends on several structural details, the crucial stage of the whole design process is CAD modeling of geometry taking into consideration desired effects, simulations of designed model and analysis of results. MEMS gyroscopes are well-known devices that find their usage and applications in many commercial, military and medical devices for measurement purposes [1, 2, 3, 4] due to low technology and fabrication price. The major disadvantage is the slow design process and development and its costs. The advantage, however, is that the final product has low power comsumption, and fast application to many PCB equipment which includes ASIC to process signal obtained from MEMS [5]. The simple output sensor signal processing makes these inertial sensors interesting in today's market.

Although MEMS gyroscope is a complex device, it consists of simple shapes that play an important role due to its influence on the performance parameters. In the case of vibratory gyroscopes, where frequency is one of the main physical quantities, vibratory adjustments decide its usage and application. Therefore, among a wide spectrum of analysis, modal analysis stands out as the main reference point for structure optimization.

The aim of this paper is to bring up modal analysis of MEMS gyroscope operation with COMSOL and Matlab/SIMULINK software. Two different geometries are assumed and simulation results are presented. The other objective of the paper is to present modal analysis results by taking into consideration spring constants and variation in the damping coefficients as an effect of temperature variation.

[1] Lodz University of Technology, Poland

3.1. INTRODUCTION

The MEMS vibratory gyroscope is a mechanical 2-degrees of freedom (DOF) spring-mass-damper system. Such devices consist of inertial mass suspended on springs that are anchored to the substrate. Depending on the type of gyroscope, all springs are anchored to the substrate or few of them only. Remaining ones are anchored to external inertial mass called inertial frame. Either internal mass or external, one is directly or indirectly connected to comb structures which are an integral part of sensor and due to its displacement, can measure the specific physical quantity for further transfer to the other one with integrated circuit support. The inertial mass is a combined electrode fingers (combs) and the movable part of gyroscope [6]. These movable fingers are extruded from all 4 sides of the mass [1, 7]. Resonator comb structures (drive direction) loaded with voltage causes vibrations, comb structures for accelerometer (sense direction) loaded with voltage, are used to detect capacitance changes in time, which in turn can be transformed in corresponding ASIC to angular velocity [8]. Some interesting geometries and simulation results can be found in papers [9, 10].

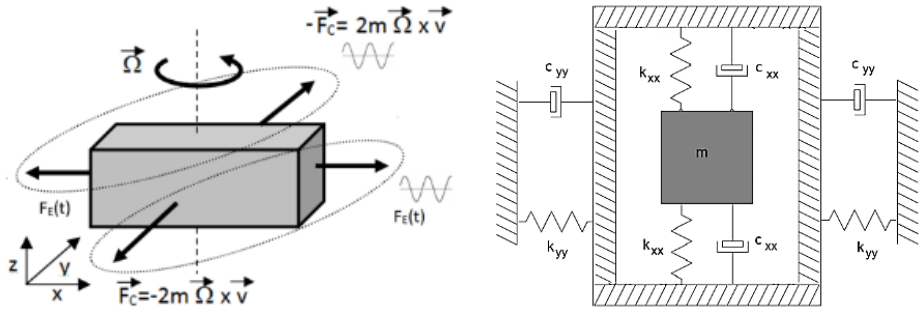

Fig. 3.1. General gyroscope and MEMS vibrating gyroscope operation principal (left) and general model of decoupled gyroscope (right)

Principle of operation of MEMS vibratory gyroscope is based on the well-known Coriolis phenomena which appears in rotating objects (Fig. 3.1) with non-zero linear velocity [4, 11]

$$F_C = -2m\left(\vec{\Omega} \times \vec{v}\right), \tag{3.1}$$

where, Ω is angular velocity, v – linear velocity, and m – mass of object. Fundamental equations governing MEMS gyroscopes can be expressed with second order differential equations

$$m_x \frac{d^2x}{dt^2} + c_x \frac{dx}{dt} + k_x x = F_D \, sin(\omega t) + 2m_y \frac{dy}{dt}\Omega, \tag{3.2a}$$

$$m_y \frac{d^2y}{dt^2} + c_y \frac{dy}{dt} + k_y y = -2m_x \frac{dx}{dt}\Omega \tag{3.2b}$$

Elements $2m_y\Omega\dot{y}$ and $2m_x\Omega\dot{x}$ are related to Coriolis force components induced by rotation. Coriolis force terms are induced by dynamic coupling between resonator and accelerometer. Ignoring the crosstalk interference element of the equation $-2m_y\Omega\dot{y}$, both equations can be written in the following form

$$m_x\frac{d^2x}{dt^2}+c_x\frac{dx}{dt}+k_xx=F_D\,sin(\,\omega t), \tag{3.3a}$$

$$m_y\frac{d^2y}{dt^2}+c_y\frac{dy}{dt}+k_yy=-2m_y\frac{dx}{dt}\Omega \tag{3.3b}$$

Often we can meet these equations which include $\zeta=\frac{c}{m\omega}$, where ζ is a damping ratio,

$$\omega_x=\sqrt{\frac{k_x}{m_x}},\ \omega_y=\sqrt{\frac{k_y}{m_y}},\ Q_x=\frac{m_x\omega_x}{c_x},\ Q_y=\frac{m_y\omega_y}{c_y}, \tag{3.4}$$

Q factor describes the behaviour of the gyroscope during damping. High Q factors reflect oscillators with low damping – they vibrate longer. Q factor value of 0.5 is a threshold which changes meaningful damping during vibrations.

In many MEMS applications, it is crucial to analyze the sensitivity of a vibrating gyroscope eigenfrequencies in relation to temperature fluctuation. Based on the above considerations, MEMS vibrating gyroscope require frequency stability under changes taking place in the environment where the device operates.

Since in the case of MEMS vibratory gyroscope, mode-matching of both vibration directions is crucial, modal analysis of such device is one of the most important steps during the design.

3.2. DESIGN AND SIMULATIONS

Model of MEMS vibratory gyroscopes were prepared in COMSOL Multiphysics software and simplified models were prepared in Matlab/SIMULINK software. A model created in COMSOL reflects the real physical device shape, whereas model in Matlab/SIMULINK implements Newton's motion equations and its complexity comes directly from the need to reflect geometry details. FEM models were simulated in stationary and eigenfrequency studies.

Geometrical dimensions and physical properties are presented in Table 3.1, 3.2 and 3.3.

Eigenfrequency calculations of particular nodes were performed in two steps:

- stationary study - computes both displacement and stress,
- eigenfrequency study - stationary study step was applied to calculate natural frequencies of particular nodes.

To compute eigenfrequencies for different entry value (for example external force), parametric sweep was applied.

Two different fundamental cases of modal analysis should be considered for MEMS inertial devices: for constant, reference temperature and for various temperature.

Table 3.1. Geometrical details of gyroscope with one inertial mass

Quantity	Value
Proof mass length/height	$1000 \cdot 10^{-6}$ m
Edge spring length	$200 \cdot 10^{-6}$ m
Device thickness	$30 \cdot 10^{-6}$ m
Drive electrode count	30
Sense electrode count	30
Gap between fingers	$26.5 \cdot 10^{-6}$ m

Table 3.2. Geometrical details of gyroscope with two inertial masses

Quantity	Value
Proof mass height	$1000 \cdot 10^{-6}$ m
Proof mass length	$200 \cdot 10^{-6}$ m
Inertial frame height	$675 \cdot 10^{-6}$ m
Inertial frame thickness	$25 \cdot 10^{-6}$ m
Device thickness	$30 \cdot 10^{-6}$ m
Drive electrode count	30
Sense electrode count	30
Gap between fingers	$26.5 \cdot 10^{-6}$ m

Table 3.3. Physical properties of polysilicon

Quantity	Value
Young's modulus	160 GPa
Poison ratio	0.22

3.3. MODAL ANALYSIS RESULTS FOR CONSTANT TEMPERATURE

In a constant temperature environment, it is assumed that the temperature has no influence on the device. It is assumed that it equals to reference temperature. Here, temperature is assumed to be 293.15 K.

Results of simulation performed in FEM software are depicted in Fig. 3.2 (for device including one common mass for both drive and sense directions) and Fig. 3.3 (for device including two inertial masses) respectively. These figures present two first modes for drive and sense directions separately, which are important in point of view vibratory gyroscope, because they are distinctly related with the particular drive and sense directions. According to the figures presented, it can be seen that the displacement vibration modes are directed towards particular motion axis. Therefore, applying forces with vectors coinciding with these directions allow the control of displacement amplitude: force controls amplitude – amplification of amplitude (taking into consideration natural frequencies). It is obvious that this considers both sensors (adjust displacement amplitude that may cause an increase in the measurement range, sensitivity and accuracy) and actuators (change displacement amplitude).

Particular natural frequencies were obtained in COMSOL with sweeping simulation use. These natural frequencies are presented later as a part of the discussion of simulation results. To ensure accurate computation of the natural frequencies, they are compared with results obtained from Matlab/SIMULINK simulations.

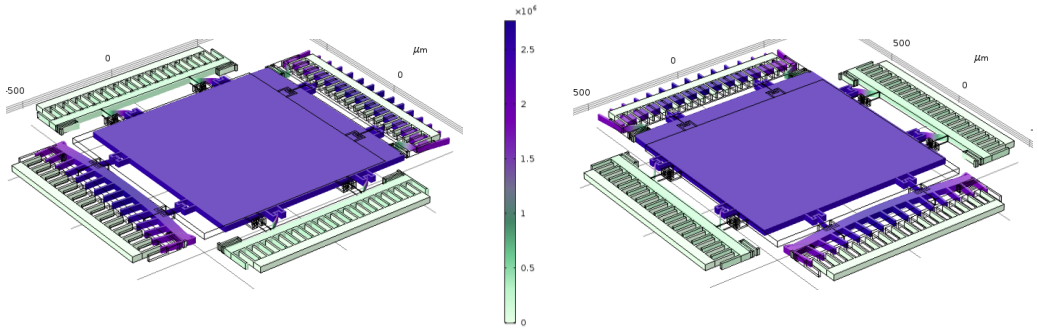

Fig. 3.2. Modal analysis of MEMS gyroscope
with one mass (left) and double (right) central springs on each side

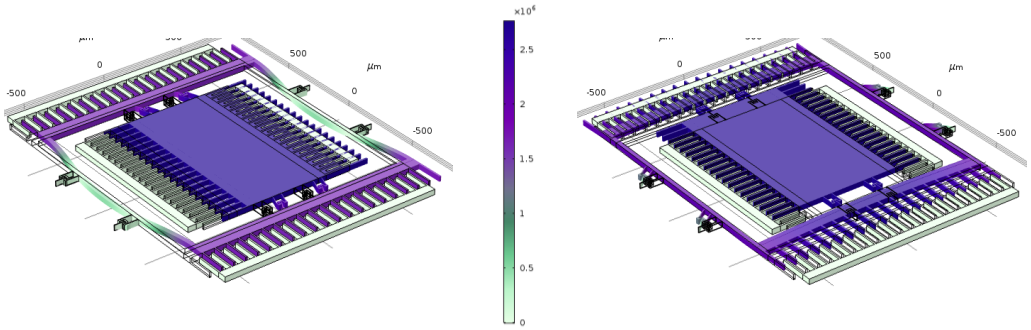

Fig. 3.3. Modal analysis of MEMS gyroscope
with inertial frame (left) and central springs (right)

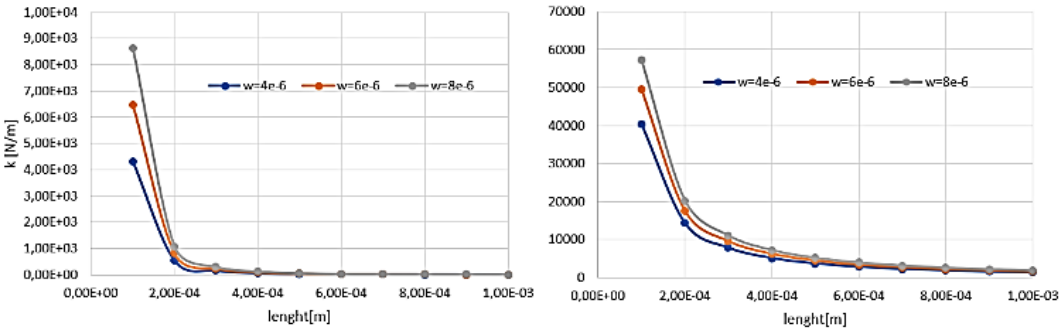

Fig. 3.4. Results of modal analysis of MEMS gyroscope
with one mass for different length of suspensions

Fig. 3.4 and 3.5 show the dependencies of eigenfrequency on the two crucial geometrical dimensions: width and length of particular suspensions. We observe, that the spring constant falls rapidly (for small spring length) and then the drop is gradual as the suspension

length increases. Similarly, modal analysis shows strong dependency of eigenfrequency on the change in this dimension. In the case of increase in the width, we observe that the eigenfrequency grows, however, for shorter suspension, this dependency is stronger than for longer suspension.

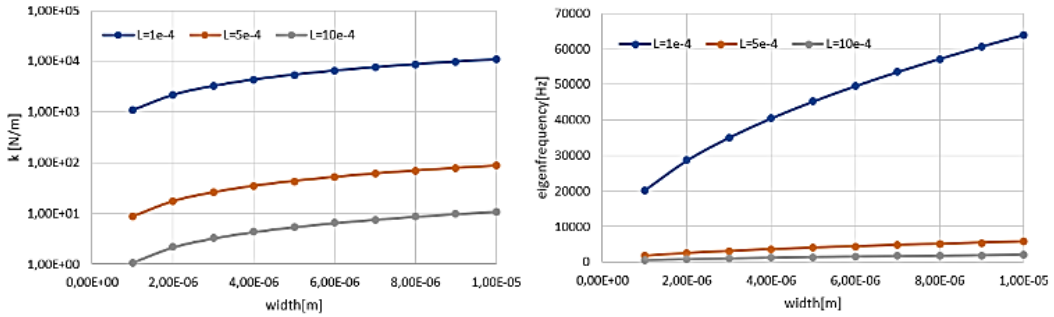

Fig. 3.5. Results of modal analysis of MEMS gyroscope
with one mass for different width of suspensions

Fig. 3.6 shows the magnitude and phase of transfer function for the first considered gyroscope (with one mass). It can be seen that this type of gyroscope is almost mode-matched - frequency difference Δf is very tiny. This difference (in case of fabricated device) is caused by inaccuracies in dimensions or fabrication imperfections. In an ideal situation - when vibrating gyroscope is mode-matched (the natural frequency of a drive axis exactly matches the natural frequency of sense axis), the primary benefit is the improvement of performance and increased sensitivity (key parameter of each microsensor - it grows in the case of drop in the frequency difference). For this kind of gyroscope, mode-matching strongly depends on the sameness of spring constants.

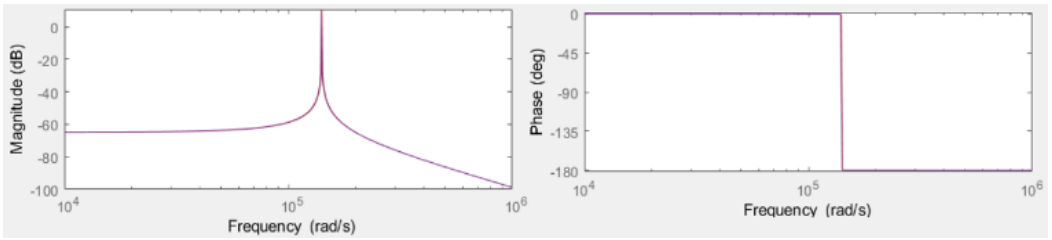

Fig. 3.6. Magnitude (left) and phase (right) of transfer function for gyroscope with one inertial mass

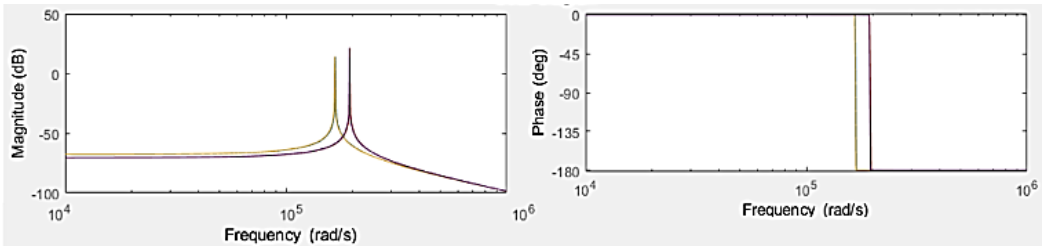

Fig. 3.7. Magnitude (left) and phase (right) of transfer function for gyroscope with two masses

Fig. 3.7 shows the magnitude and phase of the transfer function for gyroscope with two inertial masses. It is seen, that larger difference between drive and sense modes - angular frequency difference is about $0.3 \cdot 10^5$ rad/s (4777 Hz). Therefore, in the case of such structure, mode-matching is worse than in the case of single-mass configuration.

3.4. TEMPERATURE INFLUENCE ON MODAL ANALYSIS RESULTS

As the inertial sensors or actuators are mechanical structures built of solid materials, they are very susceptible to some environmental factors, which can play significant role in commercial applications. One such factors is temperature, considered by some as the crucial factor having a destructive effect on the device performance.

Basically, temperature variation has a significant influence on the material properties, including those in used modern electronics and micromechanics disciplines. These materials are thermo-sensitive in small or large extent, being potentially a source of some response to physical quantity variations, which, in turn, may be crucial in sensing or actuating process and accuracy of measurement or may be just avoided. Table 3.4 shows the thermal properties of polysilicon used in this study.

Table 3.4. Thermal properties of polysilicon

Quantity	Value
Thermal coefficient α (for ΔT=0)	$2.6 \cdot 10^{-6}$ [1/K]
Thermal coefficient of Young's modulus β (for ΔT=0)	$-80 \cdot 10^{-6}$ [1/K]

Since each solid material expands under temperature, its geometrical dimensions also change, and can be expressed by

$$l(T) = l_0(1 + \alpha \Delta T), \tag{3.5}$$

where l_0, l, α, ΔT are initial length (in T_0 temperature), length in T temperature, thermal expansion coefficient and temperature difference $T - T_0$ respectively. The next parameter which is temperature dependent is elastic modulus. When it changes, it causes variation of the gyroscope stiffness and also the resonant frequency [5, 6]

$$E(T) = E_0(1 + \alpha \Delta T), \quad k(T) = k_0(1 + \alpha \Delta T), \tag{3.6}$$

where $E(T)$, E_0 are elastic modulus for the polysilicon material at a temperature T and T_0 respectively. Similarly, k and k_0 are stiffness at temperature T and T_0 respectively. Based on gyroscope inertial mass m and stiffness k, resonant frequency ω_0 may be calculated with the following equation

$$\omega_0(T) = \sqrt{\frac{k(T)}{m}} = \sqrt{\frac{k_0(1 + \alpha \Delta T)}{m}}. \tag{3.7}$$

From the above formula, we see that the resonant frequency varies with temperature variation.

Results presented in Fig. 3.8 show how spring constant is affected by temperature variations. Spring constant was obtained in two ways, with the use of both COMSOL (FEM) and separately with SIMULINK (analytical) simulation based on the models presented here. Calculation of spring constant with FEM required model to be body loaded with specified object like Thermal Expansion, a sub-object of the Linear Elastic Material. As a result, it was observed that both modeling methods gave similar results of spring constants (for analytical calculations (one-mass gyroscope configuration): 1470 N/m, FEM simulations: 1540 N/m), however, results from FEM software are more reasonable as they provide more device accuracy and sensitiveness – and consequently better mode matching of both actuator and sensor.

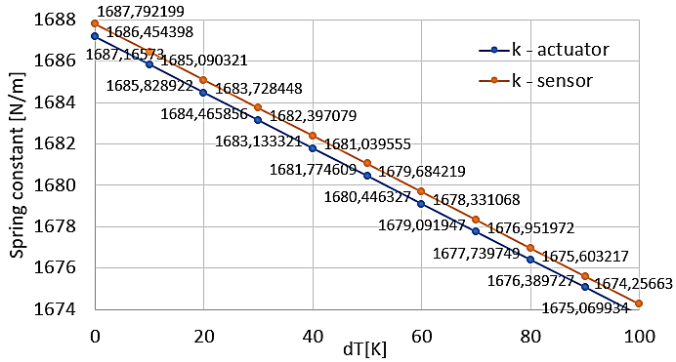

Fig. 3.8. Spring constant dependency on temperature for MEMS actuator and sensor in vibratory gyroscope with one common central mass

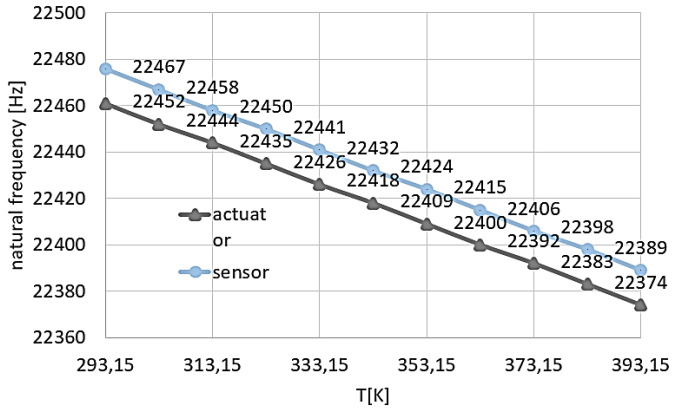

Fig. 3.9. Natural frequency dependency on temperature for MEMS actuator and sensor in vibratory gyroscope with one common central mass

Results of the sweeping simulations in terms of natural frequency dependency on temperature are shown in Fig. 3.9 and 3.10. The model also took into consideration the Young's modulus temperature dependency. For one mass decoupled MEMS device, results are presented in Fig. 3.9. It can be seen that natural frequency depends linearly on

temperature, however, frequency values for particular temperatures drop rapidly with temperature - almost 100 Hz with ΔT =100 K.

For MEMS structure with inertial frame including edge serpentine suspensions (Fig. 3.10), the results meaningfully differ. In case of actuator, natural frequency drops with temperature, whereas in the case of sensor, it increases. In contrast to structure with one mass – the natural frequencies for resonator and sensor are nonlinear.

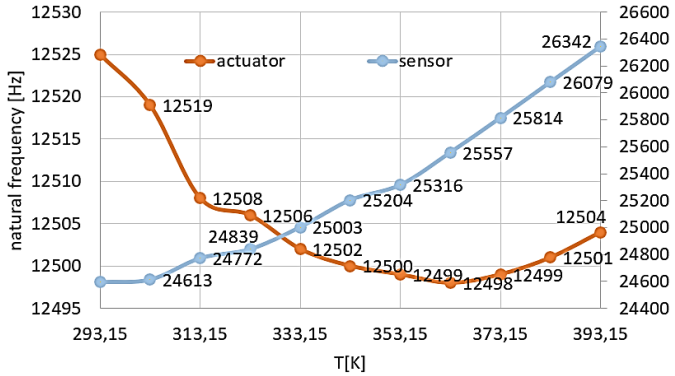

Fig. 3.10. Natural frequency dependency on temperature for MEMS actuator and sensor in vibratory gyroscope with inertial

3.5. CONCLUSIONS

Results of modal analysis are very important part of MEMS design process. First of all, it allows the detection (and fit) of frequency range of the device to operate. Secondly, it allows the matching of both drive and sense modes to obtain the maximum amplitude for sense direction (recall that this amplitude is 1000 less than for drive direction) and the resonance effect that is advisable to use. Results show that through manipulation of dimensions and geometry choice, we can decrease or increase eigenfrequency, however, the option is to manipulate suspension dimensions as the numerator of the equation (3.4) changes more than the denominator (mass of suspension changes slightly in comparison to inertial mass).

Results of simulations performed for different temperatures further show that the particular modes are temperature sensitive and have influence on natural frequency values. According to the principle of operation of vibratory gyroscope, such temperature variation will degrade the performance of the device.

REFERENCES

[1] KEMPE V, *Inertial MEMS: Principles and Practice*, Cambridge University Press, 2011.

[2] MEHREGANY M., ROY S., *Introduction to MEMS, Microengineering Aerospace Systems*, ed: H. Helvajian, Aerospace Press, Los Angeles, 1999.

[3] https://technology.ihs.com/572622/mems-market-tracker-h1-2016 (accessed: 7.03.2020).

[4] YAZDI N. et al., Micromachined inertial sensors, *Proceedings of the IEEE*, vol. 86, p. 1640-1659, 1998.

[5] JANKOWSKI M., ZAJAC P., NAPIERALSKI A., Fully differential read-out circuitry components for MEMS-based accelerometers, in: *2018 XIV-th International Conference on Perspective Technologies and Methods in MEMS Design (MEMSTECH)*, Lviv, Ukraine, p. 86-90, 2018.
[6] ZHANG G., *Sensing and Control Electronics for Low-Mass Low-Capacitance MEMS Accelerometer*, Ph.D. Dissertation, Carnegie Mellon University, 2002.
[7] LAWRENCE A., *Modern Inertial Technology: Navigation, Guidance and Control*, Springer Verlag, New York,1993.
[8] ZIMMERMANN L. et al., Airbag application: a microsystem including a silicon capacitive accelerometer, CMOS switched capacitor electronics and true self-test capability, *Sensors and Actuators*, p. 190-195, 1995.
[9] MELNYK M. et al., Application of a Genetic Algorithm for Dimension Optimization of the MEMS-based Accelerometer, in: *Proc. International Conference MIXDES*, Gdynia, Poland, p. 352-354, 2013.
[10] MAJ C. et al., Macro model of capacitive MEMS accelerometer in CADENCE environment, in: *2016 17th International Conference on Thermal, Mechanical and Multi-Physics Simulation and Experiments in Microelectronics and Microsystems (EuroSimE)*, Montpellier, p. 1-5, 2016.
[11] BOUCHAUD J., DIXON R., *MEMS Market Tracker*, 2016, https://technology.ihs.com/572622/ mems-market-tracker-h1-2016 (accessed: 7.03.2020).

DOI: 10.24427/978-83-66391-87-1_04

Andrzej KOSZEWNIK[1]

4. INFLUENCE OF ORTHOGONAL METHODS ON DESIGN PROCESS OF VIBRATION CONTROL SYSTEM FOR CANTILEVER BEAM WITH NON-COLLOCATED PIEZO-ELEMENTS

To design vibration control system for flexible structures, their mathematical model should be reduced. In this paper, we consider the influence of the model reduction on the dynamics of the real closed-loop system. A simple cantilever beam is the object of consideration since we are able to formulate the exact analytical model of such structure. As a result of reduction, the model with low frequency resonances is usually separated from the high frequency dynamics because high frequency part of the model is naturally strong damped. In order to estimate dynamical system for control purposes in the paper, we applied a few orthogonal methods such as: modal and Schur decompositions. As it is shown, all methods well calculate resonances frequencies but generate different anti-resonances frequencies. In the vibration control systems, the anti-resonances play essential role. They influence the stability and dynamics of the closed-loop systems. The controllers designed for different reduced models were applied to real full plant. Dynamics behavior of the closed-loop systems with such controllers were analyzed and compared. The theoretical considerations were confirmed by experimental investigations. In conclusion, we should carefully choose model reduction methods in the design process of the vibration control system.

4.1. INTRODUCTION

Increase of the dimensions and reduction of the masses of the mechanical structures lead to their higher flexibility and compliance to internal and external excitations. Therefore, the active vibration control systems of flexible structures gain more and more popularity. The reduction of structure mathematical models is an important problem when we want to design the active vibration control system. As we know, a model reduction simplify

[1] Bialystok University of Technology, Poland

procedure of design control system but in many cases can amplify many problems like *spillover* effect [1], research for optimal distribution of sensors and actuators [2], influence of non-collocation of sensor/actuator [3, 4], or looking for unknown damping components of the structure [5].

Some of aforementioned problems are solved by using Finite Element Method which allows to predict dynamics of the designed structure. Such solutions are used in the papers [5, 6, 7] where vibrations of flexible rotors, trusses or plates are described by the mass and stiffness matrices. This way obtained numerical model (with many eigenvectors and eigenvalues) is very helpful to describe the dynamic behavior of the investigated structures, but from control strategy point of view, it is too complicated to design a proper control law. Thus, in order to simplify the control system design process the model with large number of degree of freedoms (DOF's) should be reduced by well-known orthogonal methods [6, 7].

The modal decomposition is a classical method for the linear model reduction. According to this method, the eigenvectors and eigenvalues are used to separate the dynamics description of the particular modes and modes are divided into controlled and non-controlled ones. Apart from aforementioned modal method, often to describe the vibration of structure especially beam and bar structures, the Rayleigh-Ritz method [8] or Schur decomposition [7] are used. In all reduction methods, the eigenvalue problem of consider structure is solved to determine an approximation functions of the mode shapes and natural frequencies based on assumed boundary and initial conditions.

The influence of the model reduction on the dynamics of real closed-loop system is considered in the paper. For beam with non-collocated piezo-elements (sensor, actuator), the model is determined in process of identification procedure and next compared with others reduced order models obtained by using aforementioned orthogonal methods. Then, each obtained model is transformed to the partial-fraction form which then allows the calculation of the sum of static residuum R_0 of the model. In case of modal decomposition, the obtained model according to [6] can be expressed as

$$G(s) = \sum_{i=1}^{N} \frac{\varphi_i(k)\varphi(l)}{m_i(s^2 + 2\alpha_i s + {\alpha_i}^2 + {\omega_i}^2)} + R_0, \tag{4.1a}$$

$$G(s) = \sum_{i=1}^{N} \frac{1}{m_i} \frac{R_{i1}}{(s + \alpha_i + j\omega_i)} + \sum_{i=1}^{N} \frac{1}{m_i} \frac{R_{i2}}{(s + \alpha_i - j\omega_i)} + R_0, \tag{4.1b}$$

where $\varphi_i(k)$, $\varphi_i(l)$ – the modal amplitudes at the actuator (k) and sensor (l) locations, m_i - the i-th modal mass, $j\omega_i$ - the imaginary parts of the poles of the transfer function, α_i - the real parts of the poles, N - considered amount of mode shapes, R_{i1}, R_{i2} – residues of the transfer function for i-th mode shape.

Then, the residues of the model for each considered mode shape can be express as

$$R_{i1} = \frac{j\varphi_i(k)\varphi_i(l)}{2\omega_i}, \quad R_{i2} = \frac{-j\varphi_i(k)\varphi_i(l)}{2\omega_i}, \tag{4.2}$$

Taking into account eq. (4.1) and eq. (4.2), we can consider the most favorable indicator during design control law is a value of static residuum R_0 since

$$R_{11} + R_{12} + R_{21} + R_{22} + R_{31} + R_{32} + \cdots = 0, \tag{4.3}$$

and for $N \to \infty$ we have $R_0 \to 0$.

In order to check how this value influence the control system, the obtained models (estimated and reduced order ones) are investigated. With the help of root-locus method, the boundary gain of feedback loop is determined for each model and next verified during experimental investigations.

4.2. THE BEAM AS A CONTROL PLANT

The cantilever beam with non-collocated piezo-elements located on opposite sites of the beam, as shown in Fig. 4.1, is an object of the considerations. The piezo-stripes used during investigations work as an actuator and a sensor respectively. From strategy control point of view, the considered beam represents non-collocated system because the control and measurement places are different. The main disadvantage of such system is that the control system can lead to their unstable behavior. Therefore, in order to counteract such behavior, the control law should be carefully designed.

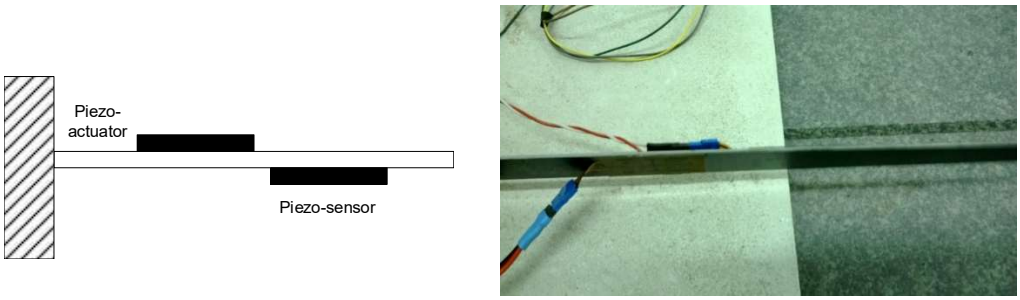

Fig. 4.1. The steel beam with the piezo-stripes as a actuator and a sensor:
scheme (left), photo (right)

4.2.1. IDENTIFICATION OF THE CONTROL PLANT

The determination of the mathematical model of the smart beam with the use of identification procedure [9, 10] was the first point of investigation. To do this, the beam as a control plant is excited by signal generated from Digital Signal Analyzer (DSA) chirp signal in form of $u(t)=5\sin(\omega t)$ in the selected frequency range 10 - 410 Hz. Next, such obtained signal is amplified by the bipolar amplifier SVRbip3/150 and applied to the piezo-actuator. At the same time, the amplitude of vibrations of the beam are measured by piezo-sensor and transformed to voltage by piezo-charge amplifier Kistler 5018A1000. As a result, the frequency response function of the beam is achieved and recorded by DSA (see Fig. 4.2b). The photo of test rig during identification procedure is shown in Fig. 4.2a.

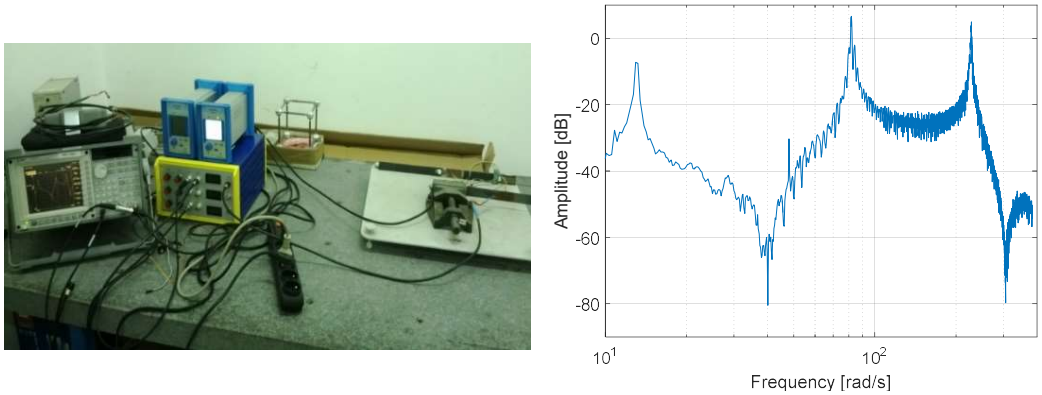

Fig. 4.2. The photo of test rig during identification procedurę (left), the frequency response function of the smart beam in the selected frequency range 10-410 Hz (right)

Taking into account Fig. 4.2b, we can see that the lowest three natural frequencies of the plant are $f_1 = 13.6$ Hz, $f_2 = 85$ Hz, $f_3 = 237$ Hz and the lowest two anti-resonances frequencies are $f_{1A} = 41.1$ Hz and $f_{1A} = 321$ Hz which will be a base for further investigations. In order to determine the mathematical model of this beam, the estimated model with different equation orders is tested. For each case, the good fitting of estimated model to experimental data was an indicator chosen to find the best order model. As it can be seen in Fig. 4.4, the best results are achieved for model with order $p = 60$. Of course from strategy control point of view, the assumed order is too high. So on further calculations, the order of this model is maximal reduced to $p = 21$ with the use of the well-known balance method. The obtained reduced order estimated model still has a good convergence between model and experimental data (Fig. 4.3b).

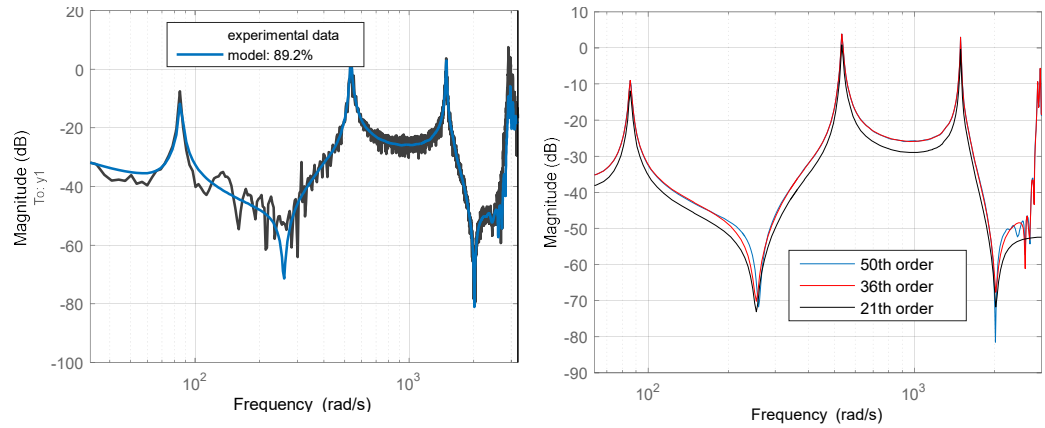

Fig. 4.3. The comparison of amplitude plot of:
experimental data and the estimated model (left), estimated reduced order models (right)

The finally estimated model is described in partial-fraction that sum of residues equals -0.0002. For this model, with help of root locus method the Evans plot are determined and shown in Fig. 4.4. Taking into account obtained plots, we can see four zeros of this model located on right half-plane which are due to two lowest frequency anti-resonances. Such location of these zeros causes that consider system with proportional control law may

be unstable especially in low frequency range. Thus, in order to ensure stability of control system for the estimated model, the boundary gain of the controller should not cross over a value of 35.2.

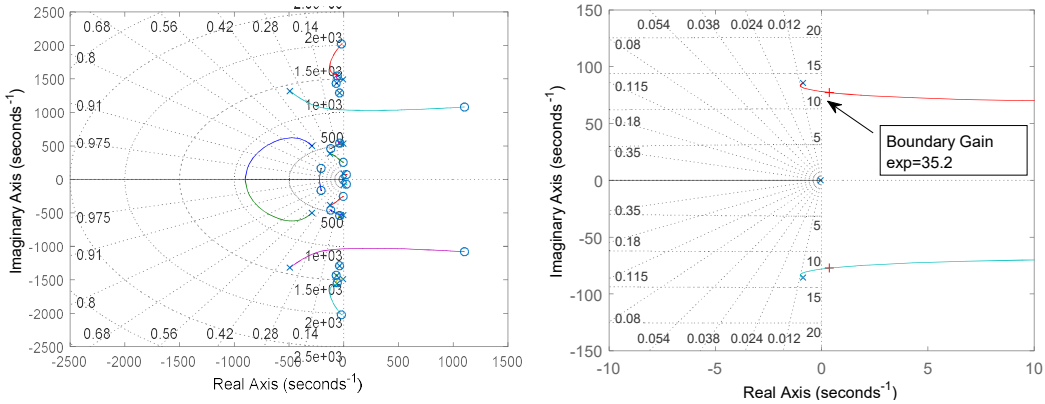

Fig. 4.4. The Evans plot for the estimated model obtained from experimental identification

4.3. INFLUENCE REDUCTION ORDER METHODS TO VALUE OF BOUNDARY GAIN

Further investigations need to check how the choice of reduction order methods influence the value of boundary gain in case of considerations of damped system. As a first method, the modal numerical decomposition method is chosen. With the help of this method, the reduced order model is determined in the frequency range of 10 - 410 Hz that contains only the first three lowest frequency resonances. Taking into account equation (4.1) and modal amplitudes of piezo-actuator and piezo-sensor to consider mode shapes, the model of the beam can be written as

$$G_{MODAL}(s) = \frac{0.0782j}{s-(-0.1+1419.4j)} + \frac{-0.0782j}{s-(-0.1-1419.4j)} + \frac{0.3433j}{s-(-0.4+513.5j)} + \frac{-0.3433j}{s-(-0.4-513.5j)} + + \frac{0.4407j}{s-(-0.9-83.8j)} + \frac{-0.4407j}{s-(-0.9+83.8j)} - 3.3931 \cdot 10^{-4}. \quad (4.4)$$

As it can be seen, the static residue of this model equals $-3.39 \cdot 10^{-4}$. It is a value close to zero, so in the next step, there is a need to check how this value influence the value of boundary gain of feedback loop. Again with the help of Evans plot, a value of this gain is estimated and results are shown in Fig. 4.5b.

As we can see in Fig. 4.5b, the obtained feedback gain is 46.5 and it is a value far from the gain obtained for estimated model. Analyses of magnitude plot (see Fig. 4.5a) also shows small differences in comparison to amplitude plot from Fig. 4.3b. Especially, it is visible in vicinity of third anti-resonance frequency that it is closer to the third natural frequency than it is in case of plots obtained from experimental identification.

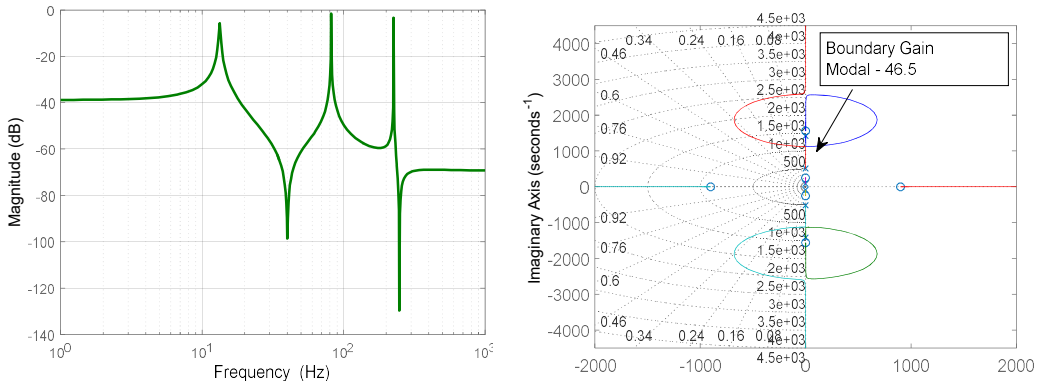

Fig. 4.5. The plots of reduced-order model obtained from modal numerical decomposition: amplitude plot (left), Evans plot (right)

4.4. MODAL ANALYTICAL MODEL

Modal analytical approach is the next method considered in the paper. The state space model of the beam with non-collocated piezo-stripes is once again used as in paper [11] with such difference that the values of particular damping coefficients for the first three lowest natural frequencies are considered in the state matrix $\boldsymbol{A}$. As a result, the damped model of smart beam can be written as

$$\begin{aligned} \dot{\boldsymbol{x}}(t) &= \boldsymbol{A}\boldsymbol{x}(t) + \boldsymbol{B}\varepsilon(U_s), \\ U_{sensor}(t) &= \boldsymbol{C}\boldsymbol{x}(t), \end{aligned} \tag{4.5}$$

where

$$\boldsymbol{A} = \begin{bmatrix} 0 & 0 & 0 & 1 & 0 & 0 \\ 0 & 0 & 0 & 0 & 1 & 0 \\ 0 & 0 & 0 & 0 & 0 & 1 \\ -{\omega_1}^2 & 0 & 0 & -2\xi_1\omega_1 & 0 & 0 \\ 0 & -{\omega_2}^2 & 0 & 0 & -2\xi_2\omega_2 & 0 \\ 0 & 0 & -{\omega_3}^2 & 0 & 0 & -2\xi_3\omega_3 \end{bmatrix},$$

$$\boldsymbol{B} = \begin{bmatrix} 0 \\ 0 \\ 0 \\ W[-U_1(x_1) + 2 \cdot U_1(x_2) - U_1(x_3)] \\ W[-U_2(x_1) + 2 \cdot U_2(x_2) - U_2(x_3)] \\ W[-U_3(x_1) + 2 \cdot U_3(x_2) - U_3(x_3)] \end{bmatrix},$$

$$\boldsymbol{C} = [k_u\varepsilon_1(t) \quad k_u\varepsilon_2(t) \quad k_u\varepsilon_3(t) \quad 0 \quad 0 \quad 0],$$

k_u - factor of electro-mechanical coupling in the piezo-sensor, $W = \frac{k_k a_b}{\rho_b A_b}$ - constant, k_k - coefficient of factor which depends on the type of piezo-actuator.

Again, taking into account equation (4.1), the obtained model from equation (4.5) is expressed in partial-fraction form as

$$G_{EXACT}(s) = \frac{0.3088j}{s-(-1.6-1489.1j)} + \frac{-0.3088j}{s-(-1.6+1489.1j)} + \frac{0.3895j}{s-(-4.3-534.1j)} + \frac{-0.3895j}{s-(-4.3-534.1j)} + \frac{0.0024j}{s-(-0.2-85.5j)} + \frac{-0.0024j}{s-(-0.2-85.5j)}. \quad (4.6)$$

Analysis of this model indicates that sum of their residue equals zero. So, taking into account this fact, we can suppose that value of feedback gain calculated for this model should approach value of 35.2. The obtained results proved that it is true, because such value is 42.2.

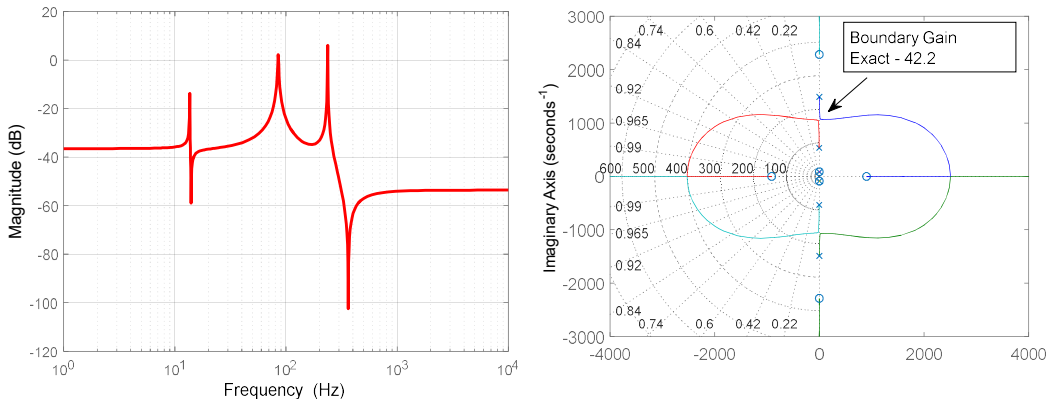

Fig. 4.6. The plots of reduced order model obtained from modal analytical decomposition: amplitude plot (left), Evans plot (right)

4.5. SCHUR DECOMPOSITION

Schur decomposition is the last orthogonal method considered in the paper. For this purpose, the state space matrix of damped model is decomposed to orthogonal matrix $\boldsymbol{U}$ which represents mode shapes and upper triangular matrix $\boldsymbol{T}$. In results of such decomposition, the order of the model is reduced according to equation (4.7) and once again express in partial-fraction form (4.8)

$$\boldsymbol{U} \cdot \boldsymbol{T} \cdot \boldsymbol{U}^{\boldsymbol{T}} = \boldsymbol{A}, \quad (4.7)$$

where: $\boldsymbol{A} = \begin{bmatrix} \boldsymbol{0} & \boldsymbol{I} \\ -\boldsymbol{M}^{-1}\boldsymbol{K} & -\boldsymbol{M}^{-1}\boldsymbol{C} \end{bmatrix}$ and $\boldsymbol{C}$ is the Rayleigh damping.

$$G_{SCHUR}(s) = \frac{0.0195 - 0.723j}{s - (-5 + 1419.5j)} + \frac{0.0195 + 0.723j}{s - (-5 - 1419.5j)} + \frac{-0.0197 + 4.575j}{s - (-13.2 + 513.5j)} + \frac{-0.0197 - 4.575j}{s - (-13.2 - 513.5j)} + \frac{0.1382j}{s - (-0.4 + 83.8j)} + \frac{-0.1382j}{s - (-0.4 - 83.8j)}. \quad (4.8)$$

Similar to previous models, also in this case, the amplitude plot (Fig. 4.7a) and root-locus curves (Fig. 4.7b) are plotted. As it is shown in Fig. 4.7b, the obtained value of boundary gain is the worst, because difference between this value and the gain obtained for estimated model equals even 14.5. Such divergence in results of course may lead to instability of the whole control system during experimental tests.

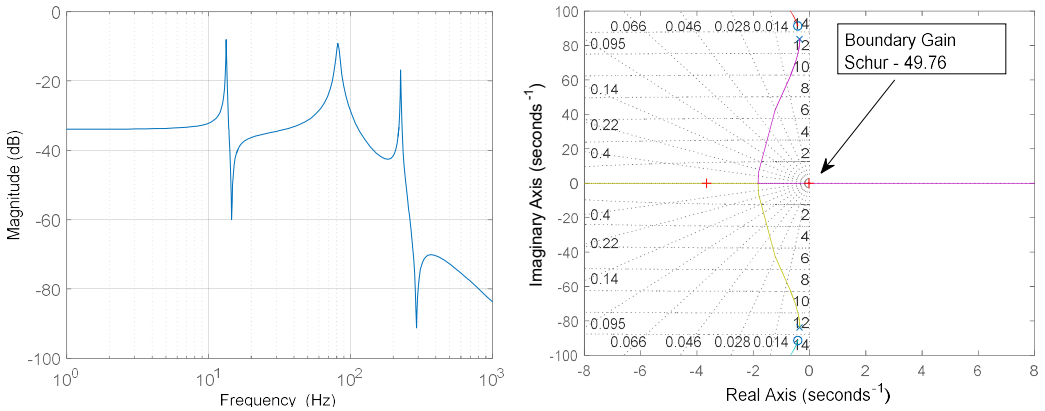

Fig. 4.7. The plots of reduced order model obtained from Schur decomposition: amplitude plot (left), Evans plot (right)

4.6. ANALYSIS OF THE CLOSED-LOOP SYSTEM WITH BOUNDARY GAIN

Next step of investigation was the analysis of designed control law in the laboratory. In this order, firstly, there is a need to prepare laboratory stand to test by proper connection of all equipment such as: DSA, DSP controller, bipolar amplifier and charge-amplifier. Next, with the help of Matlab Simulink software with inbuilt toolbox of DSP controller, there is a need to design control system (Fig. 4.8) to test this system.

Experimental investigations in the frequency domain are carried out once again using DSA that allow generation of a similar signal as it was during identification procedure. Such generated signal in the form of $u(t)$=5sin(ωt) in the selected frequency range 10 – 410 Hz according to Fig. 4.9 is added to the control signal derived from proportional controller. The new signal obtained in this manner is applied to the piezo-actuator by D/A card located on board of DSP controller. Vibrations of the beam are measured by the piezo-sensors and transmitted to A/D DS2002 card and also mounted on the DPS board. The experimental amplitude plot of the closed-loop system are obtained by using two

channels analyzer HP35670A. The first channel is connected to control signal with chirp signal but the second, to signal from charge amplifier. The amplitude plots as a result of the experiment are recorded and shown in Fig. 4.9.

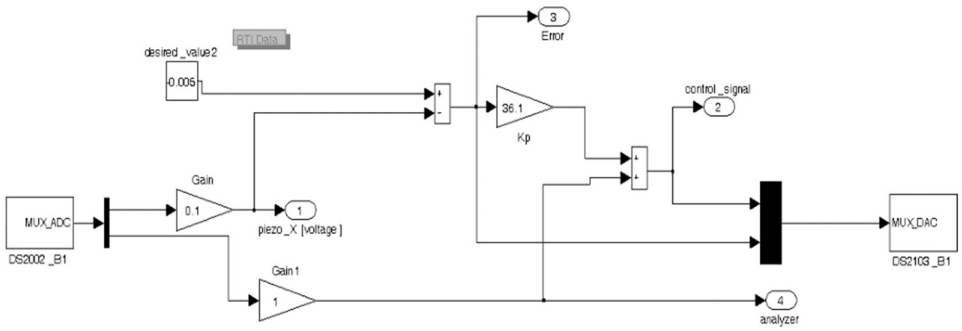

Fig. 4.8. The system designed in Simulink software with A/D and D/A cards of Dspace controller

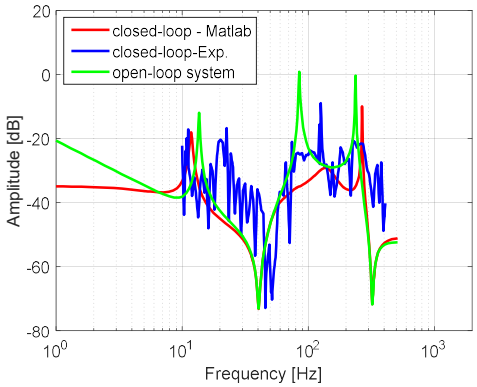

Fig. 4.9. The comparison of the amplitude plot of the open-loop system and closed-loop systems (simulation and experiment) in the selected frequency range

Analysis of the experimental amplitude plot of the closed-loop system with simulation results indicate that there exist a good fitting between this plots. Especially, it is visible in vicinity of the first peak of natural frequency, where amplitudes of both systems are similar and also their values are the same. Additionally, comparison of these results with amplitude plot of the open-loop system show us that amplitude of all natural frequencies of the considered closed loop systems are lower, about 8 - 10 dB in comparison to amplitude of peaks of the open-loop system. It means, that in the system there is an occurrence of an additional damping which damp the vibration of the considered smart beam.

4.7. CONCLUSIONS

The modern and real mechanical structures used in many applications are structures described by multi-degree of freedom mathematical models. A large number of DOF's caused that their control is a very difficult task and requires determination of a suitable

mathematical model for these structure and in some cases, also reduce order model. As it is known from literature, the choice of model reduction methods has a significant influence on the dynamics of the real closed-loop system. Thus, in order to check how orthogonal method influence the stability of the model, a simple cantilever beam with piezo-stripes actuator/sensor located in two different planes was chosen as an object of considerations.

The starting point of investigations determined estimated model of the beam from identification procedure and compared this model with others reduced order models (modal and Schur decomposition). The obtained results show that each considered reduced order methods well calculate natural frequencies, but generate different anti-resonance frequencies. Also, the obtained results (Figs. 4.5b, 4.6b, 4.7b, 4.8b) has shown, that closed-loop systems with reduced order models can be unstable in the selected frequency range, because some zeros are located on right side of Evans plots. Of course, from control point of view, such results are very dangerous. Thus, in the next step, there is a need to consider such control law that ensure stability of the whole system.

Investigations described in the paper show that a good indicator during design control law may be a sum of residue of particular orthogonal models, especially when the control system is designed using root-locus method. Then, the obtained results unequivocally indicated that the best method that gives the best result is modal analytical method. Both obtained values of the sum of residues (-3.39e-4) and boundary gain of feedback loop (42.2) are the closest to values obtained for model obtained from identification (-2.1e-4; 35.2), respectively.

Experimental investigations carried out in the lab stand confirm the above conclusion. Taking into account control scheme from Fig. 4.8, it can be seen that the set up value of gain controller ($k_p = 36.1$) during test ensures similar Bode plot as in the case of simulation analysis. For both closed-loop models (experimental and simulation), the value of first natural frequency is slightly decreasing in comparison to the first natural frequency of the open-loop system. Moreover, the amplitudes of these control systems are also decreasing, about 8 - 10 dB in comparison to the amplitude of the open-loop system especially in vicinity of resonance peaks. This proves the occurrence of additional damp in the control system.

Finally, it can concluded that analysis of the sum of residues of damped open-loop system is a good method during the design of simply control law, especially for SISO models as a cantilever beam with non-collocated piezo-elements.

REFERENCES

[1] CAVALLO A. et al., *Active Control of Flexible Structures, From Modelling to Implementation*, Springer, 2010.

[2] KOSZEWNIK A., GOSIEWSKI Z., Quasi-optimal Locations of Piezo-actuators on a Rectangular Plate, *The EPJ-Plus*, vol. 131:232, DOI: 10.1140/epjp/i2016-16232-2, 2016.

[3] PREUMONT A., *Vibration Control of Active Structures, An Introduction*, Kluwer Academic Publisher, Dordrecht, 2002.

[4] BRATLAND M., HAUGEN B., ROLVAG T., Modal analysis of active flexible multibody systems containing PID controllers with non-collocated sensors and actuators, *Finite Elements in Analysis and Design*, vol. 91, p. 16-29, 2012.
[5] GROSSARD M., CHAILET N., REGNIER S., *Flexible Robotics, Applications to Multiscale Manipulators,* John Wiley & Sons, 2013.
[6] PREUMONT A., *Twelve Lectures on Structural Dynamics*, Springer, 2013.
[7] QUARTERONI A., SACCO S., SALERI F., *Numerical Mathematics, Approximation of Eigenvalues and Eigenvectors,* Springer, New York, 2007.
[8] GRAHAM KELLY S., *Advanced Vibration Analysis*, CRC Press, 2007.
[9] JUANG J.N., *Applied System Identification*, Prentice Hall Inc., 1994.
[10] KOSZEWNIK A., GOSIEWSKI Z., Frequency Domain Identification of the Active 3D Mechanical Structure for the Vibration Control System, *Journal of Vibroengineering*, vol. 14, no. 2, p. 451-457, 2012.
[11] KOSZEWNIK A., GOSIEWSKI Z., Reduction Methods of Structure Models for Control System Purposes, *Solid State Phenomena*, vol. 248, p.119-126, 2016.

DOI: 10.24427/978-83-66391-87-1_05

Olexander BELEJ[1], Nataliia BOKLA[1], Tadeusz WIĘCKOWSKI[2]

5. DEVELOPMENT OF AN ALGORITHM FOR DETECTING ATTACKS IN SENSOR WIRELESS SYSTEMS

Wireless networks have gained immense popularity. Their widespread distribution is due to undeniable advantages over traditional cable networks: ease of deployment, user mobility in the network coverage area, easy connection of new users. On the other hand, the security of such networks often limits their application. If an attacker needs to have a physical connection to the network when attacking a wired network, then in the case of wireless networks, he can be anywhere in the network coverage area. Also, these networks are subject, including due to protocol imperfections, to specific attacks, which will be discussed below. On the other hand, the low level of security of such networks often limits their application. Also, these networks are subject, including due to protocol imperfections, to specific attacks, which will be discussed below.

In connection with the foregoing, researchers are looking for possible improvements to current protocols. In [1], the author proposes to encrypt the entire MAC protocol data unit (MPDU), including MAC headers, except for the FCS frame check sequence, which, will lead to noticeable delays in data transmission and low channel bandwidth. Another approach is to put in the control frame a hash of a certain string known only to a specific sender, by transmitting which in the future it can be uniquely identified and processed [2]. However, this method only prevents one type of attack.

In practice, to protect against network attacks, ordinary users and small organizations, as a rule, are limited to using anti-virus software, which at the present stage of development has some additional protection modules [3]. Large enterprises are forced to purchase expensive wireless intrusion detection systems (WIDS). However, currently, there are no generally accepted standards in this area; manufacturers use closed algorithms for detecting and classifying attacks. In this case, the task of attributing a fragment of network traffic to some type of attack or normal network activity can be solved by applying the methods of data mining (DM) [4].

[1] Lviv Polytechnic National University, Ukraine
[2] Wroclaw University of Science and Technology, Poland

In [5, 6], to solve this problem, the use of neural networks and the support vector method Support Vector Machine (SVM) are proposed. In [7], an approach to the organization of a neural network attack detection system based on a two-layer perceptron and Kohonen network was considered.

It is worth noting that the above studies relate to the detection of intrusions into traditional wired networks [8]. However, there are no works on the targeted use of DM methods to detect attacks specific to local wireless networks. For this reason, this material discusses the main types of attacks inherent in wireless networks, some recommended methods of protection against them, and also proposes the architecture of an attack detection system based on DM methods and evaluates the effectiveness of the attack detection algorithms used in it.

5.1. ATTACKS IMPLEMENTED IN WIRELESS NETWORKS

The attacks on wireless networks are based on intercepting network traffic from an access point or traffic between two connected stations, as well as introducing additional data into a wireless communication session. To form a better understanding of the types of wireless attacks that an attacker can carry out against a wireless network, it is important to classify them. So, attacks can be aimed at different layers of the OSI model: application, transport, network, channel and physical.

Depending on the purpose of the attack, characteristic of the 802.11 protocol family can be divided into several categories [9]: obtaining unauthorized access to the network; integrity violation; privacy violation; access violation; identity theft.

Depending on the purpose of the attack on local wireless networks, OSI models can be divided into several categories [10]:

- gaining unauthorized access to the network: rogue access point, spoofing MAC, hacking a network client, hacking access points,
- integrity violation: 802.11 frame injection, play 802.11 data, delete 802.11 data, play 802.1X EAP, play 802.1X RADIUS,
- breach of confidentiality: eavesdropping, evil twin, AP phishing, the man in the middle,
- accessibility violation: radiofrequency noise, Queensland DoS, Flood Request Probe, Associate / Authenticate / Disconnect / Deauthenticate Flood, 802.1X EAPStart, EAPFailure Flood,
- authentication Bypass: Pre-Shared Key, Identity Theft 802.1X, 802.1X EAP Downgrade, password cracking 802.1X, hacking domain accounts, hacking WPS PIN.

These attacks are based on the use of vulnerable wireless networks represented in the WVE database [11]:

- sending Probe requests with a zero-length SSID tag field (WVE-2006-0064),
- EAP Logoff attack (WVE-2005-0050),
- RTS / CTS flood (WVE-2005-0051),

- WLAN flooding with dissociation packets (WVE-2005-0046),
- WLAN flooding with deauthentication packets (WVE-2005-0045),
- KARMA wireframe (WVE-2006-0032),
- sending an invalid deauthentication reason code,
- sending too long an SSID (WVE-2006-0071, WVE-2007-0001),
- sending an Airjack beacon frame (WVE-2005-0018),
- sending invalid channel numbers in beacon frames (WVE-2006-0050).

Table 5.1. The ratio of the number of attack signatures in the training base

Normal	67343		
DoS		R2L	
Class	Quantity	Class	Quantity
neptune	41214	guess_passwd	162
smurf	2646	ftp_write	8
Pod	201	imap	11
teardrop	892	phf	4
land	18	multihop	7
back	956	warezmaster	40
U2R		Probe	
Class	Quantity	Class	Quantity
buffer_overflow	30	portsweep	2931
load-module	9	upsweep	3599
Perl	3	satan	3633
rootkit	10	nmap	1493

Table 5.2. The ratio of the number of attack signatures in the test base

Normal	9711		
DoS		R2L	
Class	Quantity	Class	Quantity
neptune	4657	guess_passwd	1231
smurf	665	ftp_write	3
Pod	41	imap	1
teardrop	12	phf	2
land	7	multihop	18
back	359	warezmaster	944
U2R		Probe	
Class	Quantity	Class	Quantity
buffer_overflow	20	portsweep	157
load-module	2	upsweep	141
Perl	2	satan	735
rootkit	13	nmap	73

Testing the wireless access level for WPA2-Enterprise. A connection is a sequence of packets starting and ending at specific points in time, between which data streams are transferred from the source IP address to the recipient IP address using a specific protocol [12]. Each connection is designated as normal or as some type of attack from four categories of attacks: Denial of Service (DoS), unauthorized obtaining of user rights Remote to Local (R2L), the unauthorized elevation of user rights to superuser User to Root

(U2R) and sensing (Probe). The ratio of the number of attacks of different types is shown in Table 5.1, 5.2.

Some of these types of attacks are the costs of the technology of radiofrequency data transmission, and also depend on the human factor and must be addressed using organizational measures. Wireless intrusion detection (WIDS) systems should be distinguished from network security hardware, except for firewalls.

5.2. ATTACK DETECTION SYSTEM

The decision on the security of any network activity in commercial products is implemented using closed algorithms, the principle of which is a commercial secret. Moreover, the declared number and types of detected attacks for different products differ, although, in reality, they belong to the same type of attacks, which is explained by the lack of standards in the classification.

The tasks of detecting and classifying attacks can be solved by using data mining (DM) methods, which allow revealing significant correlations, patterns, and trends in large amounts of data. The proposed system uses algorithms for constructing a classification model based on the support vector method, the method of k-nearest neighbors, neural networks and decision trees.

The proposed architecture of an intelligent attack detection system has a modular scheme for organizing interaction between components with a dedicated sensor subsystem and centralized management through the administrator console. The architecture of the system is shown in Fig. 5.1.

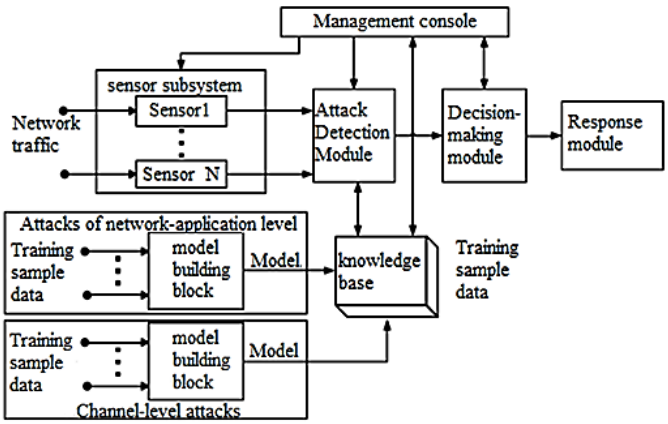

Fig. 5.1. Structure of the Attack Detection System

The basis for identifying attacks is a knowledge base, the construction of which at the stage of the initial configuration of the system provides a block for constructing a classification model. The classification model is built based on the signatures of the training sample and then used to classify real network activity.

The attack detection module of the designed attack detection system can be functionally divided into submodule for detecting attacks of the network, transport and application levels, link-level attack detection submodule.

The system operates in two models:

- configuration model, when a set of signatures is loaded into the block for constructing the classification model as input, each of which is a pair {traffic parameters vector | type of attack},
- normal operation model, when the values of the traffic parameters are supplied as input to the sensor subsystem.

The basis for identifying attacks is a knowledge base, the construction of which at the stage of the initial configuration of the system provides a block for constructing a classification model. The classification model is built based on the signatures of the training sample and then used to decide the security of any network activity. In commercial products, this is implemented using closed algorithms, the principle of which is a trade secret. Moreover, the declared number and types of detected attacks for different products differ, although, in reality, they belong to the same type of attacks, which is explained by the lack of standards in the field of wireless attacks.

As shown in the aforementioned works, the tasks of detecting and classifying attacks can be solved by using DM methods to identify significant correlations, patterns, and trends in large amounts of data.

Next, we consider in more detail the methods of DM, which form the basis of the algorithm for constructing a classifying model of the proposed system.

5.3. METHODS FOR ANALYSIS OF ATTACKS IN SENSOR WIRELESS NETWORKS

The Support Vector Method (SVM) refers to linear classification methods. Each state of the system is represented as a point in a multidimensional space, the coordinates of which are the characteristics of the system. Two sets of points belonging to two different classes are separated by a hyperplane in this space. In this case, the hyperplane is constructed so that the distances from it to the nearest instances of both classes are maximum, which ensures the greatest classification accuracy.

Fig. 5.2 shows an example of classifying objects in two-dimensional space using SVM. The figure shows a training data set, which is a set of points of the form $\{x_i, y_i\}$, $i = 1, \ldots, l$, where $x_i \in R^n, y_i \in \{1, -1\}$ is an indicator of the class to which the point belongs x_i. The classes of points are linearly separable, that is, there is such a hyperplane, on one side of which there are points of the class $y_i = 1$, and on the other of the class $y_i = -1$. Points located directly on the hyperplane satisfy the equation

$$\boldsymbol{\omega} \cdot x - \mathbf{b} = 0, \tag{5.1}$$

where the vector $\boldsymbol{\omega}$ is the perpendicular to the dividing hyperplane, the quantity $|\mathbf{b}|/\|\boldsymbol{\omega}\|$

(the absolute value of **b** divided by the modulus of the vector **ω**) determines the distance from the origin to the hyperplane, the operator "·" denotes the scalar product in the Euclidean space in which the data lies.

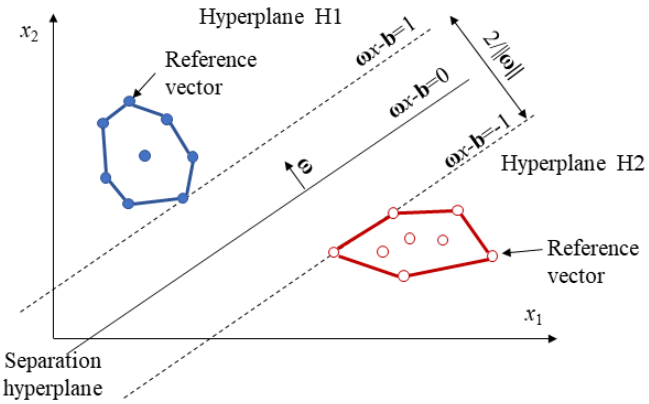

Fig. 5.2. Classification of support vectors

All points for which the condition $\boldsymbol{\omega} \cdot x_i - \mathbf{b} = 1$, lie in the hyperplane H_1 parallel to the separating hyperplane and at a distance $|1 - \mathbf{b}|/\|\boldsymbol{\omega}\|$ from the origin. Similarly, those points for which the condition $\boldsymbol{\omega} \cdot x_i - \mathbf{b} = -1$, lie in the hyperplane H_2 parallel to the plane H_1 and the separating hyperplane, at a distance $|-1 - \mathbf{b}|/\|\boldsymbol{\omega}\|$ from the origin. Thus, the distance between the plane and the positive reference vector is $1/\|\boldsymbol{\omega}\|$, and therefore, the width of the strip is $2/\|\boldsymbol{\omega}\|$.

The advantages of this method are high accuracy, generalization ability, and low computational complexity of decision making. The disadvantage is the relatively large computational complexity of constructing a classifying model.

The method for detecting attacks based on the support vector method is investigated. This was used to construct a classification model from the data of the training sample. The model was tested on attacks such as buffer overflow, rootkit, and SYN flood and showed the relevance of using the support vector method as the basis for an attack detection system.

The *k*-nearest neighbor (*k*-NN) method is a classification method whose basic principle is to assign to the object the class that is most common among the neighbors of this object. Neighbors are formed from many objects whose classes are already known, and, based on a given value of k ($k \geq 1$), it is determined which of the classes is the most numerous among them. If $k = 1$, then the object simply belongs to the class of the only nearest neighbor. The *k*-NN method is one of the simplest DM methods. The disadvantage of the *k*-NN method is that it is sensitive to the local data structure.

Neural networks make it possible to solve practical problems associated with pattern recognition and classification. A neural network consists of interconnected neurons that form the input, intermediate and output layers. Training takes place by adjusting the weights of neurons to minimize classification errors. The advantages of neural networks are their ability to automatically acquire knowledge in the learning process, as well as the ability to generalize. The main disadvantage is sensitivity to noise in the input data.

Decision trees are a tree structure of *leaves* and *branches*. On the edges of the decision, the tree is written the attributes that the objective function depends on, the values of the objective function are written in the *leaves*, and the attributes that distinguish the objects are written in the other nodes. To classify a new object, you need to go down the tree from the root to the leaf and get the corresponding class, the path from the root to the leaf acts as classification rules based on the values of the attributes of the object.

The advantages of decision trees are the simple principle of their construction, good interpretability of the results, the disadvantage is the low accuracy of classification.

Further, to identify the most effective method for constructing a classification model with a wireless attack detection system, a comparison of the considered DM methods will be given.

5.4. ANALYSIS OF CYBER ATTACKS IN SENSOR WIRELESS SYSTEMS

The recognition accuracy of the considered types of attacks using SWS was assessed by comparing the classification results using various DM methods. Based on the above classification of attacks by OSI model levels, attacks on local wireless networks are divided into two groups:

- physical and link-layer attacks that are specific to wireless networks;
- attacks from the network to the application layers inherent in any technology for organizing local area networks, including Ethernet.

The corresponding submodule of attack detection of the proposed system during the experiments uses the signatures of the NSL KDD-2009 base as an example of a network and application-layer attacks. To form a training sample of wireless attacks of the channel and network levels, a test local wireless network with access protection technology WPA2-PSK was organized. The collected packages were analyzed and reduced to the form used in the NSL-KDD-2009 database.

Initially, 41 attributes were used to describe the attacks in the NSL-KDD-2009 database, which reflect the application, transport, and network layers of the OSI model. The selected features are presented in Table 5.3. To describe attacks characterized by a large number of connections to the destination node, a window lasting two seconds was selected (DoS attacks), as well as a window of 100 connections to the same node (Probe).

The first step was the processing of data from the database since for the error-free operation of the algorithms, all attributes must have numerical values distributed between zero and one. For this, text attributes were converted to binary, while numerical ones were normalized concerning the minimum and maximum values.

After that, the data of the training sample were fed to the input of the building block of the classifying model, which forms the basis of the knowledge base, by various DM methods. Then, the attack detection module classified the records of the test set based on the corresponding model according to the criteria contained in the knowledge base and assigned a label to the class of network activity.

Table 5.3. Important traffic settings for network and application layers

Features	Description	Type
Characteristics of the TCP compound		
duration	Connection time (s)	numerical
protocol_type	Transport layer protocol	text
service	Application layer service	text
flag	Status of connection	binary
src_bytes	Incoming stream, byte	numerical
dst_bytes	Outbound stream, byte	numerical
land	The addresses are the same, 0 otherwise	binary
wrong_fragment	Number of incorrect fragments	numerical
urgent	Number of urgent packages	numerical
Session Features		
hot	Number of *hot* indicators	numerical
num_failed_logins	Number of failed login attempts	numerical
logged_in	Successful entry	binary
root_shell	Access with administrative credentials	binary
num_root	Number of access attempts with administrative credentials	numerical
num_shells	Number of attempts to use the command line	numerical
num_access_files	Number of operations with access control files	numerical
Stats in 2 seconds / 100 connections		
count / dst_host_count	Number of connections with a matching host	numerical
serror_rate/ dst_host_serror_rate	% connection with error SYN	numerical
rerror_rate / dst_host_same_src_port_rate	% connections with REJ error /% connections with the same source port	numerical
same_srv_rate / dst_host_same_srv_rate	% of connections with the same service	numerical
diff_srv_rate / dst_host_diff_srv_rate	% connection to various services	numerical
srv_count / dst_host_srv_count	Number of connections with matching service	numerical
srv_serror_rate / dst_host_srv_serror_rate	% connections with SYN error	numerical
srv_rerror_rate / dst_host_srv_rerror_rate	% connections with error REJ	numerical
srv_diff_host_rate / dst_host_srv_diff_host_rate	% connections with different hosts	numerical

Based on the coincidence of the estimated and actual class labels, the effectiveness of attack detection was evaluated by the following criteria.

1. The total percentage of correctly classified attacks A (accuracy)

$$A = \frac{TP + TN}{N}, \tag{5.2}$$

where TP is the number of true-positive records, TN is the number of true-negative records, N is the total number of classified records.

2. The accuracy of the classification P (precision):

$$P = \frac{TP}{TP + FP}, \tag{5.3}$$

where FP is the number of false-positive records.

3. Completeness of classification R (recall):

$$R = \frac{TP}{TP + FN}, \tag{5.4}$$

where FN is the number of false-negative entries.

The traffic parameters used to describe the data link attack signatures are shown in Table 5.4. The experiments were carried out according to the algorithm shown in Fig. 5.3.

Table 5.4. Important traffic settings for network and application layers

Features	Description	Type
802.11 Protocol Features		
frame_ type/subtype	Frame Type / Subtype	text
protocol_type	Link Protocol Type	text
source_address	Source MAC Address	text
destination_address	Destination MAC address	text
Length	Frame size, bytes	numerical
SSID	SSID tag value	text
sequence_number	Frame number	numerical
fragment_number	Fragment Number	numerical
DS_status	Distributed system sharing	numerical
more_fragments	More fragments for transmission, 0 otherwise	binary
retry	Retransmission of the previous frame, 0 otherwise	binary
pwr_mgt	The client is in power saving mode, 0 otherwise	binary
more_data	Buffered frames for transmission, 0 otherwise	binary
protected_flag	Frame data is encrypted, 0 otherwise	binary
order_flag	Processing frames strictly in order, 0 otherwise	binary
duration	ACK + SIFS Transmission Duration, μs	numerical
chan_number	Channel number	numerical
signal	The signal level of the transmitter, %	numerical
TX_rate	Baud Rate, Mbps	numerical
cipher	Used encryption algorithm	textual
reason_code	Deauthentication Reason Code	numerical
Statistics in 2 seconds		
mng_frm_count	The number of management personnel	numerical
ctrl_frm_count	The number of control frames	numerical
probe_count	Number of connection requests	numerical
frag_count	The average number of fragmented packets	numerical

The support vector method was implemented using the SVS C-SVC library LibSVM, and the radial basis function (RBF) was used as the kernel function. The maximum learning error was limited to 10^{-5}.

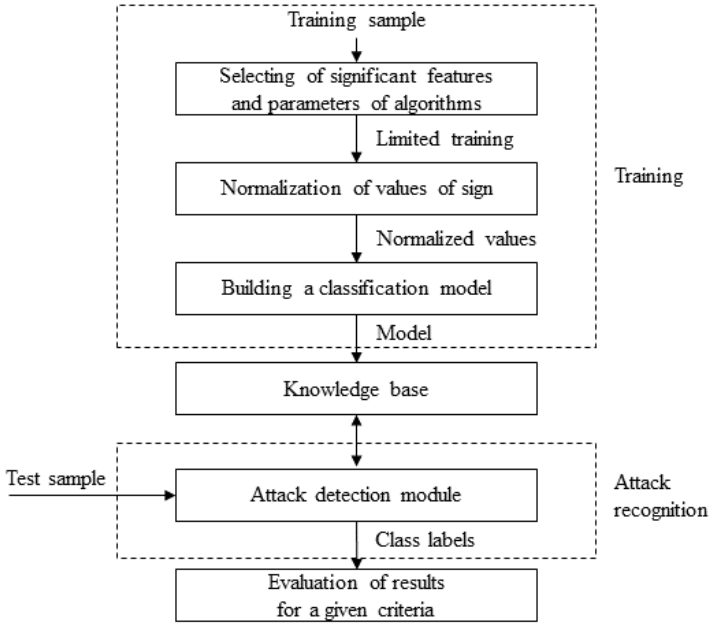

Fig. 5.3. Algorithm for attack detection in sensorless systems

The classification results using various DM methods are shown in Tables 5.5 and 5.6.

When classified by the method of *k*-nearest neighbors experimentally, as the optimal parameters of the algorithm, we chose a value of *k* equal to five, and the metric is the Manhattan distance.

The neural network was implemented as a multilayer perceptron with two hidden layers. Training with duration of 1500 cycles was carried out using the back propagation algorithm of the error. The maximum learning error was 10^{-7}.

Table 5.5. Network Application Layer Attack Performance Indicators

Group	Network activity class	Support Vector Method		k-nearest neighbors		Neural network		Decision trees	
		fullness	accuracy	fullness	accuracy	fullness	accuracy	fullness	accuracy
DoS	neptune	98.97	99.98	97.25	97.50	99.36	99.98	97.32	99.93
normal	normal	96.56	92.28	96.55	93.63	97.07	87.25	97.10	90.98
R2L	guess_passwd	76.69	100	66.86	95.48	66.37	97.03	65.72	99.88
DoS	smurf	100	99.70	97.59	100	95.19	99.53	100	100
Probe	satan	93.74	76.47	94.83	76.76	90.75	81.84	96.19	80.62
U2R	buffer_overflow	25.00	62.50	35.00	100	0	0	25.00	62.50
DoS	back	98.05	98.60	99.44	100	96.10	97.73	77.16	92.33
R2L	warezmaster	59.11	99.11	82.20	99.74	16.10	98.06	63.56	100
DoS	pod	95.12	72.22	95.12	72.22	82.93	70.83	95.12	46.99
Probe	nmap	98.63	93.51	97.26	91.03	79.45	90.62	98.63	74.23
Probe	ipsweep	97.16	93.84	97.16	74.86	97.87	79.31	99.29	88.05
probe	portsweep	91.08	56.30	85.35	73.22	89.17	61.67	84.71	54.07
DoS	teardrop	83.33	21.28	83.33	14.08	75.00	18.75	100	24.49
DoS	land	57.14	100	57.14	100	0	0	14.29	100
Average		83,61	83.27	84.65	84.89	70.38	70.19	79.58	79.58

Table 5.6. Link Level Attack Performance Indicators (in %)

Class	Support Vector Method		k-nearest neighbors		Neural network		Decision trees	
	fullness	accuracy	fullness	accuracy	fullness	accuracy	fullness	accuracy
Normal	98.03	92.49	97.65	99.26	94.37	99.38	95.48	95.11
rogue_client	100	37.56	6.22	20	32.44	20	100	69.02
EAPOL_logoff_flood	8.82	100	26.85	100	0.12	100	44.08	100
auth_flood	85.14	94.03	100	93.67	100	92.50	97.30	100
EAPOL_start_flood	100	100	100	50.58	100	44.14	100	100
deauth_flood	100	99.10	100	99.75	100	84.39	100	100
caffe_latte	0	0	100	100	100	70.97	100	100
Chopchop	100	62.86	100	100	100	3.28	100	2.27
client_fragment	97.44	99.77	100	99.89	100	96.98	100	100
AP_fragment	98.73	97.01	99.75	98.25	100	98.26	100	100
data_replay	99.82	98.13	100	99.98	99.96	99.53	100	100
MAC_spoofing	100	6.63	100	10.91	0	0	0	0
evil_twin_AP	100	100	100	64.78	100	94.30	100	94.90
EAP_replay	100	100	100	100	100	100	100	100
beacon_flood	100	100	100	99.95	99.91	100	100	99.86
RTS/CTS_flood	99.82	99.82	100	84.64	100	91.49	100	91.68
fake_auth	55.56	100	66.67	85.71	77.78	10.45	100	100
Average	84.90	81.61	88.07	82.79	82.62	70.92	90.40	85.46

Decision trees were built using the standard operator of the RapidMiner environment, the minimum threshold for the formation of a new node was chosen to be 4, the minimum number of leaves of the node was one, and the maximum number of levels was 10.

As can be seen from Table 5.5, the methods of support vectors and k-nearest neighbors showed close results in the course of detecting attacks, the decision tree and the neural network performed slightly worse. The low percentage of detection of certain types of attacks, such as warezmaster, guess_passwd, buffer_overflow, and land, is caused by the uneven quantitative distribution of training samples for different classes - the predominance of normal signatures and attacks of the DoS and Probe categories. For the same reason, some of the attacks were classified incorrectly, so their results are not presented in Table 5.5. However, according to the indicators in Table 5.6, the *k*-nearest-neighbor method and decision tree are superior to SVM and neural networks in solving the task of detecting link-layer attacks. Thus, the analysis of experimental data shows that the algorithms used to demonstrate different values of attack detection performance indicators depending on the type of network activity and the level of the OSI model at which the attack is implemented.

In this regard, it is proposed to use an ensemble of four developed algorithms and one arbiter, which determines the final class of network activity by weighted voting. The architecture and functioning principles of the proposed ensemble will be the essence of further research.

5.5. CONCLUSIONS

This material provides an overview of network attacks that are relevant for local wireless networks, presents the architecture of the proposed attack detection system based on the use of DM methods for recognizing attack data, and compares these methods during experiments to detect the considered types of attacks.

In general, the methods showed high accuracy and completeness of detection during the experiments, from which it can be concluded that the proposed approach to detecting attacks in local wireless networks is practical.

REFERENCES

[1] OLUSOLA A., OLADELE A., ABOSEDE D., Analysis of KDD'99 Intrusion Detection Dataset for Selection of Relevance Features, in: *Proceedings of the World Congress on Engineering and Computer Science*, San Francisco, vol. 1, p. 162-168, 2010.

[2] NGUYEN T., NGUYEN B., PHAM H., An efficient solution for preventing Dis'ing attack on 802.11 networks, in: *2012 International Conference on Green Technology and Sustainable Development: Journal of Engineering Technology and Education*, Hochiminh, p. 395-403, 2012.

[3] BELEJ O. et al., Features of application of data transmission protocols in wireless networks of sensors, in: *Advanced information and communication technologies, AICT–2019: proceedings of the 3rd International Conference*, Lviv, Ukraine, p. 317–322, 2019.

[4] MULAY S., DEVALE P., GARJE G., Intrusion Detection System using Support Vector Machine and Decision Tree, *International Journal of Computer Applications*, vol. 3, no. 3, p. 40-43, 2010.

[5] SUN T., ZHANG J., YANG Y., Review on the development and future trend of the intrusion detection system (IDS), in: *2016 International Conference on Communication and Electronics Systems (ICCES)*, Coimbatore, p. 1-6, 2016.

[6] AHMED M. R., CUI H., HUANG X., Smart integration of cloud computing and MCMC based secured WSN to monitor the environment, in: *2014 4th International Conference on Wireless Communications, Vehicular Technology, Information Theory and Aerospace & Electronic Systems (VITAE),* Aalborg, p. 1-5, 2014.

[7] HAN W. et al., Quantitative Assessment of Wireless Connected Intelligent Robot Swarms Network Security Situation, *IEEE Access,* vol. 7, p. 134293-134300, 2019.

[8] DONGARE S. P., MANGRULKAR R. S., Implementing energy-efficient technique for defense against Gray-Hole and Black-Hole attacks in wireless sensor networks, in: *2015 International Conference on Advances in Computer Engineering and Applications,* Ghaziabad, p. 167-173, 2015.

[9] ALSHEIKH M.A. et al., Machine Learning in Wireless Sensor Networks: Algorithms, Strategies, and Applications, *IEEE Communications Surveys & Tutorials,* vol. 16, no. 4, p. 1996-2018, 2014.

[10] EL MOURABIT Y. et al., Intrusion detection system in Wireless Sensor Network based on mobile agent, in: *2014 Second World Conference on Complex Systems (WCCS),* Agadir, p. 248-251, 2014.

[11] SREERAM I., VUPPALA V.P.K., HTTP flood attack detection in application layer using machine learning metrics and bio-inspired bat algorithm, *Applied Computing and Informatics*, vol. 15, p. 1-5, 2019.

[12] NANDITA S. et. al., Designing of an online intrusion detection system using rough set theory and Q-learning algorithm, *Neurocomputing*, vol. 111, p. 161-168, 2013.

DOI: 10.24427/978-83-66391-87-1_06

Viktoriia BORTNIKOVA[1], Vladyslav YEVSIEIEV[1], Iryna BOTSMAN[1],
Igor NEVLIUDOV[1], Kostiantyn KOLESNYK[2], Nazariy JAWORSKI[2]

6. QUERIES CLASSIFICATION USING MACHINE LEARNING FOR IMPLEMENTATION IN INTELLIGENT MANUFACTURING

Today, information retrieval systems have plays an important role in intellectual manufacturing. Such systems would provide a speed with large volumes of data, system speed and etc. More roles in such system is search queries. The search queries are arrays of digital text information that can be big data, coming up to several hundred billion gigabytes or higher. In order to increase the speed of operation with such data in information retrieval systems, it is necessary to classify them.

For task it is known: production section, 1000 search queries of arbitrary form and content and 5 search queries categories (error message, production section, the equipment state, sensors search, and system parameters).

So here is the task lay down of the information retrieval systems speed increasing in manufacturing at the expense search queries classification by machine learning methods.

6.1. RESEARCH OBJECTIVE

Here is the task lay down of the information retrieval systems speed increasing in manufacturing at the expense of the search queries classification by machine learning methods. For this task, it is known:

- production section,
- 1000 search queries of arbitrary form and content,
- search queries categories: error message, production section, the equipment state, sensor search, system parameters,
- only one value for each category can be assigned to each search query, and a set of possible values for each category is known beforehand,

[1] Kharkiv National University of Radio Electronics, Ukraine
[2] Lviv Polytechnic National University, Ukraine

- the search queries need to be analyzed and categorized into several unrelated categories, and the search query content should be defined as one of them,
- when classifying search queries, categories are defined in advance, with clustering they are not specified, and even information about their number may not be available. It is necessary to perform mathematical statement of the search queries classification task. To do this, consider the existing formulations of the classification problem.

Formally, the classification problem is the next: an array of text search queries $T = \{t_1,\ t_2,\ \ldots,\ t_i\}$ and an array of possible classes $C = \{c_1,\ c_2,\ \ldots,\ c_i\}$ are set. There is an unknown target dependency – a transform image $f: T \times C \to \{0; 1\}$, that is set

$$f(t_i, c_i) = \begin{cases} 0, \text{if } t_i \notin c_j, \\ 1, \text{if } t_i \in c_j. \end{cases} \quad (6.1)$$

It is necessary to form a classifier $f'(t_i, c_j)$ that is as close as possible to $f(t_i, c_j)$. With such statement of search queries classification task, there is no known additional information about the classes and the search queries text other than those that can be derived from the search query itself. The classification will be accurate when the resulting search query classifiers transform the image

$$f': T \times C \to \{0; 1\}.$$

The search query class will be the limit if such degree of similarity will yield

$$f': T \to [0; 1].$$

Described statement of the problem refers to the tasks of machine learning by precedents or training with a teacher [1]. In the general case, the training sample *N* is formed that is a set of search queries related by the previously unknown regularity. This sample is necessary for the classifier training and determining the values of its parameters, with which the classifier produces a better result. Next, in the system, the decisive rules will be determined, by which the search queries set division for given classes occur.

In the set task, each search request must respond only to one class $c \in C$, and then there will be unambiguous classification.

Thus, it is necessary to solve several tasks for the search queries classification:

- search query text pre-processing,
- search queries attributes identification,
- search queries attributes dimensionality decreases,
- classifier development and training by the machine learning methods,
- classification quality assessment,
- obtaining a classifier model,
- classifier testing for new data.

For the classification algorithm, choosing the particular qualities of each algorithm should be taken into account and as a result, it is necessary to conduct research. It is also necessary to resolve the issues of determining the attribute set, their number and the methods of calculating weight numbers, and also of the need to select some algorithms parameters during the training step.

In the deep learning algorithms, the classification accuracy depends on the availability of a training sample of the appropriate size, and the preparation of such sample is a very laborious process.

6.2. NORMALIZATION OF SEARCH QUERY DATA

Each search query text *T* consists of

$$T = S \cup W, \tag{6.2}$$

where S is the word's array of the search query text $S = [word_1 \dots word_n]$, n is the word's number, and W is the set of words that do not carry semantic meaning (unions, pronouns, articles, numbers, signs, etc.).

To simplify the work with the search query texts, suppose that W can also be defined as a set S, that is

$$T = [word_1 \dots word_n] \tag{6.3}$$

Pre-processing of the search query text is necessary before its conversion into numerical values and further work on it. First of all, the noise component must be removed from text, particularly, removal of words that do not carry a semantic meaning. As noted above, such words are unions, pronouns, articles, numbers, signs, and so on.

6.2.1. TOKENIZATION

To do this, we first need to split up the search query for words or phrases *tokens* (*tokenization*), taking into account the specifics of the search query text, i. e. *technological process* should be perceived as one or two *tokens*. To implement *tokenization*, use N-gram [2-3]. N-grams are of several types. The most common search queries when using tokenization are unigrams and bigrams. Also, there are the symbolic N-grams in which the text is not fragmented into separate words, but on the characters segments of a certain length [2-5]. A comparative analysis was conducted, the results of which are given in Table 6.1. Several variants of search query tokenization in the form of the unigrams, the bigrams and the 3-character N-grams were analyzed for the example of 3 requests: *workpiece location 8*, *technological operation 3* and *sensors status 26 in production line 2*.

As Table 6.1 shows, the best variant would be to use either unigrams or bigrams, because the character N-gram divides the search query text into unrelated letters that is difficult for further processing.

Table 6.1. Results of search queries tokenization by N-grams

Search queries	Unigrams	Bigrams	3-character N-grams
Technological operation 3	[technological, operation, 3]	[technological operation, 3]	[tec, hno, log, ica, lo, per, ati, on, 3]
workpiece location 8	[workpiece, location, 8]	[workpiece location, 8]	[wor, kpi, ece, lo, cat, ion, 8]
sensors status 26 in production line 2	[sensors, status, 26, in, production, line, 2]	[sensors status, 26 in, production line, 2]	[sen, sor, s s, tat, us, 26 in, np, rod, uct, ion, li, ne , 2]

For unigram, the search query text will be written as

$$T = [word_1, word_2, \dots, word_n]. \tag{6.4}$$

6.2.2. CALCULATE QUALITY PARAMETERS OF THE SEARCH QUERY TEXT DEFINITION

After the search query splitting (*tokenization*) into *words*, it is necessary to perform its syntactic and spelling check, as well as to determine its unmeaning and informativeness [6]. As a generalized estimate of the search query text, the next expression can be used

$$\lambda = \frac{\omega_1 \cdot E + \omega_2 \cdot O + \omega_3 \cdot V + \omega_4 \cdot P}{\sum_{j=1}^{4} \omega_j}, \tag{6.5}$$

where E is the calculated value of the search query text syntactic correctness; O is the estimated value of the search query text spelling correctness; V is the estimated value of the search query text unmeaning; P is the estimated value of the search query text informativeness; ω_i is weight coefficients that represent the significance of one or another parameter in the overall assessment. It should be noted that

$$\sum_{j=1}^{4} \omega_j = 1,$$

then (6.5) simplifies to

$$\lambda = \omega_1 \cdot E + \omega_2 \cdot O + \omega_3 \cdot V + \omega_4 \cdot P. \tag{6.6}$$

It is necessary to determine the weight coefficients for each of the parameters. This can be performed using the methods of ranking and assigning points [6]. Expertise is conducted by the experts group of 20 people who are experts in the field of automation and computer-integrated technologies and have different age categories (Table 6.2).

Weighting coefficients that represent the significance of one or another parameter in the overall assessment

$$\omega_1 = \frac{64}{200} = 0.305, \quad \omega_2 = \frac{36}{200} = 0.18,$$
$$\omega_3 = \frac{61}{200} = 0.305, \quad \omega_4 = \frac{42}{200} = 0.21. \tag{6.7}$$

The obtained values of weight coefficients can be substituted to (6.6) [7]

$$\lambda = 0.305 \cdot E + 0.18 \cdot O + 0.305 \cdot V + 0.21 \cdot P. \tag{6.8}$$

Next, we consider how it is possible to calculate quality parameters of the search query text definition.

Table 6.2. Expert polls results

Expert	Parameters important for evaluating search query text (rank)				Expert	Parameters important for evaluating search query text (rank)			
	V	*E*	*P*	*O*		*V*	*E*	*P*	*O*
1	4	3	2	1	11	3	2	1	4
2	3	2	4	1	12	3	1	4	2
3	3	2	4	1	13	3	1	4	2
4	3	1	4	2	14	3	1	4	2
5	2	1	4	3	15	2	1	4	3
6	2	4	1	3	16	4	2	3	1
7	4	2	3	1	17	3	2	4	1
8	4	1	2	3	18	2	1	4	3
9	4	1	2	3	19	2	4	1	3
10	4	3	2	1	20	3	1	4	2
Sum	33	20	28	19	Sum	28	16	33	23

The syntax check of a search query text involves checking of the search query text syntactic correctness that can be calculated as follows

$$E = 1 - \begin{cases} 2 \cdot \frac{s}{n}, \text{ if } \frac{s}{n} < 0.5, \\ 1, \text{ if } \frac{s}{n} \geq 0.5, \end{cases} \tag{6.9}$$

where s is the syntax errors number, n is the total words number in the search query.

It must be taken into account that the syntactic correctness of the search query text E must take on values from 0 to 1, the value 0 means that all words in the search query text are syntactically correct and 1 means that all words in the search query text are syntactically incorrect.

So if the number of syntax errors is greater than half of the total words number in the search query text, the text should be evaluated as syntactically incorrect. And if errors number is less than the threshold value, the estimated value will be equal to the doubled ratio of the syntax errors number to the total words number.

The search query text spell checking involves the follows spelling correctness calculation

$$O = 1 - \begin{cases} 2 \cdot \frac{o}{n}, \text{ if } \frac{o}{n} < 0.5, \\ 1, \text{ if } \frac{o}{n} \geq 0.5, \end{cases} \tag{6.10}$$

where o is number of spelling mistakes.

It should be noted that the search query text spelling correctness O must also take on values from 0 to 1. The value 0 means that all words in the search query text are spelled correctly, and 1 means that all words in the search query text are spelling mistaken. For the analysis of the search queries texts quality, it is necessary that, with the spelling mistakes number greater than half the total of words number in the search query text, the text will be evaluated as illiterate. And in case when the errors number is less than the threshold value, the assessment value will be equal to doubled ratio of spelling errors number to total words number.

Checking the search query text unmeaning involves checking for presence of meaningful expressions, phrases, words that do not carry semantic meaning in the search query text. It can be calculated as follows

$$V = 1 - \begin{cases} 2 \cdot \frac{v}{n}, \text{ if } \frac{v}{n} < 0.5, \\ 1, \text{ if } \frac{v}{n} \geq 0.5, \end{cases} \tag{6.11}$$

where v is the number of spelling mistakes.

The unmeaning of search query text V should fall in the range from 0 to 1. The value of 0 means that in the search query text completely absent of words without semantic meaning. And value of 1 means that the search query text is entirely composed of words without semantic meaning (but in practice, as a rule, such search queries texts have a random character of appearance). Thus, when the number of words that does not carry a semantic meaning in the search query text is more than half of the total words number, the text must be evaluated as the text with the maximum amount of unmeaning. When the number of words without semantic meaning in the search query text is less than the threshold value, the assessment value will be equal to the doubled ratio of the number of words without semantic meaning in the search query text to the total words number in the search query.

Checking of the search query text for informativity allows determining the search query text quality, taking into account the possible repetition of expressions, phrases, words. And in such a way, semantic meaning of the search query text can be displayed. Informative content of the search query text can be calculated as follows

$$P = \begin{cases} \frac{p}{n}, \text{ if } 0.3 < \frac{p}{n} < 0.8, \\ 1, \text{ if } \frac{v}{n} \geq 0.8, \\ 0, \text{ if } \frac{v}{n} \leq 0.3, \end{cases} \quad (6.12)$$

where p is the number of different search query words.

It should be taking into account that the information content of the search query text of the P must also take on values from 0 to 1. The value 0 corresponds to the search query text, which contain repetitive word, and 1 means that all words in the search query text differ. Having in consideration the statistics that threshold value, which corresponds to 0 in the search queries text, is rarely encountered, then (6.14) is converted as follows.

For values less than or equal to 0.3, the informative content of the search query text is equal to 0, with values greater than 0.8 informative content is 1, and for range from 0.3 to 0.8 value is unchanged.

6.2.3. STEMMING

Thus, after search query text *tokenization* and its syntactic and spelling checking, as well as unmeaning and informative determining, it is necessary to perform *stemming*. That means cutting off the words flexions and suffixes, so that the rest of the part remains the same for all grammatical word forms. The results of stemming are similar to the word root definition. But stemming algorithms are based on other principles and the results after its use often differ from the morphological *word* root. There are several variants of the stemming algorithms that differ in accuracy and productivity. They are: search by table, clipping of flexions and suffixes, lemmatization, stochastic algorithms, hybrid approach, prefixes clipping, matching search [4]–[7].

A comparative analysis of the features, advantages and disadvantages of known stemming algorithms was carried out. In this analysis, the search query text specifics of the stemming algorithm base was researched. As an example, the term *technological operation*, which is tokenized as: [*technological*, *operation*], was analyzed [8].

Based on the analysis, it can be concluded that in the future research, the algorithm of flexions and suffixes clipping will be used. It is compact and productive and will allow the words stemming in the search queries text to be realized. After search query converting into the words sequence, converting them into the attributes vector can be started.

6.3. TRAINING AND TESTING A SEARCH QUERY CLASSIFIER USING MACHINE LEARNING

Next, we set out the search query text as the list of pre-processed words T^*. Each word of the search query $word_n \in T^*, n = \overline{1, n'}$ has its own quality rating λ and weighing

coefficient W relative to the search query text $t_j \in T$. Thus, each search query text can be represented as a vector of the weighing coefficient of its words

$$\vec{t}_j = \langle W_{1j}, \dots, W_{ij} \rangle.$$

The weighing coefficient of search queries is standardized by taking into account equations (6.7), (6.9), (6.11), (6.13), and (6.15)

$$0 < W_{ij} < 1, \ \forall i,j: 0 \le i \le |T^*|, \ \ 0 \le j \le |T|.$$

Thus, a dictionary of 121 words for the search query classification can be presented in the matrix form of 121 × 1119 elements, where each line corresponds to the weighing coefficients of the meaningful search query words.

The development of a classifier for the search query classification is carried out using a neural network. One of the types of neural networks is learned networks [9]. This network type is used to formalize tasks that include the recognition of search query texts. In the process of learning the network automatically changes its parameters, such as the weighing coefficient of the layers and, if necessary, the number of hidden layers. In general, the neural network must have an input layer, hidden layers, and an output layer.

The main points of the search query classification using the neural network are as follows:

- the matrix is forming in which the values of the input layer X and the output layer Y are present; the X value is equal to the value of the processed dictionary and the value of Y corresponds to the specified value of the search query characteristics,
- selecting the required number of neural network layers,
- selecting the required number of neural network hidden layers,
- generating random values of the weighing coefficients for all neurons in the network,
- adjustment of the weighing coefficients of all neurons in the network to achieve the minimum error value,
- obtaining a trained neural network,
- evaluation of the received classifier.

The neuron input layer is the search query text converted in the dictionary form, which is considered in section 2, that is, the size of the input layer is equal to the size of the processed dictionary of 121 elements, and each neuron of the input layer is fed as a normalized number (from 0 to 1).

The output layer size for the search query classification task equals to the number of possible target values. The search query characteristics should have the following values in accordance with the appeal: system error; state of the production line; state of the technological equipment; sensors and system parameters. Then the neurons number in the output layer will be equal to 5. When training the network for each characteristic value, it is necessary to determine in advance the reference unique set of numbers that we expect to get at the output layer.

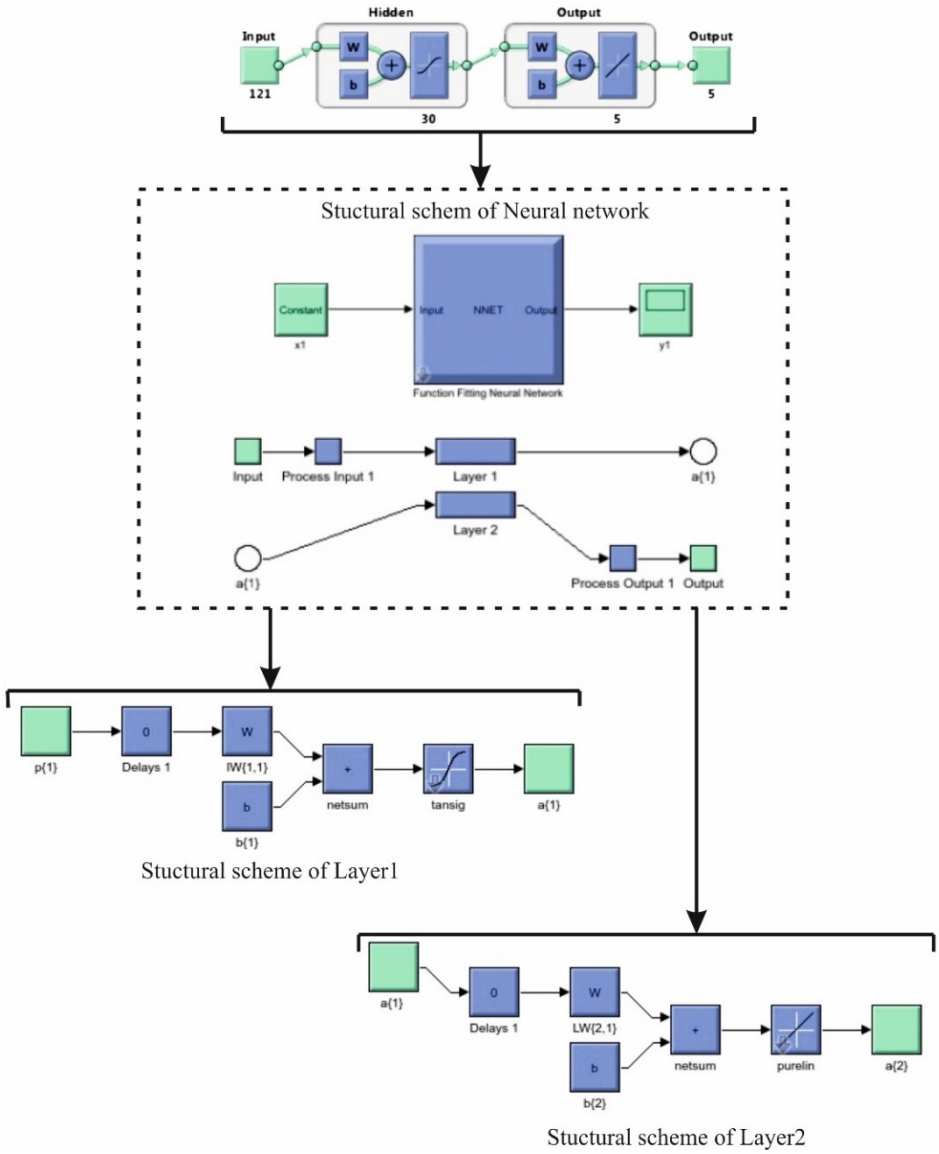

Fig. 6.1. Neural network architecture

The number of neurons in each layer needs to be determined in advance. After learning the network, each output neuron must also have a value from 0 to 1.

For training neural network, the *toolNeuralFitting* is used, in which there is a need to set the value of the inputs and targets sequence [9]. The data matrix for network learning is a pre-processed dictionary that is stored as a matrix of 121 × 1119 elements. And the vector of the output layer is *Targets*, that is, pre-processed categories (matrix values with the size of 5 × 1119 elements).

After putting in the values of the input and output layers, process of the neural network learning, which is an iterative process, begins. In the network learning process, the number and dimension of hidden layers were changed.

Experimentally determined that the best result is given by a neuron network consisting of two layers (Fig. 6.1). The hidden layer has a dimension of 30 neurons (that is approximately 1/4 of the dictionary size). And the second layer has a dimension of 5 neurons (that is 1/6 of the first layer size).

To check the network productivity, the regression can be evaluated (Fig. 6.2). The graph shows the relationship between the *Dataset* and *Outputs* (targets) for *Training*, *Validation*, and *Testing* data. For perfect fit, the data should get along the 45-degree line, where the network outputs are equal to the targets.

As can be seen from Fig. 6.2, the adjustment is good enough for all datasets, and the values of *R* in each case is 0.73 or higher. If more precise results are needed, it is possible to retrain the network with changed start weighing coefficients, that may lead to improved network after retraining, or vice versa.

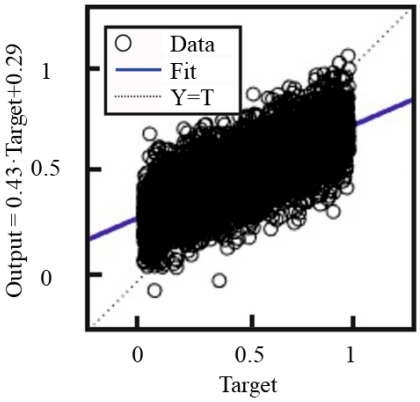

Fig. 6.2. Model productivity evaluation

We further evaluate the network productivity using the error histogram (Fig. 6.3). In Fig. 6.3, the blue columns indicate the learning data (*Training*), the green columns show check data (*Validation*), and red columns show the test data (*Testing*).

The histogram shows overshoot that are data points, where fitting is much worse than for most data. Fig. 6.3 shows that although most errors fall within the range between 0.8927 and 0.8548, there is a training point with error of 17 and verification checkpoints with errors of 12 and 13. These overshoots are also seen in the regression graph (Fig. 6.2). The first point corresponds to a point with the target of 0.5979 and is displayed at 0.3066.

The overshoots checking using the error histogram allows to determine the data quality and determine the data points that differ from the rest of the data set.

The mean-square error can also be evaluated on the validation data for successive training periods (*epoch*) and it is possible to see the changes dynamics in the learning status.

To classify the search queries in the information retrieval systems, preparation of the training sample was formed. In order to process the search queries texts, a *tokenization* of a search query for words or phrases was made initially. It was determined that the best fit for this task is using the unigram.

After *tokenization*, the syntax and spelling checking were performed, and the search query text unmeaning and informativeness were determined. To reduce the dictionary size, the *stemming* algorithm was used. Thus, the set of 1000 queries was first converted into a dictionary of 3200 elements, and as a result, the dictionary was obtained in the matrix form of 121×1119 elements.

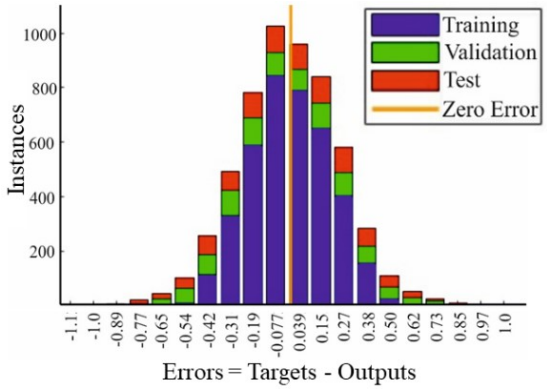

Fig. 6.3. Histogram of errors

The classifier was trained using a neural network. The classifier productivity evaluation was performed according to the error value, the noise component, the system training status and the training speed.

6.4. CONCLUSIONS

Based on the research and evaluation of the obtained learning results of the neural network, we can conclude that it is necessary to conduct further research in the direction of improving the learning outcomes of the network. To do this, it is necessary to conduct a more in-depth study aimed at improving the quality of the classifier and determining a more universal approach to solving the task of search query classification for information retrieval systems in intelligent manufacturing.

Further, the introduction of such neural network will increase the speed of information retrieval systems work by classifying search queries for 5 specified categories.

REFERENCES

[1] GUAND N., WANG X., *Computational Design Methods and Technologies: Applications in CAD, CAM and CAE Education*, IGI Global, 2012.

[2] ZHANG X., ZHAO J., LECUN Y., Character-level convolutional networks for text classification, in: *Proc. Neural Inform. Processing Systems Conf. (NIPS 2015)*, https://arxiv.org/abs/1509.01626, 2015 (accessed: 28.11.2018).

[3] JURAFSKY D., MARTIN J. H., *N-gram Language Models, Speech and Language Processing*, online https://web.stanford.edu/~jurafsky/slp3/3.pdf, (accessed: 28.11.2018).

[4] VIJAYARANI S., ILAMATHI J., NITHYA M., Preprocessing Techniques for Text Mining, *International Journal of Computer Science & Communication Networks*, vol. 5(1), p. 7-16, 2014.
[5] LABOREIRO G. et al., Tokenizing micro-blogging messages using a text classification approach, in: *Proceedings of the Fourth Workshop on Analytics for Noisy Unstructured Text Data*, Toronto, Canada, 2010.
[6] Universitat Pompeu Fabra, *How to write a streaming algorithm*, online https://essentia.upf.edu/documentation/extending_essentia_streaming.html, (accessed: 28.11.2018).
[7] LOVINS J. B., *Development of a Stemming Algorithm*, Mechanical Translation and Computational Linguistics, 1968.
[8] BORTNIKOVA V. et al., Search Query Classification Using Machine Learning for Information Retrieval Systems in Intelligent Manufacturing, in: *Proc. 15th International Conference ICTERI 2019 (ICTERI 2019)*, p. 460-495, 2019.
[9] KIM P., *MATLAB Deep Learning: with Machine Learning, Neural Networks and Artificial Intelligence*, Springer Science, 2017.

DOI: 10.24427/978-83-66391-87-1_07

Wiktor JAKOWLUK[1]

7. FRACTIONAL-ORDER LTI SYSTEM IDENTIFICATION USING INTEGER-ORDER STATE-SPACE MODEL

The optimal input signal design is a technique of generating an informative excitation signal to estimate the model parameters with maximum accuracy. In the paper, a novel optimal input formulation and a numerical scheme for fractional-order LTI system identification are presented. The Oustaloup recursive approximation (ORA) method is used to determine the fractional-order differentiation in an integer-order state-space form. Then, the proposed method is used to obtain an optimal input signal for fractional-order system parameter estimation from the interval $0.5 \leq \alpha \leq 2.0$. The methodology presented in this paper has been verified using numerical examples, and the experiment results have been discussed.

7.1. INTRODUCTION

Fractional-order calculus has received a lot of attention in different scientific fields, including precise system modeling and automatic control problems [1, 2]. It has been shown that fractional-order models guarantee a more exact system dynamics depiction because real-life processes appear to be of non-integer order [3, 4]. The fractional-order calculus is the generalization of integration and differentiation where the power is of fractional-order [5]. Many reports have been devoted to study the accuracy of the non-integer calculus in application to different domains, e.g.: bioengineering [6], physics [7, 8], chaos theory [9], control systems [10, 11] and fractional signal processing [12, 13].

It is clear that the rise of interest in the fractional-order calculus domain has a relationship with the increasing availability of high-performance computational packages. Adaptation of the methods of the fractional-order estimation to real-life industrial problems should bring about quality improvement and cost minimization. Moreover, fractional-order approximation methods used for automatic control purposes

[1] Bialystok University of Technology, Poland

results in the improvement of control loops. Fractional-order calculus is often applied to robotics and automation for the system identification and automatic control purposes [2]. The control performance evaluation has a great impact on the economic condition of the real-life processes. In contrast to the fractional-order controllers, a conventional PID controller has been shown to be unsatisfactory for industrial applications due to its limited tuning flexibility [14].

The optimal excitation signal design task concerns the optimal control methods for linear and nonlinear integer-order systems. The main goal of this paper is to introduce a novel optimal input design formulation and the numerical scheme for fractional-order system identification. The methodology is presented using the LTI inertial model. The Oustaloup recursive approximation (ORA) method has been used to exact approximation of the non-integer order operator, which is then transformed into a zero-pole transfer function [15]. The estimation results are then used for a transfer function conversion into an integer-order state-space form. The problem appears for fractional-orders ($\alpha > 1$) during the transfer function conversion into the state-space form, when the order of the numerator is equal to the order of the denominator. This issue has been solved by augmenting a fractional-order system dynamics with one extra state. An optimal input design task for non-integer order linear time-invariant system identification has been verified by numerical examples in an order range from the interval (0.5, 2.0). The problems of the optimal input design, in the context of the integer-order system identification, are considered in earlier works of the author [16, 17, 18].

7.2. FRACTIONAL-ORDER CONTROL PROBLEM

The problem of the fractional-order calculus is a generalization of integral and differential operators to a non-integer operator ${}_aD_t^\alpha$. The continuous operator of the fractional-order α is given by

$$ {}_aD_t^\alpha = \begin{cases} \dfrac{d^\alpha}{dt^\alpha} & \Re(\alpha) > 0, \\ 1 & \Re(\alpha) = 0, \\ \displaystyle\int_a^t (d\tau)^{-\alpha} & \Re(\alpha) < 0, \end{cases} \tag{7.1} $$

where: a, t - denote the limits of the process and α is the set for all complex numbers. The fractional-order calculus is the special case of a classical integer-order differential equations task. Linear fractional-order continuous-time SISO dynamic system is comensature-order if all powers of a derivative are integer multiples of the order q in such a way that $\alpha_k, \beta_k = kq$, $q \in R^+$, and is given by the following equation [1, 2]

$$ \sum_{k=0}^{n} a_k D_t^{\alpha_i} y(t) = \sum_{k=0}^{m} b_k D_t^{\beta_i} u(t), \tag{7.2} $$

where: a_k, b_k are model constant coefficients. The discrete-time formulation for different orders can be discovered from [19]. The LTI model is of rational-order if $q = r^{-1}$, and $q \in R^+$. Using the Laplace transformation to equation (2), and applying zero initial conditions to the input-output specification of the fractional-order model, the transfer function formulation can be written as

$$G(s) = \frac{Y(s)}{U(s)} = \frac{b_m s^{\beta_m} + b_{m-1} s^{\beta_{m-1}} + \cdots + b_0 s^{\beta_0}}{a_n s^{\alpha_n} + a_{n-1} s^{\alpha_{n-1}} + \cdots + a_0 s^{\alpha_0}}. \tag{7.3}$$

The continuous-time system of commensurate-order q can be modified to obtain the pseudo-rational transfer function formula $H(\lambda)$ in the form

$$H(\lambda) = \frac{\sum_{k=0}^{m} b_k \lambda^k}{\sum_{k=0}^{n} a_k \lambda^k}, \tag{7.4}$$

where $\lambda = s^q$. On the basis of this conception, pseudo-rational description of the fractional-order linear time-invariant model can be formulated by a state-space equation given by

$$\begin{aligned} {}_0D_t^{\alpha} x(t) &= Ax(t) + Bu(t), \\ y(t) &= Cx(t) + Du(t). \end{aligned} \tag{7.5}$$

For the model parameters estimation purposes, the difference equation representing input-output dynamics of the system is more useful than the state-space formulation. However, the state-space model description provides multiple input and multiple output (MIMO) fractional-order systems representation.

7.3. FRACTIONAL-ORDER OPERATOR APPROXYMATION

The problem of approximating the fractional-order system by an integer-order one has been presented in [1]. The Oustaloup recursive approximation (ORA) method, which has a very good fitting to the fractional-order transfer functions is widely used in practice. We focus our attention on the Oustaloup recursive approximation algorithm during the experiments. Choosing the appropriate frequency fitting range, the problem of a fractional differentiator or a fractional integrator estimation can be solved using following formulas

$$s^{\alpha} \approx K \prod_{k=1}^{N} \frac{s + \omega_k^{'}}{s + \omega_k}, \tag{7.6}$$

where poles, zeros and a gain of the filter can be obtained from

$$\omega_k^{'} = \omega_b \cdot \omega_u^{(2k-1-\alpha)/N}, \tag{7.7}$$

$$\omega_k = \omega_b \cdot \omega_u^{(2k-1+\alpha)/N}, \tag{7.8}$$

$$K = \omega_h^{\alpha}, \tag{7.9}$$

$$\omega_u = \sqrt{\frac{\omega_h}{\omega_b}}. \tag{7.10}$$

Where N is the order of the approximation, and ω_b, ω_h are the selected frequency fitting range. The order of the approximation is $2N + 1$, and considering higher orders of N the approximation results should be more accurate.

The Oustaloup filter provides an exact fitting to a fractional operator in a chosen frequency interval, and a orders range [4]. Thus, for the fractional-order operators, where $\alpha \geq 1$ one should separate a fractional order using the following formula

$$s^{\alpha} = s^n s^{\gamma}, \tag{7.11}$$

where $n = \alpha - \gamma$ is the integer part of α and s^{γ} is solved according to (7.6) using Oustaloup recursive approximation. The transfer function obtained from ORA filter has been used to transform the external model form into the integer-order internal state-space representation. In general, the n-th order transfer function obtained from the pole-zero formula is as follows

$$H(s) = \frac{Y(s)}{U(s)} = \frac{b_0 s^n + b_1 s^{n-1} + \cdots + b_{n-1} s + b_n}{s^n + a_1 s^{n-1} + \cdots + a_{n-1} s + a_n}, \tag{7.12}$$

where a and b are the factors of the polynomials in descending powers of s, and $a_0 = 1$. Then, it is possible to determine an optimal input signal for the fractional-order system identification using integer state-space equation [15].

Since the choice of the state coefficients can differ, the transfer function representation can also be different. Referring to publication [20], the fractional order operator ${}_{t_0}D_t^{\alpha}$ has the following form

$${}_{t_0}D_t^{\alpha} x(t) \approx \begin{Bmatrix} \dot{z} = A_F z + B_F u \\ x = C_F z + D_F u \end{Bmatrix}, \tag{7.13}$$

where the corresponding matrices are as follows

$$A_F = \begin{bmatrix} -a_{n-1} & -a_{n-2} & \cdots & -a_1 & -a_0 \\ 1 & 0 & \cdots & 0 & 0 \\ 0 & 1 & \cdots & 0 & 0 \\ \vdots & \vdots & \cdots & \vdots & \vdots \\ 0 & 0 & \cdots & 1 & 0 \end{bmatrix}, \tag{7.14}$$

$$B_F = [1 \quad 0 \quad 0 \quad \ldots \quad 0]^T, \tag{7.15}$$

$$C_F = \begin{bmatrix} (b_n - a_n b_0)(b_{n-1} - a_{n-1} b_0) \cdots \\ \cdots (b_2 - a_2 b_0)(b_1 - a_1 b_0) \end{bmatrix}, \tag{7.16}$$

$$D_F = b_0 = d. \tag{7.17}$$

To solve the problem of the optimal input design for fractional-order model identification, there is a need to approximate the fractional-order operator, and transform this problem, to be solved using one of the available software packages for optimal control.

7.4. OPTIMAL INPUT GENERATION PROBLEM

To illustrate the efficacy of this technique to fractional-order system parameter estimation, using the ORA filter, we have selected Riots_95 toolbox, which has been developed to solve the optimal control problems [21]. The optimal excitation signal design for fractional-order system identification that minimizes objective function is as follows

$$\begin{aligned} J = g\left(C_F z(t_0) + D_F u(t_0), C_F z(t_f) + D_F u(t_f)\right) \\ + \int_{t_0}^{t_f} l(C_F z + D_F u, u, t) dt, \end{aligned} \tag{7.18}$$

subject to the system dynamics

$$\dot{z}(t) = A_F z + B_F\big(h(C_F z + D_F u, u, t)\big), \tag{7.19}$$

with respect to the initial conditions

$$z(t_0) = \frac{x_{t_0} T}{C_F T}. \tag{7.20}$$

The real state-space variable $x(t)$ formulation is given by

$$x(t) = C_F z(t) + D_F u(t), \tag{7.21}$$

where x is the state-space vector, $t \in [t_0, t_f]$ is time duration. The potential set of constraints is as follows

$$u(t) \in \langle u_{min}(t), u_{max}(t) \rangle, \tag{7.22}$$

$$\big(C_F z(t_0) + D_F u(t_0)\big) \in \langle u_{min}(t_0), u_{max}(t_0) \rangle. \tag{7.23}$$

The convergence of the optimization is related with the vector T selection. Regarding to vector B_F, which is described by the matrix (7.15), vector T is given by

$$T = [1 \quad 0 \quad 0 \quad \ldots \quad 0]^T. \tag{7.24}$$

The angular pulsation for the Oustaloup approximation has been selected as [0.01, 100] rad/s. The selection of the frequency range depends on the discretization of the control duration corresponding to the software algorithm for solving OCP problems, a wide fitting range increases the computational effort. The final time has been chosen as $t_f = 1.5\ s$. The selection of the Oustaloup filter order N has been based on the below rule

$$N = log(\omega_h) - log(\omega_b). \tag{7.25}$$

The frequency range selection for the ORA method is a very important step because a narrow bandwidth results in a lack of the fit.

7.5. FRACTIONAL ORDER SYSTEM IDENTIFICATION

The problem of an optimal input design for the fractional-order LTI system identification is presented in this chapter. The optimal control method for fractional-order model approximation in the state-space form has been presented in [20]. The main purpose of this method is to represent the optimal input design problem using the Lagrange form with the chosen set of constraints. To verify the suitability of this method to the system parameter identification purposes, a fractional inertial model has been selected

$$G(s) = \frac{k}{s^{\alpha}T + 1}, 0.5 \leq \alpha \leq 2.0, \tag{7.26}$$

where $k = 1$ is the gain of the model, and $T = a_1/a_0 = 1$ is the time constant. The fractional -order LTI system should be presented by the state-space equation given by

$$\begin{aligned} {}_0D_t^{\alpha}x(t) &= Ax(t) + Bu(t), \\ y(t) &= Cx(t) + Du(t) + v(t), \end{aligned} \tag{7.27}$$

where $u(t)$, $y(t)$ are the input and output vectors, $x(t)$ is the state vector, $A,\ B,\ C,\ D$ are the state-space matrices describing the system dynamics, and $v(t)$ is a stationary random Gaussian noise process. The main objective of the system parameter identification is to maximize the sensitivity of the state variable to the unknown model parameter [22]. The Cramer-Rao definition provides a lower bound for the variance of an unbiased parameter to be identified. Applying the above definition to input design purposes, one can obtain the parameter estimate which is lowered, for optimal inputs

$$cov(A, B, C, D) \geq M^{-1}. \tag{7.28}$$

The optimal input signal problem for fractional-order inertial system identification is verified in this paper. According to the Cramer-Rao rule, the sensitivity of the state variable $x(t, d)$ to the parameter d (i.e. the gain of the open-loop system) has been maximized. The objective function formulated based on [22] is as follows

$$J_\alpha(u) = \int_0^{t_f} x_d^2(t,d)\,dt, \tag{7.29}$$

the sensitivity of the state variable is

$$x_d(t,d) = \frac{\partial x(t,d)}{\partial d}, \tag{7.30}$$

subject to input energy

$$\int_0^{t_f} u(t)^T u(t)\,dt \le E. \tag{7.31}$$

The presented method is appropriate only for models with the fractional order values $\alpha \le 1.0$. For the fractional order values α from the interval (1.0, 2.0), it is necessary to extend the state-space equations by one extra state. The problem formulation for solving this task would be presented in the further part of the current section. In general case, an optimal input signal design to the fractional-order inertial LTI system identification is formulated by the state-space model

$$\begin{gathered} {}_0D_t^\alpha x = Ax + Bu, \\ y = Cx, \end{gathered} \tag{7.32}$$

where: $A = -1$, $B = 1$, and $C = 1$ are model parameters (according to (7.32)), with the initial condition

$$x(0) = 5. \tag{7.33}$$

The reformulated performance criterion to be maximized has the following form

$$J_\alpha(u) = \int_0^{t_f} (C_F x_d(t) + u)^2 dt, \tag{7.34}$$

with respect to the constraints

$$\begin{gathered} -1 \le u(t) \le 1, t \in [0, t_f], \\ \int_0^{t_f} (t_f - t)^{2(1-\alpha)}\, u(t)^T u(t) dt \le 1, t \in [0, t_f]. \end{gathered} \tag{7.35}$$

The controllability Gramian [13] of fractional order α is used to the energy cost minimization purposes. The term $(t_f - t)^{2(1-\alpha)}$ under the integral (7.35) is designated to

neutralize the singularity at $t = t_f$. This component is also used to ensure the convergence of the integral. The reformulated system dynamics has the following form

$$\dot{z} = A_F z + B_F(-(C_F z + D_F u) + u), \tag{7.36}$$

with the initial conditions

$$z(0) = [5 \quad 0 \quad \cdots \quad 0]^T. \tag{7.37}$$

The equation (7.32) can be reformulated to solve the fractional-order model identification for non-integer orders $\alpha > 1.0$. For this purpose, the system dynamics should be extended by another state variable. The cost function (7.34) is maximized for order values from the interval $(1.0 < \alpha \leq 2.0)$ considering the following dynamics

$$\begin{aligned} \dot{x}_1 &= C_F x_2 + D_F u, \\ {}_0D_t^{\beta} x_2 &= A_F x_2 + B_F(-(C_F x_2 + D_F u) + u), \end{aligned} \tag{7.38}$$

it was assumed that $\beta = \alpha - 1$, and the initial conditions are: $x_1(0) = 5$, $x_2(0) = 0$. The previous problem can be presented by the state equation given below

$$\begin{aligned} \dot{x} &= C_F z + D_F u, \\ \dot{z} &= A_F z + B_F(-(C_F z + D_F u) + u), \end{aligned} \tag{7.39}$$

subject to the constraints, and the initial conditions described by equations (7.35), and (7.37). The fractional-order optimal input design problem is to be solved using the Runge-Kutta method.

7.6. EXPERIMENTAL RESULTS

The frequencies for the Oustaloup method has been chosen from the interval $[10^{-2}, 10^{2}]$ rad/s. The order of the ORA filter has been obtained using equation (7.25) with $N = 4$. The Oustaloup filter frequencies have been chosen to fit in with the discretization of the integration method used by Riots_95 [21]. This toolbox should be included in Matlab kit as a separate library, and allows to solve optimal control problems containing fixed, and the free final time tasks.

The optimal input design problem for fractional LTI system identification is then generated for the arbitrarily selected parameters (7.32) $A = -1$, $B = 1$, $C = 1$, and the chosen time period $t = [0, 1.0]$ seconds, using the sequential quadratic programming (SQP) algorithm. The final extended period of the time t_f would certainly cause notable computational effort. The fractional-order model initial conditions have been selected according to (7.37), and the initial condition of the input signal has been fixed on $u(0) = 1$. The optimal input signal trajectory $u(t)$ has been limited to the range of motion $[-1, +1]$ in order to prevent sudden changes of the input signal. The optimal input signals were obtained using the 4th order Runge-Kutta method with grid interval of 0.01 sec.

The optimal input signals and the state variables to fractional-order inertial LTI system generated for different orders of the state-space model (7.32) (i.e. $0.5 \leq \alpha \leq 1.0$) are shown in Fig. 7.1. As seen, the input signals are considerably different, while the value of the order of α decreases. For the state-space model orders of $\alpha \leq 1.0$, the input signal transition reduces its duration, while the control signal obtained for $\alpha = 0.5$ is substantially a step input signal (i.e. yellow solid line).

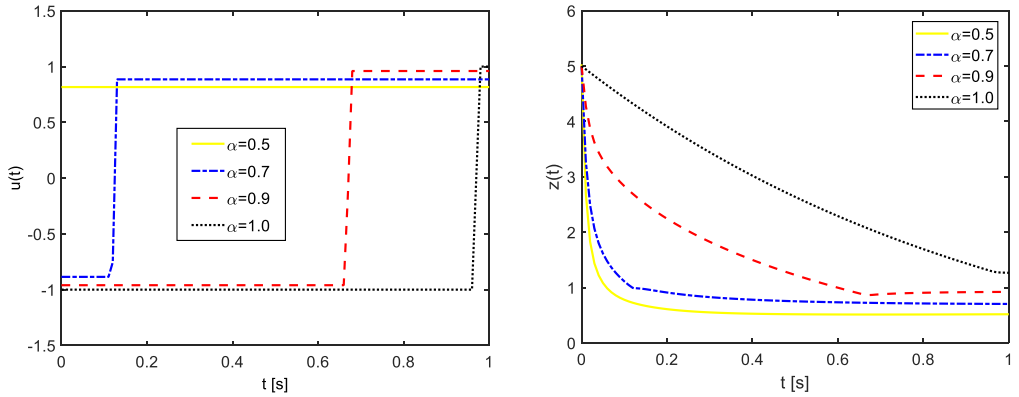

Fig. 7.1. The optimal excitation signal $u(t)$ and the state variable $z(t)$ to the fractional inertial system as function of time t for orders from the interval $0.5 \leq \alpha \leq 1.0$

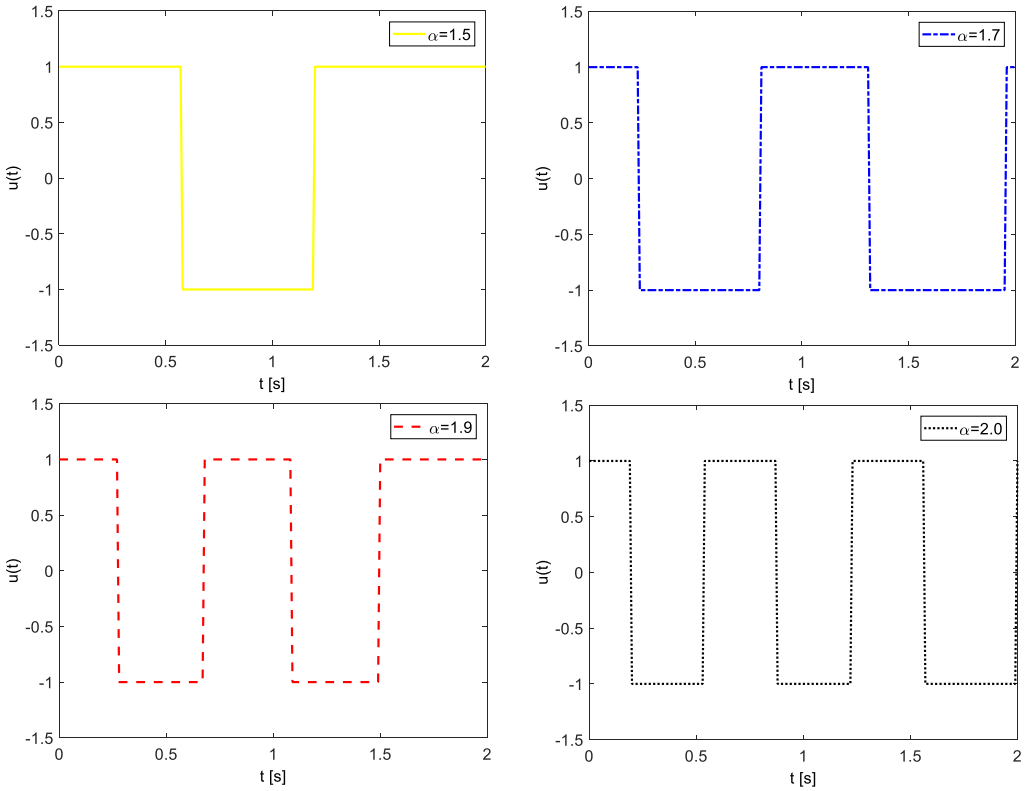

Fig. 7.2. The optimal input signals $u(t)$ to the fractional-order inertial system as function of time t for orders from the interval $1.0 < \alpha \leq 2.0$

The plot shown on the right side of Fig. 7.1 presents the reformulated state variables $z(t)$ to the fractional-order inertial system as a function of time for various orders of α from the interval $0.5 \leq \alpha \leq 1.0$. As it has already been indicated, the sensitivity of the state variable $x(t, d)$ to the parameter d (i.e. the gain of the open-loop system) has been maximized. The parameter d is the gain of the non-integer model (7.27) after the Oustaloup approximation operation. The imprecise estimation of the gain can lead to instability of the open-loop system especially using rapidly changing input signals. The examples of the optimal inputs to the fractional-order inertial system identification as a function of time for different orders of α from the interval $1.5 \leq \alpha \leq 2.0$ are shown in Fig. 7.2. The fractional-order system identification for $\alpha \geq 1.0$ requires the extension of the state-space equation by an additional state subject to (7.39). It can be noted that increasing the value of the system order, the input signal is characterized by the increased number of the oscillations.

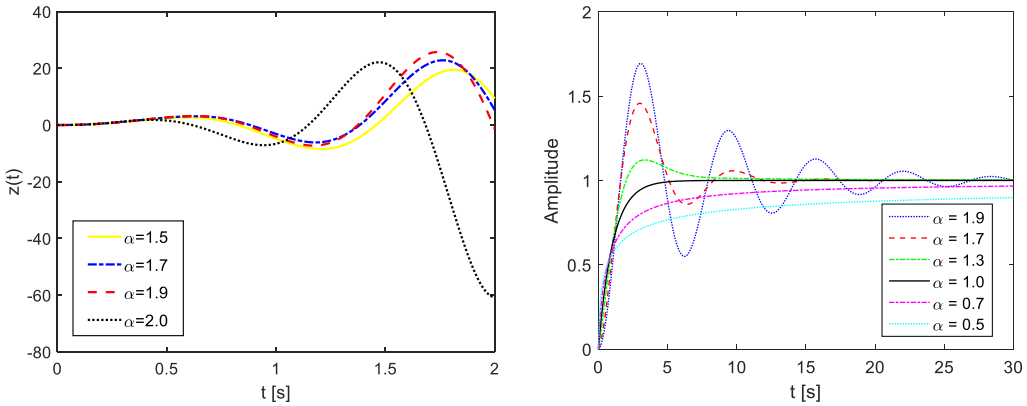

Fig. 7.3. The state-space variable $z(t)$ to the fractional-order inertial system as function of time t, and the step responses comparison for different order values

As it has been shown in Fig. 7.3, since increasing the order of the fractional system from the interval of $1.5 \leq \alpha \leq 2.0$, the model's response starts to become oscillatory. The left panel of Fig. 7.3 shows the waveforms of the state variable $z(t)$ of the fractional-order inertial system as a function of the time. The comparison of the step responses to the inertial system using various values of α is shown on the right panel of the Fig. 7.3. It can be noticed that the step responses for orders $\alpha \leq 1$ are aperiodic, however conventional first-order inertial system step response can be observed for $\alpha = 1$. The step responses have oscillatory form for the fractional system orders $\alpha \geq 1$. Finally, it should be stated that presented methodology cannot be used for fractional-order systems, where $\alpha > 1$. This inconvenience is related to the fact that the approximated transfer function numerator has the higher order than the order of the denominator. Consequently, it is impossible to convert a zero-pole transfer function to the state-space form. This problem can be solved by augmenting the fractional-order system dynamics with one extra state.

7.7. CONCLUSIONS

In this paper, we have proposed a novel optimal input design formulation for the fractional-order system identification. The methodology for finding an optimal input solution is verified using the numerical examples. The model design is based on accurate Oustaloup recursive approximation process and has been then used for the fractional-order operator estimation in the integer-order transfer function form. If the transfer function numerator order is equal to the denominator order, the conversion of a transfer function to a state-space form is allowed. The technique presented in this paper enables the solution of the optimal input signal for fractional-order system identification. The problem solution is based on the state variable sensitivity to the fractional-order system parameter d (i.e. the gain of the state-space system) minimization, subject to a set of constraints imposed on input signal. Increasing the gain of the system makes the system underdamped, and in an extreme case, leads to instability of the open-loop system. Consequently, a precise gain value approximation is a significant task during the fractional-order system identification. It has been noticed that the most significant loss in the objective function value has been obtained for α value from 0.9 to 1.0. This loss of the performance is the consequence of the fractional-order differentiator conversion into the integer-order form.

The most significant step has been to reformulate our optimal input design problem, represented by the Lagrange formulation with the set of constraints, into a twin fractional-order input design. Then it is possible to solve the optimal input signal problem using one of the available toolboxes for solving optimal control problems. The numerical simulations confirm that the result obtained for the fractional-order case study (i.e. for $\alpha = 1$) is the same as the one received from the integer-order input design problem. The numerical examples also confirm that for fractional order values $\alpha > 1$, there is need to augment the state-space equations by one extra state. Moreover, the selection of appropriate frequencies for the Oustaloup recursive technique is also a very important design step.

The present study was supported by a grant WZ/WI-IIT/4/2020 from the Bialystok University of Technology and funded from the resources for research by the Ministry of Science and Higher Education.

REFERENCES

[1] MONJO C.A. et al., *Fractional orders Systems and Controls: Fundamentals and Applications. Advances in Industrial Control*. Springer Verlag, doi: 10.1007/978-1-84996-335-0, 2010.

[2] CHEN Y., PETRAS I., XUE D., Fractional order control - a tutorial, in: *Proceedings of the American Control Conference (ACC'09)*, p. 1397–1411, 2009.

[3] TORVIG P. J., BAGLEY R. L., On the appearance of the fractional derivative in the behaviour of real materials. *Transactions of the ASME*, vol. 51(4), p. 294–298, 1984.

[4] OUSTALOUP A. et al., Frequency-Band Complex Noninteger Differentiator: Characterization and Synthesis. *IEEE Transactions on Circuits and Systems, Fundamental Theory and Applications*, vol. 47(1), p. 25–40, 2000.

[5] MILLER K., ROSS B., *An introduction to the fractional calculus and fractional differential equations*, J. Wiley & Sons, 1993.

[6] MAGIN R. L., *Fractional Calculus in Bioengineering*, Begell House Publishers, 2006.

[7] HILFER R., *Applications of Fractional Calculus in Physics*, World Scientific, Singapore, 2000.

[8] WEST B., BOLOGNA M., GRIGOLINI P., *Physics of Fractal Operators*, Springer, New York, 2003.

[9] PETRAS I., *Fractional-Order Nonlinear Systems*, Springer, New York, 2011.
[10] PODLUBNY I., *Fractional Differential Equations*, Academic Press, San Diego, 1999.
[11] VALERIO D., COSTA J., *An Introduction to Fractional Control*, IET, London, 2013.
[12] SHENG H., CHEN Y. D., QIU T. S., *Fractional Processes and Fractional-order Signal Processing*, Springer, London, 2012.
[13] MOZYRSKA D., TORRES D. F. M., Modified optimal energy and initial memory of fractional continuous-time linear systems, *Signal Processing*, vol. 91(3), p. 379-385, 2011.
[14] MONJE C. et al., Tuning and autotuning of fractional order controllers for industry applications, *Control Engineering Practice*, vol. 16(7), p. 798–812, 2008.
[15] JAKOWLUK W., Fractional-Order Linear Systems Modeling in Time and Frequency Domains, in: *16th IFIP TC8 Int. Conference in Computer Information Systems and Industrial Management*, Springer, Heidelberg, p. 502–513, 2017.
[16] JAKOWLUK W., Optimal input signal design for a second order dynamic system identification subject to D-efficiency constraints, in: *14th IFIP TC8 Int. Conference in Computer Information Systems and Industrial Management*, Springer, Heidelberg, p. 351–362, 2015.
[17] JAKOWLUK W., Plant friendly input design for parameter estimation in an inertial system with respect to D-efficiency constraints, *Entropy*, vol. 16(11), p. 5822‑5837, 2014.
[18] JAKOWLUK W., Free Final Time Input Design Problem for Robust Entropy-Like System Parameter Estimation, *Entropy*, vol. 20(7), p. 528, 2018.
[19] MOZYRSKA D., Multiparameter Fractional Difference Linear Control Systems, *Discret. Dyn. Nat. Society*, vol. 2014, p. 8, 2014.
[20] TRICAUD C., CHEN Y., Solving fractional order optimal control problems in riots_95 a general–purpose optimal control problem solver, in: *3rd IFAC Workshop on Fractional Differentiation and its Applications*, Ankara, Turkey, 2008.
[21] SCHWARTZ A., POLAK E., CHEN Y., *Riots a Matlab toolbox for solving optimal control problems. Version 1.0 for Windows*, http://www.schwartz-home.com/RIOTS/, 1997 (accessed: 12.04.2020).
[22] KALABA R., SPINGRAN K., *Control, identification, and input optimization*. Plenum Press, New York, 1982.

DOI: 10.24427/978-83-66391-87-1_08

Mykhaylo ANDRIYCHUK[1], Uliana MARIKUTSA[2]

8. MODELING MATERIALS WITH DESIRED REFRACTIVE INDEX

The explicit solution to the diffraction problem on a set of small particles, supplemented into homogeneous material, is used for modeling the materials with the desired refractive index. The consideration concerns to the case of acoustic scalar scattering and the solution to initial scattering problem is built using an asymptotic approach. The closed form solution is reduced for the scattering problem. This lets an explicit formula for the refractive index of the resulting inhomogeneous material to be obtained. The numerical calculations show the possibility of getting the specific values of refractive index including its negative values.

8.1. INTRODUCTION

The materials with the specific physical properties, in particular with negative refractive index play an important role in the process of improving the radiation performances of the different IC and radioelectronic devices. Such materials are used widely for improving the radiation performances of microstrip antennas of different types, microwave filters and field transformers. There are different approaches to forming specific properties of the medium (material) by embedding into it a series of inclusions. This leads to the formation of the physical properties of resulting material that are different to those that are inherent to the properties of initial material. The theoretical prediction of the existence of such materials was made in the pioneer work [1] and thereon, such materials were designed by the variety recipes. As early as the eighties of the last century, these materials received the name *chiral* and began to be used in various areas of antenna technology [2], manufacturing of electronic devices [3], [4], and telecommunications equipment [5]. The goal of this paper is to propose the numerical approach (based on [6] and [7]) for modeling the material with the specific refractive index, including its negative values. The approach foresees reducing

[1] Ivan Franko National University of Lviv, Ukraine
[2] Lviv Polytechnic National University, Ukraine

an explicit solution to the respective acoustic scattering problem, and the explicit formula for the resulting refractive index based on the asymptotic solution to acoustic wave scattering problem on a set of big number of embedded particles of small size. The chapter is organized as follows: Section 8.2 is devoted to statement of diffraction problem and outline of application limits of geometrical and physical parameters of the material under consideration. The analytical form of solution will be derived in Section 8.3, and the numerical aspects of solving the respective system of linear algebraic equations (SLAE) will be presented here. The explicit formula for the refractive index of resulting inhomogeneous material will be derived in Section 8.4. The numerical results, related to exactness of asymptotic solution to the initial diffraction problem and properties of material with obtained refractive index will be presented in Section 8.5. A short conclusion finalizes the discussed topic under consideration.

8.2. STATEMENT OF SCATTERING PROBLEM

A combination of both the asymptotic method and numerical simulation is used to solve the problem of creating a material with specified scattering characteristics, particularly, with a given refractive index. The initial diffraction problem is solved by assumption: $ka \ll 1$, and $d \gg a$, a is the characteristic size of the particle, d is the distance between adjacent particles, $k = 2\pi/\lambda$ is the wave number.

An asymptotic solution to the scattering problem on many particles by assumptions: $d = O(\sqrt[3]{a})$, and $M = O(a^{-1})$ was obtained in [6], M is the total number of particles contained in a given domain $D \subset R^3$.

The impedance boundary conditions

$$\zeta_m = q(x_m)/a^{\kappa} \tag{8.1}$$

are prescribed on the boundary S_m of m-th particle, where ζ_m is boundary impedance, $x_m \in D_m$, $q_m = q(x_m)$; $q(x)$ is arbitrary function, continuous in $\overline{D}$; $Im\, q \leq 0$, and $d = O(a^{(2-\kappa)/3})$, where $M = O(1/a^{2-\kappa})$, and $\kappa \in (0,1)$.

The incident field satisfies Helmholtz equation in the whole R^3, by this, the scattered field satisfies the radiation conditions. We assume that a small particle is a sphere of radius a with center in point x_m, $1 \leq m \leq M$.

The full field u_M satisfies equation

$$[\nabla^2 + k^2 n_0^2(x)]u_M = 0 \text{ in the domain } R^3 \setminus \bigcup_{m-1}^{M} D_m, \tag{8.2}$$

and boundary conditions

$$\partial u_M/\partial N = \zeta_m u_M \text{ in } S_m, \text{ where } 1 \leq m \leq M, \tag{8.3}$$

and

$$u_M = u_0 + v_M, \tag{8.4}$$

u_0 is the solution of problem (8.2) – (8.4) at M=0 (namely, when D does not contain the particles), $u_0 = e^{ik\alpha\cdot x}$ is the incident field, and field v_M satisfies the radiation conditions.

Let $q(x)$ belong to $C(D)$, $\Delta_p \subset D$ is arbitrary subdomain of D, and $K(\Delta_p)$ is the total number of particles in Δ_p determined by

$$K(\Delta_p) = 1/a^{2-\kappa} \int_{\Delta_p} N(x)dx \cdot [1 + o(1)] \quad \text{at} \quad a \to 0, \tag{8.5}$$

where function $N(x) \geq 0$ is given and continuous in domain D.

It was substantiated in [6] that there exists some specific field $u_e(x)$ (limiting field), which satisfies the next condition

$$lim_{a\to 0}\|u_e(x) - u(x)\| = 0, \tag{8.6}$$

and solution to the initial diffraction problem (8.2) – (8.4) can be sought from the equation

$$u(x) = u_0(x) - 4\pi \int_D G(x,y)q(y)N(y)u(y)dy, \tag{8.7}$$

where $G(x,y)$ is the Green function for Helmholtz equation (8.2) for the case of absence of the particles. This fact allows us to use the approximate solution $u_e(x)$ instead of exact solution $u(x)$ and to obtain an explicit formula for refractive index of constructed inhomogeneous material.

8.3. THE SEMIANALYTICAL FORM OF SOLUTION TO SCATTERING PROBLEM

In order to derive the explicit formula for approximate field, we introduce the concept of limiting (effective) field $u_e(x)$. In paper [6], it was substantiated that the exact solution to problem (8.2) – (8.4) can be presented in the form

$$u_M(x) = u_0(x) + \sum_{m=1}^{M} \int_{S_m} G(x,y)\, v_m(y)dy. \tag{8.8}$$

Despite the fact that this last equation contains an unknown function $v_m(y)$ in the integrand, in contrast to formula (8.7), where all functions in the integrands are known, it is used to obtain an approximate solution to the original diffraction problem. For this goal, we define the effective field $u_e(x,a) = u_e^{(m)}(x)$, which acts on the m-th particle as

$$u_e(x) = u_M(x) - \int_{S_m} G(x,y)v_m(y)dy, \quad x \in R^3, \tag{8.9}$$

and the next relation for the neighboring points is valid $|x - x_m| \sim a$. We present the exact formula (8) in form

$$u_M(x) = u_0(x) + \sum_{m=1}^{M} G(x, x_m) R_m + \sum_{m=1}^{M} \int_{S_m} [G(x, y) - G(x, x_m)] v_m(y) dy\,, \tag{8.10}$$

where the values R_m are

$$R_m = \int_{S_m} v_m(y) dy. \tag{8.11}$$

Using the known relation for function $G(x, y)$ from [8], and the asymptotic formula for values R_m [6], we obtain the next formula for $u_M(x)$

$$u_M(x) = u_0(x) + \sum_{m=1}^{M} G(x, x_m) R_m + o(1) \text{ at } a \to 0 \text{ for } |x - x_m| \geq a. \tag{8.12}$$

The values R_m are defined by the asymptotic formula

$$R_m = -4\pi q(x_m) u_e(x_m) a^{2-\kappa} [1 + o(1)], \text{ if } a \to 0, \tag{8.13}$$

and asymptotic formula for function v_m is

$$v_m = -q(x_m) u_e(x_m) \cdot \frac{1}{a^{\kappa}} \cdot [1 + o(1)], \text{ if } a \to 0. \tag{8.14}$$

Using last two formulas, we obtain the asymptotic representation of the effective field in the vicinity of particles

$$u_e^{(j)}(x) = u_0(x) - 4\pi \sum_{m=1, m \neq j}^{M} G(x, x_m)\, q(x_m) u_e(x_m) a^{2-\kappa} [1 + o(1)], \tag{8.15}$$

which is valid in the domains $|x - x_j| \leq a$, where $1 \leq j \leq M$.

In order to calculate the values of the effective field everywhere using formula (8.15), we should know the values $u_e(x_m)$. They can be easily obtained as solutions to the following SLAE

$$u_j = u_{0j} - 4\pi \sum_{m=1, m \neq j}^{M} G(x_j, x_m)\, q(x_m) u_m a^{2-\kappa} \text{ for } j = 1, \ldots, M, \tag{8.16}$$

where $u_j = u(x_j)$ and $j = 1,2, \ldots, M$. The matrix of SLAE (8.16) is diagonally dominant, therefore it is convenient for solving numerically. It was proven in [9] that this SLAE has a unique solution for sufficiently small a.

In order to justify the exactness of solution to SLAE (8.16), which is used for determination of the effective field, we derive different SLAE, corresponding to the

limiting equation (8.7). Let us divide the domain D, where the small particles are located, into an union of the small non-intersecting cubes Δ_p with centers at points y_p, the side of such cubes can be chosen as $O(d^{1/2})$. Because the limited quantity of cubes cannot give whole D, we consider their smallest partition that contains D, and define values $n_0^2 = 1$ in the cubes, which do not belong to domain D.

In order to find the solution to equation (8.7), we apply the collocation method proposed in [9]. In accordance with this method, we obtain such SLAE

$$u_j = u_{0j} - 4\pi \sum_{p=1, p\neq j}^{P} G(x_j, x_p)\, q(y_p) N(y_p) u_p |\Delta_p|, \qquad j = 1, \ldots, P \tag{8.17}$$

where P is the number of cubes that form a partition of D, y_p is a center of p-th cube, $|\Delta_p|$ is its volume. Since the value of d is small, diameter Δ_p can be of an order larger than distance d between particles. Since $P \ll M$, then solving SLAE (8.17) is much easier that solving SLAE (8.16) in terms of the number of calculations.

As a result, we have two different SLAE (8.16) and (8.17). Solving both the SLAE, we can compare their solutions and evaluate the area of accuracy of asymptotic solution (8.15). This evaluation has also a practical importance as allows the determination of the optimal parameters of the domain D, which provide the possibility to create the refractive index that is the closest to the desired one.

8.4. REFRACTIVE INDEX OF THE OBTAINED MATERIAL

The explicit formula (8.7) for the effective field opens the way to determining the refractive index of the obtained material. It is important from the practical point of view, how the calculated refractive index $n_M^2(x)$ differs from those obtained from the theoretical assumptions. We confine here by the real refractive index and formulate the constructive algorithm to obtain the desired one. It consists of three steps.

- Step 1: using known $n_0^2(x)$ and unknown $n^2(x)$, we calculate function $p(x) = k^2[n_0^2(x) - n^2(x)] = p_1(x)$.
- Step 2: using the relation $p(x) = 4\pi q(x) N(x)$ we determine

$$N(x)q(x) = \frac{p_1(x)}{4\pi}. \tag{8.18}$$

  Equation (8.18) for two unknown functions $q(x)$ and $N(x)$ has infinite number of solutions $\{q(x), N(x)\}$, for which the conditions $N(x) \geq 0$ are fulfilled. In this connection, the solution to (8.18) we determine as

$$q(x) = \frac{p_1(x)}{4\pi N}. \tag{8.19}$$

  Calculation of $N(x)$ and $q(x)$ by (8.19) finalized Step 2 of our procedure.
- Step 3: is completely constructive and its goals are the following:
  - to create on the small particle of radius a the necessary impedance $q(x_m)/a^{\kappa}$;

- to embed the particles that satisfies the properties (8.19) into domain with the initial properties.

The application of the above algorithm was considered in [10] for the case of complex function $q(x)$, the above algorithm can be applied if material is lossless.

8.5. NUMERICAL MODELING

8.5.1. Checking the applicability of asymptotic solution

Exactness of solution of the limiting equation (8.7)

The computational check for the determination of the exactness of solution to (8.7) foresees carrying out the calculations with a set of different problem's parameters. We calculate the absolute and relative errors in the process of growth of the number of collocation points. The dependence of error of the parameter $p = \sqrt[3]{P}$, where P is the total number of the small domains (cubes) in D for $k = 1.0$, $l_D = 0.5$, and $a = 0.01$ for the different values of function $q(x)$ are shown in Fig. 8.1 and Fig. 8.2 (dimension of k is cm^{-1}, and linear sizes of D are prescribed in cm) respectively. The solution, which corresponds to $p = 20$ ($P = 20^3$), is considered as a benchmark.

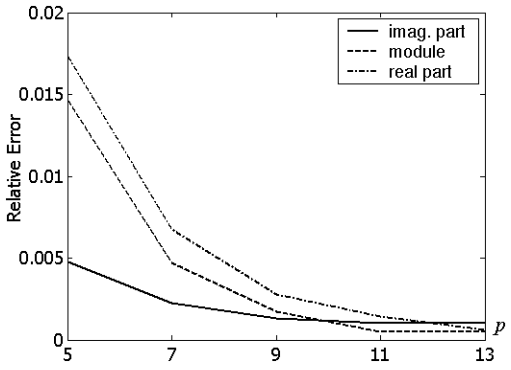

Fig. 8.1. The relative error versus parameter p, $q(x) = k^2(0.008 - 0.0011i)$

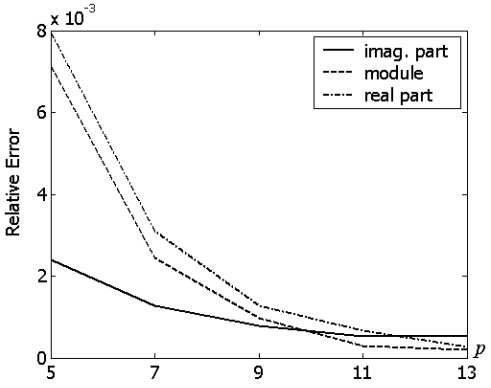

Fig. 8.2. The relative error versus parameter p, $q(x) = k^2(0.008 - 0.0027i)$

The relative error of solution to (8.7) is equal to 1.05% and 0.023% for the real and imaginary parts if $p = 5$ (5^3 collocation points), it diminishes to 0.72% and 0.053% respectively at $p = 6$ (6^3 collocation points), and to values 0.287% and 0.018% at $p = 8$ (8^3 collocation points), (see Fig. 8.1). This error is less than 0.009% for the real part of solution if $p = 12$, it tends to zero if value p grows. The error depends of the values of function $q(x)$ too, it diminishes if the imaginary part of $q(x)$ decreases (see Fig. 8.2). The error of real part of solution if $p = 19$ is equal to 0.009%, and error of imaginary part is thousandths of a percent. The obtained results confirm that calculation of the values of

approximate field can be carried out with the high enough accuracy, and this accuracy is attained in a wide range of the geometrical and physical parameters of the material under investigation.

The results of computations show that the relative error depends of the parameter k to a large extent. In Fig. 8.3 and Fig. 8.4, the error is shown at $k = 2.5$ and $k = 0.75$ respectively, $q(x) = k^2(0.008 - 0.0011i)$. One can see that the error is of one order larger at $k = 2.5$. The maximal error (if $p = 5$) at $k = 0.75$ is less on 27% than those for $k = 1.0$.

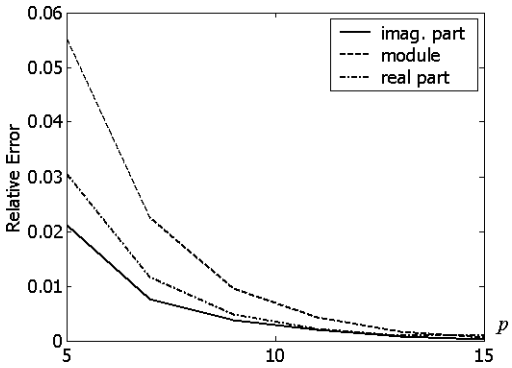

Fig. 8.3. The relative error versus parameter p, $k = 2.5$

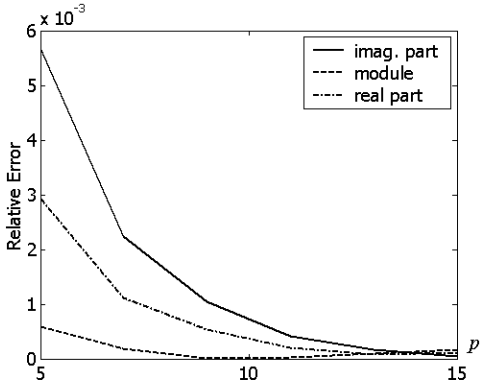

Fig.8.4. The relative error versus parameter p, $k = 0.75$

Comparison of solutions to limiting equation (8.7) and asymptotic SLAE (8.16)

In the previous subsection, we consider the solution to SLAE (8.17) with $p = 20$ as benchmark solution to equation (8.7). The maximal value of relative error for this p does not exceed 0.009% for wide range of the problem's parameters. The numerical calculations are presented for the different sizes of D and different functions $N(x)$. The obtained results for small values m are shown in Table 8.1 for $l_D = 1.0$, $k = 1.0$, and $N(x) = 40$. The values of a_{est}, which are received by formula (8.20), when the expected number $K(\Delta_p)$ of particles is changed by M. For this case, the radius of particle is determined as

$$a_{est} = \left(M / \int_{\Delta_p} N(x)dx \right)^{1/(2-\kappa)}. \qquad (8.20)$$

Table 8.1. The optimal parameters of domain D at small m, $N(x) = 40$

m	8	10	12	14	16
a_{est}	0.1397	0.0682	0.0378	0.0247	0.0152
a_{opt}	0.1054	0.0603	0.0369	0.0252	0.0169
d	0.1329	0.1099	0.0917	0.0787	0.0679
Relative error	2.47%	0.42%	0.41%	1.09%	0.77%

The values of a_{opt} in the third row correspond to the optimal values of radius a, which guarantees the minimal error for module of solution to equation (8.7) and system (8.16).

In the fourth row, the values of distance d between particles are shown. The maximal value of error is attained at $m = 8$, the error diminishes if m grows. The numerical results for large m with the same initial data are shown in Table 8.2. The minimal error of solution is attained at $m = 65$ (total number of particles M=27.46·10^4), and it is equal to 0.20%.

Table 8.2. The optimal parameters of domain D at large m, $N(x) = 40$

m	25	35	45	55	65
a_{est}	0.0079	0.0024	0.00121	6.45·10^{-4}	3.96·10^{-4}
a_{opt}	0.0076	0.0022	0.0010	6.31·10^{-4}	3.89·10^{-4}
d	0.0514	0.0329	0.0241	0.0198	0.0171
Relative error	0.53%	0.31%	0.34%	0.23%	0.20%

Table 8.3 contains the comparable results for $N(x) = 4$ with the same set of initial data. One can see that the relative error diminishes if the number M of particles increases (one should note that the relative error depends on parameters a and l_D too). This error tends to relative error of solution to equation (8.7) if the value of m becomes larger than 80 ($M = 5.12 \cdot 10^5$).

Table 8.3. The optimal parameters of domain D at large m, $N(x) = 4$

m	25	35	45	55	65
a_{est}	9.98·10^{-4}	3.30·10^{-4}	1.51·10^{-4}	8.19·10^{-5}	4.99·10^{-5}
a_{opt}	1.02·10^{-3}	3.32·10^{-4}	1.51·10^{-4}	8.20·10^{-5}	4.99·10^{-5}
d	0.0526	0.0345	0.0256	0.0204	0.0169
Relative error	0.19%	0.09%	0.1108%	0.06%	0.02%

Investigation of difference between solutions to SLAE (8.16) and (8.17)

The comparison of solutions to SLAE (8.16) and (8.17) was carried out for the different values of a at different p and m. The relative error of SLAE (8.16) diminishes if p increases while m remains constant. As an example, if p increases to 50%, then the relative error diminishes to 11.7% (if $p = 8$ and $p = 12$, $m = 15$).

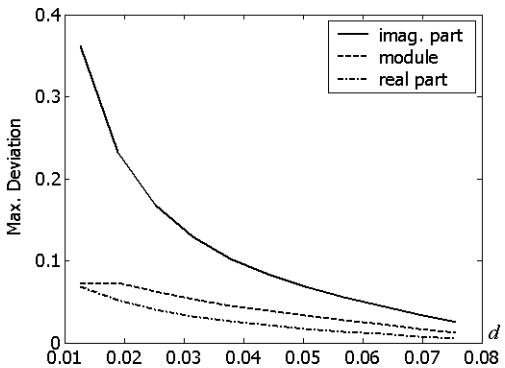

Fig. 8.5. Dependence of deviation of the solution's components of distance d between particles, $N(x) = 10$

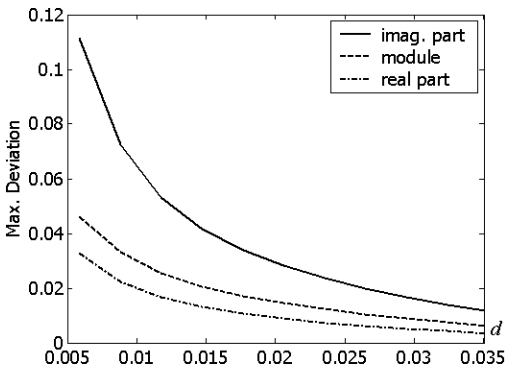

Fig 8.6. Dependence of deviation of the solution's components of distance d between particles, $N(x) = 30$

The differences in solutions to SLAE (8.16) and (8.17) in the real part, imaginary part, and module are shown in Figs. 8.5 and 8.6 if $p = 7$ and $m = 15$. By this, the difference of real parts do not exceed 3.9% at $a = 0.01$, it is less than 3.3% at $a = 0.007$, and it is less than 1.85% if $a = 0.004$, $d = 9a$, and $N(x) = 20$. Respectively, this difference is less than 0.075% if $p = 11$, $a = 0.001$, and $N(x) = 30$, $d = 15a$ (m is the same). The numerical results, obtained for a wide range of d, show that its optimal value exists, and starting from this value, the deviations of solutions begin to increase again. Such optimal values of d are presented in Table 8.4 for the different constant $N(x)$. The results obtained testify that the optimal distance between particles increases if the number of particles grow. For the small number of particles, the optimal distance is of the same order that a, for the set number of particles ($M = 15^3$, namely $m = 15$). This distance is of an order larger. The values of the minimal and maximal errors, which are attained for the optimal d, are shown in Table 8.5.

Table 8.4. Optimal values of d for the different constant $N(x)$

	Value of $N(x)$				
	10	20	30	40	50
$a = 0.004$	0.0711	0.0468	0.0468	0.0469	0.0381
$a = 0.01$	0.0864	0.0559	0.0595	0.0594	0.0496

Table 8.5. The relative error of solution to SLAE (8.16) in % (min/max) for the optimal d

	Value of $N(x)$				
	10	20	30	40	50
$a = 0.004$	0.69/0.09	5.17/0.48	0.48/0.109	0.95/0.121	0.28/0.06
$a = 0.01$	2.39/0.19	1.67/0.29	0.51/0.09	2.4/0.41	1.47/0.17

The obtained results allow us to conclude that the optimal value of d diminishes slower, when function $N(x)$ grows, additionally this trend is more significant for the smaller a.

5.2. Modeling the material with the desired refractive index

Numerical calculations are carried out for the case $N(x) = const$. For simplicity, we consider the case when a given domain D consists of the same subdomains Δ_p. This limit is not essential for the numerical modeling.

Numerical calculations were performed for the case when $D = \bigcup_{p=1}^{P} \Delta_p$, and $P = 20^3$, D is some cube with side $l_D = 0.5$ and particles are placed uniformly in domain D (the relative error of the solution to system (8.16) does not exceed 0.01% for this P). Let the initial domain D be the material with the initial refractive index $n_0^2(x) = 1$. Then the values $N(\Delta_p)$ can be calculated using the formula (8.5). On the other hand, we can choose the number m such that $M = m^3$ is closest to number $N(\Delta_p)$. It is easy to see that the corresponding $n^2(x)$ for such M is calculated by such formula

$$\tilde{n}^2(x) = -\frac{4\pi M q(x)}{k^2} + n_0^2 \tag{8.21}$$

that is, the obtained value of the refractive index differs on $n^2(x)$. To obtain the minimum difference, we choose numbers m_1 and m_2 that satisfy the inequality $M_1 < N(\Delta_p) < M_2$ where $M_1 = m_1^3$ and $M_2 = m_2^3$. Therefore, if we have the value $N(\Delta_p)$ for the fixed a, we can obtain the numbers M_1 and M_2, and to calculate also the nearest to the $n^2(x)$ values by the formula (8.21).

The dependence of the maximal relative error for the calculated values of $\tilde{n}^2(x)$ on radius a of a particle is shown in Fig. 8.7 for $N(x)$=50 for complex function $q(x)$ (in Figs. 8.7 – 8.9, the solid and dashed lines correspond to the real part and imaginary part).

The obtained results testify that the relative error considerably depends on the parameters M_1, M_2, and $K(\Delta_p)$. This error is smallest if the value of numbers M_1 or M_2 are much closer to value $K(\Delta_p)$. The error has periodic character that is defined by the properties of functions $K(\Delta_p)$ and by the values of parameters M_1 and M_2. The mean of error in the period grows if a increases. The comparable results are shown in Fig. 8.8 and Fig. 8.9 at $N = 20$ and $N = 50$ respectively.

The minimal value of error 0.49% is attained for $a = 0.015$ and it is equal to 0.51% if $a = 0.008$, and 0.26% if $a = 0.006$ for $N(x) = 5, 20, 50$ respectively.

The uniform placement of particles in domain D is the simplest from the practical point of view. Using the data, given in Figs. 8.7 – 8.9, we can evaluate the number M of particles, which is necessary to obtain the refractive index more closer to the desired one (at given parameter l_D of domain D). The respective results are shown for $l_D = 0.5$ in Fig. 8.10. The values $m = \sqrt[3]{M}$ are shown on the y axis. The solid, dashed and dot-dashed lines correspond to values $N(x) = 5, 20, 50$ respectively. The knowledge about the optimal number of particles in the domain D is the subsequent step to creating a material with the given refractive index.

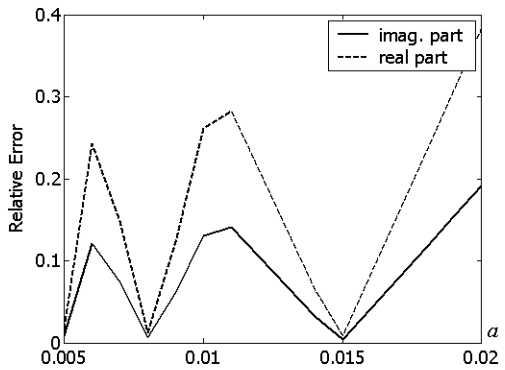

Fig. 8.7. The maximal relative error of the modeled refractive index $\tilde{n}^2(x)$, $N = 5$

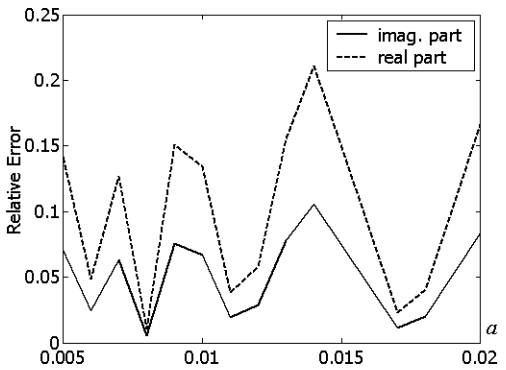

Fig. 8.8. The maximal relative error of the modeled refractive index $\tilde{n}^2(x)$, $N = 20$

The data shown in Fig. 8.10 testify that the optimal number of particles diminishes if their radius a grows. The estimation $\sqrt[3]{a^{(2-\kappa)}}$ determines the distance d between particles. This distance differs from that is determined by uniform placement of particles in D. As an example, for $N = 5, a = 0.0107$ it is equal to 0.1361, and the calculated d is equal to 0.119 and 0.159 for $m = 5$ and $m = 4$ respectively. The computations show that the relative difference between these two values of d is quite proportional to the relative error of the refractive index.

Since this value d does not depend on the diameter of D in accordance to estimation $d = \sqrt[3]{a^{(2-\kappa)}}$, it can be applied as an additional parameter for optimization while choosing the alternative values of m. On the other hand, we can evaluate the number of particles in D by the known formula [10]. With $K(\Delta_p)$, we can calculate the quantity M of particles if they are distributed uniformly in D. The distance between particles is calculated easy too if l_D is prescribed.

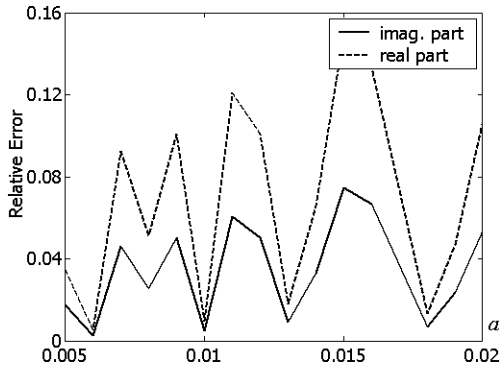

Fig. 8.9. The maximal relative error of the calculated refractive index $\tilde{n}^2(x)$, $N = 50$

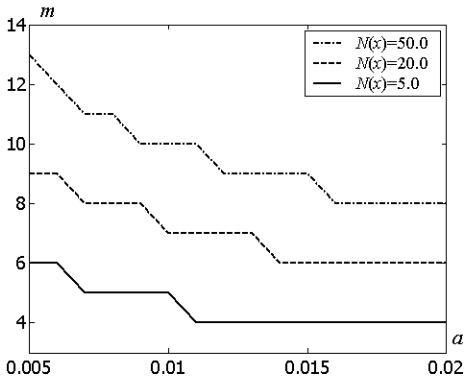

Fig. 8.10. The optimal value of m versus radius a of particles for different $N(x)$

8.6. CONCLUSIONS

The asymptotic approach has been developed to solve the problem of acoustic scattering on a set of small size particles (bodies) placed in a homogeneous material. The scattering problem is reduced to solving a corresponding SLAE whose dimension is equal to the number of particles. The solutions of this system are used in the formula of explicit representation of the components of the scattered field. Numerical calculations are performed that determine the accuracy of the obtained solution depending on the physical parameters of the problem.

The obtained numerical results demonstrate the possibility of applying the proposed technique to create materials with specified acoustic properties, in particular the refractive index. A constructive algorithm for modeling the material with the desired refractive index is proposed.

The results of numerical modeling open up the possibility of engineering solutions for practical applications. As an example, uniform placement of particles is the easiest way to

engineering design, and the answer to how many particles should be placed in a given domain is given by the numerical simulation results.

The engineering problems regarding the placement of a large number of small particles in a given domain D and creating on their surface the necessary impedance $\zeta = q(x)/a^{\kappa}$ require the separate technological solutions.

REFERENCES

[1] VESELAGO V. G., The electrodynamics of substances with simultaneously negative values of ε and μ, *Soviet Physics Uspekhi*, vol. 10, no 4, p. 509–514. doi:10.1070/PU1968v010n04ABEH003699, 1967.

[2] OGIER R., FANG Y. M., SVEDENDAHL M., Near-complete photon spins electivity in a metasurface of anisotropic plasmonic antennas, *Physics Reviev X*, vol. 5, p. 041019, 2015.

[3] PENDRY J. B., SCHURIG D., SMITH D. R., Controlling electromagnetic fields, *Science*, vol. 312, p. 1780–1782, 2006.

[4] YANG Y. et al, Circularly polarized light detection by a chiral organic semiconductor transistor, *Nature Photonics*, vol. 7, p. 634–638, 2013.

[5] CHALABI H., SCHOEN D, BRONGERSMA M. L., Hot-electron photodetection with a plasmonic nanostripe antenna, *Nanotechnology Letters*, vol. 14, p. 1374–1380, 2014.

[6] RAMM G., Wave scattering by many small particles embedded in a medium, *Physics Letters A*, vol. 372, p. 3064-3070, 2008.

[7] RAMM A. G., Electromagnetic wave scattering by small impedance particles of an arbitrary shape, *Journal of Applied Mathematics and Computing* (JAMC), vol. 43, no 1, p. 427–444, 2013.

[8] RAMM A. G., Many body wave scattering by small bodies and applications, *Journal of Mathematical Physics*, vol. 48, no 10, p. 1035-1–1035-6, 2007.

[9] RAMM A. G., A Collocation method for solving integral equations, *International Journal of Computing Science and Mathematics*, vol. 3, no 2, p. 122–128, 2009.

[10] ANDRIYCHUK M. I., RAMM A. G., Scattering by many small particles and creating materials with a desired refraction coefficient, *International Journal of Computing Science and Mathematics*, vol. 3, no 1/2, p. 102–121, 2010.

DOI: 10.24427/978-83-66391-87-1_09

Artur PRUSINOWSKI[1], Roman KACZYŃSKI[1]

9. METHODS OF EFFECTIVELY FORMING FIBER COMPOSITES IN FUSED DEPOSITION MODELING

The chapter presents methods of forming fiber composites in the extrusion head used in the Fused Deposition Modeling printing technique. Designs of two printhead layout solutions were presented. In both cases, the numerical simulations showed the correctness of the construction and compliance with the assumptions. A method for estimating the effective content of reinforcements in composites obtained by these methods was presented. The influence of process variables on the geometrical properties of composites has been demonstrated. Materials reinforced with carbon fibers - regardless of their percentage content - showed elastic nature in a static tensile test. The tensile strength of the tested composites increases in direct proportion to the percentage of fiber content in the composite.

9.1. INTRODUCTION

Along with the growing interest in rapid prototyping with the help of the technique of Fused Deposition Modeling - FDM, the demand for specialized composite materials has also increased. Natural steps were attempts to transfer methods for the preparation of composite materials for 3D printing techniques. The methods of obtaining this type of composites can be divided into three groups:

- adding reinforcements at the stage of filament forming in a screw extruder [1],
- using prefabricated mass-produced composite [2],
- feeding continuous reinforcement directly to the head of a production machine working in the FDM technique [3,4].

The work focuses on the third method that allows strict controlling of the amount of composite produced and simple changing of matrix material depending on the application.

[1] Bialystok University of Technology, Poland

The numerical simulations of heat transport of the first version of the head with symmetrical feeding of matrix material allowed the identification of particularly vulnerable parts of the system [5]. Analysis of PLA polymer extrusion with variable amounts of material fed to the head made it possible to determine the optimal work program for filament feeders. Comparative research on the results of numerical simulation of the flow with experimental research was carried out [6].

Existing methods for determining the percentage of composite components used in conventional manufacturing methods may not be sufficiently accurate for Additive Manufacturing methods due to the properties of laying materials and process variables not found in other methods.

9.2. METHODS OF FORMING FIBROUS COMPOSITES

9.2.1. EXTRUSION HEADS DESIGNS

Each of the methods for forming polymer composites reinforced with appropriately directed carbon fibers must meet a number of criteria relating to the technology itself, the materials used and the structure. It was assumed that the reinforcing fibers could be oriented in relation to the surrounding matrix material and the surface of the element, the possibility of applying the method to 3D FDM printing technology, ensuring the possibility of interference in the technological parameters of the process, that allowed obtaining the desired physical properties of materials and obtaining even distribution of the reinforcing material, no excessive fiber concentration in the composite.

After analyzing the assumptions regarding the technology for forming fiber composite, mixing of components in a specially constructed extrusion head adapted to a 3D printing machine using FDM technology was adopted as the appropriate method of obtaining the composite material.

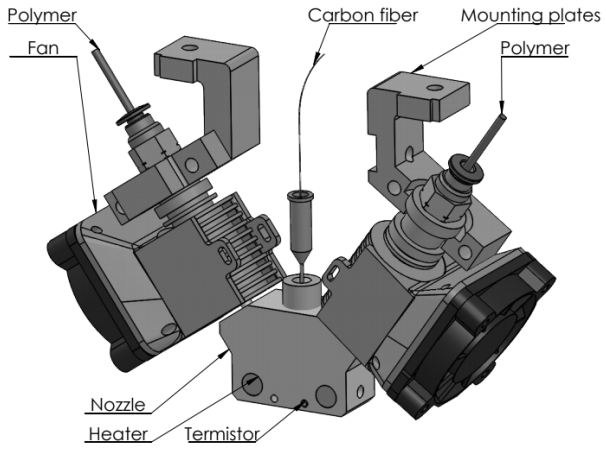

Fig. 9.1. Head with symmetrical feeding of matrix material

Two designs of extrusion heads have been developed that allowed the formation of fiber composites at the stage of fabrication of the detail in the FDM technique. In the first system (Fig. 9.1) matrix material is fed symmetrically to the extrusion axis through two transport channels, while the continuous fiber is transported through the center of the system. The central position is occupied by the base detail, which is the frame of the entire structure and is responsible for the transport of heat generated by a heating resistor located on the rear wall of the detail. The thermistor is responsible for the continuous reading of the operating temperature and is coupled to the heating element via the machine control software. The extrusion nozzle is a replaceable part of the head and can be adjusted to obtain the correct diameter of the extruded composite. In the upper part of the system, there are two filament feeders, which were designed as roller systems. Two plastic transport channels - 3 - simultaneously act as system heat sinks with mounted fans on each of them. It counteracts plasticizing the material too far from the outlet opening and reduces the possibility of stepper motors heating up.

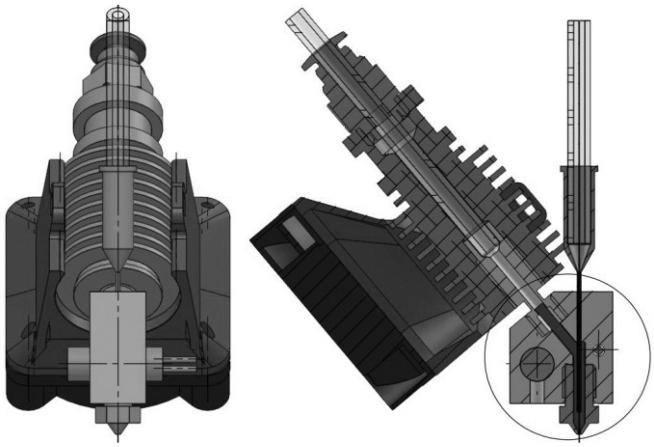

Fig. 9.2. Head with asymmetrical feeding of matrix material

The second head, shown in Fig. 9.2, is based on feeding matrix material from one side only. This allows you to simplify the entire system and its control. Each of the presented methods allow us to obtain the proper orientation of the reinforcing fibers in relation to the surrounding matrix material and ensures a simple change of the components of the composite depending on current research and manufacturing needs.

9.2.2. NUMERICAL SIMULATION OF MATERIAL FLOW IN THE HEAD

The next stage of the work was to perform numerical simulations of the flow of matrix material and short carbon fibers through the designed extrusion nozzle. A two-phase material flow was assumed, in which the polymer was presented as the liquid phase and the carbon fiber as the solid phase. ANSYS software with the FLUENT module was used for calculations. Carbon fibers have been modeled as a discrete phase of the DPM model and simplified to spheres of the same volume and density as a fiber with a length of 1 mm

and diameter 7μm. The deformation and rotation of the solid phase were taken into account that allowed us to obtain close to real flows. All these treatments allowed us to obtain a two-phase material flow through the system.

The flow of matrix material through the system was adopted as the liquid phase of the simulation. The simulated polymer was ABS, which is a frequently used material in this type of heads. The adopted model of a non-Newtonian fluid being an approximation of the polymer flow taking into account its viscosity was chosen the Bird - Carreau model [7]

$$\eta = \eta_\infty + (\eta_0 - \eta_\infty)(1 + \lambda^2 \dot{\gamma}^2)^{\frac{n-1}{2}}, \tag{9.1}$$

where η_∞- coefficient of maximum shear viscosity [Pa·s]; η_0- zero shear viscosity coefficient [Pa·s]; λ - times [s]; n - power law index; $\dot{\gamma}$ - shear rate [s^{-1}].

The material data for the simulation were determined on the basis of tests carried out while extruding ABS through a technologically convergent head used for a given work [8]. Table 9.1 shows the data included in the simulation.

Table 9.1. ABS material data adopted for simulation [8]

Parameter	Value
density	944
zero shear viscosity coefficient [Pa·s]	2404
coefficient of maximum shear viscosity[Pa·s]	0
time [s]	0.07
Power law index	0.037

One of the stages of the research was to conduct a quantitative analysis of thermoplastic and carbon fiber flows at various volumetric and mass material expenditure. Quantitative distribution tests of the extruded composite from the nozzle were carried out with a constant volume flow of matrix material and variable flow of reinforcing fiber. Table 9.2 shows the input data adopted for the simulation.

Table 9.2. Data for simulation

Parameter	Flow value				
	80%	90%	100%	110%	120%
Plastic volumetric capacity [m^3/s]	$4.811 \cdot 10^{-9}$				
Mass flow rate of carbon fiber [kg/s]	$6.414 \cdot 10^{-6}$	$7.216 \cdot 10^{-6}$	$8.018 \cdot 10^{-6}$	$8.82 \cdot 10^{-6}$	$9.622 \cdot 10^{-6}$

An analysis of the calculated standard deviations of the obtained courses of the distribution of reinforcing fibers in the extruded material depending on the mass expenditure of carbon fiber fed to the system was performed. Fig. 9.3 shows the standard deviation of the amount of fiber at the exit of the nozzle at different amounts of fiber being fed.

The graph shows small deviations in the significant range of the extrusion head output hole - the same amount of fiber is given in the range. An increase in the value of the standard deviation at the walls can be observed, which may be due to certain errors in the numerical analysis and the distribution of the finite element mesh. All deviation values

differ by a maximum of 0.03%. The fiber distribution does not change significantly depending on the mass expenditure of the reinforcing material at a constant value of the volumetric expenditure of the matrix material.

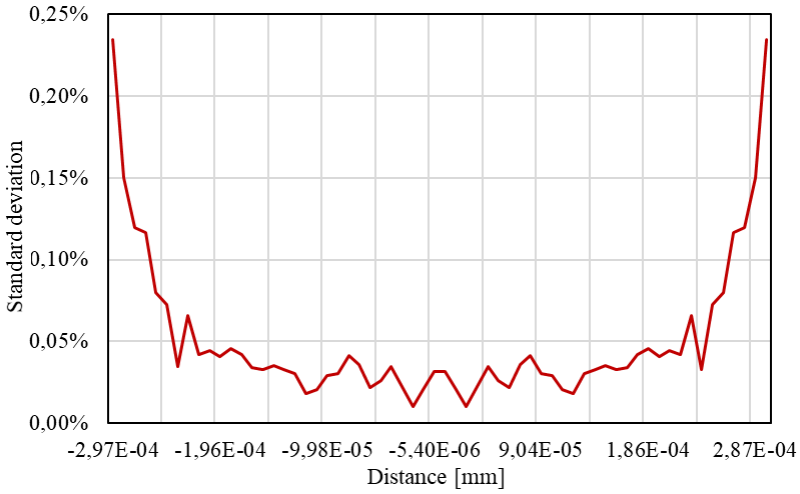

Fig. 9.3. Graph of the standard deviation of the amount of carbon fibers at the exit of the nozzle with different amounts of fiber fed

Numerical simulations carried out as part of research on the flow of material in the system showed mixing of matrix and reinforcing material streams as they passed through the extrusion nozzle and the concentration of fibers in the center of the hole at the exit of the system. Changes in the value of the mass expenditure of the reinforcing material and the volume expenditure of the material in the examined range do not significantly affect the operation of the system, the obtained flows and the distribution of composite components at the outlet of the system.

9.3. METHOD OF ESTIMATING THE EFFECTIVE CONTENT OF FIBERS IN DETAILS

Elements formed from fibrous composites using the FDM technique can significantly differ in terms of macroscopic internal structure from similar geometrical elements made using classical techniques of forming composite details. Additive manufacturing techniques enable precise control of arrangement of a single material path and place it as intended.

To the proposed method for estimating the effective content of reinforcements, the following initial assumptions were adopted:

- the detail is made using the FDM technique,
- the composite consists of one type of matrix material and one type of reinforcing material,
- composite material paths are applied in layers, i.e. on a two-dimensional plane,
- the height of the applied material layer and the width of a single track is constant.

The coefficient of the effective content of fibers in the details of fiber composites made using the FDM technique was determined by the following

$$W_F = \frac{\sum_{i=1}^{N} L_{Fi} \cdot d^2 \cdot \pi \cdot f \cdot sin\,(\alpha)}{\sum_{i=1}^{N} L_{Ci} \cdot 4 \cdot h \cdot s}, \tag{9.2}$$

where: h - height of a single layer, s - path width, L_{Fi} - number of reinforced paths in the layer, L_{Ci} - total number of paths in the layer, N – number of model layers, d – diameter of the reinforcing fiber, f – number of fibers in a single path, $sin(\alpha)$ – deviation of the fiber axis from the reference plane.

Using the presented method, it is possible to determine the effect of track height and width on the gain content factor. Fig. 9.4 shows a graph made on the basis of calculations in which a fixed number of layers and paths in the model, a constant angle of deviation of the composite paths as well as an equal amount of reinforcing material were adopted.

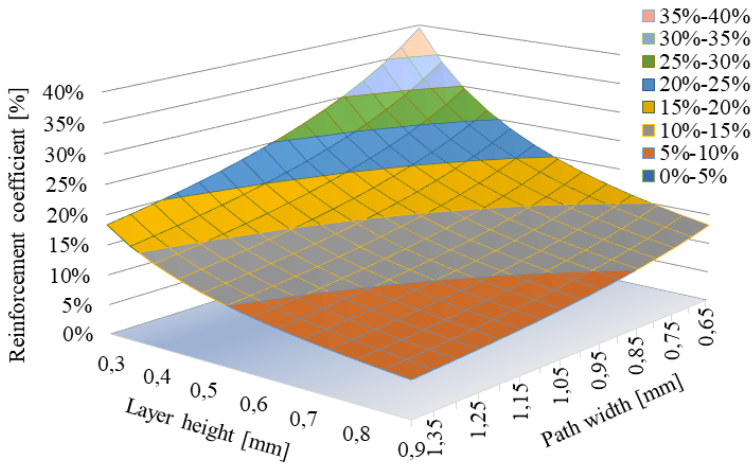

Fig. 9.4. The effect of track height and width on the gain content factor

The graph shows that as the height of the material layer and the width of a single track decreases, the ratio of effective reinforcement content increases. It is possible to control the amount of gain obtained composite materials without changing the amount of reinforcing fiber fed - it is only necessary to correct the process variables at the level of control software.

The presented formula allows taking into account the different number of reinforced paths in individual layers and the deviation of the cross-section of the path from the adopted reference plane. Anisotropic properties of the obtained composites were taken into account.

The calculated effective fiber reinforcement value is potentially more accurate method in comparison to a method based on the matrix / reinforcement volume ratio without specifying the orientation. The formula can be easily implemented in some CAD software.

9.4. MECHANICAL PROPERTIES OF FORMED FIBER COMPOSITES

The industrial application of fibrous polymer composites that can be used in 3D printing requires testing of their strength properties. Tensile strength tests of obtained materials were carried out. This is one of the most common methods of assessing the properties of materials, mainly because of its simplicity and the speed of obtaining results. The object of the study were polymer composites of the ABS matrix and reinforcement in the form of continuous carbon fibers of varying the percentage of the resulting material. The matrix was an acrylonitrile-butadiene-styrene polymer - ABS, while the reinforcement was a continuous carbon fiber Torayca® T300-1000 66 TEX. The tests were performed on the MTS 858 Mini Bionix testing machine. The influence of the number of reinforcing fillers in the volume of the test sample on the tensile strength of the material was examined.

Fig. 9.5 presents a comparative graph of static tensile tests of materials with an ABS matrix and various fiber content as well as material without additional reinforcing elements. A test sample made only of polymer showed elastic - plastic character during stretching, obtaining over 5% elongation at break - not shown in the graph.

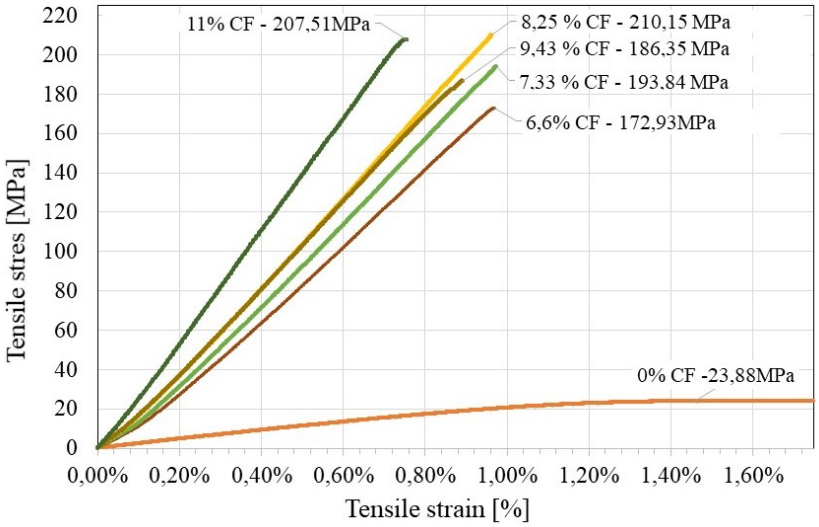

Fig. 9.5. Tensile strength of ABS / CF composites
with reinforcement content {0%; 6,6%; 7,33%; 8,25%; 9,43%; 11%}

The maximum stress in the ABS sample was 23.88 MPa with a relative strain of 1.40%. Materials reinforced with carbon fibers showed elastic nature of stretching. The sample with 8.25% carbon fibers achieved a breaking stress of 210.15 MPa. The tensile strength of the tested composites increases in direct proportion to the percentage of fiber content in the composite.

9.5. CONCLUSIONS

The paper presents the method for estimating the effective content of reinforcements and forming fiber composites using the FDM technique. It has been demonstrated that it is possible to control the amount of reinforcing material in such a composite only by interfering with the height and width of the applied material path, with a constant amount of reinforcing fiber applied. Anisotropicity of obtained composites was taken into account. The calculated effective fiber reinforcement value is potentially a more accurate method compared to that based on the matrix / reinforcement volume ratio throughout the composite without specifying the orientation.

Materials reinforced with carbon fibers - regardless of their percentage content, showed elasticity in a static tensile test. The tensile strength of the tested composites increase in direct proportion to the percentage of fiber content in the composite.

REFERENCES

[1] SEZE H.K., EREN O., FDM 3D printing of MWCNT reinforced ABS nano-composite parts with enhanced mechanical and electrical properties, *Journal of Manufacturing Processes*, vol. 20, p. 339-347, 2019.

[2] CAMINERO M. et al., Impact damage resistance of 3D printed continuous fiber reinforced thermoplastic composites using fused deposition modelling, *Composites Part B*, vol. 148, p. 93-102, 2018.

[3] HOU Z. et al., 3D printed continuous fiber reinforced composite corrugated structure, *Composite Structures*, vol. 18, p. 1005-1010, 2018.

[4] IBRAHIM Y., MELENKA G., KEMPERS R., Fabrication and tensile testing of 3D printed continuous wire polymer composites, *Rapid Prototyping Journal*, vol. 24, p. 1131-1141, 2018.

[5] PRUSINOWSKI A., KACZYŃSKI R., Simulation of processes occurring in the extrusion head used in additive manufacturing technology, *Acta Mechanica et Automatica*, vol. 11, p. 317-321, 2018.

[6] PRUSINOWSKI A., KACZYŃSKI R., MOTYL P., Analysis of FDM extrusion head design as application reinforced composite materials productions, *Mechanisms and Machine Science*, vol. 73, p. 2769-2778, 2019.

[7] CARREAU P.J., DE KEE D.C.R., CHHABRA P., *Rheology of polymeric systems: principles and applications*, Hanser Publishers, Munich, 1997.

[8] WANG H.H. et al., The Failure Analysis and Simulation of an ABS Extrusion Die, *Procedia Engineering*, vol. 130, p. 1419-1424, 2015.

DOI: 10.24427/978-83-66391-87-1_10

Yaroslav SOKOLOVSKYY[1], Volodymyr SHYMANSKYI[1],
Maryana LEVKOVYCH[1], Yaroslav KASPRYSHYN[1]

10. PARAMETRIC IDENTIFICATION AND MODELING OF RHEOLOGICAL BEHAVIOR OF MATERIALS WITH FRACTAL STRUCTURE DURING HEAT TREATMENT

The technological process of thermal treatment of capillary-porous materials, characterized by the influence of several factors on the material as load, humidity and temperature was considered. Mathematical models of non-isothermal moisture transfer and viscoelastic deformation, taking into account the fractal structure of the environment were constructed. One-dimensional mathematical models of deformation-relaxation processes in environments with fractal structure characterized by the effects of memory, spatial nonlocality and self-organization were considered. Taking into account that the fractional parameters of fractal models allow us to describe the deformation-relaxation processes in comparison with traditional methods more fully, the optimal approximation method, the Proni's method was proposed. This method allows us to reduce the problem of identification of the fractional parameters which are part of the creep and relaxation kernels structure, to finding the solutions of systems of linear equations. Software to implement the obtained models was developed.

10.1. INTRODUCTION

Investigation of deformation-relaxation processes have shown that using fractional integrate-differential apparatus for modeling those processes allows the implementation of experimental data to identify model parameters [3, 5, 7] more appropriately on the basis of physical considerations. Particularly important are the works devoted to research of regular and irregular modes of the process of heat treatment of capillary-porous materials. Using this scheme makes it possible to take into account the effects of *memory*

[1] National Forestry University of Ukraine, Ukraine

and self-organization of material. Initially, studies have been carried out to find an effective method for identifying fractal parameters of models [1, 7].

Replacing real environment properties with their idealized models is based on the fact that some of the properties appear most clearly. Then, by removing some irrelevant factors, the ideal model can be constructed. It can be characterized by these dominant characteristics of real environment. In particular, considering only the properties of elasticity and viscosity, it is possible to construct the simpler rheological models that are used in viscosity theory studies. They can be formed by series or parallel connection of the elastic element, behavior of which obeys the Hooke's law, and the viscous one, obeys the Newton's law of viscosity [12, 16].

The simpler models which are constructed by that way will not take into account material properties such as *memory*, the complex nature of spatial correlations, and the self-organizing effects typical for a wood [8]. Therefore, it is suggested to use the fractional-order integro-differentiation mathematical apparatus to record the Newton's law of viscosity. It allows us to take into account the above mentioned properties of material.

This work is devoted to solving the actual scientific task of increasing the efficiency of mathematical modeling of heat and mass transfer processes and visco-elastic deformation of capillary-porous materials taking into account the effect of *memory* and self-organization in the heat treatment process to provide appropriate quality of the material.

The algorithm for the identification of fractal parameters of models was developed, which is based on the use of the iterative method and co-ordinate descent. The experimental data of wood creep was approximated using fractional exponential operators also identified relationship between the fractional component and materials species, temperature and humidity fields.

The characteristics of heat and moisture transfer processes and stress-strain state during heat treatment process taking into account the fractal structure of material with different thermo-mechanical material parameters drying modes were analyzed.

10.2. DEFINITION OF THE PROBLEM

10.2.1. THE VISCOELASTIC DEFORMATION PROBLEM

The mathematical model of the rheological behavior of anisotropic capillary-porous materials in the heat treatment process taking into account the fractal structure of the environment can be described by equations of equilibrium with fractional order γ $(0 < \gamma \leq 1)$ in spatial coordinates x_1 and x_2 for the sample with such spatial dimensions $\Omega = \{x_1; x_2\} = \{[0; l_1] \times [0; l_2]\}$ [11-15]

$$C_{11}\left(\frac{\partial^\gamma \varepsilon_{11}}{\partial x_1^\gamma}(1-\bar{R}_{11})-\frac{\partial^\gamma \varepsilon_{T1}}{\partial x_1^\gamma}+\tilde{R}_{11}\right)+C_{12}\left(\frac{\partial^\gamma \varepsilon_{22}}{\partial x_1^\gamma}(1-\bar{R}_{12})-\frac{\partial^\gamma \varepsilon_{T2}}{\partial x_1^\gamma}+\tilde{R}_{12}\right)$$
$$+2C_{33}\left(\frac{\partial^\gamma \varepsilon_{12}}{\partial x_2^\gamma}(1-\bar{R}_{33}^2)-\frac{\partial^\gamma \varepsilon_{T3}}{\partial x_2^\gamma}+\tilde{R}_{33}^2\right)=0, \quad (10.1)$$

$$C_{21}\left(\frac{\partial^\gamma \varepsilon_{11}}{\partial x_2^\gamma}(1-\bar{R}_{21})-\frac{\partial^\gamma \varepsilon_{T1}}{\partial x_2^\gamma}+\tilde{R}_{21}\right)+C_{22}\left(\frac{\partial^\gamma \varepsilon_{22}}{\partial x_2^\gamma}(1-\bar{R}_{22})-\frac{\partial^\gamma \varepsilon_{T2}}{\partial x_2^\gamma}+\tilde{R}_{22}\right)$$
$$+2C_{33}\left(\frac{\partial^\gamma \varepsilon_{12}}{\partial x_1^\gamma}(1-\bar{R}_{33}^1)-\frac{\partial^\gamma \varepsilon_{T3}}{\partial x_1^\gamma}+\tilde{R}_{33}^1\right)=0. \quad (10.2)$$

The coefficients are defined as deformation vectors $\varepsilon^T=(\varepsilon_{11},\varepsilon_{22},\varepsilon_{12})$, $\varepsilon_T=(\varepsilon_{T1},\varepsilon_{T2},\varepsilon_{T3})^T$, vector components ε_T caused by changes in temperature ΔT and moisture content ΔU, assuming

$$\begin{aligned}\varepsilon_{T1}&=\alpha_{11}\Delta T+\beta_{11}\Delta U,\\ \varepsilon_{T2}&=\alpha_{22}\Delta T+\beta_{22}\Delta U,\\ \varepsilon_{T3}&=0,\end{aligned} \quad (10.3)$$

where $\alpha_{11},\alpha_{22},\beta_{11},\beta_{22}$ - coefficients of temperature expansion and humidity drying, $\overline{C}_{ij}$ - components of the elasticity tensor of the orthotropic body, $\bar{R}_{ij}$, $\tilde{R}_{ij}$ - value of integrals of relaxation kernels of fractional-differential models

$$\begin{aligned}\int_0^\tau R_{ij}(\tau-z,T,U)dz&=\bar{R}_{ij},\\ \int_0^\tau R_{ij}(\tau-z,T,U)\frac{\partial^\gamma \varepsilon_{T1,T2}}{\partial x_k^\gamma}dz&=\tilde{R}_{ij},\\ \int_0^\tau R_{ij}(\tau-z,T,U)\frac{\partial^\gamma \varepsilon_{T3}}{\partial x_2^\gamma}dz&=\tilde{R}_{33}^2.\end{aligned} \quad (10.4)$$

We set the following boundary and initial conditions

$$\begin{aligned}\varepsilon_{ij}\big|_{x_j=0}&=0,\\ \varepsilon_{ij}\big|_{x_j=l_j}&=0,\\ \varepsilon_{ij}\big|_{t=0}&=0,(j=1,2).\end{aligned} \quad (10.5)$$

Also the stress-deformable state of wood components should satisfy the equation of equilibrium.

10.2.2. THE HEAT-MASS TRANSFER PROBLEM

The mathematical model of the distribution of temperature-humidity fields in capillary-porous materials with a fractal structure, the stress-strain state of which is

discussed in the paragraph 10.2.1, is described by a system of differential equations in partial derivatives of fractional order by time τ and spatial coordinates x_1 and x_2 [13, 14]

$$\begin{aligned} c\rho\frac{\partial^\alpha T}{\partial\tau^\alpha} &= \lambda_1\frac{\partial^2 T}{\partial x_1^2} + \lambda_2\frac{\partial^2 T}{\partial x_2^2} + \varepsilon\rho_0 r\frac{\partial^\alpha U}{\partial\tau^\alpha}, \\ \frac{\partial^\alpha U}{\partial\tau^\alpha} &= a_1\frac{\partial^2 U}{\partial x_1^2} + a_2\frac{\partial^2 U}{\partial x_2^2} + a_1\delta\frac{\partial^2 T}{\partial x_1^2} + a_2\delta\frac{\partial^2 T}{\partial x_2^2}. \end{aligned} \tag{10.6}$$

Those equations are solved using the appropriate initial conditions

$$\begin{aligned} T(\tau, x_1, x_2)|_{\tau=0} &= T_0(x_1, x_2), \\ U(\tau, x_1, x_2)|_{\tau=0} &= U_0(x_1, x_2). \end{aligned} \tag{10.7}$$

And boundary conditions of the third order

$$\begin{cases} \lambda_i\left.\dfrac{\partial T}{\partial n}\right|_{x_i=l_i} + \rho_0(1-\varepsilon)\beta\left(U|_{x_i=l_i} - U_P\right) = \alpha_i\left(T|_{x_i=l_i} - t_c\right), \\ a_i\delta\left.\dfrac{\partial T}{\partial n}\right|_{x_i=l_i} + a_i\left.\dfrac{\partial U}{\partial n}\right|_{x_i=l_i} = \beta\left(U_P - U_{x_i=l_i}\right), \end{cases} \tag{10.8}$$

$$\begin{cases} \lambda_i\left.\dfrac{\partial T}{\partial n}\right|_{x_i=0} + \rho_0(1-\varepsilon)\beta\left(U|_{x_i=0} - U_P\right) = 0, \\ a_i\delta\left.\dfrac{\partial T}{\partial n}\right|_{x_i=0} + a_i\left.\dfrac{\partial U}{\partial n}\right|_{x_i=0} = 0, \end{cases} \tag{10.9}$$

where, $T(\tau, x_1, x_2)$ - temperature, $U(\tau, x_1, x_2)$ - humidity, $c(T, U)$ - thermal capacity, $\rho(U)$ - density, ρ_0 - basis density, ε - phase transition coefficient, r - heat of vaporization, $\lambda_i(T, U)$ - coefficients of thermal conductivity, $a_i(T, U)$ - coefficients of humidity conductivity, $\delta(T, U)$ - thermogradient coefficient, t_c - ambient temperature, U_p - relative humidity of the environment, $\alpha_i(t_c, v)$ - heat transfer coefficient, $\beta(t_c, \phi, v)$ - moisture transfer coefficient, α - fractional order of derivative by the time ($0 < \alpha \leq 1$).

10.3. IDENTIFICATION OF FRACTIONAL-EXPONENTIAL CREEP KERNELS BY APROXIMATION THE EXPERIMENTAL DATA USING THE PRONI METHOD

The mathematical model (10.1)-(10.2) of viscoelastic deformation in fractal media for the one-dimension case can be written using the Boltzmann-Volterr's integral equation [6]

$$\varepsilon(\tau) = \sigma_0 G(\tau) + \int_0^\tau \Pi(\tau - z, T, U) D_z^\alpha \sigma(z) dz, \tag{10.10}$$

$$\sigma(\tau) = \varepsilon_0 G'(\tau) + \int_0^\tau R(\tau - z, T, U) D_z^\beta \varepsilon(z) dz, \quad (10.11)$$

where $\alpha = \alpha(T,U)$, $\beta = \beta(T,U)$ fractional order of the derivative which are dependent on temperature T and moisture U; $\sigma(\tau)$ - tension; ε_0, σ_0 - the value of deformation and tension on the initial time τ_0; $G(\tau), G'(\tau)$ - time dependent functions; $\Pi(\tau - z, T, U)$, $R(\tau - z, T, U)$ - creep and relaxation kernels (memory functions), D_z^α, D_z^β - fractional derivatives by the variable z with the order α, β $(0 \le \alpha, \beta \le 1)$ respectively.

The general view of the creep kernel for fractional-differential rheological models (10.1)-(10.5) will be as follows [9]

$$\Pi(t) = \frac{1}{E\tau^\beta} t^{\beta-1} E_{\psi_1,\psi_2}(\phi), \quad (10.12)$$

where E - modulus of elasticity, $E_{\psi_1,\psi_2}(\phi)$ - the Mittag-Leffler's function, $\tau = \eta E^{-1}$ (η -the coefficient of viscosity), $\psi_1 = \psi_1(\alpha,\beta)$, $\psi_2 = \psi_2(\alpha,\beta)$, $\phi = \phi(t,\alpha,\beta)$.

Since the Proni's approximation method, which is valid for a linear combination of exponential functions [2], will be used to parameters identification of creep data, the equation (10.11) will be transformed.

The two-parameter Mittag-Leffler's function is given by the formula [18]

$$E_{\alpha,\beta}(\tau) = \sum_{j=0}^{\infty} \frac{\tau^j}{\Gamma(\alpha j + \beta)}. \quad (10.13)$$

Taking into account equation (10.12) and the corresponding substitutions, we rewrite the appearance of the creep kernel (10.11) as follows

$$\Pi(s) = \sum_{i=0}^{n} A_i e^{-\lambda_i s}, \quad (10.14)$$

where $A_i = A_i(\alpha,\beta)$, $\lambda_i = \lambda_i(\alpha,\beta)$ - amplitudes and indices depend on the fractional parameters α, β, $s = ln\,\tau \Rightarrow \tau = e^s$.

In [4], it is pointed out that for functions which have the form such as $\Pi(s)$ there is some definite linear relationship between its $(n+1)$ equidistant values

$$\sum_{i=0}^{n} c_i \Pi(s + ih) = 0, \quad (10.15)$$

where c_i - searching constant values ($c_n = 1$), h - the time interval is longer than between two consecutive values.

Since (10.13) is a solution of equation (10.14), then parameters λ_i can be found by using this method [2]. Let $e^{-\lambda_i h} = \xi_i$ then to determine each value ξ_i we need to solve the algebraic equation

$$c_0 + \sum_{i=1}^{n} c_i \xi^i = 0. \tag{10.16}$$

To determine c_i the following system of linear equations must be solved

$$\begin{cases} \Pi_1^* c_0 + \Pi_2^* c_1 + \ldots + \Pi_n^* c_{n-1} + \Pi_{n+1}^* = 0, \\ \Pi_2^* c_0 + \Pi_3^* c_1 + \ldots + \Pi_{n+1}^* c_{n-1} + \Pi_{n+2}^* = 0, \\ \ldots \\ \Pi_n^* c_0 + \Pi_{n+1}^* c_1 + \ldots + \Pi_{2n-1}^* c_{n-1} + \Pi_{2n}^* = 0, \end{cases} \tag{10.17}$$

where $\Pi_1^*, \Pi_2^*, \ldots, \Pi_{2n}^*$ - ordinates.

Finding from (10.14) the n solutions $\xi = \xi_1, \xi_2, \ldots, \xi_n$ we can find the parameters λ_i

$$\lambda_i = -\frac{ln\, \xi_i}{h}. \tag{10.18}$$

To determine the amplitudes A_i, you must determine the n ordinates $\Pi_1^*, \Pi_2^*, \ldots, \Pi_n^*$ and also find the solution of the following system of linear equations

$$\begin{cases} A_1^{'} + A_2^{'} + \ldots + A_m^{'} = \Pi_1^*, \\ A_1^{'} p_1 + A_2^{'} p_2 + \ldots + A_m^{'} p_m = \Pi_2^*, \\ \ldots \\ A_1^{'} p_1^{n-1} + A_2^{'} p_2^{n-1} + \ldots + A_m^{'} p_n^{n-1} = \Pi_n^*, \end{cases} \tag{10.19}$$

where $p_i = e^{-\lambda_i h}$, $A_i^{'} = \frac{A_i e^{-\lambda_i s_0}}{\lambda_i}$, $i = \overline{1,n}$, $s_0 = ln\, \tau_0$ - initial moment.

The fractionally-exponential creep kernels can be identified according to the following experimental data [17], which are given in Table 10.1.

Table 10.1. Experimental creep data

k	Π_k [mm]	k	Π_k [mm]	k	Π_k [mm]	k	Π_k [mm]
1	2.2	7	2.82	13	2.93	19	0.88
2	2.31	8	2.85	14	2.94	20	0.86
3	2.61	9	2.87	15	1	21	0.84
4	2.68	10	2.9	16	0.9	22	0.79
5	2.73	11	2.91	17	0.85	23	0.77
6	2.75	12	2.93	18	0.87	24	0.74

To determine the fractional parameters α and β it is sufficient to distinguish two exponential functions for each rheological model. Accordingly, the 2^n ordinates are required to find λ_i parameters. To do this, let us divide the experimental data into 4 groups by summing up six ordinates in each. As a result, we get $\Pi_1^* = 15.28$, $\Pi_2^* = 17.28$, $\Pi_3^* = 9.49$, $\Pi_4^* = 4.88$. The system of linear equations (16) will bring the form

$$\begin{cases} 15.28 c_0 + 17.28 c_1 + 9.49 = 0, \\ 17.28 c_0 + 9.49 c_1 + 4.88 = 0. \end{cases} \tag{10.20}$$

That gives, $c_0 = 0.0373$, $c_1 = -0.5822$. The algebraic equation (10.15) will have the form

$$\xi^2 - 0.5822\xi + 0.0373 = 0, \tag{10.21}$$

the roots are respectively equal $\xi_1 = 0.5089$, $\xi_2 = 0.0733$.

The initial time moment according to our experimental data is $\tau_0 = 10^3$ h and step $\Delta t = 500$ h. Taking into account the corresponding replacement of variables, the h value in formula (10.18) will be equal to 37.29. The values of λ_i will be as follows: $\lambda_1 = 0.0181$, $\lambda_2 = 0.0701$.

Here are the obtained creep kernels for the Maxwell's, Voigt's and Kelvin's fractional-differential models [9]

$$\Pi_M(\tau) = \frac{1}{E\tau_{rel}^{\beta}}\left(\frac{\tau^{\beta-1}}{\Gamma(\beta)} + \frac{\tau_{rel}^{\alpha}\tau^{\beta-\alpha-1}}{\Gamma(\beta-\alpha)}\right), \qquad 0 \le \alpha < \beta \le 1, \tag{10.22}$$

$$\Pi_F(\tau) = \frac{1}{E\tau_{rel}^{\beta}}\tau^{\beta-1}E_{\beta-\alpha,\beta}\left(-\frac{\tau^{\beta-\alpha}}{\tau_{rel}^{\beta-\alpha}}\right), \qquad 0 \le \alpha < \beta \le 1, \tag{10.23}$$

$$\Pi_K(\tau) = \frac{\tau^{\beta-1}}{E\tau_{rel}^{\beta}}E_{\beta,\beta}\left(-\frac{\tau^{\beta-\alpha}}{\tau_{rel}^{\beta-\alpha}}\right), \qquad 0 \le \alpha \le 1;\ 0 < \beta \le 1, \tag{10.24}$$

where τ_{rel} – relaxation time.

Accordingly, for the Maxwell's model, the parameters will be determined from the ratios $\lambda_1 = 1 - \beta$, $\lambda_2 = 1 + \alpha - \beta$. From where we find the fractional-differential parameters as $\alpha = 0.0520$, $\beta = 0.9819$.

Using formula (10.12), we find parameters λ_1 and λ_2 for the Voigt and Kelvin models, which will have the following form: $\lambda_1 = 1 + \alpha - 2\beta$, $\lambda_2 = 1 - \beta$. The fractional-differential parameters will have the following values: $\alpha = 0.8779$, $\beta = 0.9299$.

The parameters α and β which describe the creep kernel are functionally dependent on the humidity and temperature of the medium. The experimental creep data were investigated at temperature $T = 23$℃, humidity $U = 65\%$ and elastic modulus $E = 13800$ MPa.

In the expressions describing the creep kernels, the parameter $\tau = \eta E^{-1}$ is still unknown. We can determine it by finding the amplitudes A_i. To do this, we must solve the system of linear equations (10.18)

$$\begin{cases} A_1' + A_2' = 15.28, \\ A_1' p_1 + A_2' p_2 = 9.49. \end{cases} \tag{10.25}$$

Since λ_i and h are known, then $p_1 = e^{-0.6749}$, $p_2 = e^{-2.6139}$. Having found $A_1' = 19.2008$ and $A_2' = -3.9208$, when $s_0 = 6.9078$ we obtain the following values of amplitudes $A_1 = 0.3938$, $A_2 = -0.4460$. Since A_2 is not in the range of amplitude

values, we find the τ parameter from equation $A_1 = \tau^{-\beta}/\big(E\Gamma(\beta)\big)$. For Maxwell and Voigt models the parameter $\tau_{M,F} = 0.155 \cdot 10^{-3}$, for Kelvin is $\tau_K = 0.975 \cdot 10^{-2}$.

10.4. RESULTS OF SIMULATIONS

10.4.1. IDENTAFICATION OF PARAMETERS

For the sample of pine wood, whose modulus of elasticity is $E = 13{,}8$ MPa with the humidity value $W = 45\%$, the fractional-differential parameters identification were conducted for the Maxwell, Kelvin and Voigt models by the Proni's method. The deformation curves (10.12) were identified from the experimental wood creep data [10, 17] for the Voigt model (Fig. 10.1), as well as for the Maxwell and Kelvin models. They were investigated under constant load and in the absence thereof.

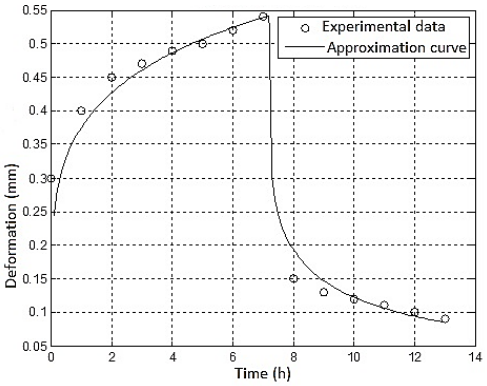

Fig. 10.1. Identification of fractional-differential parameters for the Voigt model at wood humidity *W*=7.5 %

The obtained functions of deformations depending on time are similar to the well-known model of hygro (thermo)-mechanical deformations which describe the processes in wood when the load, temperature and humidity are changed. The developed model also takes into account the formation of residual deformations which are characterized by the *memory* effects of wood. According to Fig. 10.1 after unloading of the material, the creep deformities remain. The maximum deviation of the approximate values from the experimental ones does not exceed 6.7%. It can be concluded that approximation in the form of a linear combination of Mittag-Leffler's functions is an effective tool for extrapolation of the experimental creep data of wood.

After analyzing the data from Fig. 10.2 and Fig. 10.3, the dependence between the identified fractional parameter α and the initial temperature, moisture content and wood species was established. For materials with higher density, it deviates slightly from the value $\alpha = 1$. It means, these parameters have small influence on the fractional properties of those materials. When the initial temperature or humidity, are lower these properties are more pronounced.

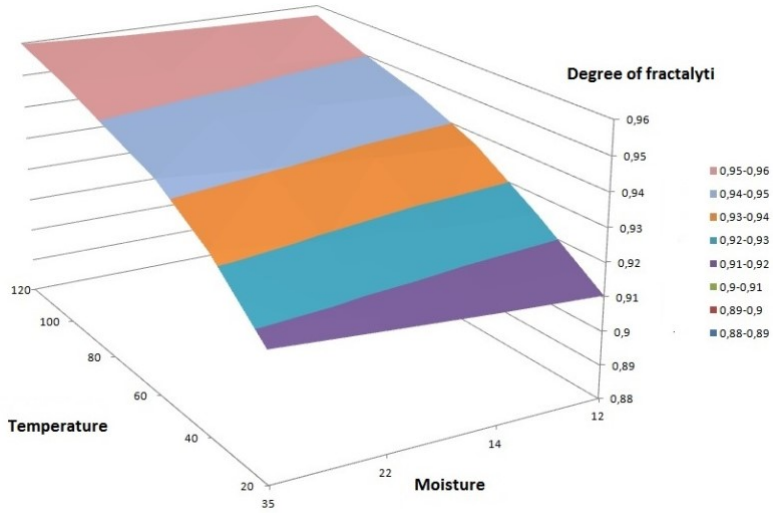

Fig. 10.2. Fractional parameter α for oak depending on temperature and humidity

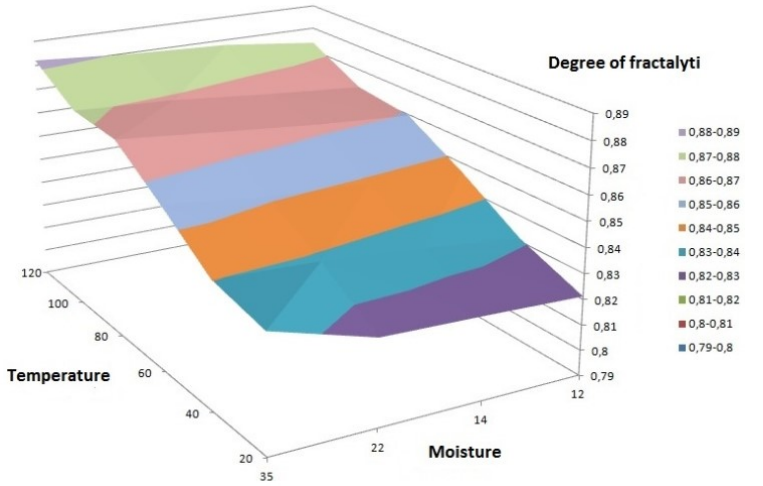

Fig. 10.3. Fractional parameter α for pine depending on temperature and humidity

Thus, the experimental data of wood creep are approximated using fractional-exponential functions and their fractional parameters are distinguished. They describe the influence of the fractal structure of the material. The coefficients of creep and relaxation kernels which are necessary for implementation of the mathematical model of heat-mass transfer (10.6)-(10.9) and viscoelastic deformation (10.1)-(10.5) of capillary-porous materials with fractal structure are obtained.

10.4.2. THE VISCOELASTIC DEFORMATION

Let us carry out the numerical implementation of the mathematical model (10.1)-(10.5) of viscoelastic deformation using the fractional-Voigt model as a basis. Considering the results of identification, we will select the following values of

parameters: $E = 5.19$ GPa, $W = 45\%$, fractional order of the model $\alpha = 0.8856$. The finite-difference method described in [9, 12, 14, 15] is used to find the numerical solution of the two-dimensional viscoelastic deformation problem. The dynamics of the stress components σ_{12} for different wood species depending on change of fractal items is shown as an example.

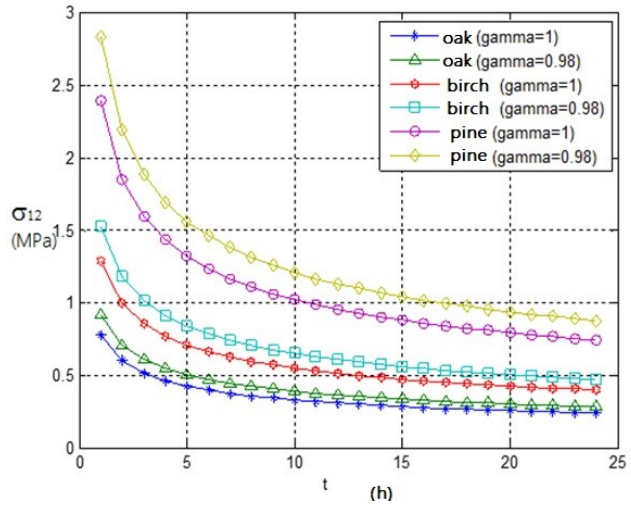

Fig. 10.4. Dynamic of the stress components σ_{12}

The influence of fractal parameters on the dynamics of stresses and strains components is analyzed (Fig. 10.4). It is determined that the difference between the stress components assuming fractal and monolithic structures does not exceed 16.7% for wood with higher density, but for the wood with lower density it reaches 19.6 - 24%.

10.5. CONCLUSIONS

Taking into account the two-parameter Mittag-Leffler's function and the corresponding substitutions, the general form of the original problem is reduced to the linear combination of exponential functions. After the transformations, the Proni's method can be applied. Fractional-differential parameters for Maxwell, Kelvin, and Voigt models of viscous-elastic deformation are identified. The properties of fractional models of viscoelastic deformation in fractal media are taken into account. As we presented, some other conditions must be fulfilled in order to apply the Proni's method described above.

The obtained results can be used for further investigation of mathematical models of viscoelastic deformation and heat transfer processes in fractal media.

For the fractional Voigt model for hardwood, the identification method (iterative method) was chosen correctly, since the approximated curves are in good agreement with the experimental data. During the study of the creep of the capillary-porous material during drying, it is possible to record the formation of residual deformations, the

magnitude of which is defined as the difference between the viscoelastic deformations in the initial state (heated or wet wood) and the end state (chilled or dry wood). Residual stresses describe the memory effect of wood during drying.

REFERENCES

[1] CHANG T. S., SINGH M. P., Mechanical model parameters for viscoelastic dampers, *Journal of Engineering Mechanics*, p. 581-584, 2009.

[2] HRISANOV N. N., Integral'nyj metod aproksimacii eksperimental'nyh dannyh eksponencial'nymi funkciyami, *Vestn. Sam. gos.tekhn. un-ta. Ser. Fiz.-mat.nauki*, vol. 12, 195-199, 2001.

[3] KILBAS A., SRIVASTAVA H. M., TRUJILLO J. J., *Theory and Applications of Fractional Differential Equations*, Elsevier, 2006.

[4] LANCOSH K., *Prakticheskie metody prikladnogo analiza*, GIFML, 1961.

[5] LIU H.-Y., HE J.-H., LI Z.-B., Fractional calculus for nanoscale flow and heat transfer, *International Journal of Numerical Methods for Heat & Fluid Flow*, vol. 24, no. 6, p. 1227–1250, 2014.

[6] POBEDRYA B. E., Modeli linejnoj teorii vyazko-uprugosti, *MTT*, no. 6, p. 121-134, 2005.

[7] PODLUBNY I., *Fractional differential equations, Mathematics in science and engineering,* Academic Press, San Diego, vol. 198, 340 p., 1999.

[8] RABOTNOV Y. N., *Elementy nasledstvennoj mekhaniki tverdyh*, monograph M. Nauk, 384 p., 1977.

[9] SOKOLOVSKYY Y. I., MOSKVITINA M. V., Matematychne modeliuvannia deformatsiino-relaksatsiinykh protsesiv z vykorystanniam drobovoho poriadku, *Visnyk Natsionalnoho universytetu «Lvivska politekhnika», Kompiuterni nauky - informatsiini tekhnolohii*, no. 826, p. 175-184, 2015.

[10] SOKOLOVSKYY Y. I., DENDIUK M. V. Rezultaty eksperymentalnykh doslidzhen obernenoi povzuchosti ta skladovykh deformatsii derevyny v poperek volokon, *Lisove hospodarstvo, lisova, paperova i derevoobrobna prom-st, Lviv: UkrDLTU*, vol. 27, p. 73-77, 2002.

[11] SOKOLOVSKYY Y. et al., Mathematical modeling of deformation-relaxation processes under phase transition, in: *CEUR Workshop Proceedings 2300*, p. 83-86, 2018.

[12] SOKOLOVSKYY Y. et al., Mathematical models of biophysical processes taking into account memory effects and self-similarity, *Informatics & Data-Driven Medicine*, vol. 2255, p. 215-228, 2018.

[13] SOKOLOVSKYY Y. et al., Mathematical modeling of nonequilibrium physical processes, taking into account the memory effects and spatial correlation, in: *9th International Conference on Advanced Computer Information Technologies, ACIT 2019*, p. 56-59, 2019.

[14] SOKOLOVSKYY Y., SHYMANSKYI V., Mathematical modelling of non-isothermal moisture transfer and rheological behavior in cappilary-porous materials with fractal structure during drying, *Computer and Information Science*, vol. 7, no. 4, p. 111-122, 2014.

[15] SOKOLOVSKYY Y, SHYMANSKYI V., LEVKOVYCH M., Mathematical modeling of non-isotermal moisture transfer and visco-elastic deformation in the materials with fractal structure, in: *XI-th International Scientific and Technical Conference Computer Science and Information Technologies CSIT-2016*, Lviv, Ukraine, p. 91-95, 2016.

[16] SOKOLOVSKYY Y, SINKEVYCH O., Software and algorithmic support for representation of CAD models in 2D von Neumann neighborhood, in: *CEUR Workshop Proceedings 2300*, p. 215-218, 2018.

[17] TONG L., Creep of wood under a large span of loads in constant and varying environments, part 1: Experimental observations and analysis, *Holzalsroh- und Werkstoff*, vol. 51, p. 400-405, 1993.

[18] VASILEV V. V., SIMAK L. A., Drobnoe ischislenie i approksimacionnye metodi v modelirovanii dinamicheskih system, *Nauchnoe izdanie*, Kiev, Ukrainy, 256 p., 2008.

DOI: 10.24427/978-83-66391-87-1_11

Paweł OSTAPKOWICZ[1]

11. FILTERING TECHNIQUES TO IMPROVE EFFICIENCY OF LEAK LOCALIZATION IN PIPELINES

This chapter deals with issues connected to the detection of leaks in liquid transmission pipelines. Such pipelines are especially exposed to the risk of leakages. The occurrence of a leakage usually leads to huge economical, environmental and social effects. Therefore, leak detection systems (LDS) are installed in transmission pipelines. LDS allows 24 h monitoring of the integrity of the pipeline, where its overall scope of the operational tasks includes detection, localization and estimation of leak intensity.

There are a number of ways to implement LDS [1, 12]. Of fundamental significance appear to be the methods based on measurements of flow parameters in the pipeline, such as mass/ volume flow, pressure and temperature. These methods are called *analytical (indirect, internal or software based) methods*. Their reviews are available in [1, 12].

Pipeline operators are interested in such LDS solutions that would enable leak detection of less than 1% nominal flow intensity. It is important to achieve such aim, when the occurrence of a leak is in both steady as well as in transient state, i.e. related to an operating point change, valve's aperture and closure, pump's start-up or stoppage. The transient state cases still pose a significant issue to solve.

Apart from the system's ability to detect any kind of leakage, another important issue is the precise localization of a leak point. In both the tasks, the response time also plays a significant role.

In order to determine where a leak has occurred, various localization procedures are used. Among them, there are procedures based on the calculation of pressure gradients [9, 10]. Gradient based localization procedures are used both in simplified as well as very advanced solutions of analytical methods.

On the whole, simplified methods have proved to be efficient when the pipeline operates in steady state. The author, in cooperation with other researchers, conducted experimental studies of selected standard and improved proprietary solutions of such methods. The results of the studies are presented in [5, 6, 7]. The proposed solutions were specifically

[1] Bialystok University of Technology, Poland

aimed at detecting leaks. An essential element of their assessment was the estimation of the performance indexes, such as possible leakage detection level and response time [7] as well as resistance to interference simulated by noises added to acquired measured signals [6]. After detecting a leak, leak localization procedures were carried out and their results were also presented. Another experimental research, conducted with participation, involved changing around 10% of the nominal flow rate in conjunction with a simultaneous simulation of a single leakage in the transient state. It has been proved that for such a large change of the pipe's operating point, simplified methods can also be successfully used for leakage diagnosis in transient states, i.e. for specific operational conditions [8].

As an example of advanced analytical methods, the so-called automatic control approach methods [2, 4] can be mentioned here. Such solutions use a mathematical model of liquid flow dynamics described in the state-space. Common solution for further analysis is an implementation of state observers [3, 4]. These methods are very complex and costly. One of many problems is also building the pipeline's mathematical model and developing its solutions.

Gradient based localization procedures are not as fast as the localization procedures based on negative pressure wave detection [6, 8]. However, compared to those procedures, they are more reliable, i.e. offer lesser risk of missing a leak.

The basic requirement that determines the precision of the leakage localization is an accurate estimation of nominal pressure values. Such an estimate applies to individual measurement points that are included in the calculations. In practice, this means the need to use high accuracy pressure sensors. Next, using the acquired data samples, nominal values are calculated. Most often, averaging of a given set of data samples is applied here, i.e. an average value is calculated.

In the case of transmission pipelines, accurate pressure measurements are not an easy task. Pressure sensors are mounted on the inlet and outlet and along the pipeline. Considering a typical section of a transmission pipeline of 30–100 km in length, this means long distances of individual pressure sensors from a place where the control room of LDS is located. Apart from sensors, numerous additional devices are also used, including A/D converters, communication modules for wire or no-wire data transmission. The measurement system with such extensive and complex structure is difficult to protect from the impact of interference.

Errors and noises generated by measurement devices, in combination with disturbances that occur in the flow, generally result in the quality deterioration of measurement data. It is evident that bad quality of the data will influence LDS and generate false results of diagnosis, as observed in [12].

Consequently, the localization of a leak may not be very accurate, with errors in real pipelines ranging from a few hundred meters up to several kilometres. The errors can be even worse for small leakages, including the ones that have less than 1% nominal flow intensity.

In this work, the attention is focused on a widely used gradient based localization procedure that uses gradient increments instead of the gradients themselves. We consider this procedure to localize single low intensity leaks in the event of the use of unfiltered as

well as filtered measurement data. A localization error in function of time response determined as a performance index is used in the assessment of compared variants of procedure implementation.

Two different single leak scenarios are considered. The first one concerns an occurrence of a leak in a steady state. The other scenario assumes a leak in a transient state. The research used measurement data obtained during experiments carried out on a model pipeline. Intensity of simulated leaks was between 0.2–0.8% of the nominal flow rate.

11.1. SCENARIOS OF SINGLE LEAK OCCURRENCE – PHENOMENA RELATED TO LEAK

In general, analytical methods consider hydraulic phenomena related to leak occurrence. An in depth understanding of these phenomena and their impact on the measured flow parameters is crucial.

Knowledge of these issues is also important for the leak localization procedure and its application to the two single leak scenarios described below. In addition, it also makes it easier to determine the requirements that the expected use of measurement data filtration should meet.

11.1.1. Scenario #1: single leak occurred during steady-state pipeline conditions

Let us consider a leak free (leak proof) pipeline that works under stationary conditions. As a result, the pressure measured at the inlet and outlet, as well as at some points along the pipe and also the flow rate signals (measured both at the inlet and outlet) have stabilized values. This is illustrated by Figs. 1a and 1b, corresponding to the time interval A. If a leak occurs at the coordinate point z_{leak}, it results in pressure and flow changes in the pipeline. In the case of a pressure change, two distinct phenomena are observed.

The first one involves the spread of negative pressure waves in the pipeline. Such waves originate due to a sudden drop in pressure at the leak point, and spread downstream and upstream through the pipeline at the sound speed. These waves are recognized as a change in the measured pressure signals which, in the time domain, typically takes a shape of a slope. The slope is usually curvilinear in shape with varying degrees of inclination. The beginning of the change i.e. bending point corresponds to the wavefront. It should be noted that the waves take evidently visible fronts in the case of sudden leaks whereas for gradually growing leaks, the wavefronts are more smoothed. Behind the wavefront, the pressure in the pipeline gets lower with the increase in the distance from the leak point.

The other phenomenon consists in the change of the pressure distribution along the pipeline, in comparison with a steady state with no leak. Assuming that pressure gradient $G_0 = dp/dz$ is constant over the whole length of the pipeline, then pressure distribution is represented by a straight line, as shown in Fig. 11.2a (curve 0). After a certain time, the transient state is transformed into a new steady state. This new steady state is shown in Fig. 11.1a as the time interval C. Then the pressure drop line is composed of two straight

segments, as shown in Fig. 11.2a (curve 1). The inclinations of both lines are described by pressure gradients G_{in} and G_{out}, where $G_{in} < G_0$ and $G_{out1} < G_0$.

In the case of a flow rate change, we can observe an increase of the flow rate in the section from the inlet to the leak point, and the decrease in the section from the leak point to the outlet. More detailed description of the phenomena related to this scenario of leak occurrence can be found in [6].

11.1.2. Scenario #2: single leak occurred during transient-state pipeline conditions

This scenario is represented by pressure (measured at the inlet and the outlet, and also at several points along the pipe) and flow rate signals (measured at the inlet and the outlet) which are shown in Fig. 11.1c and 11.1d.

At the very beginning, the pipeline operates in a steady state without leakage. It is marked by the time interval A. Next, a technological operation is carried out involving a change of the delivery rating of a pump, which is actually aimed at changing the flow rate of the medium pumped through the pipeline. The implementation of this operation results in a transient state, marked by the time interval B1. During this operation, i.e. in the transient state, a single leakage appears at the coordinate point z_{leak}. The occurrence of a leak causes an additional transient state, marked by the time interval B2. This state will overlap with the transient state caused by the change in the delivery rating of a pump.

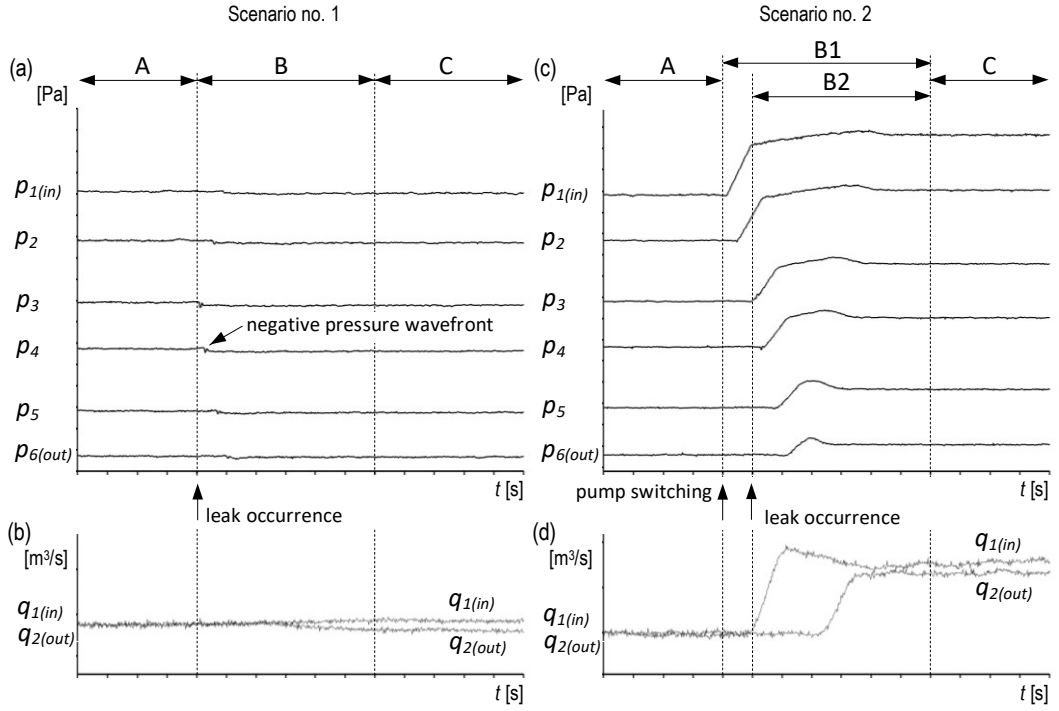

Fig. 11.1. Signals in the pipeline before and after leak occurrence:
(a), (b) pressure and flow rate; (c), (d) pressure and flow rate

As in the previous scenario, the resulting leak is accompanied by the propagation of negative pressure waves. The visibility of the fronts of these waves, apart from the previously mentioned conditions, will depend on the dynamics of pressure changes caused by the technological operation.

Assume further that the technological operation of changing the pump's rotation velocity is completed and that the failure of the pipeline at the point of leakage will have fixed dimensions. Thus, after a certain time, medium flow in the pipeline gets stabilized in a new steady-state operating point represented in Figs. 11.1c and 11.1d as the time interval C. Then, the measured pressure and flow rate have stabilized values. Similarly, as in the previous scenario, the new line of pressure drop along the pipeline is different from the line of pressure drop prior to the leak, i.e. corresponding to the time interval A. Now, the line is composed of two straight segments.

11.2. CHARACTERISTICS OF GRADIENT BASED LEAK LOCALIZATION PROCEDURES

Gradient based localization procedures [5, 9, 10, 11] take advantage of the accompanying leakage of pressure changes (drops) in the pipeline. Such procedures may be useful for leaks that occurred at one or even several locations along the pipeline. Two variants of such procedures can be distinguished.

The first variant, so-called classical procedure uses phenomenon of change in the pressure distribution along the pipeline described above in section 11.1. This procedure consists in the calculation of the abscissa of the intersection point of two straight lines, which are shown in Fig. 11.2a (curve 1), using the following relationship

$$z_{leak} = \frac{p_{out} - p_{in} - G_{out} \cdot l}{G_{in} - G_{out}}, \tag{11.1}$$

where: l - length of the pipeline, G_{in}, G_{out} - pressure gradients after the leak occurrence in the section between the beginning of the pipeline and the leak point and in the section between the leak point and the end of the pipeline, p_{in}, p_{out} - pressure after the leak occurrence for the initial and final cross-section of the pipeline.

In order to determine gradients G_{in} and G_{out}, it is necessary to install at least four pressure sensors in the pipeline, two in the front and two behind the leak point. However, in practice, the other variant is used more often. This procedure, instead of pressure distribution $p(z)$ (Fig. 11.2a), uses the distribution of pressure increases $\Delta p(z)$ in the pipeline (Fig. 11.2b), which allows the reduction of the negative impact of pressure measurement errors. In particular, it relates to systematic errors of measurement.

The method of locating the leakage site is similar here, i.e. it involves determining the abscissa of the two straight lines that correspond to the pipeline sections before and after the leak point. These two straight lines are shown in Fig. 11.2b. Then, a calculation is made using the following relationship

$$z_{leak} = \frac{\Delta p_{out} - \Delta p_{in} - \Delta G_{out} \cdot l}{\Delta G_{in} - \Delta G_{out}}, \tag{11.2}$$

where: $\Delta G_{in}, \Delta G_{out}$ - increments of pressure gradients in the section between the beginning of the pipeline and the leak point and in the section between the leak point and the end of the pipeline, $\Delta p_{in}, \Delta p_{out}$ - increments of pressure for the initial and final cross-section of the pipeline.

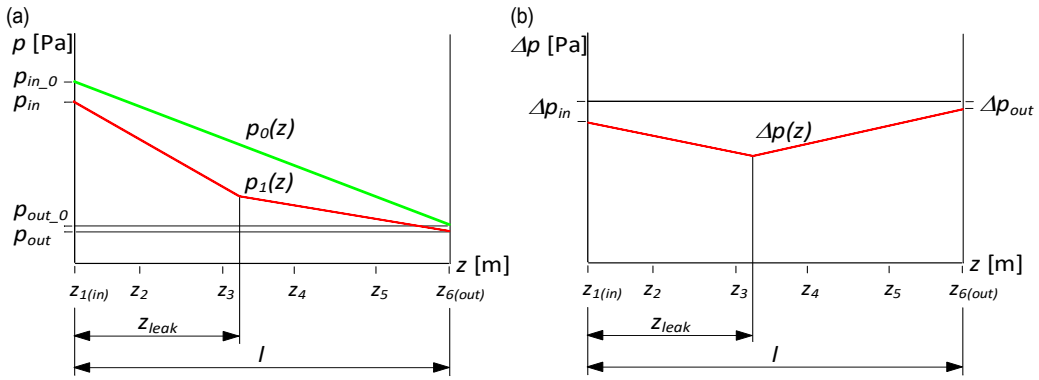

Fig. 11.2. Lines of distributions during no-leak conditions and after leak occurrence: (a) pressure, (b) pressure increases

Both procedures do not require the measured pressure signals to be sampled at very short periods, unlike in the case of the localization procedures based on negative pressure wave detection. In real pipelines, sampling periods range from a few seconds to several minutes.

Fig. 11.3. Laboratory model of the pipeline used during experiments

The increase in pressure and gradients taken into account in (11.2) are usually calculated as the differences between the values of pressure and gradients in steady state before and after the occurrence of the leak. It refers to the use of measurement data corresponding to

the intervals A and C (Fig. 11.1). Using the measurement data that correspond to both these ranges, the nominal pressure values used in the calculations are estimated. In practice, such estimation requires the use of time windows covering a certain number of data samples. A significant disadvantage may be the fact that the accuracy of the estimate increases with the amount of the data available, which means extension of the total time needed to localize leak (response time). Hence, there is a need to determine the localization error in function of the time response.

11.3. EXPERIMENTAL IMPLEMENTATION OF THE SELECTED LOCALIZATION PROCEDURE WITH USED DATA FILTERING

11.3.1. THE PILOT PIPELINE INSTALLATION

The laboratory model of the transmission pipeline for water pumping (Fig. 11.3) has been built in the Faculty of Mechanical Engineering of the Bialystok University of Technology in Poland. Its total length is close to 400 m, including the main pipe section of 380 m long which is made of polyethylene tubes (HDPE) of 34 mm internal diameter and 40 mm external diameter.

The pipeline installation is equipped with a variable flow pump, two semi-open tanks (on inlet and outlet) of 300 dm^3 capacity each. On the pipeline, two electromagnetic volume flow meters (at the inlet and outlet at coordinates $z_{in} = -6.5$ and $z_{out} = 382.2$ m) and seven pressure transducers (in the main pipe section at coordinates $z_{1(in)} = 1$, $z_2 = 61$, $z_3 = 141$, $z_4 = 201$, $z_5 = 281$, $z_6 = 341$ and $z_{7(out)} = 378$ m and one thermometer (at the inlet) have been installed.

In order to simulate leakages, automatically controlled proportional solenoid valves equipped with interchangeable diameter orifices are used. The valves can be installed at selected points along the entire length of the main pipeline section.

11.3.2. CONDITIONS OF EXPERIMENTS

An overview of the experiments is shown in Fig. 11.4. These experiments correspond to the two leakage scenarios as described in section 11.1.

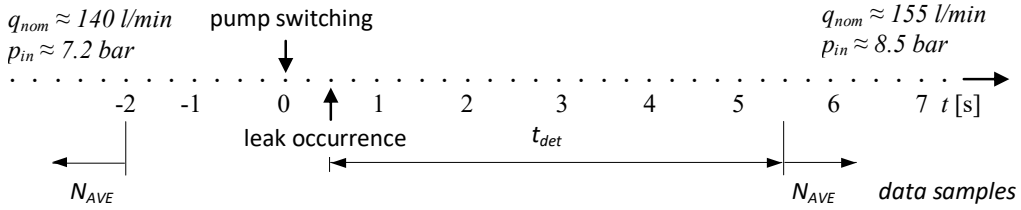

Fig. 11.4. Time scenario of experiments

The leaks were simulated at some selected points in the pipeline with the coordinates 75, 195 and 315 m by rapid opening of electromagnetic valves. The data on leakage intensity is given in Table 11.1. During the experiment, the flow rate and pressure signals were sampled at the rated frequency equal to $f_p = 100$ Hz. In addition to the experiments with simulated leaks, similar experiments deprived of leakage simulation were carried out.

Table 11.1. Places and intensities of simulated leaks

Leaks					
[m]	[%]	[m]	[%]	[m]	[%]
75	0.21	195	0.26	315	0.23
	0.21		0.26		0.24
	0,43		0.44		0.43
	0,43		0.44		0.49
	0.81		0.69		0.73
	0.81		0.69		0.81

11.3.3. PROPOSED FILTERS

For liquid transmission pipelines, the measured pressure signals usually contain the disturbing noise and interference caused by the flow and measurement effects. Very often, a high level of signal interference can make it difficult to observe the changes in the signal value. In particular, this refers to small leaks when pressure changes in the pipeline caused by the leaks are relatively small. Then, if ratio of the measured signal value of pressure changes to the interference and the level of measurement noises is not satisfactory, the identification of such changes seem to be very difficult. Another important problem is the lack of suitable relation of the level of the pressure changes to the whole pressure transmitter range as well as with respect to uncertainty and systematic errors of the measurement.

Therefore, it is necessary to utilize appropriate filtering of the measured pressure signals. Taking into account the specificity of the selected localization procedure, we consider the use of time series data filtering techniques. For such a digital filtering approach, the following requirements should be defined:

- possibly good mapping changes of the measured pressure signals,
- smoothing fluctuations of the measured pressure signals.

At the beginning, we assume the use of the following three time series data filtering techniques.

- Moving average filter.
  Such filtering is effective in reducing the noise component of the signal data set, but has the tendency to blur slopes. We use this filter according to formula

$$y(n) = \frac{x(n-k) + x(n-k+1) + \cdots + x(n) + \cdots + x(n+k-1) + x(n+k)}{N}, \quad (11.3)$$

where: $y(n)$ is the output, $x(n)$ are samples of the input signal, N is number of samples.

- Moving median filter.
  This type of filtering possesses good noise reduction, particularly impulsive type noise and has very good ability to track slopes. We employ a variant of this filter corresponding to formula

$$y(n) = med[x(n-k), x(n-k+1), \ldots, x(n), \ldots, x(n+k-1), x(n+k)]. \quad (11.4)$$

- Recursive filter.
  This type of filtering is also called recursive averaging with fading memory (exponential smoothing). It has noise reduction advantage and depending on the weight factor, is also able to retain signal data that are changing rapidly. The filter is described by formula

$$y(n) = \alpha \cdot y(n-1) + (1-\alpha) \cdot x(n), \quad (11.5)$$

  where: $y(n-1)$ is the output in the previous moment resulting from the applied sampling period, α is the weight factor $0 < \alpha < 1$.

11.3.4. THE RESULTS

All the above filtering techniques are relatively simple to implement. An exemplary result of their implementation with respect to the measured pressure signals are shown in Figs. 11.5 and 11.6. The results in Fig. 11.5 relate to the first leak occurrence scenario, whereas the ones in Fig. 11.6 refer to the second scenario. The pressure signals correspond to extreme external pressure sensors mounted in the pipeline.

It should be explained here that the pressure signals shown in Figs. 11.5 and 11.6, correspond to the sampling frequency after it has been reduced to the level equal to $f_p = 10$ Hz. This value is sufficient to observe the dynamics of pressure change, especially in the case of the second leak scenario. The same parameter is also used in further analysis.

The moving average filter is implemented with a number of samples $N = 41$, and the median filter also utilizes the same number of samples. The recursive filter has the weight factor equal to $\alpha = 0.900$.

Analyzing the plots in Fig. 11.5, we can observe that the best mapping changes of the measured pressure signals are achieved for both the average and median filters, whereas the recursive filter generates the output with a time delay. The outputs of individual filters are different with respect to the smoothing of fluctuations of the original signals. The best result is observed for the average filter, whereas the output of the median filters is not very smoothed. Similarly, this refers to the output of the recursive filter.

The plots in Fig. 11.6 show significant differences for each of the compared filters. In particular, this is true of the slope mapping ability that is an effect of pump switching. Such a signal change is only satisfactorily mapped by the median filter. The averaging filter

distorts the slope due to the data averaging process. As a result, the filter output overtakes the edge of the slope, whereas behind the slope, it is set to a new level with a delay. On the other hand, the recursive filter generates an output that lags considerably behind the beginning of the slope, and its stabilization behind the slope is slow. We can also observe that the original signals have been smoothed differently by these filters.

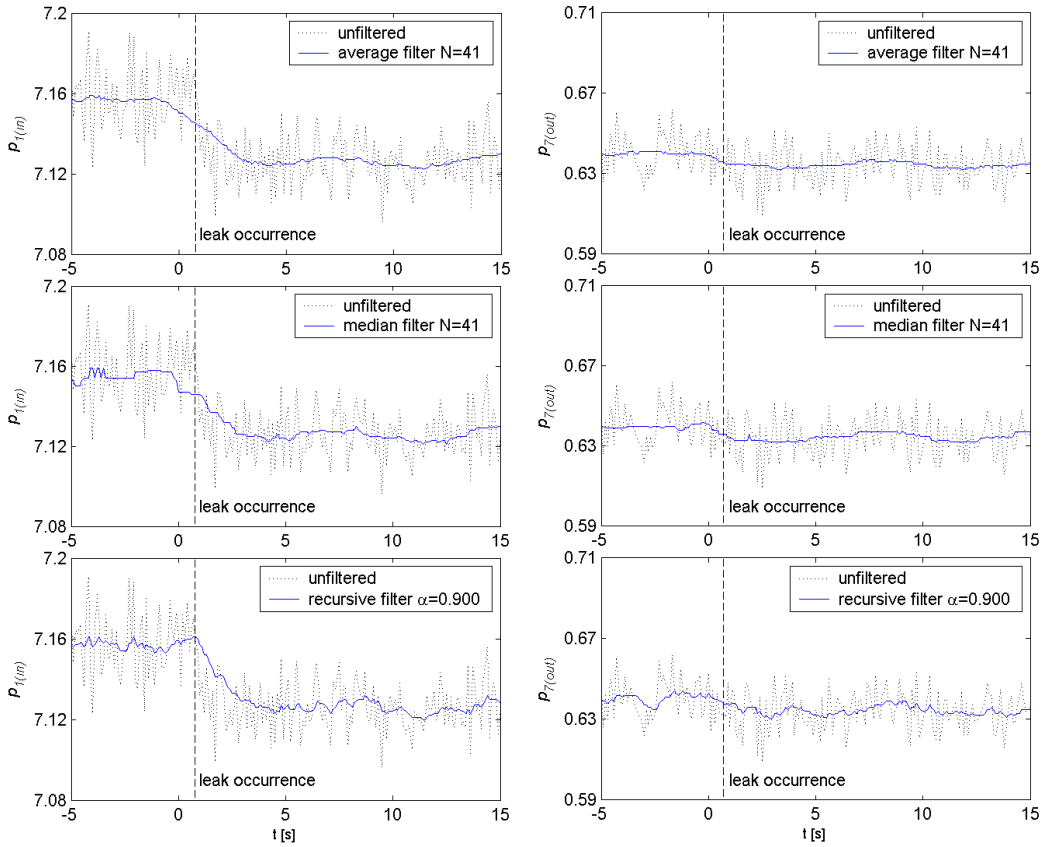

Fig. 11.5. Unfiltered and filtered data refer to the leak about 0.45% of the nominal flow rate (the scenario #1)

A more precise definition of the conditions and requirements for the implementation of the leak localization procedure will be helpful in solving the problem of filter selection and its settings.

The moment of starting the procedure should be taken into account. This moment should correspond to the detection of a leak by a relevant algorithm. It is also important to bear in mind the general assumption that we are interested in achieving the best possible accuracy of the leak localization in the shortest possible time.

Let us assume that for all the experiments, the leak detection time counted from the moment of its occurrence is $t_{det} = 5\text{s}$. Such value corresponds to the results of the experimental studies presented in [6, 8], where the algorithms designed to detect a leak were tested for similar scenarios of leak occurrence.

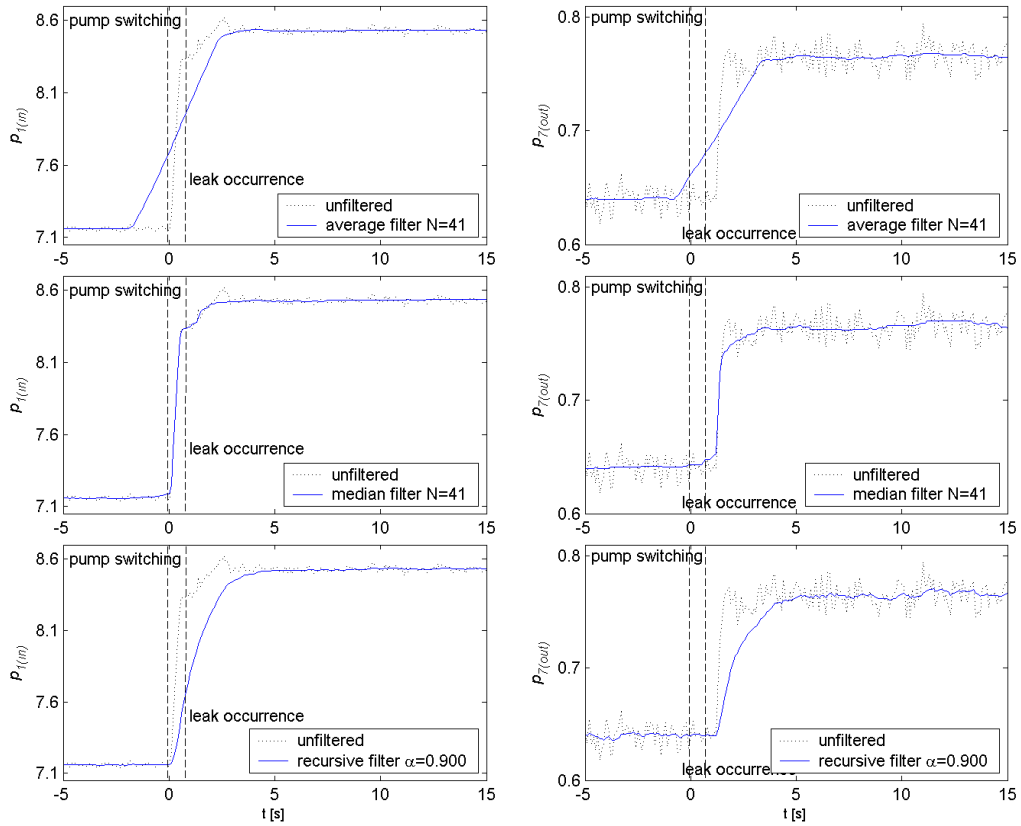

Fig. 11.6. Unfiltered and filtered data refer to the leak about 0.45% of the nominal flow rate (the scenario #2)

In view of the above, it seems unreasonable to further increase the number of input samples N in the case of both the average and median filters. We must remember about the $(N-1)/2$ samples that should be additionally taken into account when determining the time of leak localization. Another problem that can be seen in Figs. 11.5 and 11.6 is the need to backward shift the end of the range used to calculate the nominal pressure values in a non-leakage condition. Initially, the end of the interval was supposed to correspond to 0 on the timeline. To avoid this requirement, it is possible to move the filter output from sample $y(n)$ to sample $y(n+k-i)$, that is related to the average filter. However, the existing option, i.e. with the filter output corresponding to the sample $y(n)$, is further considered. Therefore, the end of this interval has been moved to -2 on the timeline (Fig. 11.4). In the case of a recursive filter, further improvement of the signal smoothing effect can be achieved by changing the setting of parameter α. Yet, this will further increase the output delay.

It should also be kept in mind that apart from the signal filtration itself, the averaging of the obtained output samples of the filters will also be used. In order to obtain the best results of leak localization in the shortest possible time, this effect may be actually caused by the applied signal filtering in terms of reducing its fluctuations. It is important here to

obtain stable values of the filter output signal. Hence, for the purpose of further analysis, additionally a recursive filter setting was adjusted, assuming $\alpha = 0.980$.

The averaged leak localization errors in function of time response obtained for both leak scenarios are shown in Fig 11.7. The results concern the use of both unfiltered and filtered measured signals.

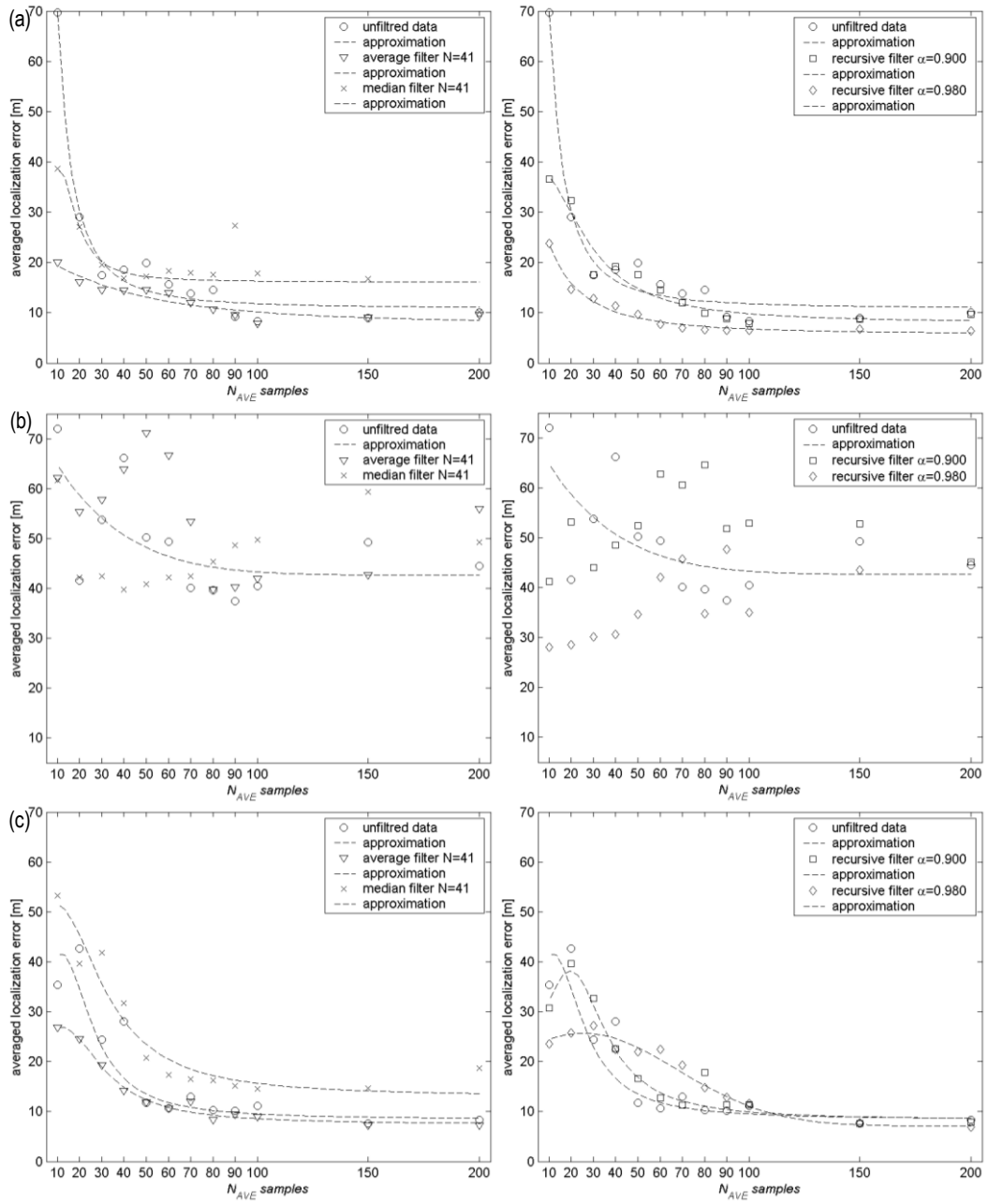

Fig. 11.7. Distributions of the averaged leak localization error:
(a) scenario #1, (b) scenario #2, (c) scenario #2, when data corresponding to the non-leak state are used from another experiment without simulated leak

The mean error was calculated by making use of the localization errors obtained for each of the experiments (Table 11.1). The leakage site calculations were performed according to procedure (11.2). For the calculation of both gradients and their increments, the data corresponding to four sensors were used, including two sensors located at the inlet or the outlet of the pipeline, and another two sensors nearest to the leak point. The response time is represented by the number of samples N_{AVE} that were taken into account when estimating the nominal pressure values for the non-leaked and leaked states (Fig. 11.4). Such estimates were made using the calculated mean value for the considered set of samples. Identical numbers of samples N_{AVE} were taken into account for both states. If, for a given experiment, the calculated leakage point exceeded the coordinates of the pipeline length, its value was assumed to be the appropriate extreme coordinate.

While analyzing the results obtained for the first leak scenario (Fig. 11.7a), we might state that the proposed filtering techniques have made it possible to achieve a significant reduction of the localization error in function of time response. In particular, it relates to the use of recursive filtering with the setting $\alpha = 0.980$.

It can be also noticed here (Fig. 11.7a) as for the others examined variants (Figs. 11.7b and 11.7c) that the amount of the data used for the estimation of nominal pressure values exerts a substantial influence on the accuracy of the localization of a leak point.

It is worth noting that the median filter is not the best averaging filter, hence for virtually all considered variants, the final location errors always have the highest level.

For the second scenario, averaged location errors have much higher levels and dispersion (see Fig. 11.7b). Of the filters used, only recursive filters reduce the levels of average leakage localization errors compared to the results obtained for unfiltered signals. For both of these filters, it is worth noting the build-up of a location error along with an increase of the amount of the samples N_{AVE}. This may be due to delays in the operation of filters, where slow stabilization of the filter response significantly affects the resulting averaging result. In general, the results obtained here confirm known problems with the exact localization of the leak point in the case of transient states.

However, in the case of the additionally examined variant for the second leak scenario (Fig. 11.7c), when the data corresponding to the non-leak state are used not from the time period before pump switching, but from another experiment without simulated leak where identical time period is considered as for standard calculation (Fig. 11.4), we can observe decreasing errors.

Such a variant is purely theoretical. But, it can show, that except for the above mentioned problems related to the second leak scenario, there may be errors of pressure measurement. In fact, the errors in function of the whole pressure transmitter range are taken into account here. This additional improvement of the localization procedure based on gradient increments may require applying metrological characteristics of pressure sensors, i.e. calibration data given by their producers.

11.4. CONCLUSIONS

This work presents very simple and efficient filtering techniques to improve the accuracy of the localization procedure based on gradient increments. The procedure can be successfully used to localize a location of leakage that occurred during steady-state pipeline conditions. It also shows possibilities of using the procedure to localize a leak point related to the occurrence of a leak in transient state.

The effectiveness of the filtering techniques has been proven by the results of localization errors in function of time response. They relate to the use of real measured pressure signals obtained for the experiments with simulated small leaks between 0.2–0.8% of nominal flow rate. The experiments were carried out on the pilot pipeline described earlier.

REFERENCES

[1] ADEGBOYE M.A. at al., Recent Advances in Pipeline Monitoring and Oil Leakage Detection Technologies: Principles and Approaches, *Sensors*, vol. 19, no. 11, article number 2548, 2019.

[2] BILLMAN L., ISERMANN R., Leak Detection Methods for Pipelines, *Automatica*, vol. 23, no. 3, p. 381–385, 1987.

[3] DELGADO-AGUINAGA J.A. et al., Multi-leak Diagnosis in Pipelines based on Extended Kalman Filter, *Control Engineering Practice*, vol. 49, p. 139–148, 2016.

[4] KOWALCZUK Z., GUNAWICKRAMA K., Detecting and locating leaks in transmission pipelines, in: *Fault Diagnosis: Models, Artificial Intelligence*, *Applications*, Korbicz K.J., Koscielny J.M. (Eds.), Springer-Verlag, Berlin, p. 822–864, 2004.

[5] OSTAPKOWICZ P., Leak Location for Liquid Transmission Pipelines using Gradient-type Method - Case Study, *Pomiary Automatyka Kontrola – Measurement Automation and Monitoring*, vol. 57, no. 11, p. 1311–1316, 2011.

[6] OSTAPKOWICZ P., Leak Detection in Liquid Transmission Pipelines using Simplified Pressure Analysis Techniques Employing a Minimum of Standard and Non-standard Measuring Devices, *Engineering Structures*, vol. 113, p. 194–205, 2016.

[7] OSTAPKOWICZ P., BRATEK A., Possible Leakage Detection Level in Transmission Pipelines using Improved Simplified Methods, *Eksploatacja i Niezawodność – Maintenance and Reliability*, vol. 18, no. 3, p. 469–480, 2016.

[8] OSTAPKOWICZ P., BRATEK A., Leak detection in liquid transmission pipelines during transient state related to a change of operating point, in: *Advanced and Intelligent Computations in Diagnosis and Control,* Kowalczuk Z. (Ed.), Springer International Publishing, p. 253–265, 2016.

[9] SIEBERT H., ISERMANN R., Leckerkennung und Lokalisierung bei Pipelines durch on-line Korrelation mit einen Prozesrechnes, *Regelungstechnik*, vol. 25, no. 3, p. 69–74, 1977.

[10] SOBCZAK R., A Liquid Leak Location Gradient-type Method for Pipelines, *Przemysł Chemiczny (Chemical Industry)*, vol. 81, no. 10, p. 651-655, 2017.

[11] SOWINSKI J., DZIUBINSKI, M., Analysis of the Impact of Pump System Control on Pressure Gradients during Emergency Leaks in Pipelines, in: *10th Conference on Interdisciplinary Problems in Environmental Protection and Engineering (EKO-DOK)*, Polanica Zdroj, April 16-18, 2018.

[12] TURKOWSKI M., BRATEK A., SLOWIKOWSKI M., Methods and Systems of Leak Detection in Long Range Pipelines, *Journal of Automation, Mobile Robotics & Intelligent Systems*, vol. 1, no. 3, p. 39–46, 2007.

DOI: 10.24427/978-83-66391-87-1_12

Yaroslav SOKOLOVSKYY[1], Oleksiy SINKEVYCH[1],
Roman VOLIANSKYI[2], Ihor KAPRAN[1]

12. DEVELOPMENT SOFTWARE FOR STUDY THE WOOD DRYING CHAMBER BY USING A THREE-DIMENSIONAL MATHEMATICAL MODEL BASED ON CELLULAR AUTOMATA

The paper describes the study of the drying processes of capillary-porous materials by using the CAD model of wood drying chamber. The study involves the determination of temperature and humidity in the stack of dried wood by using cellular automata. To accomplish this task, we developed a three-dimensional mathematical model of heat transfer of wood in the drying process. In order to use this mathematical model in practice, we described the ways of representing the CAD model in the form of multidimensional arrays whose elements are 3D cubes, as well as special schemes of the relation between the edges of these 3D cubes. This representation allows us to make the most effective use of the developed mathematical model, which is described by an interconnected system of partial differential equations in time derivatives and spatial coordinates. Also in this paper, the results of the calculations in the form of graphs of change in the temperature and humidity of the stack of dried wood according to time iterations are shown. In order to take simpler results, we developed a radial basis artificial neural network.

12.1. INTRODUCTION

This type of work involves modeling and investigating methods of drying wood in forestry chambers. The object of the study in this case is aerodynamic processes. To calculate the parameters of the wood drying agent, SolidWorks Flow Simulation software application will be used with the theory of cellular automata. In the second case, it is supposed to represent the investigated CAD model in 2D von Neumann neighborhoods. In this work, we also develop software that is based on well-designed algorithms using the

[1] National Forestry University of Ukraine, Ukraine
[2] Dniprovsk State Technical University, Ukraine

SolidWorks API. In addition, we develop a radial basis artificial neural network that will determine the parameters of the wood drying agent in a given face of the selected 3D cube and at a given point in time.

12.2. CAD MODEL AND ITS PRESENTATION IN 2D NEIGHBORHOOD OF VON NEUMANN

12.2.1. CAD MODEL OF THE CHAMBER

This paper investigates the CAD model of a wood drying chamber that we previously designed in SolidWorks environment. This CAD model consists of several components, including walls, doors and ceiling of the wood drying chamber, stacked lumber, humidifying nozzles, water heaters and axial fans. All components are combined into one large assembly (Fig. 12.1).

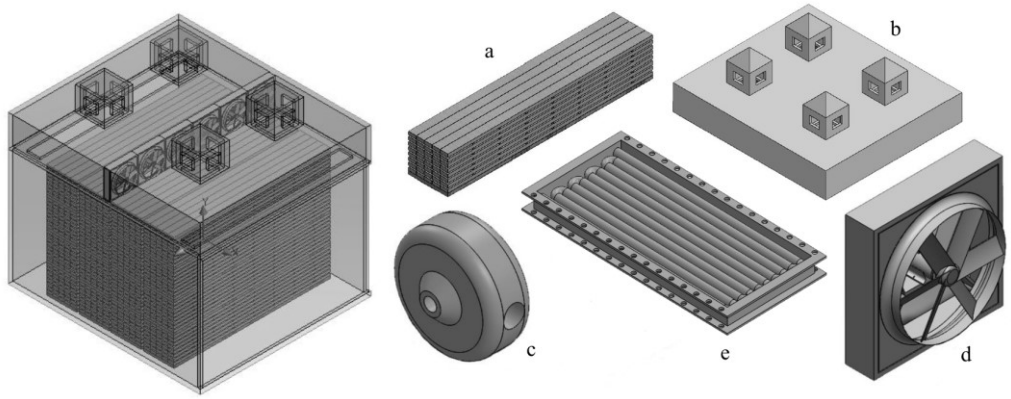

Fig. 12.1. Investigated CAD model in SolidWorks environment (a – stack of lumber; b – ceiling of the drying chamber; c – moisturizing nozzle; d – axial fan; e – water heater)

In total, we can have five types of water heaters, humidifying nozzles and axial fans. The choice of the type of equipment required depends directly on the physical dimensions of the wood drying chamber. Various types of equipment differ in geometric dimensions, capacity heater, the maximum volume of air that passes per minute and other.

The basic geometric dimensions and drawings of moisturizing nozzles used in this CAD model of the wood drying chamber are shown in Figure 12.2 and characteristics of water heaters and axial fans shown in Figure 12.3.

In this paper, the focus will be on the stacks of lumber, for which we developed a corresponding three-dimensional mathematical model of heat transfer of wood in the drying process [1].

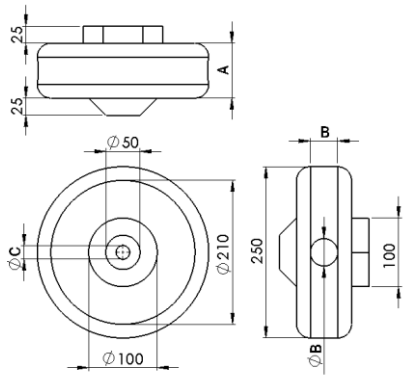

Type	A, mm	B, mm	C, mm
AN#1	60	30	10
AN#2	70	35	15
AN#3	80	40	20
AN#4	90	45	25
AN#5	100	50	30

Fig. 12.2. Characteristics of moisturizing nozzles

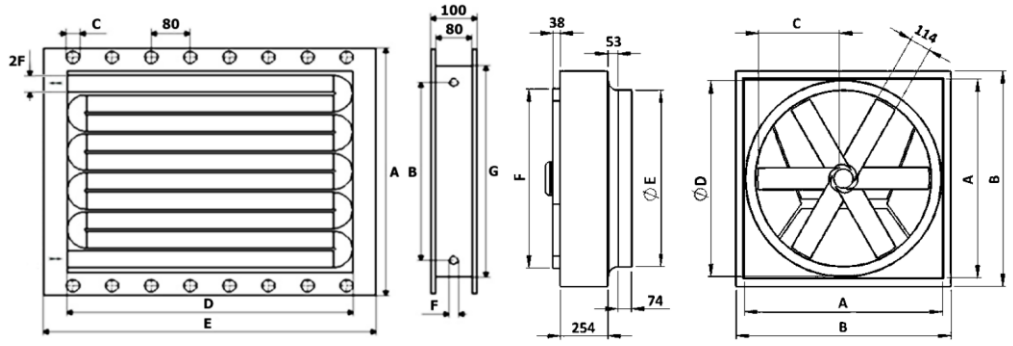

Type	A, mm	B, mm	C, mm	D, mm	E, mm	F, mm	G, mm	N
DRH#1	528	375	26	602	680	18	450	16
DRH#2	555	402	26	730	808	19	477	20
DRH#3	582	429	26	858	935	20	504	24
DRH#4	609	456	26	1014	1092	21	531	28
DRH#5	636	483	26	1239	1316	22	558	32

Type	A, mm	B, mm	C, mm	D, mm	E, mm	F, mm
VO#1	654,10	743	232,2	638,9	538,5	652,5
VO#2	754,10	843	282,2	738,9	638,5	752,5
VO#3	854,10	943	332,2	838,9	738,5	852,5
VO#4	954,10	1043	382,2	938,9	838,5	952,5
VO#5	1054,10	1143	432,2	1038,9	938,5	1055,5

Fig. 12.3. Drawings and characteristics of axial fans and water heaters

12.2.2. MODEL IN 2D NEIGHBORHOOD OF VON NEUMANN

To study the proposed CAD model of a wood drying chamber by using cellular automata, it is necessary to present it in the form of 2D neighborhood von Neumann 1st order. In Fig. 12.4, an example of a graphical breakdown of one stack of lumber is shown where it is unfolding in 2D neighborhood von Neumann [2].

In a similar way, all existing components of the CAD model of the wood drying chamber are broken down. In order to use cellular automata to investigate the parameters of the wood drying agent in the CAD model under study, in addition to splitting it into 3D cubes, it is also necessary to develop links between these 3D cubes. For this task, we used the connections on the tangent faces of different 3D cubes. Fig. 12.5 shows a general view of making such connections using the example of one of the lumber [3].

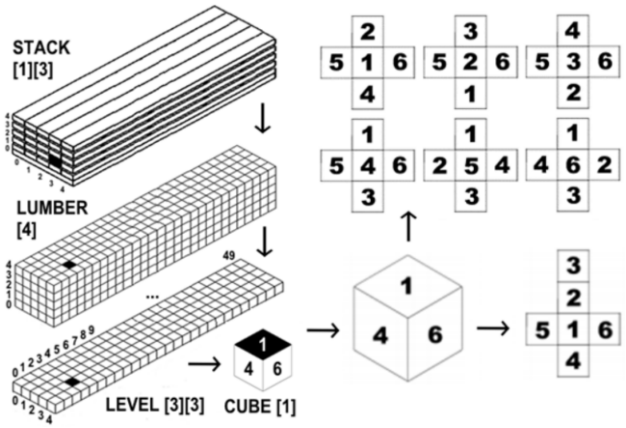

Fig. 12.4. View of a graphical breakdown of a stack of lumber

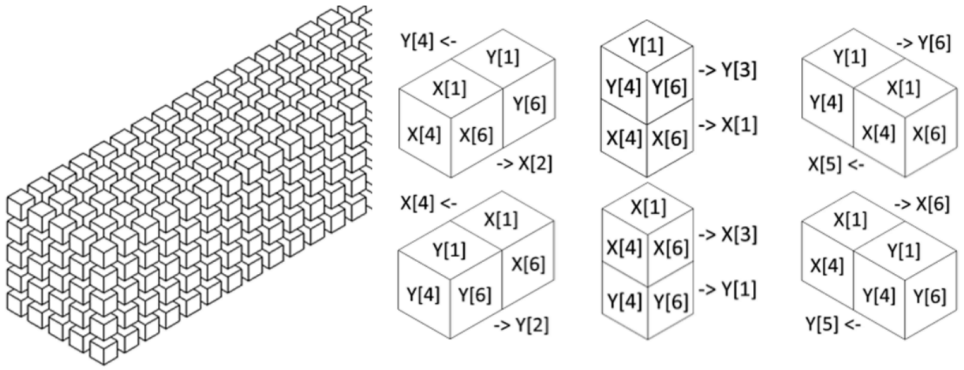

Fig. 12.5. The process of making connections between adjacent 3D cubes

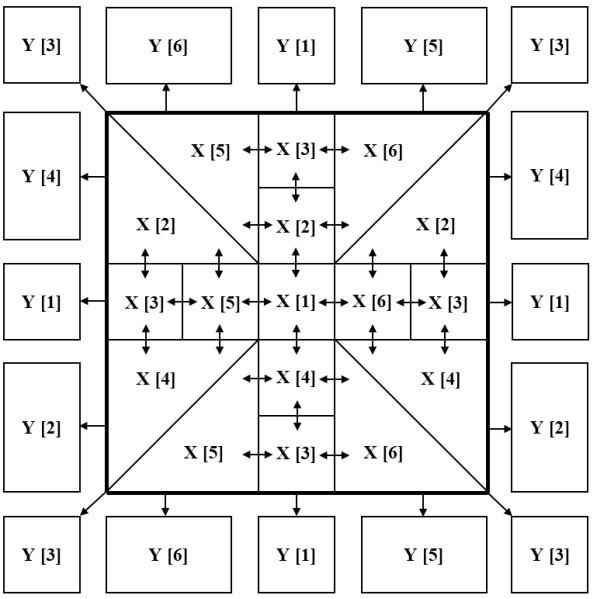

Fig. 12.6. The scheme of the relationship of the faces between two adjacent 3D cubes

With a graphical way of making connections between adjacent 3D cubes, we developed an appropriate diagram of the relationship between all faces of two adjacent 3D cubes (Fig. 12.6). The notations *X* and *Y* are two adjacent 3D cubes, and the numbers adjacent to them are responsible for the faces of this 3D cubes [4].

12.3. DEVELOPMENT OF 3D MATHEMATICAL MODEL OF HEAT TRANSFER IN THE DRYING PROCESS

12.3.1. DESCRIPTION OF THE DEVELOPED MATHEMATICAL MODEL

To determine the parameters of the wood drying agent, a three-dimensional mathematical model of heat transfer of wood in the drying process was constructed. This three-dimensional model is described by an interconnected partial differential system of partial time derivatives and spatial coordinates and has the following form

$$\begin{cases} c\,\rho\,\dfrac{\partial T_i}{\partial t} = \lambda_1 \dfrac{\partial^2 T_i}{\partial x^2} + \lambda_2 \dfrac{\partial^2 T_i}{\partial y^2} + \lambda_3 \dfrac{\partial^2 T_i}{\partial z^2} + \varepsilon\,\rho_0\, r \dfrac{\partial U_i}{\partial t}, \\ \dfrac{\partial U_i}{\partial t} = a_1 \dfrac{\partial^2 U_i}{\partial x^2} + a_2 \dfrac{\partial^2 U_i}{\partial y^2} + a_3 \dfrac{\partial^2 U_i}{\partial z^2} + a_1 \delta \dfrac{\partial^2 T_i}{\partial x^2} + a_2 \delta \dfrac{\partial^2 T_i}{\partial y^2} + a_3 \delta \dfrac{\partial^2 T_i}{\partial z^2}, \end{cases} \quad (12.1)$$

where $(x, y, z, t) \in \Omega$, domain $\Omega = \{0 \le x, y, z \le l; 0 \le t \le \tau\}$, $T_i = T_i(x, y, z, t)$ – temperature, $U_i = U_i(x, y, z, t)$ – moisture content, c – specific heat, ρ – density, i – serial number of 3D cube, t – time, x, y, z – coordinates of the 3D cube location, $\{\lambda_1, \lambda_2, \lambda_3\}$ – coefficients of thermal conductivity, ε – phase transition coefficient, ρ_0 – basic density, r – specific heat of vaporization, $\{a_1, a_2, a_3\}$ – humidity coefficients, δ – thermo gradient coefficient.

Initial conditions that relate to a period of constant drying rate of wood have also been developed as follows

$$T_i(0, x, y, z) = T_0(x, y, z), \qquad U_i(0, x, y, z) = U_0(x, y, z). \quad (12.2)$$

In general, the developed mathematical model can be implemented by using finite element methods or differences.

12.3.2. BOUNDARY CONDITIONS ACCORDING TO THE CREATED 3D CUBES

For this three-dimensional model, we developed boundary conditions of the third kind, which correspond to each of the faces of the created 3D cubes. Such a representation makes it possible to apply this mathematical model in the study of the parameters of the agent of drying wood by using cellular automata [5].

Generally, the boundary conditions developed are as follows:

$$\begin{cases} \lambda_j \dfrac{\partial T_i}{\partial n}\Big|_{\{x,y,z\}\in\partial\Omega} + \rho_0(1-\varepsilon)\cdot\beta\left(U_i\Big|_{\{x,y,z\}\in\partial\Omega} - U_p\right) = \alpha\left(T_i\Big|_{\{x,y,z\}\in\partial\Omega} - T_c\right), \\ a_j\delta\dfrac{\partial T_i}{\partial n}\Big|_{\{x,y,z\}\in\partial\Omega} + a_j\dfrac{\partial U_i}{\partial n}\Big|_{\{x,y,z\}\in\partial\Omega} = \beta\left(U_p - U_i\Big|_{\{x,y,z\}\in\partial\Omega}\right), \end{cases} \quad (12.3)$$

where j – index ($j = 1, 2, 3$), α – coefficient of heat exchange, β – moisture exchange coefficient, l – the length of each face (all faces are equal to each other), $U_p(T_c, \varphi)$ – equilibrium humidity, T_c – ambient temperature, φ – relative humidity.

12.4. SOFTWARE DEVELOPMENT FOR RESEARCH OF CAD MODEL BY USING CELLULAR AUTOMATA

12.4.1. GRAPHICAL INTERFACE

To study the CAD model, a software in the Microsoft Visual Studio 2010 application using programing language C# was developed. This program has several tabs, one of which is responsible for working with cellular automata (Fig. 12.7).

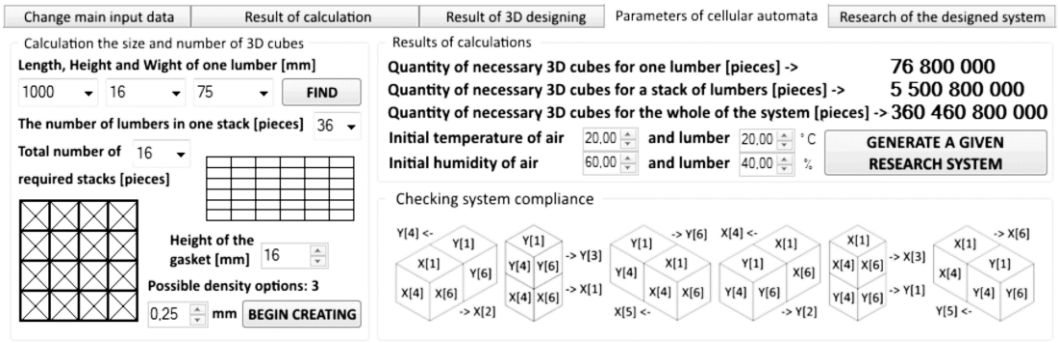

Fig. 12.7. View the tab of the developed software for working with cellular automata

With this software, the user can enter the size of the lumber, their number in one stack and the total number of stacks. Based on this data, the program can generate a three-dimensional array of data, the size of which will depend on the separation density of the studied CAD model, which is entered by the user. By manipulating the size of the separation density into 3D cubes, the user can get the most accurate calculation results [6].

12.4.2. UML DIAGRAMS

To work with the created three-dimensional array, we developed 12 classes, which can move objects of different classes among themselves. In this regard, instances of the developed classes have associative relationships, which are shown in the developed class diagram (Fig. 12.8).

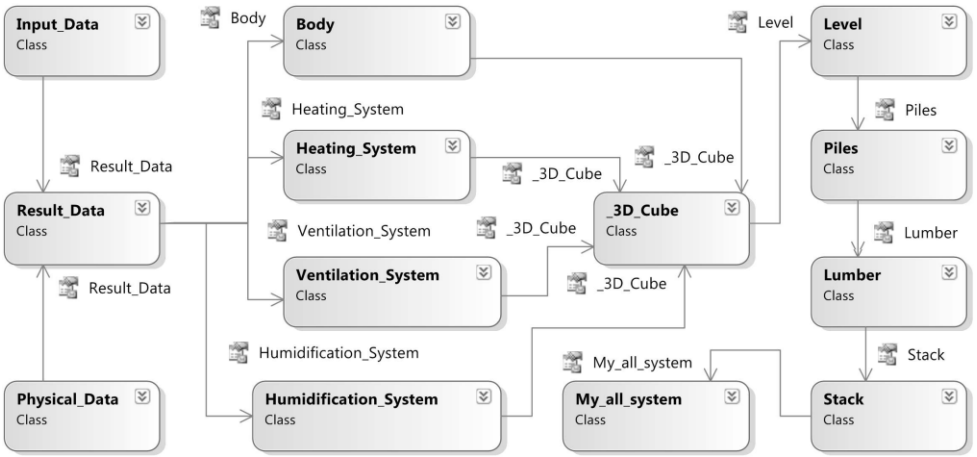

Fig. 12.8. The appearance of a class diagram

The sequence diagram (Fig. 12.9) shows the interaction of objects of the developed classes with each other. This diagram shows only those classes that are directly involved in investigating the parameters of a wood drying agent by using cellular automata [7].

To better understand all the functionality of the developed software, you can use the diagram of use (Fig. 12.10).

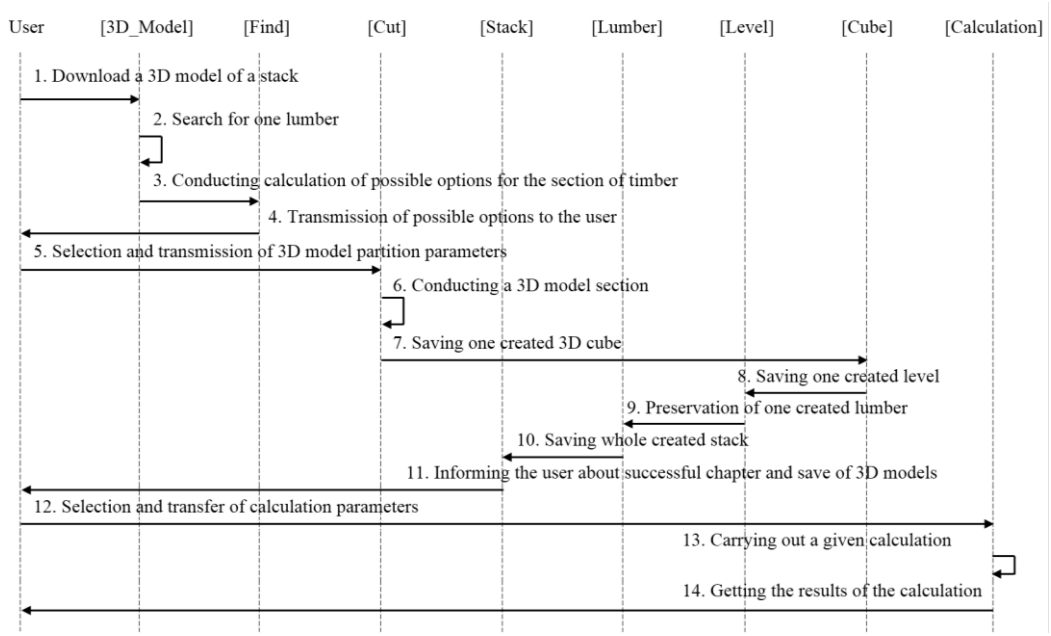

Fig. 12.9. The appearance of a sequence diagrams

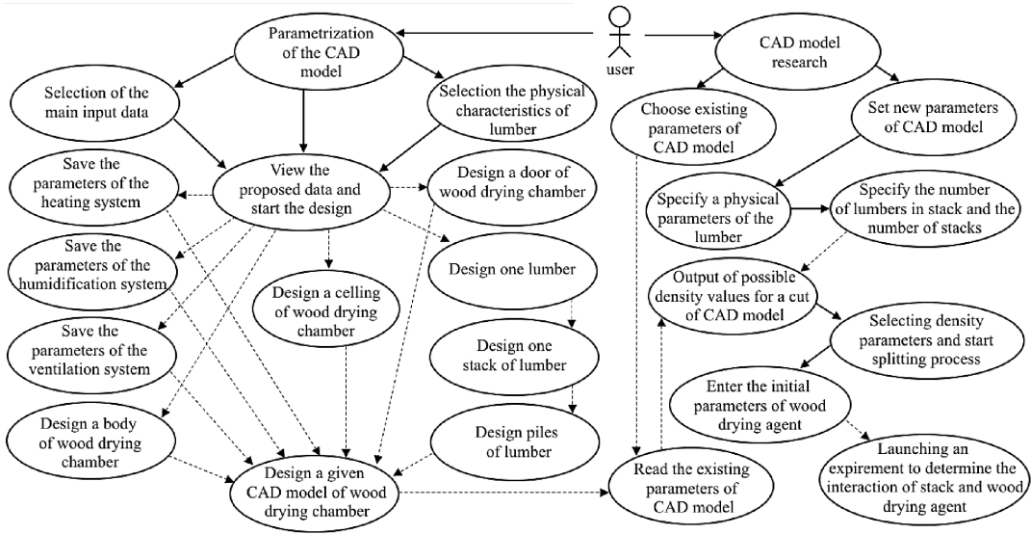

Fig. 12.10. The appearance of a using diagram

12.5. CALCULATION RESULTS

12.5.1. EXPERIMENT IN SOLIDWORKS FLOW SIMULATION

To determine the change parameters of agent timber, an experiment using SolidWorks Flow Simulation was carried out. As a result of this experiment, we obtained the numerical values of temperature and relative humidity of the air masses in the wood drying chamber. In addition, we obtained a trajectory of motion of air masses, based on which the surface of change of temperature and relative humidity in the upper layers of the CAD model were taken.

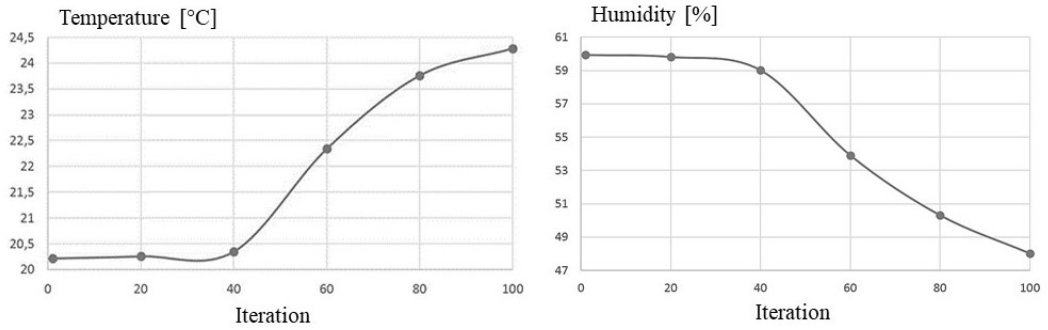

Fig. 12.11. Graph of temperature and humidity in wood

As a result of 100 iterations, we obtained average numerical values of the temperature and humidity. Based on these data, the corresponding graphs (Fig. 12.11) were constructed. These graphs show that the *Y* axis is responsible for the average values and the *X* axis for the

iteration numbers. Based on the obtained data, we constructed graphs of temperature and relative humidity changes of the wood drying agent in space and time (Fig. 12.12).

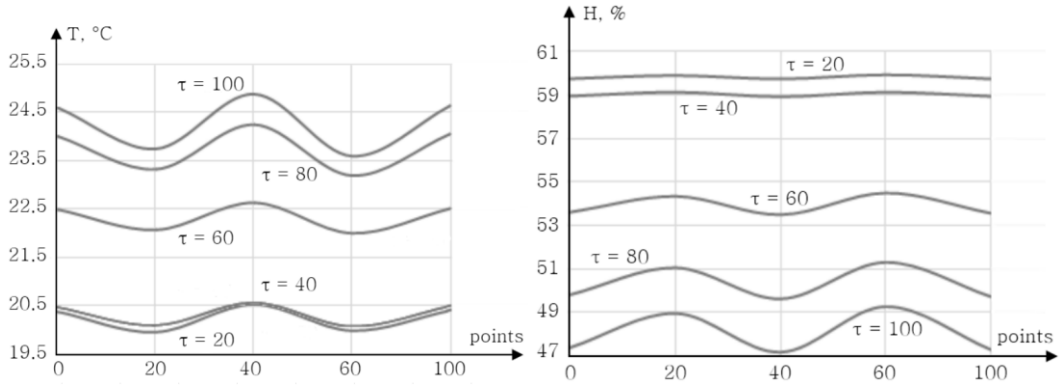

Fig. 12.12. Graphs of temperature and relative humidity changes in space and time

12.5.2. DYNAMIC EXPERIMENT BASED ON 3D CUBES

Therefore, at the beginning of the experiment, we have a huge number of 3D cubes whose faces have initial values. Next, we select one 3D cube, which in the course of the experiment will have a change in the numerical values of its faces according to the developed mathematical model. We will call this 3D cube *X*1 and denote the numbers of its faces in square brackets [8].

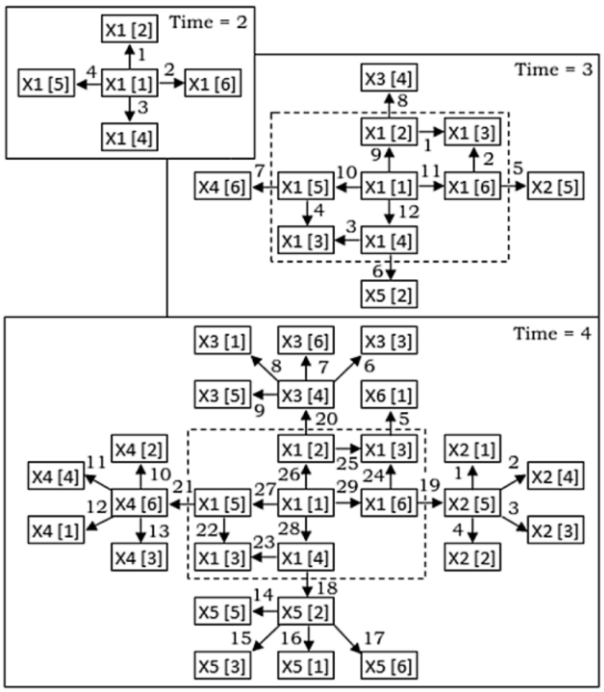

Time	0	1	2	3	4
X1 [1]	20,00	20,03	20,05	20,09	20,12
X1 [2]	20,00	20,00	20,03	20,05	20,09
X1 [3]	20,00	20,00	20,00	20,03	20,05
X1 [4]	20,00	20,00	20,03	20,05	20,09
X1 [5]	20,00	20,00	20,03	20,05	20,09
X1 [6]	20,00	20,00	20,03	20,05	20,09
X2 [1]	20,00	20,00	20,00	20,00	20,03
X2 [2]	20,00	20,00	20,00	20,00	20,03
X2 [3]	20,00	20,00	20,00	20,00	20,03
X2 [4]	20,00	20,00	20,00	20,00	20,03
X2 [5]	20,00	20,00	20,00	20,03	20,05
X3 [1]	20,00	20,00	20,00	20,00	20,03
X3 [3]	20,00	20,00	20,00	20,00	20,03
X3 [4]	20,00	20,00	20,00	20,03	20,05
X3 [5]	20,00	20,00	20,00	20,00	20,03
X3 [6]	20,00	20,00	20,00	20,00	20,03
X4 [1]	20,00	20,00	20,00	20,00	20,03
X4 [2]	20,00	20,00	20,00	20,00	20,03
X4 [3]	20,00	20,00	20,00	20,00	20,03
X4 [4]	20,00	20,00	20,00	20,00	20,03
X4 [6]	20,00	20,00	20,00	20,03	20,05
X5 [1]	20,00	20,00	20,00	20,00	20,03
X5 [2]	20,00	20,00	20,00	20,03	20,05
X5 [3]	20,00	20,00	20,00	20,00	20,03
X5 [5]	20,00	20,00	20,00	20,00	20,03
X5 [6]	20,00	20,00	20,00	20,00	20,03
X6 [1]	20,00	20,00	20,00	20,00	20,03

Fig. 12.13. Performing 0-4 iterations of the experiment when changing the temperature values

In the course of the experiment, the faces of *X*1 will transfer the change of their numerical values to adjacent faces of other 3D cubes, which we will call *XN*, where *N* is the ordinal number of 3D cubes. To determine the number of tangent faces in adjacent 3D cubes, we can use the developed scheme of relations, which is shown in Fig. 12.6.

An example of performing this experiment, when selecting the initial first face for *X*1 is shown in Fig. 12.13. Since the experiment involves a large number of iterations, we have shown only the first four. At the same time, we consider that at the first and second iterations (time = 1, 2) the numerical values of only the eigenvalues for *X*1 are realized. Beginning with the third iteration (time = 3), we can observe the process of transmitting numerical values for the faces of neighboring *XN*. In addition, this figure shows the temperature values for all involved faces of the selected 3D cubes [9].

12.5.3. USING A RADIALLY BASED ARTIFICIAL NEURAL NETWORK

In order to obtain numerical values in any 3D cube and at any time, we have created a radial basis artificial neural network. This network contains three layers. The first conventional input layer distributes the sample data for the first layer of weights.

The second layer contains hidden neurons with radially symmetric activation function. The third layer of the network is the source. Such a radial basis network with R inputs is presented in Fig. 12.14.

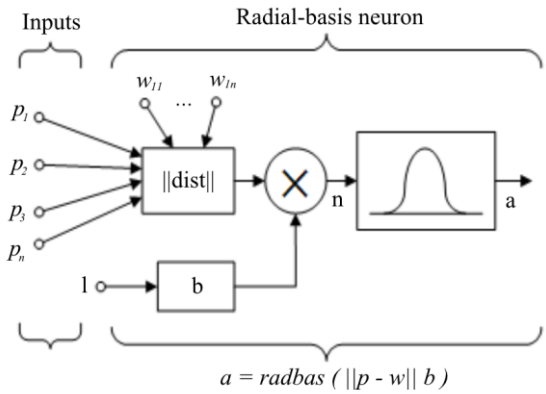

Fig. 12.14. Radial basis artificial neural network

The input of the activation function for a given artificial neural network is defined as the modulus of difference of the vector of weights w and the vector of input p multiplied by the displacement b. This function will have a maximum equal to one with zero input. As the distance between the vectors w and p decreases, the output of the radial basis function will increase. Therefore, the radial basis neuron will act as an indicator that generates a unit value when the input p is identical to the weight vector w. The offset b can adjust the sensitivity of neurons *radbas*.

In order to take full advantage of this artificial neural network, it is necessary to have arrays of the input training sample. These arrays are obtained by performing the first 100 iterations of the experiment. In general, we have the following arrays:

- Input - coordinates of the 3D cube, time, number of its face, type sought;
- Temperature - temperature values;
- Humidity - humidity values.

In total, each of the training sample arrays contain at least 600 datasets. These arrays are shown in Fig. 12.15.

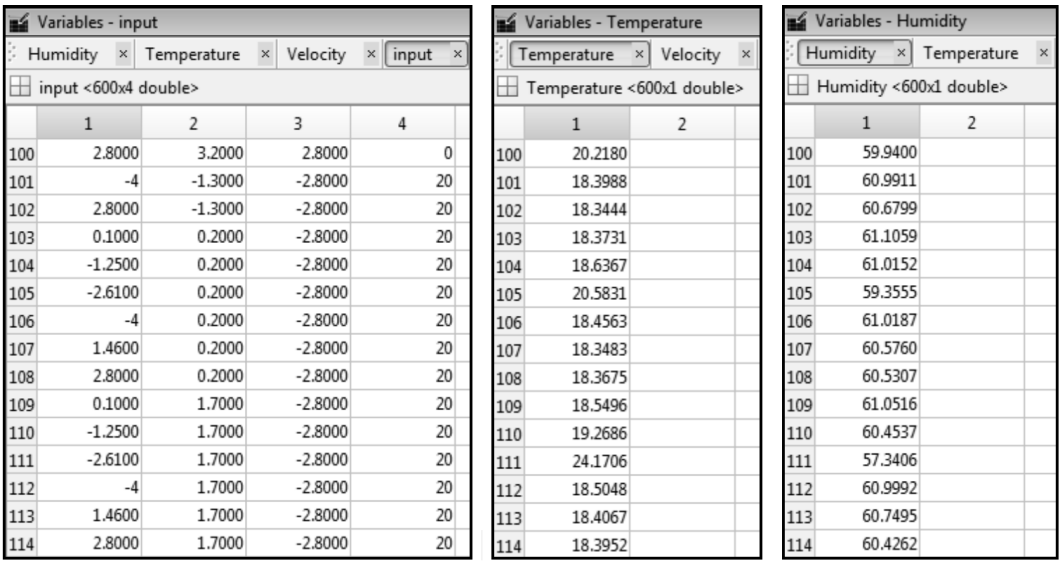

Variables - input

Humidity | Temperature | Velocity | input

input <600x4 double>

	1	2	3	4
100	2.8000	3.2000	2.8000	0
101	-4	-1.3000	-2.8000	20
102	2.8000	-1.3000	-2.8000	20
103	0.1000	0.2000	-2.8000	20
104	-1.2500	0.2000	-2.8000	20
105	-2.6100	0.2000	-2.8000	20
106	-4	0.2000	-2.8000	20
107	1.4600	0.2000	-2.8000	20
108	2.8000	0.2000	-2.8000	20
109	0.1000	1.7000	-2.8000	20
110	-1.2500	1.7000	-2.8000	20
111	-2.6100	1.7000	-2.8000	20
112	-4	1.7000	-2.8000	20
113	1.4600	1.7000	-2.8000	20
114	2.8000	1.7000	-2.8000	20

Variables - Temperature

Temperature | Velocity

Temperature <600x1 double>

	1	2
100	20.2180	
101	18.3988	
102	18.3444	
103	18.3731	
104	18.6367	
105	20.5831	
106	18.4563	
107	18.3483	
108	18.3675	
109	18.5496	
110	19.2686	
111	24.1706	
112	18.5048	
113	18.4067	
114	18.3952	

Variables - Humidity

Humidity | Temperature

Humidity <600x1 double>

	1	2
100	59.9400	
101	60.9911	
102	60.6799	
103	61.1059	
104	61.0152	
105	59.3555	
106	61.0187	
107	60.5760	
108	60.5307	
109	61.0516	
110	60.4537	
111	57.3406	
112	60.9992	
113	60.7495	
114	60.4262	

Fig. 12.15. The appearance of the training sample arrays

With a training sample, we have created a feature that allows the use of artificial neural network. This *Mynetwork* feature is as follows:

```
Function Result = Mynetwork (x, y, z, time, number, type, temperature, humidity)
    If type = = 'T'
        Net = newrbe (input', temperature');
    End
    If type = = 'H'
        Net = newrbe (input', humidity');
    End
Result = sim (net, [x, y, z, number, time]');
```

As a result of using this function, we obtain the required numerical value according to the given coordinates and the face number of the desired 3D cube [10]. The use of the developed *Mynetwork* function is as follows:

```
>>   res = Mynetwork (21, 18, 16, 214, 1, 'T', Temperature, Humidity)
res = 24.9542
>>   res = Mynetwork (21, 18, 16, 214, 1, 'H', Temperature, Humidity)
res = 61.0484
```

From this example, you can see that x=21, y=18, z=16, time=214 second and the face of select 3D cube is equal one. In addition, it can been seen that in the first case, we selected the temperature and in the second case, we selected the relative humidity. As a result of using developed *Mynetwork* function, the artificial neural network showed the following results: $T = 24.95°C$ and $H = 61.05\%$.

12.6. CONCLUSIONS

In this work, we performed a series of experiments in SolidWorks Flow Simulation, based on which we determined the parameters of the wood drying agent. In addition, to determine the parameters of a wood drying agent by using the theory of cellular automat, we developed a mathematical model. To use this theory, we presented a CAD model in the form of 2D Von Neumann neighborhoods in 1-order. Based on the obtained data, we got the graphs of aerodynamic flows in the CAD model. In addition, we developed and tested an artificial neural network that determine the temperature and humidity of any face of the selected 3D cube at a given point in time.

REFERENCES

[1] PROHOROENKO V. P., *SolidWorks. Practical guidance*, Binom-Press, 448 p., 2004.
[2] VON NEUMANN J., *Theory of Self-Reproducing Automata*, Univ. Illinois Press, 742 p., 1966.
[3] SOKOLOVSKYY Y., SINKEVYCH O., Software for Automatic Calculation and Construction of Chamber Drying Wood and its Components, in: *XII International Conference MEMSTECH 2016*, Lviv, Ukraine, Publishing House Lviv Polytechnic, p. 209-213, 2016.
[4] DUDAREVA N., ZAGAYKO S., *SolidWorks 2009 on examples*, Sank-Petersburg, BHV, 530 p., 2009.
[5] BILEY P.V., *Theoretical foundations of thermal processing and drying of wood*, Kyiv, AGE, 360 p., 2005.
[6] SOKOLOVSKYY Y., SINKEVYCH O., Calculation of Drying Agent in Drying Chambers, in: *XIV International Scientific and Technical Conference CADSM 2017*, Ukraine, Publisher PE Vezha i Ko, p. 27-31, 2017.
[7] ALBAHARI J., ALBAHARI B., *C# 5.0. Directory. Full description language*, Williams, p. 1008, 2013.
[8] TOFFOLI T., MARGOLUS N., *A Cellular Automata Machine*, World, 280 p., 1991.
[9] SOKOLOVSKYY Y., SINKEVYCH O., Software and algorithmic support for representation of CAD models in 2D von Neumann neighborhood, in: *Proceedings of International CEUR Workshop ACIT 2018*, vol. 2300, Cesce Budejovice, Czech Republic, p. 215-218, 2018.
[10] WOLFRAM S., *A new kind of science*, Champaign, Wolfram Media Inc., 1197 p., 2002.

DOI: 10.24427/978-83-66391-87-1_13

Tomasz HUŚCIO[1]

13. DEVELOPMENT OF CONTROL SYSTEM FOR CENTRAL HEATING BOILER

As a result of legislative action in the European Union and its individual member states, the demand for high-quality equipment has grown in recent years with respect to the individual heating sector, particularly from the perspective of high energy efficiency and environmental protection, as well as convenience and inexpensiveness of operation.

In 2013, the European Commission adopted a Clean Air Policy Package for Europe [1]. This package of measures aims to achieve full compliance with existing air quality legislation by 2020 and further improve Europe's air quality by 2030 and thereafter [2].

The gradual withdrawal of coal from energy production necessitates the application of low-emissions sources of energy production, such as wind and solar energy, water (rivers, tides and sea waves), biomass, new nuclear power plants, as well as extension of the lifetime of existing sources that can operate in a safe manner [3].

The high level of air pollution caused by solid fuel combustion installations, particularly those with outdated, traditional designs, makes it necessary to design and implement heating systems based on renewable energy sources and heating systems with modern central heating boilers. The International Energy Agency (IEA) forecasts that, in 2040, 60% of heat will be generated from renewable energy sources, i.e. pellet in boilers and furnaces, biogas, biomethane and biofuels [4, 5].

Article [6] shows a system based on solar thermal collectors, a biomass boiler and an innovative reversible hybrid heat pump/ORC concept for addressing heating, cooling and domestic hot water demand of residential buildings. The main findings from the SDEWES conferences of 2021 within the field of renewable energy and the systems analyses used to design complex renewable energy systems are presented in [7]. The computer model was developed in order to build a system for process control in the building's heating system with installation using renewable energy sources – a solar photovoltaic panel, a HHO gas generator and a pellet boiler is presented in [8].

The implementation of the anti-smog act is to lead to improvement of air quality in individual regions of Poland. This is an amendment to the Environmental Protection Law

[1] Bialystok University of Technology, Poland

(art. 96) [9]. The provisions of this act are to contribute to improvement of our health and enhance our living standard. The anti-smog act indicates the types of heating equipment approved for use and the types of fuels prohibited from use, in short, what can be burned and in what. In the case of buildings heated with a solid-fuel boiler (coal or pellet), the anti-smog act permits the use of class 5 flue gas purity boilers, i.e. those that have a certificate issued in compliance with standard PN-EN 303-5:2012 [10] or boilers meeting the requirements of eco-design according to the Regulation of the European Commission [11].

Existing heating systems must be continuously modified and optimized to meet technological requirements concerning the efficiency of using the energy of fuels in burners and the affordability of implementing new solutions.

In this chapters the results of work involving the development of a control system for a modern central heating boiler utilizing a renewable energy source – biomass are presented and discussed.

13.1. HEATING SYSTEM WITH CENTRAL HEATING BOILER UTILIZING A RENEWABLE ENERGY SOURCE – BIOMASS

13.1.1. DEVELOPMENT OF A CENTRAL HEATING AND DOMESTIC HOT WATER INSTALLATION SCHEMATIC

A simplified schematic diagram of the installation, with two central heating circulations (circulation 1, circulation 2), domestic hot water circulation, and with additional floor heating, is presented in Fig. 13.1. To improve the diagram's readability, the protective installation in the form of collector pipes, safety pipes, etc. is not shown.

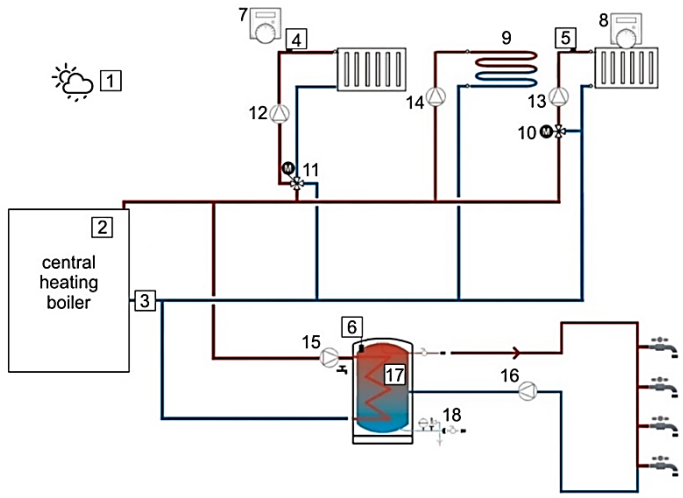

Fig. 13.1. Schematic diagram of central heating and domestic hot water installation [14]

The following components are marked in Fig. 13.1: external temp. sensor (1), boiler water temp. sensor (2), temp. sensor for water returning from installation to boiler (3), temp. sensors of central heating supply in loop 1 (4), temp. sensors of central heating supply in loop 2 (5), domestic hot water temperature sensor (6), room regulator 1 (7), room regulator 2 (8), floor heating (9), 3-way valve with drive (10), 4-way valve with drive (11), circulating pump of central heating loop 1 (12), circulating pump of central heating loop 2 (13), circulating pump of floor heating loop (14), domestic hot water circulating pump 1 (15), domestic hot water circulating pump 2 (16), domestic hot water tank (17), cold water supply from network (18).

The heating installation should be open, i.e. must be equipped with a collector vessel as well as with: safety, collector, overflow, signaling and venting pipes. The collector vessel, safety pipes, collector pipe, signaling pipe and overflow pipe must be placed in a space where the air temperature is greater than zero. If heating loops 1 and 2 and the domestic hot water circulation are active in the installation and equipped, accordingly, with circulating pumps (12), (13), (14), (15), then the appropriate temperature sensors (4), (5) and (6) must also be installed. Temp. sensors of central heating supply in loop 1 (4) and loop 2 (5) are indispensable if the controller is to support the actuator of the mixing valve for the given loop. Optionally, room regulators (7, 8) make it possible to maintain a set temperature in rooms, as desired by the residents.

13.1.2. CENTRAL HEATING BOILER UTILIZING A RENEWABLE ENERGY SOURCE – BIOMASS

The central heating boiler is presented in Fig. 13.2. The boiler consists of two main components standing next to each other: the boiler proper (1) and fuel tank (2) with a unit of feeders. The application of two feeders made it possible to separate the fuel dispenser from the combustion chamber. Thanks to this, there is no possibility of flashback to the fuel dispenser, and moreover, it does not have to be tightly closed. The main feeder (3) is a spring revolving slowly in a pipe, moving fuel from the lower part of the dispenser upward, from where it falls through pipe (4) onto a second feeder (worm), which feeds fuel to the combustion chamber.

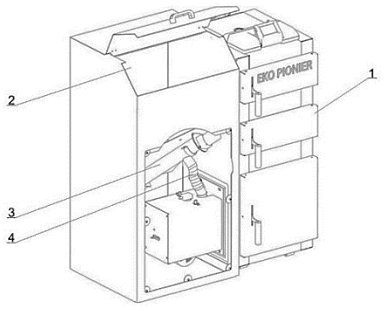

Fig. 13.2. Appearance of boiler with removed guard of feeders [14]

Figure 13.3 presents the cross-section of the central heating boiler. The following are marked in Fig. 13.3: burner inlet (1), insulation (2), water jacket (3), flue gas swirler (4), exterior housing (5), exhaust fan (6), water temperature sensor in boiler (7), boiler controller (8), small door for boiler cleanout (9), large door to combustion chamber (10).

The boiler is equipped with two fans: an intake blower, supplying the appropriate amount of air to the combustion chamber, and exhaust fan (6), making it possible to discharge flue gas through the furnace flue to the chimney. There are 2 holes at the top of the boiler. The hole on the right side (viewing from the front), is intended for insertion of the boiler water temperature sensor (9), and the hole on the left side serves for installation of the capillary tube of the boiler's resettable thermal protection.

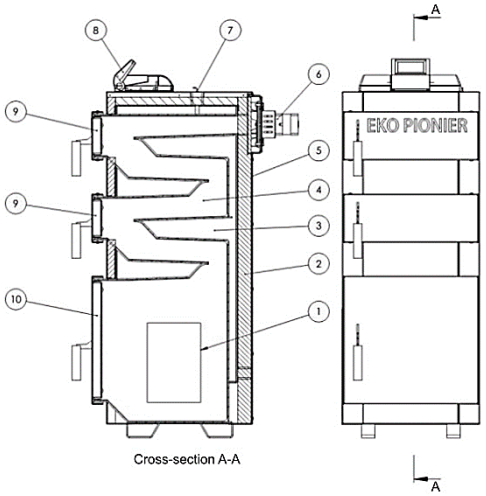

Fig. 13.3. Cross-section of the central heating boiler [14]

The flue is situated on the top rear of the boiler, with two holes: the larger one serves for fastening of the lambda sensor, and the smaller one for fastening of the flue gas temperature sensor (Fig. 13.4). The lambda sensor makes it possible to measure oxygen content in flue gas. This enables precise dosage of the fuel-air mixture at individual stages of the biomass combustion process. The flue gas temperature sensor has an additional clamping ring, preventing the sensor from being pushed into the flue.

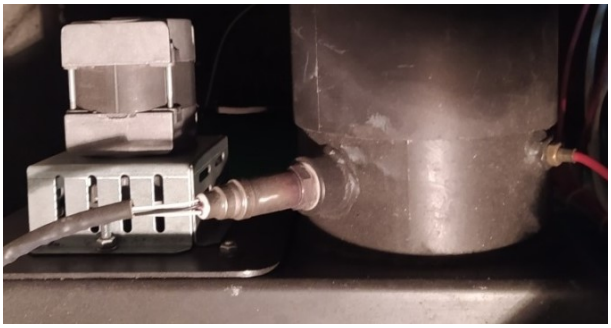

Fig. 13.4. Lambda sensor and flue gas temperature sensor

1.3. BURNER FOR CENTRAL HEATING BOILER

Figure 13.5 shows the prepared 3D model of the burner for the central heating boiler. The model was prepared using SOLIDWORKS software. The burner's principle of operation is described in works [12, 13].

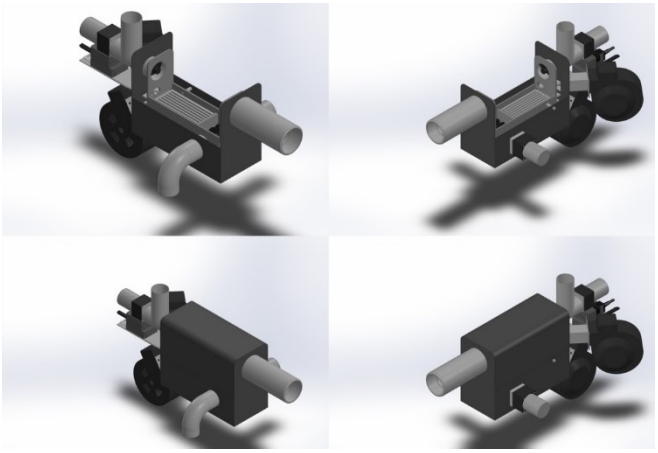

Fig. 13.5. 3D model of burner for central heating boiler

13.2. DEVELOPMENT OF CONTROL SYSTEM FOR CENTRAL HEATING BOILER

13.2.1. STAGES OF CONTROL SYSTEM DEVELOPMENT

Development of the control system for the central heating boiler was carried out according to the following stages:

- designing of control system,
- selection of appropriate equipment and software,
- preliminary preparation of PLC, HMI software for the combustion process,
- installation of automation (input automation components, controller, actuators),
- installation of indispensable cabling for communication and control of system components (fuel feeder, exhaust fan, igniter fan, igniter),
- final preparation of PLC software for the combustion process,
- analysis of the created control system's operation in the burner – boiler system,
- process optimization and necessary corrections of the PLC code,
- final preparation of human – machine interface (HMI),
- final start-up,
- tests of safety systems,
- realization of checklist and CE certification,
- development of documentation.

13.2.2. ASSUMPTIONS FOR DEVELOPMENT OF CONTROL SYSTEM FOR CENTRAL HEATING BOILER

The control system of the central heating boiler should make it possible to following assumptions.

- Automate the fuel ignition process in the burner using an electric heater (igniter) and fan generating a stream of hot air.
- Control of combustion process parameters:
  - dosing of the appropriate fuel-air mixture at individual stages of the biomass combustion process, i.e. feeding of a specific amount of fuel and supply of required portions of air from the environment to sustain biomass combustion,
  - the process of cleaning the grate situated in the gasifying chamber, which should be performed automatically at regular time intervals (cyclically).
- Constant-value (programmed) temperature regulation in individual rooms of the building, at the set level.
- Constant-value (programmed) regulation of domestic hot water temperature.
- In the case where water in the boiler reaches a temperature of 95^{o}C, the fuel (pellet) feeder and intake blower should be disconnected, and in addition, an alarm sound signal should be activated. Restart of the furnace requires the user's intervention.
- Damage to any of the temperature sensors should result in suspension or limitation of the boiler's operation and in the activation of an alarm sound signal.

13.2.3. SELECTION OF AUTOMATION COMPONENTS

Based on adopted assumptions and analysis of components of the heating system individual automation components were selected for the designed control system: input automation components (table 13.1), actuators (table 13.2) and FuzzyLogic 500 controller – Cherokee [15].

Actuators entering into the burner's equipment: intake blower, igniter, motor of ash collector feeder. Actuators entering into the boiler's equipment: exhaust fan, motor of fuel feeder. Other components of the control system, i.e. circulating pumps of central heating loops, circulating pump of floor heating loop, circulating pumps of domestic hot water, water valve actuators, mixing valve actuator, are selected depending on the sizes of central heating installation components, i.e. diameters of pipes in the hydraulic installation and the investor's budget.

Figure 13.6 presents the connections of individual input components and actuators to the terminals of the selected controller. The controller was integrated with a graphical, color and touch LCD, enabling value changes of the most important parameters and monitoring of other parameters involved in boiler operation.

According to the adopted assumption concerning protections:

- the controller controls the operation of sensors, and in the event where any sensor is damaged, the boiler's operation is suspended or limited, an interrupted sound signal is generated, and the appropriate message is displayed on the screen,

- if water temperature in the boiler exceeds 95℃, the boiler's active thermal protection will be engaged, and an interrupted sound signal will be activated. The controller sends the signal for disconnection of fuel feeders, the igniter and intake blower, thanks to which the burning process is interrupted. To restart the boiler, the RESET button on the controller's housing must be pressed.

Individual input automation components of the control system are listed in table 13.1.

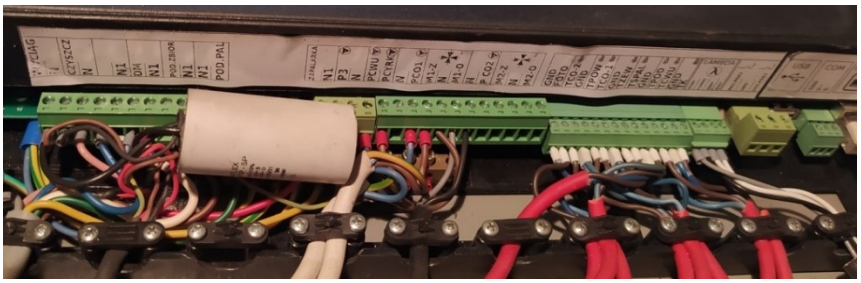

Fig. 13.6. Input and output terminals of the FuzzyLogic 500 controller – Cherokee

Table 13.1. Input automation components

Designation	Component	Installation site
TK	Boiler water temperature sensor	Boiler's jacket or point where the highest boiler water temp. is present
TCWU	Domestic hot water temperature sensor	Measuring hole of domestic hot water tank
TPOD	Feeder temperature sensor	Fastened by a band on the worm feeder in such a way that it adheres well to the surface
FOTO	Flame brightness sensor (optional)	In a special sleeve in the burner's wall
TSPAL	Flue gas temperature sensor	In the top rear part, in the flue (Fig. 13.4)
TCO1 TCO2	Central heating supply temperature sensors in loop 1 / in loop 2	Fastened by a clamping ring to outlet pipes after the pumps and valves
LAMBDA	Lambda sensor	In the top rear part, in the flue, in a special sleeve (Fig. 13.4)
TZEW	Outside temperature sensor	Fastened to the exterior wall of the building, on the north side, far from heat sources (window, door), and in such a manner, that it is not directly exposed to sunlight.
REG. POK.	Room regulator	Situate far from heat sources in the room (TV, window, heater, etc.) where the set temperature is to be maintained; according to the guidelines of the selected device's manufacturer.
TPOW	Temperature sensor of water returning to the boiler	Fastened in direct contact with the return pipe, as close to the boiler as possible, and shielded with heat-resistant foam.

Designations of individual actuators are found on the controller's terminals (Fig. 13.6) and listed in table 13.2. Components responsible for the burner's operation (fans, feeders and igniter) should be connected to points N and N1.

Table 13.2. Actuators

Designation	Component
WYCIĄG	Exhaust fan
POW. WTÓRNE	Intake blower
PODAJ. 2	Connection point for feeder found in burner
PODAJ. 1	Connection point for feeder supplying fuel directly from the tank (main feeder)
ZAP	Igniter
P3 or P. DODATK	Additional pump (e.g. for floor heating)
PCWU	Domestic hot water pump
PCYRK	Circulating pump working according to a user-defined weekly schedule
PCO1 and PCO2	Central heating pumps
M1Z and M1O M2Z and M2O	Connection points of mixing valve actuator. The digit in the description signifies the loop in which the actuator is found (1 or 2), and the letter at the end specifies the function of the connection point (Z for closing and O for opening).
N	Connection point to neutral power supply busbar
N1	Connection point to burner's neutral power supply busbar

2.4. DEVELOPMENT OF HMI

The layout of the human-machine interface (HMI) panel, enabling value changes of the most important parameters and monitoring of other parameters involved in boiler operation, is shown in Fig. 13.7. Figure 13.8 presents a touch LCD display integrated with the FuzzyLogic 500 – Cherokee controller.

a) b)

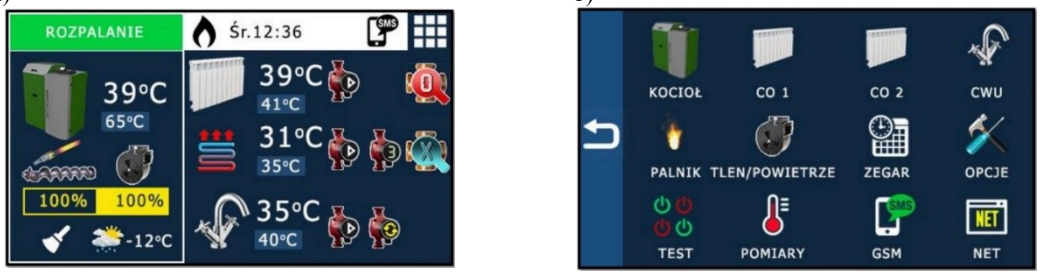

Fig. 13.7. Design of HMI panel layout: a) main screen; b) main menu [15]

a) b)

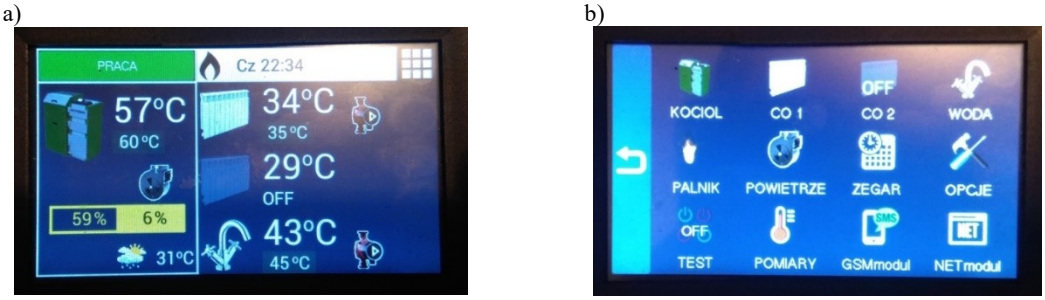

Fig. 13.8. LCD display integrated with FuzzyLogic 500 – Cherokee controller: a) main screen; b) main menu

13.3. TESTS OF THE CONTROL SYSTEM FOR CENTRAL HEATING BOILER

13.3.1. GOAL OF THE TESTS

The goal of the tests of the control system for the central heating boiler was to verify assumptions accepted at the control system designing stage. To meet this goal, the correctness of operation of the central heating boiler with the designed and developed control system was checked under normal operating conditions. Moreover, the quality of burning of pelletized biomass fuels was checked.

The heating system of the boiler integrated with the FuzzyLogic 500 – Cherokee controller [15], cooperating with the input automation components and actuators presented in section 13.2.3, was tested. The technical specifications of the tested boiler are identical to those of the EP-12 boiler [14].

13.3.2. TEST RESULTS

As a result of tests performed for set water temperatures in individual loops (central heating, domestic hot water), correct operation of the following was determined: pelletized biomass feeding system, automatic fuel ignition system, system for stoking the combustion process in the gasifying chamber, automatic grate cleaning system, system feeding air to the mixing chamber. Moreover, the correctness of operation of protection systems was checked, i.e.:

- in the case of simulated damage to selected sensors, the boiler's operation was suspended or limited, and an interrupted sound signal was generated. The appropriate message was displayed on the LCD screen,
- in the case of exceeded boiler water temperature (95°C), forced for testing purposes, the boiler's active thermal protection was engaged, and an interrupted sound signal was generated. Fuel feeders, the igniter and intake blower were disconnected, thanks to which the burning process was interrupted. Boiler restart was possible after pressing the RESET button on the controller's housing.

Simultaneously, the quality of the combustion process in the burner chambers was checked, and emissions of harmful substances were measured. As a result of conducted tests, high quality of the combustion process was determined, and contents of harmful substances (Carbon monoxide (CO), particulate matter) were determined to be at an acceptable level, according to PN-EN 303-5:2012 [10] and eco-design requirements as per the Regulation of the European Commission [11].

13.4. CONCLUSIONS

Air pollution is the most harmful to health and the environment out of all types of pollution. Boiler designs with modern burners, fired by biomass, should be characterized by high energy efficiency and compliance with environmental protection standards. The efficiency of the combustion process is determined by the amount of heat obtained. The quality of the combustion process can be evaluated by the efficiency of the fuel processing equipment. The higher the efficiency, the more energy is obtained from combustion of a unit of fuel. One should also remember that, for the purpose of minimizing environmental hazards, besides modern boiler and burner designs, selection of fuel of proper quality and correct selection of flue gas discharge installations, the designing and implementation of an appropriate control system is also necessary. Inadequate control system solutions result in elevated emissions of harmful substances into the atmosphere and reduces the efficiency of the combustion process, which increases operating costs as a result. Some conclusions are presented in the following points.

- The selected FuzzyLogic 500 – Cherokee advanced microprocessor controller is intended for the regulation of the boiler's operating parameters according to adopted assumptions.
- Real-time clock functions make it possible to configure weekly work schedules for circulating pumps and the burner.
- Optional room regulators make it possible to maintain a set temperature in rooms, as desired by the residents.
- Measurement of flue gas temperature and oxygen content in flue gas by the lambda sensor makes it possible to achieve high energy efficiency of the boiler. The lambda sensor is the most important component responsible for the combustion process and increases the boiler's operating efficiency substantially. This directly leads to limitation of its operating costs and adverse environmental impact.
- The designed and implemented control system fulfills the adopted assumptions. The automatically modified time of fuel feeding and amount of supplied air, appropriate for current conditions and required for proper performance of the combustion process, significantly raises its eco-friendliness and efficiency, which consequently translates to economical boiler operation.
- The designed control system and burner construction ensure high quality of the combustion process and harmful substances at an acceptable level, according to PN-EN 303-5:2012 [10] and eco-design.
- Having in mind the above advantages of the heating boilers utilizing a renewable energy source – biomass with selected FuzzyLogic 500 microprocessor controller, electrostatic precipitators used for the removal of fly ash are not required. Commercial designs of electrostatic precipitators used for the removal of fly ash particles from small residential boilers are presented in the publication [15].

REFERENCES

[1] *Clean Air Programme*, https://ec.europa.eu/environment/air/clean_air/index.htm (accessed: 10.10.2020).

[2] *European Environment Agency – Policy context*, http://www.eea.europa.eu/themes/air/policy-context (accessed: 10.10.2020).

[3] *Energy Policy Review, European Union 2020 - Country report*, https://www.iea.org/reports/european-union-2020 (accessed: 18.10.2020).

[4] KWINTA W., *Renewable energy sources in Poland and the world*. *RES – indispensable for the world*, https://inzynieria.com/energetyka/odnawialne_zrodla_energii/rankingi/58459,odnawialne-zrodla-energii-w-polsce-i-na-swiecie,pozycja-rankingu-warianty-dalszego-wzrostu-oze (In Polish) (accessed: 10.10.2020).

[5] *Global Energy Review 2020. Flagship report*, https://www.iea.org/reports/global-energy-review-2020, (accessed: 16.10.2020).

[6] PALOMBA V. et al., Implementation of a solar-biomass system for multi-family houses: Towards 100% renewable energy utilization, *Renewable Energy*, vol. 166, p. 190-209, 2020.

[7] ØSTERGAARD P. A. et al., Recent advances in renewable energy technology for the energy transition, *Renewable Energy*, vol. 179, p. 877-884, 2021.

[8] KOMITOV N., SHOPOV N., RASHEVA V., Model of a building heating system with renewable energy sources, in: *E3S Web of Conferences 2007*, p. 02006, 2020.

[9] *Environmental Protection Law*, https://www.lexlege.pl/prawo-ochrony-srodowiska/art-96/ (In Polish), (accessed: 16.10.2020).

[10] PN-EN 303-5:2012 Heating boilers – Part 5: Heating boilers for solid fuels, manually and automatically stoked, nominal heat output of up to 500 kW – Terminology, requirements, testing and marking.

[11] Commission Regulation (EU) 2015/1189 of 28 April 2015 implementing Directive 2009/125/EC of the European Parliament and of the Council with regard to ecodesign requirements for solid fuel boilers (Text with EEA relevance), https://op.europa.eu/pl/publication-detail/-/publication/8809cda2-2f6e-11e5-9f85-01aa75ed71a1/language-en/format-PDFA1A (accessed: 16.10.2020).

[12] HUŚCIO T., KOWALEWSKI A., Modern burner for central heating boilers utilizing renewable energy source – biomass, in: *16th International Scientific Conference Engineering for Rural Development*, vol. 35, no. 1, p. 89–103, 2005.

[13] KOWALEWSKI A. *Palnik do kotłów c.o. wykorzystujący źródło energii odnawialnej. (Burner for central heating boilers utilizing a renewable energy source).* Patent nr PL 231605 B1, Patent Office of the Republic of Poland, 2016.

[13] *Operation and maintenance documentation of pellet-fired central heating water boilers*, http://www.pionier-elektryk.pl/?page=dokumenty (In Polish) (accessed: 20.10.2020).

[14] *Instruction manual of FuzzyLogic 500 – Cherokee controller*, http://www.pionier-elektryk.pl/?page=dokumenty (In Polish) (accessed: 20.10.2020).

[15] JAWOREK A. at al., Particulate matter emission control from small residential boilers after biomass combustion. *Renewable and Sustainable Energy Reviews*, vol. 137, p. 110446, 2021.

DOI: 10.24427/978-83-66391-87-1_14

Mykhaylo MELNYK[1], Andriy KERNYSKYY[1],
Mykhaylo LOBUR[1], Andrzej ŁUKASZEWICZ[2]

14. DETERMINATION OF THE NOISE SOURCE HEIGHT BASED ON THE VEHICLE TYPES

In this work, we present a developed mathematical model for determining the height of a dominant noise source in a transportation flow of vehicles. The theoretical approach proposed in [1, 2] which uses road noise forecasting methods to improve the accuracy of methods for determining the noise barriers effectiveness was experimentally substantiated.

14.1. INTRODUCTION

Today, designers of noise barriers that have to protect from the linear noise sources apply methods that do not take into account specifics of a modern traffic. It is apparent that in the '80s and even '90s, the percentage of trucks in the vehicle flow was much larger and scientists who developed these methods and regulations believed that the percentage of trucks was no more than 60%. Besides this, different methods use different sources of noise height position above the road. For example, the VDI-2720 method [3] recommends a height of 0.5 m for noise sources, and *Guide to the design and calculation of building protection from transport noise* [4] recommends 1 m.

The task of investigating at which height the major noise sources in vehicles are located and constructing a mathematical model for determining the height of the dominant noise source in the vehicle flow as a function of speed, to improve the accuracy of methods for determining the effectiveness of noise barriers is urgent.

[1] Lviv Polytechnic National University, Ukraine
[2] Bialystok University of Technology, Poland

14.2. DETERMINATION OF THE NOISE SOURCE HEIGHT

The results obtained in the frame of the Harmonoise and Imagine [5] projects were intended for use by the EU Member States during the creation of noise maps and other purposes related to the evaluation of noise pollution and city noise protection. In the framework of these projects, experimental studies of sound power levels from individual sources of noise in cars and trucks were conducted. The main sources of noise are the tires and road surface interaction, as well as the car exhaust system. The results of the experiments are presented in Fig. 14.1 and Fig. 14.2.

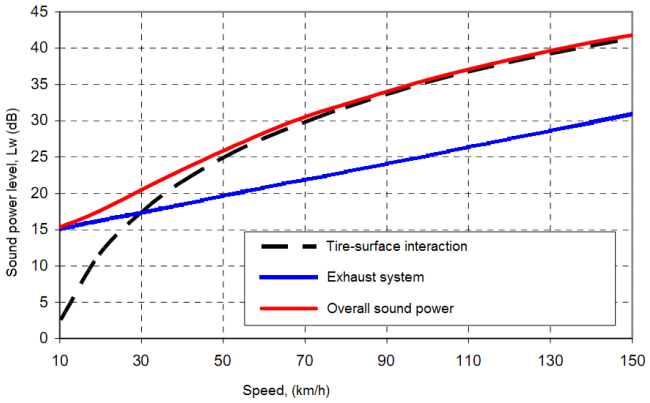

Fig. 14.1. Dependence of sound power level of speed for cars [6]

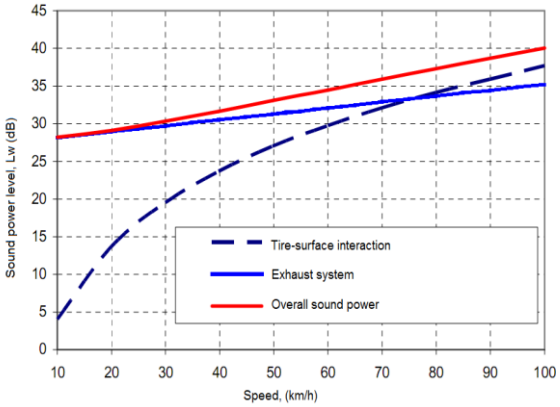

Fig. 14.2. Dependence of sound power level of speed for trucks [6]

The three curves of the graph (Fig. 14.1) represent the dependence of the sound power level rate for cases where the interaction is assessed separately for automobile tire and coated roads, exhaust system and the overall level of sound power for automobiles. A similar graph for trucks is shown in Fig. 14.2. As seen on the graph in Fig. 14.1 for the car sound power level of interaction between car tires and the coated road starts to dominate above the sound of the power exhaust system at speed 30 km/h. Therefore, we propose to take this fact into account when determining the shielding effectiveness of sound energy. A mathematical model allows an accurate determination of the height of

the dominant source of noise above the road and improve the accuracy of methods to define the efficiency of sound barriers.

In the work [6] based on experimental data, the height of the main noise sources in cars and trucks were found. For automobiles, the height noise source position is 0.3 m for the exhaust system and 0.01 m for the noise source from the interaction of car tires with the road surface (Fig. 14.3). For trucks, the noise source from the interaction of tires with the road surface is 0.01 m and the noise source height from the exhaust system is larger and amounts to 0.7 m (Fig. 14.3).

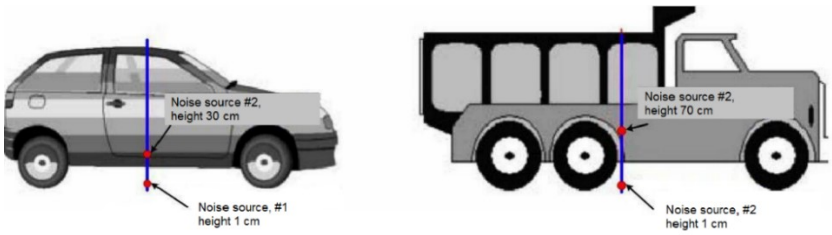

Fig. 14.3. Placing the main sources of noise in cars and trucks [6]

We used a designed subsystem to determine the effectiveness of noise barriers to calculate the influence of height on the screening efficiency for different values of the distances between the screen and the noise. It was found that at small distances between the point of observation of the noise barriers and the source noise, the change of the height of the dominant sources of noise from 1 cm to 70 cm, which is typical of trucks, makes the difference in 1 dB, and typical height for the dominant sources of noise in cars from 1 cm to 30 cm gives the difference of 0.5 dB. Therefore, for trucks and cars, the height of noise sources positions will be 0.7 m and 0.3 m respectively, while the sound power level of interaction between car tires with the road surface will be greater than the level of sound power of exhaust system at 1 dB for trucks and 0.5 dB for cars. From the graph presented in Fig. 14.2, it follows that the height of the dominant noise source for trucks at the speed of 85 km/h is 0.7 m. At higher speeds, the difference between sound power level of interaction between car tires with the road surface and the exhaust system is not increased significantly. Considering the previous fact and that the source of noise from the exhaust system is higher, it follows that this noise source will make a significant contribution to the emission of sound energy. Based on the above, for trucks, we propose to take the height of the dominant sources of noise at 0.7 m above the road surface regardless of the speed.

Analyzing the graph for cars in Fig. 14.1, the height of the noise source position for speeds up to 32 km/h will be constant and equal to 0.3 m. If the difference between the level of the sound from the exhaust system and tire interaction with the surface is over 10 dB [7], there is no need to take into consideration the noise from the exhaust system. Therefore, for speeds above 100 km/h, the noise from the exhaust system can be neglected. That means, the height of the noise source is 0.01 m (corresponding to the height of the noise source of the interaction of the tire with the road surface). For speeds

in the range of 32 to 100 km/h, the height of the noise source will vary in proportion to speed. Based on the above, the following mathematical expression was constructed

$$h_{h,car} = \begin{cases} 0.3 & \text{at } V < 32[\text{km/h}], \\ -0.0043 \cdot v + 0.4365 & \text{at } 32 \le V < 100[\text{km/h}], \\ 0.01 & \text{at } V > 100[\text{km/h}], \end{cases} \quad (14.1)$$

where $h_{S,car}$ is a height of the dominant noise sources for cars [m], V is an average speed of cars [km/h]

$$v = \frac{V \cdot [h]}{1000}.$$

Applying the Heaviside function [8] to the expression (14.1)

$$H(x) = \begin{cases} 0, & x < 0, \\ 1, & x \ge 0, \end{cases}$$

a model of the height of the dominant sources of noise in the traffic flow is the following

$$h_{S,car} = \frac{3H(32 - V_H)}{10} + H(V_H - 32)H(99 - V_H)\left(\frac{873}{2000} - \frac{43 \cdot V_H}{10000}\right) + \frac{H(V_H - 99)}{100}, \quad (14.2)$$

where $V_H = \frac{V \cdot [h]}{[km]}$, $x \in \mathbb{R}$.

Expression (14.2) allows us to determine the height of the dominant noise sources in the traffic flow depending on the speed.

Table 14.1. Dependence of equivalent sound level of traffic for a distance of 10 m from noise sources

Trafic intensity, vehicles/hour	Trucks	Cars	Difference between cars and trucks [dB]	Total
	Leq [dB]	Leq [dB]		Leq [dB]
200	61.1	57.3	3.7	62.5
400	64.1	60.4	3.7	65.5
600	65.8	62.1	3.7	67.2
800	67.1	63.4	3.7	68.5
1000	68.0	64.3	3.7	69.5
1200	68.8	65.1	3.7	70.2
1400	69.5	65.8	3.7	70.9
1600	70.1	66.4	3.7	71.5
1800	70.6	66.9	3.7	72.0
2000	71.1	67.3	3.7	72.5

Some methods of predicting road noise do not allow us to determine separately the noise level from different categories of vehicles, so the task is to investigate the change in

the equivalent noise level in 10% of trucks, depending on the intensity of traffic. For different vehicle intensities, 10% of trucks and a distance of 10 m from the noise source, equivalent noise levels were calculated. Based on the calculations, it was discovered that the difference between the equivalent noise level from cars and trucks remains constant and does not change with the change of intensity. The results obtained are presented in Table 14.1.
Graphical dependence is shown in Fig. 14.4. was built based on data from Table 14.1.

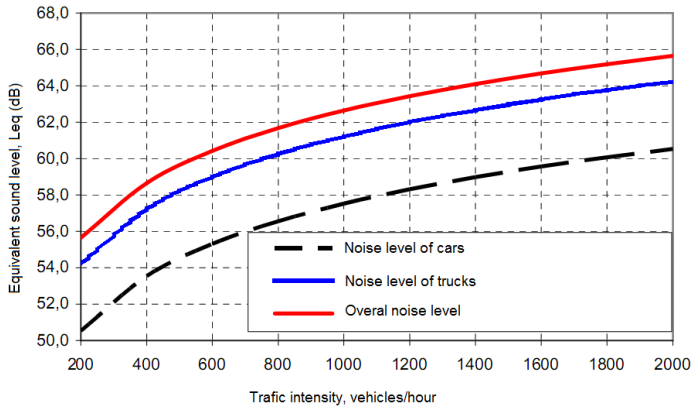

Fig. 14.4. Dependence of equivalent sound level of car traffic

Analyzing the above-listed graph, one can say that the difference between the equivalent noise level from cars and trucks is constant and does not change when the intensity is changed.

Table 14.2. Dependence of equivalent sound level of traffic for a distance of 25 m from the noise sources

Trafic intensity, vehicles/h	Trucks	Cars	Difference between trucks and cars [dB]	Total
	Leq [dB]	Leq [dB]		Leq [dB]
200	50.5	55.6	3.7	54.2
400	53.5	58.7	3.7	57.2
600	55.3	60.4	3.7	59.0
800	56.5	61.7	3.7	60.3
1000	57.5	62.6	3.7	61.2
1200	58.3	63.4	3.7	62.0
1400	59.0	64.1	3.7	62.7
1600	59.6	64.7	3.7	63.3
1800	60.1	65.2	3.7	63.8
2000	60.5	65.6	3.7	64.2

It was investigated whether this difference remains constant when the distance is changed from the noise source. For this purpose, an equivalent noise level with different traffic intensity was calculated for a distance of 25 m from the noise source whose values are given in Table 14.2. As seen from the gained results (Table 14.2), the difference between the equivalent noise level from cars and trucks by changing the distance to the source of noise is also constant. In this regard, determining what percentage of trucks in

the vehicle stream will have an equivalent noise level will prevail, this value will be true for any distance and intensity. The next step will be to define the equivalent sound level depending on the percentage of trucks in the traffic flow. The calculated data are given in Table 14.3 and Fig. 14.5.

Table 14.3. Dependence of equivalent sound level of the percentage of trucks in the flow of vehicles

Percentage of trucks	Total	Trucks	Cars	Difference between trucks and cars, [dB]
	Leq [dB]	Leq [dB]	Leq [dB]	
0.1	50.6	34.2	50.5	-16.3
10	55.6	54.2	50.1	4.2
20	57.9	57.2	49.6	7.7
30	59.4	59	49	10
40	60.5	60.3	48.3	11.9
50	61.4	61.2	47.5	13.7
60	62.1	62	46.5	15.5
70	62.8	62.7	45.3	17.4
80	63.3	63.3	43.5	19.7
90	63.8	63.8	40.5	23.2

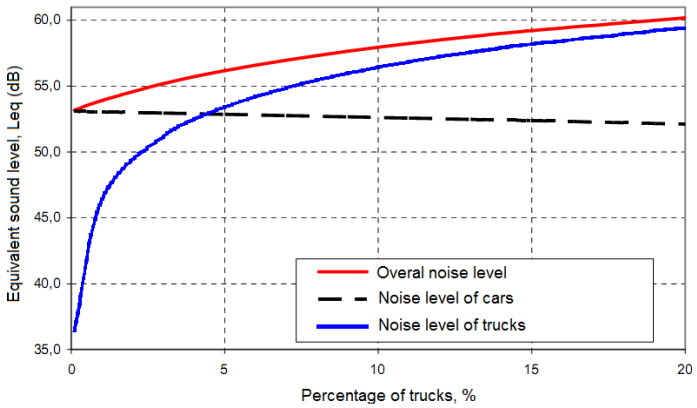

Fig. 14.5. Dependence of equivalent sound level of the percentage of trucks

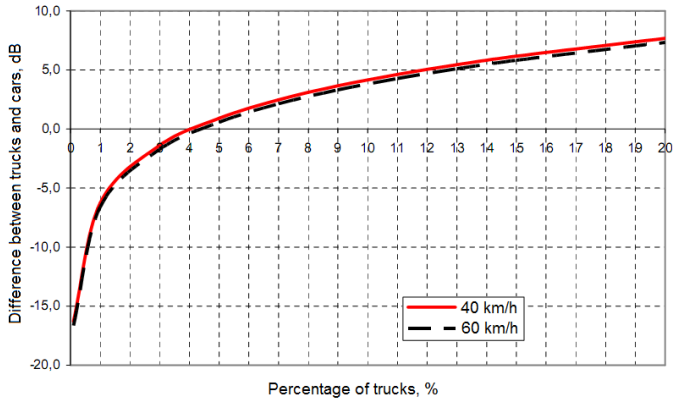

Fig. 14.6. The difference of equivalent sound levels between trucks and cars

Studies showed (Fig. 14.5 and Fig. 14.6) that when the number of trucks in the traffic flow is more than 4%, the height of the noise source will be the same as that of trucks and will be independent of the speed of 0.7 m. When the number of trucks is less than 0.5%, the height of the source noise will be determined from (14.1). The height of the dominant noise source for traffic flows consisting of 0.5% to 4% of trucks will be determined by the following relationship

$$h_S = 0.198 \cdot p - 0.089, \tag{14.3}$$

where p is the percentage of trucks in the traffic flow [%].

Therefore, to determine the height of the dominant noise source in the flow of vehicles, depending on the speed and percentage of trucks, we constructed the following relation

$$h_S = \begin{cases} 0.3 & \text{at } V < 32[\text{km/h}] & \text{at } p \le 0.5, \\ -0.0043v + 0.4365 & \text{at } 32 \le V < 100[\text{km/h}] & \text{at } p \le 0.5, \\ 0.01 & \text{at } V \ge 100[\text{km/h}] & \text{at } p \le 0.5, \\ 0.198p - 0.089 & & \text{at } 0.5 < p \le 4, \\ 0.7 & & \text{at } p > 4. \end{cases} \tag{14.4}$$

Applying the Heaviside function to the expression (14.4) we wrote it as follows

$$h_S = H(0.6 - p) \times h_{S,car} + H(p - 0.6)H(4.1 - p)\left(\frac{99 \times p}{500} - \frac{89}{1000}\right) + \frac{H(p - 4.1) \times 7}{10}. \tag{14.5}$$

Expression (14.5) can be used to determine the height of the dominant sources of noise in the traffic flow depending on the speed and percentage of trucks. By determining the exact height of the noise source position, we can more accurately determine the effectiveness of noise barriers.

In summary, the resulting model can be used to determine the dominant noise source for passenger cars and trucks separately. Accordingly, it can be used to improve the accuracy of road noise forecasting methods that allow the determination of noise levels separately for trucks and cars.

14.3. CONCLUSIONS

Mathematical models to determine the dominant noise sources for cars and trucks, as well as in the flow of vehicles were created that allowed the increase in the accuracy of forecasting methods of road noise and methods for determining the efficiency soundproofed screens.

The project is financed by the Polish National Agency for Academic Exchange, No. PPI/APM/2018/1/ 00049/U/001.

REFERENCES

[1] MELNYK M., LOBUR M., KERNYTSKYY A., Information model of computer-aided noise barriers design system, in: *Monitoring środowiska: Proceedings of 1st International Conference*. Krakow, Poland, p. 24, 2010.

[2] Melnyk M., LOBUR M., PETSUKH A., Structure development of computer-aided noise barriers design system, in: *Proceedings of the VIth International Conference (MEMSTECH'2010)*, Lviv, p. 235 – 236, 2010.

[3] VDI-Richtlinie 2720, *Schallschutz durch Abschirmung im Freien*, Verein Deutscher Ingenieure, Dusseldorf, p. 1-14, 1991.

[4] *Guide to the design and calculation of building protection from transport noise* (in Russian), Striyizdat, Moscow, p. 30, 1982.

[5] Imagine Project, http://www.imagine-project.org (accessed: 10.09.2020)

[6] GRAAFF E., *Road source model*, Imagine Project informal document no. GRB-48-6, 2008.

[7] GOST ISO 362-2006 (ISO 362:1998, IDT), *Noise from vehicles - acoustics - measurement of noise emitted by accelerating road vehicles*, Gosstrandart, Moscow, p. 17, 2007.

[8] VOLKOV I. K., KANATNIKOV A. N., *Integral transformations and operational calculus*, Bauman MGTU Publishing House, Moscow, p. 228, 2002.

LIST OF THE AUTHORS

Mykhaylo ANDRIYCHUK	Ivan Franko National University of Lviv, Ukraine ORCID: 0000-0001-9380-8807
Olexander BELEJ	Lviv Polytechnic National University, Ukraine ORCID: 0000-0003-4150-7425
Nataliia BOKLA	Lviv Polytechnic National University, Ukraine ORCID: 0000-0002-8919-6622
Viktoriia BORTNIKOVA	Kharkiv National University of Radio Electronics, Ukraine ORCID: 0000-0002-6215-7797
Iryna BOTSMAN	Kharkiv National University of Radio Electronics, Ukraine ORCID: 0000-0003-1110-9602
Tomasz HUŚCIO	Bialystok University of Technology, Poland ORCID: 0000-0001-5971-4188
Wiktor JAKOWLUK	Bialystok University of Technology, Poland ORCID: 0000-0003-0942-8903
Mariusz JANKOWSKI	Lodz University of Technology, Poland ORCID: 0000-0002-6050-3975

Nazariy JAWORSKI — Lviv Polytechnic National University, Ukraine
ORCID: 0000-0003-1312-7302

Roman KACZYŃSKI — Bialystok University of Technology, Poland
ORCID: 0000-0001-5736-5367

Ihor KAPRAN — National Forestry University of Ukraine, Ukraine

Yaroslav KASPRYSHYN — National Forestry University of Ukraine, Ukraine
ORCID: 0000-0003-1118-9059

Andriy KERNYTSKYY — Lviv Polytechnic National University, Ukraine
ORCID: 0000-0001-8188-559X

Kostiantyn KOLESNYK — Lviv Polytechnic National University, Ukraine
ORCID: 0000-0001-9396-595X

Andrzej KOSZEWNIK — Bialystok University of Technology, Poland
ORCID: 0000-0001-6430-6007

Maryana LEVKOVYCH — National Forestry University of Ukraine, Ukraine
ORCID: 0000-0002-0119-3954

Mykhaylo LOBUR — Lviv Polytechnic National University, Ukraine
ORCID: 0000-0001-7516-1093

Andrzej ŁUKASZEWICZ — Bialystok University of Technology, Poland
ORCID: 0000-0003-0373-4803

Cezary MAJ — Lodz University of Technology, Poland
ORCID: 0000-0001-6897-0378

Uliana MARIKUTSA — Lviv Polytechnic National University, Ukraine
ORCID: 0000-0002-9514-7413

Mykhaylo MELNYK — Lviv Polytechnic National University, Ukraine
ORCID: 0000-0002-8593-8799

Andrzej NAPIERALSKI — Lodz University of Technology, Poland
ORCID: 0000-0002-3844-3435

Jacek NAZDROWICZ — Lodz University of Technology, Poland
ORCID: 0000-0001-8523-8170

Igor NEVLIUDOV — Kharkiv National University of Radio Electronics, Ukraine
ORCID: 0000-0002-3833-9582

Paweł OSTAPKOWICZ — Bialystok University of Technology, Poland
ORCID: 0000-0003-0430-4696

Artur PRUSINOWSKI — Bialystok University of Technology, Poland
ORCID: 0000-0001-6945-2388

Roman TROCHIMCZUK — Bialystok University of Technology, Poland
ORCID: 0000-0002-0614-5222

Volodymyr SHYMANSKYI — National Forestry University of Ukraine, Ukraine
ORCID: 0000-0002-7100-3263

Oleksiy SINKEVYCH — National Forestry University of Ukraine, Ukraine
ORCID: 0000-0001-6651-5494

Yaroslav SOKOLOVSKYY — National Forestry University of Ukraine, Ukraine
ORCID: 0000-0003-4866-2575

Adam STAWIŃSKI — Lodz University of Technology, Poland

Michał SZERMER — Lodz University of Technology, Poland
ORCID: 0000-0002-9294-701X

Roman VOLIANSKYI — Dniprovsk State Technical University, Ukraine
ORCID: 0000-0001-5674-7646

Tadeusz WIĘCKOWSKI — Wroclaw University of Science and Technology, Poland
ORCID: 0000-0001-6908-3244

Vladyslav YEVSIEIEV — Kharkiv National University of Radio Electronics, Ukraine
ORCID: 0000-0002-2590-7085

INFORMATION ABOUT THE AUTHORS

Mykhaylo I. ANDRIYCHUK (M'95, SM'03) received M.Sc. degree in computational mathematics from the Lviv National University, Ph.D. degree in application of computational techniques from the Kyiv National University, and D.Sc. degree in mathematical modeling from the Lviv Polytechnic National University in 1976, 1987, and 2015, respectively. He is employed by the Pidstryhach Institute for Applied Problems of Mechanics and Mathematics (IAPMM), Lviv, Ukraine. Currently, he is the Head of Department of the Numerical Methods in Mathematical Physics at the IAPMM. He is author and co-author to more than 160 papers in the scientific journals and international conference proceedings, which concern to the diffraction and antenna synthesis theory, optimization methods and nonlinear integral equations. He is a visiting professor at the Lviv Polytechnic National University. He is a co-author of the monograph *The antenna synthesis according to the amplitude radiation pattern. Numerical methods and algorithms* (Kiev, Naukova Dumka Publ., 1993), and author of monograph *Antenna synthesis through the characteristics of desired amplitude* (Newcastle, UK, Cambridge Scholars Publ., 2019).

Olexander I. BELEJ is an associate professor of CAD Department of Lviv Polytechnic National University from 2018. Since 1998, he worked as a software engineer and system administrator for various companies, since 2000, he worked as scientist and teacher on information technology, modeling and control of complex processes and systems, mining systems and forecasting data. His research interest includes: intelligent data analysis, synergetic modeling, cryptographic algorithms development, neural network modeling, software protection of data with closed and public key, databases and data warehouses. He is the author of more than 100 scientific works, co-author of 6 monographs, 3 manuals, participated in more than 60 international scientific-practical conferences.

Roman KACZYŃSKI is a professor at the Faculty of Mechanical Engineering, Bialystok University of Technology, Poland. He has been working since 1979 in the Department of Fundamentals of Machinery Design at the Faculty of Mechanical Engineering in Bialystok. From 2009, he was the head of the Department of Production Engineering, from 2014 he is the head of the Department of Machine Construction and Operation. His scientific achievements include 112 publications and two scientific monographs. He obtained 9 patents and has 6 patent applications, of which, three have been implemented in industry. As part of his research work, he is involved in modeling the friction process and wear of sliding bearings of carbon fiber-reinforced polymers, controlling transient processes of kinematic systems based on structural-energy theory of friction and thermal processing technology for micro and nano - modification of thermoplastic machine elements based on polymers.

Ihor KAPRAN is an assistant at the Information Technology Department of the National Forestry University of Ukraine. In 2008, he graduated from the National Forestry University of Ukraine with a major in *Automation of production processes and computer-integrated technologies* and received a master's degree. From 2008 to 2011, he studied at the postgraduate course of the National Forestry University of Ukraine. He conducts research in the field of mathematical modeling and control of stress-strain state of wood in the process of drying wood. Structural analysis methods and parametric optimizations.

Yaroslav KASPRYSHYN is a PhD student in the Information Technology Department of the National Forestry University of Ukraine. In 2014, he completed Master's degree with honors in Applied and Theoretical Statistics of the Faculty of Mechanics and Mathematics at the Kyiv-Mohyla Academy. The main direction of scientific research includes modeling of deformation-relaxation processes in environments with fractal structure.

Andriy KERNYTSKYY is an associate professor in the Department of Computer Aided Design, Institute of Computer Science and Information Technology, Lviv Polytechnic National University. He received Ph.D. from Institute of Machine Design Fundamentals at the Warsaw University of Technology in 2003.
His research interests include CAx technologies, information systems development, artificial intelligence, problems of acoustics, forecasting problems.

Mariana LEVKOVYCH is an assistant in the Department of Information Technology, the National Forestry University of Ukraine. In 2014, she completed Master's degree with honors in Applied and Theoretical Statistics of the Faculty of Mechanics and Mathematics at the Ivan Franko Lviv National University. In 2017, she completed her postgraduate studies at the National Forestry University of Ukraine. She is Candidate of Technical Sciences, the dissertation was defended at the Lviv Polytechnic National University in 2019. The main direction of scientific research is in mathematical modeling of interconnected heat-mass transfer and deformation-relaxation processes in capillary-porous materials.

Mykhaylo LOBUR is a professor, Head of the Department of Computer-Aided Design Systems in Lviv Polytechnic National University. He obtained the distinguished titles *Honored Scientist of Ukraine*, *Excellence in Education of Ukraine*, Doctor of honoris causa of Donetsk National Technical University (2013), Lodz University of Technology *Honored for Lodz Polytechnic* (2011). His research interests include MEMS - design, simulation and analysis, implementation of VHDL-AMS, design of technological processes, organizational aspects of technological process modeling.

Andrzej ŁUKASZEWICZ received Ph.D. in applied mechanics from Warsaw University of Technology, Institute of Machine Design Fundamentals in 2003. Since 1997, he is a scientist and teacher with the Faculty of Mechanical Engineering, Bialystok University of Technology. In 2007, he obtained CSWA (Certified SolidWorks Professional) as the first academic teachers in Poland. He received six times *The Best Leader a – Scientific Supervisor* award in Polish SolidWorks Student Competition. In 2010, he was invited as plenary speaker with the topic *SolidWorks based CAx education directed for industrial practice* to the SolidWorks World, Anaheim, USA. He is the author or co-author of over 150 peer-reviewed papers and book chapters. In 2019, he was awarded the Silver Honor Badge of Polish Society of Mechanical Engineers and Technicians. His main research topics are: CAD, CAx, thermoelastic FEA, modelling of friction welding processes and UAV design and manufacturing.

Cezary MAJ was born in Lodz, Poland, in 1982. He received the M.Sc. degree in electronics from Lodz University of Technology (TUL), Poland, in 2005 and Ph.D. degree in microelectronics from both TUL and Institut National des Sciences Appliquées de Toulouse (INSA), France. He specializes in microelectronics and his research focuses on modelling, fabrication and characterization of microsystems. He took part in few projects connected with the development of sensors for various applications. Recently, he is involved in MEMS modelling, investigation of thermal problems in current multicore processors, developing of accelerometers and gyroscopes for medical purposes and developing of electronics for fiber optic gyroscopes.

Uliana B. MARIKUTSA received the M.Sc. degree in information systems, and Ph.D. degree in computer systems and components with doctoral thesis titled *Information and measurement system for rapid detection of toxic chemicals in the air environment* in 1998, and 2009 respectively, from the Lviv Polytechnic National University (LPNU), Ukraine. Now, she works as an assistant professor in the Department of Computer Aided Design Systems, Institute of Computer Science and Information Technologies at the NULP. Dr. Marikutsa participates at the international scientific and educational cooperation under the programs Trans-European Mobility Programme for University Studies, Narodowa Agencja Wymiany Akademickiej (NAWA). She has been serving as an active member of the Organizing Committee of the International Scientific Conference on the Experience of Designing and Application of CAD Systems in Microelectronics (CADSM) and the International Conference on Perspective Technologies and Methods in MEMS Design (MEMSTECH). Her scientific interests are the development of mathematical models of heat transfer processes in microelectronic devices, design and development of components of information-measuring systems

Mykhaylo MELNYK is an associate professor at the Department of Computer Aided Design Systems, Lviv Polytechnic National University, Ukraine. From 2011 to 2015, he was an assistant with the Department of Computer Aided Design Systems, Faculty of Computer Science and Information Technology, Lviv Polytechnic National University, and since 2015, he is an associate professor with CAD Department. His main research interests lie in the prediction of road noise, noise barriers, database design, computerized information systems, acoustics of buildings, MEMS.

Jacek NAZDROWICZ was born in Poddębice, Poland, in 1975. He received M.Sc. degrees in technical physics, computer sciences, marketing and management, mathematics from Lodz University of Technology, Poland, in 2001, 2002, 2004 and 2018 respectively and Ph.D. degree in economics sciences from Lodz University of Technology in 2013. His research interests include modelling and simulation of MEMS devices and their application in medicine. He participated in EduMEMS project *Developing Multidomain MEMS Models for Educational Purposes*. Now, he participates in Strategmed project (supported by the National Center for Research and Development). He has the following certifications: MCSA Windows 2012, MS SQL Server 2012 and Storage Area Network (SAN) Specialist. Since 2016 he also works in Fujitsu Technology Solutions in Lodz in Remote Infrastructure Management Department in Storage Team as a Storage Engineer (SAN Infastructure, Brocade, Netapp, Eternus products). He educates in many data storage and backup technologies (IBM, DELL/EMC, Hitachi, Fujitsu).

Artur PRUSINOWSKI received B.Sc. in mechatronics from Silesian University of Technology, Gliwice, Poland, in 2014, and M.Sc. in mechanical engineering from Bialystok University of Technology, Bialystok, Poland, in 2016. Currently, he is a PhD student at the Faculty of Mechanical Engineering, Bialystok University of Technology. His research interests include Rapid Prototyping techniques and Additive Manufacturing techniques. His research focuses on improving the techniques of forming fiber composites in 3D Fused Deposition Modeling (FDM) printing and testing the properties of these materials. The outcome of this research was to develop leadership in research projects and obtain patent rights to the head used in the FDM.

Oleksiy SINKEVYCH is an assistant at the Information Technologies Department of the National Forestry University of Ukraine. In 2013, he graduated with honors from the Technological College of Lviv Polytechnic National University (Ukraine) with a degree in Computer Networks and Systems Service. In 2017, he graduated with honors from the National Forestry University of Ukraine (Lviv). In 2018, he successfully completed an internship at the University of Sustainable Development (Federal Republic of Germany, Eberswalde) under the Erasmus + Academic Mobility Program (KA1). He is pursuing research in the following areas: information technologies for modeling and analysis of thermomechanical processes in integrated computer aided design systems, and SolidWorks Flow Simulation environment. In addition, he is engaged in object-oriented analysis and design of software, including the use of the theory of cellular automata. As part of his scientific work, he has published more than 30 scientific works, 12 of which are indexed in the Scopus database.

Volodymyr SHYMANSKYI is an associate professor of the Information Technology Department at the National Forestry University of Ukraine. In 2008, he graduated from the Faculty of Applied Mathematics and Informatics at the Ivan Franko Lviv National University and received Master of Applied Mathematics and Teacher of Informatics. Candidate of Technical Sciences - defended his dissertation at Lviv Polytechnic National University in 2016. The main direction of scientific researches is: mathematical modeling of nonequilibrium physical processes in environments with fractal structure. As part of his scientific work, he published 35 scientific papers, 6 of which are indexed in the Scopus database. According to the results of scientific activity, the scientist was awarded the Regional State Administration and Regional Council Award for Young Scientists (2019).

Yaroslav SOKOLOVSKYY is the Head of the Information Technology Department of National Forestry University of Ukraine. In 1991, he obtained the title Candidate of Physics and Mathematics. He is a Doctor of Technical Sciences since 2002. He further obtained the academic title of professor in 2003. The main directions of scientific research is mathematical modeling of interconnected heat-mass transfer and deformation-relaxation processes in capillary-porous materials; information technology of production processes design; design of CAE/CAD/CAM systems. Under his leadership, fifteen candidates (PhD) dissertation and one doctoral dissertation were defended. He has received two international grants under ISSEP in the field of basic research and under the DAAD program (Universität Hamburg, Germany).

Adam STAWIŃSKI was born in Zgierz, Poland, in 1988. He received the MSc degree in Biotechnology with specialization in Medical Biotechnology from the Medical University of Lodz, Poland, in 2012. Since 2017, he attends PhD studies at the Lodz University of Technology. His research area of interests include the use of IT techniques for analyzing and processing medical and biomedical data, with the special emphasis on Big Data and Artificial Intelligence. He participated in IRS project *Developing of framework for intelligent, distributed control systems for business and industry*. Now, he participates in Strategmed project *Development of innovative system for evaluation and rehabilitation of human imbalance* and in sPParTAN project *Creation and development of personalized protective thermally active clothing*. Since 2016, he has been working in Lodz University of Technology, Department of Microelectronics and Computer Science as a specialist in the field of medical and IT project coordinator.

Roman TROCHIMCZUK is an assistant professor at the Bialystok University of Technology, Faculty of Electrical Engineering, Department of Automatic Control and Robotics, Bialystok, Poland. He received a M.Sc. degree in Automatic Control and Robotics from the Bialystok University of Technology, Faculty of Mechanical Engineering, Bialystok, Poland in 2000. He received Ph.D. degree in Automatic Control and Robotics, specialty: mechatronics from Faculty of Mechanical Engineering and Robotics, AGH University of Science and Technology, Cracow, Poland, in 2009. Since 2002, he has been a researcher and an academic teacher. His scientific interests are mainly mechatronic modelling of robot systems, medical robotics, and kinematic and dynamics analysis of the positioning systems of robots and manipulators, theory machine and mechanism, FEM analysis of mechanism with using CAD/CAE systems. He is an active member of International Society of Medical Robotics, Association of Polish Committee of Theory of Machines and Mechanisms, Association of Polish Mechanical Engineers and Technicians SIMP, and Polish Society of Theoretical and Applied Electrical Engineering.

Roman VOLIANSKYI is currently an associate professor in the Electrical Engineering Department at the Dniprovsk State Technical University. He earned his Engineer degree in Electric Drives from Dniprodzerzhinsk State Technical University, Dniprodzerzhinsk, Ukraine in 1999, his Master degree in Electric Drives in 2000 from the same university, and his PhD in Electrical Engineering from the National Mining University, Dnipropetrovsk, Ukraine in 2005. As part of his PhD thesis work, he solved the control optimization problem for an electric drive with backlash in gear. His research interest include various areas of optimization and control, electromechanical and electrotechnical systems with regular and chaotic dynamics.
The most recent achievement is the use of interval math for designing mathematical backgrounds to solve optimization problems for linear and nonlinear dynamical systems from a single viewpoint. He is serving as an editorial member in three international journals and has served as reviewer and TPC member in several IEEE conferences. R. Volianskyi has over 30 publications in international journals and conference proceedings and more than 50 in all-Ukrainian ones.


Politechnika
Białostocka